Structural investigation of silicon after ion-implantation using combined x-ray scattering methods.

Luciana Capello

N° d'ordre 60-2005 Année 2005

THESE

présentée devant

l'UNIVERSITE CLAUDE BERNARD-LYON 1

en cotutelle avec

l'UNIVERSITÁ DEGLI STUDI DI TORINO

pour l'obtention

du DIPLOME DE DOCTORAT

présentée et soutenue publiquement le

11 mai 2005

par

Mlle CAPELLO Luciana

TITRE :

Structural investigation of silicon after ion-implantation using combined x-ray scattering methods.

Directeurs de thèse :

M CANUT Bruno / M LAMBERTI Carlo

JURY :

M THEVENARD Paul, Président

M METZGER Till Hartmut

M LEVALOIS Marc

M RIEUTORD François

M TRUCCATO Marco

0.1 Aims of the work

The present work focuses on the development and application of a combination of x-ray scattering methods, namely grazing-incidence diffuse x-ray scattering (GI-DXS), x-ray specular reflectivity and conventional x-ray diffraction, able to investigate the structure of ultra-low energy ion-implanted Si. In particular, GI-DXS is a synchrotron-based technique of surface scattering, which is particularly suited to investigate the properties of the defects confined into thin crystalline layers. The interest of the industrial and scientific community in the characterisation of the unavoidable defects present after ion-implantation and annealing is strong. Indeed, this is justified by the dopant-defect interactions, which increasingly affect the final performance of the Si-based devices as a consequence of their continuous size reduction.

This work has been carried out at the European Synchrotron Radiation Facility (ESRF) in Grenoble (F) and, in particular, in the Surfaces and Interfaces Group, where both the instrumentation available and the skills of the research team have contributed to enable its realisation.

In order to improve the understanding of the ultra-shallow junctions formation in Si following ultra-low energy ion implantation, the European project IMPULSE started in November 2001 and lasted 3 years. The present PhD thesis has been performed in the framework of this research project with a partial financing of the European community.

0.2 Acknowledgments

First, I would like to acknowledge T. H. Metzger, scientist in charge of the beamline ID01 at the ESRF, for being a motivating teacher and a patient supervisor during the whole three years of my PhD. At the same time, this work would have not been possible without the help of my university official supervisors B. Canut, from the University Lyon I "C. Bernard", and C. Lamberti, from the University of Torino.

While writing this manuscript, I went through all of my PhD work. In my memory, each chapter and each experiment are associated with the precious collaboration and support from a number of colleagues and friends.

From the IMPULSE consortium, I'd like to thank M. Servidori, from CNR-IMM of Bologna, for his suggestions and help with the data interpretation, T. Feudel, M. Herden and D. Gehre, from AMD Saxony of Dresden, for the sample preparation. In addition, M. Werner and J. van den Berg, from the University of Salford, for the fruitful collaboration in the x-rays and MEIS compared analysis, D. Giubertoni and M. Bersani, from the ITC of Trento, for the SIMS profiles. For the TEM images, I'd like to thank L. Ottaviano, C. Spinella and G. Mannino, from the CNR-IMM of Catania.

From the FRENDTECH consortium, I acknowledge F. Cristiano, from the CNRS of Toulouse, W. Lerch and S. Paul, from the Mattson Thermal Products of Dornstadt, for the interesting discussion and the sample preparation.

The help on the theory and simulations was really appreciated from V. Holy, from University of Prague, K. Nordlund, from University of Helsinki and U. Pietsch, from University of Potsdam.

The whole staff of the beamline ID01 has to be acknowledged indeed for its help during the experiments and the friendly daily support. They deserve to be mentioned: A. Malachias, M. Sztucki, T. Schülli and K. Reinhold, i.e. the students and former students. B. Jean, B. Krause, O. Plantevin and G. Carbone (especially for the proof reading of the manuscript), i.e. the post-docs and former post-docs. C. Mocuta, H. Djazouli, P. Boesecke, R. Taffut, L. Petit and D. Fernandez.

A special thank to Fred and my family, who always encouraged my work from outside the ESRF.

0.3 Table of contents

0.4 Guideline for reading the manuscript

Chapter 1: Ion implantation and damage annealing in Si: an introduction

This chapter is an introduction to ion implantation and damage annealing in Si based on the current understanding of such phenomena. In the first section of this chapter, the use of ion implantation for the fabrication of Si-based microprocessors is addressed. The second part concerns some basic aspects of the physics related to ion implantation in Si. In the final section, the most common techniques for the structural characterisation of ion-implanted Si are summarised.

Chapter 2: Theoretical background

Grazing incidence diffuse x-ray scattering (GI-DXS) is the main experimental technique used in the present work for the investigation of the structural properties of ion-implanted Si. In Ch. 2, the theoretical background of this experimental method is described starting from the specific literature available on this subject. Sec. 2.1 contains the explanation of the origin of the defect-induced diffuse x-ray scattering (DXS) and a summary of the theory of the DXS for point and extended defects applied to bulk crystals. The use of the grazing-incidence scattering geometry enables the near-surface sensitivity of the x-rays. For this reason, it is needed in order to study the structure of ultra-low energy ion implanted Si. The physics related to the evanescent wave scattering is briefly reported in Sec. 2.2. Finally, in Sec. 2.3, the results from the theory of the GI-DXS technique are discussed.

Chapter 3: Methods and experimental details

In the first part of this chapter, the main features of the beamline ID01 at the European Synchrotron Radiation Facility (ESRF), where all the x-ray experiments were carried out, are described. In the following section, the set-up for grazing incidence experiments is explained in details due to its importance for the use of near-surface sensitive x-ray scattering

techniques. In the second part of the chapter, the GI-DXS data acquisition is illustrated and one example of GI-DXS data analysis is given. The combination of GI-DXS, specular reflectivity (SR), conventional x-ray diffraction (XRD) and grazing incidence diffraction (GID) for the complete structural characterisation of ion-implanted Si will be the subject of the final section of this chapter.

Chapter 4: Solid phase epitaxial regrowth of Si amorphised by As implantation

A study of the evolution of the structural properties of Si during solid phase epitaxial regrowth at low temperature after arsenic ion implantation is reported. Simultaneously, the influence of impurity atoms in Si on the GI-DXS signal is studied. The results from SR, conventional XRD and GI-DXS are presented and discussed. At the end of the chapter, a comparison with the corresponding results obtained by medium energy ion scattering (MEIS) is given.

Chapter 5: Influence of the pre-amorphisation on the structural properties of ion-implanted Si

In this chapter, the influence of the amorphisation of the Si substrate before the dopant-implantation (PAI) on the final structural properties of the implanted samples is investigated. The study of the preamorphisation effect, reported in this chapter, was used as a test for the capabilities of the x-ray techniques. The advantages and drawbacks of the use of x-ray scattering methods with respect to other experimental techniques, such as transmission electron microscopy and MEIS, will be discussed in the final section.

Chapter 6: Evolution of the structural properties during isothermal annealing

Once established the sensitivity and strength of the combined x-ray scattering methods, namely GI-DXS, XRD and SR, the structural properties of a PAI sample series during isothermal annealing were studied to investigate and model their evolution. The results from the x-ray scattering methods are compared to those obtained by MEIS and secondary ion mass spectrometry.

Chapter 7: Study of {113}-defects during isothermal annealing

The atomistic simulation of the DXS signal from {113}-defects published in [1.62] was the staring point for pioneering experiments aimed to the detection of such defects in Si. The

evolution of {113}-defects in Ge pre-amorphised Si samples was investigated during isothermal annealing at 800°C.

Chapter 8: General conclusions and outlook

This chapter contains the general conclusions and possible future directions for this research. The results from the analysis of each sample series are reported in details at the end of the corresponding chapters.

Appendix: The IMPULSE project

The work reported in the present PhD thesis has been performed within the European project ion-IMPlantation at Ultra-Low energy for future SEmiconductor devices (IMPULSE). The collaboration developed among the research institutes participating in the IMPULSE project has made it possible to provide the comparison of the x-ray-based experimental results with the ones from the other structural techniques. This Appendix contains a brief summary of the activities of the IMPULSE project in order to better appreciate the role of the ESRF partner in the frame of this research consortium.

0.5 Glossary

Abbreviation	Meaning
113	{113}-defect
{1Hex}ZD	Stable structure of zig-zag {113}-defect
a/c interface	Amorphous-to-Crystalline interface
APM	Ammonium Peroxide Mixture
CMOS	Complementary Metal-Oxide Semiconductor
Cz Si	Czochralski-grown Si
DECJ	Drain Extension Channel Junction
DL	Dislocation Loop
DXS	Diffuse X-ray Scattering
DWBA	Distorted Wave Born Approximation
EOR	End-Of-Range
Epi Si	Epitaxially-grown Si

ESRF	European Synchrotron Radiation Facility
FDL	Faulted Dislocation Loop
GID	Grazing Incidence Diffraction
GI-DXS	Grazing Incidence Diffuse X-ray Scattering
HDS	Huang Diffuse Scattering
HRTEM	High Resolution Transmission Electron Microscopy
I	Interstitial
IC	Integrated Circuit
IRD	Stable structure of linear {113}-defect
ITRS	International Technology Roadmap for Semiconductor
Lg	Gate Length
MOS	Metal-Oxide Semiconductor
MEIS	Medium Energy Ion Scattering
NMOS	N-channel Metal-Oxide Semiconductor
SF	Stacking Fault
SiI	Si self-interstitial
SIMS	Secondary Ion Mass Spectrometry
SPER	Solid Phase Epitaxial Regrowth
SR	Specular Reflectivity
SWS	Stokes-Wilson Scattering
PAI	Pre-Amorphising Implant
PDL	Perfect Dislocation Loop
PMOS	P-channel Metal-Oxide Semiconductor
PSD	Position Sensitive Detector
RBS-C	Rutherford Backscattering in Channelling geometry
R_{cl}	Radius of a defect cluster
R_p	Mean projected range for an implanted ion
RTA	Rapid Thermal Annealing
RTP	Rapid Thermal Processing
TDS	Thermal Diffuse Scattering
TED	Transient Enhanced Diffusion
TEM	Transmission Electron Microscopy
USJ	Ultra Shallow Junction
V	Vacancy

XRD	X-Ray Diffraction
X_j	Junction depth

Symbol	Meaning
α_i	Incident angle
α_c	Critical angle for total external reflection
α_f	Exit angle
$\Delta a/a$	Strain of the Si lattice parameter *a*
d	Length or thickness
I_{sym}	Symmetric component of the defect-induced DXS
I_{asym}	Asymmetric component of the defect-induced DXS
Λ	Scattering depth
L_h	Static Debye-Waller factor
q_r	Reduced scattering vector in the radial direction
q_a	Reduced scattering vector in the angular direction
q_z	Reduced scattering vector in the vertical direction
ρ	Density of SiI's
ρ_{el}	Electronic density

Crystallographic notation (according to the *Journal of Applied Physics*):

Symbol	Meaning
(hkl)	Plane or set of parallel planes
(h, k, l)	Point designed by coordinates
[hkl]	Direction
{hkl}	Class (group) of symmetry-equivalent planes
$\langle$hkl$\rangle$	Class (group) of symmetry-equivalent directions

1. Ion implantation and damage annealing in Si: an introduction

In this chapter, an introduction to ion implantation and damage annealing in Si is given. In the first section of this chapter, the use of ion implantation for the fabrication of Si-based microprocessors is discussed. The second part concerns some basic aspects of the physics related to ion implantation in Si. In the final section, the most common analytical techniques for the structural characterisation of such systems are summarised.

1.1 Future semiconductor technology

Ion implantation is a central step in the processing of Si-based integrated circuits (IC's). In the following, the requirements for the fabrication of future generation devices and the role ion implantation plays in complementary metal-oxide semiconductor (CMOS) technology will be briefly described. As the main focus of this work is the characterisation of ultra-shallow junctions (USJ's), the use of ultra-low energy ion implantation for their production will be discussed.

1.1.1. Future trends for device technology in Si-based manufacturing

The evolution of the electronics during the last decade has been dramatic. Following the invention of IC's in 1959, the degree of integration of such circuits has been doubled every 12 -18 months, as dictated by the well-known "Moore's law". This law, made by Gordon Moore, one of the founders of Intel, has a merely economic intent and states that "the industry intends to invest sufficient funds into research and development and capital equipment to shrink the feature size at that rate" [1.1]. This implies a reduction in the size of the system chip and an increase of IC functionality for equivalent chip size. Other aspects contribute to cut down production costs of smaller devices, e.g. lower power consumption and less internal and external transistor interconnections. In addition to these advantages, the shrinking of the transistors goes along with higher performance of the overall system and increased device reliability [1.2].

Following "Moore's law" for the past 40 years, companies were fabricating, in 2003, devices in the 90 nm technology node targeting their future products to the 65 nm technology node for the 2005. A technology node is defined by the minimum size of the designed features. The gate length (Lg) is one of the main characterising parameters of a technology node, as will be shown in Sec. 1.1.2. Figure 1.1 shows the trend for the size reduction of

CMOS devices at AMD company [1.3]. The Lg is going to reduce from 50 nm, for the 90 nm technology node in 2003, to 13 nm, for the 22 nm generation in 2011, with major improvement in the device performance.

A number of technical challenges have been solved to reach the size of today devices. However, existing materials and technology are approaching their physical limits and other more challenging technology breakthroughs will be required in the near future.

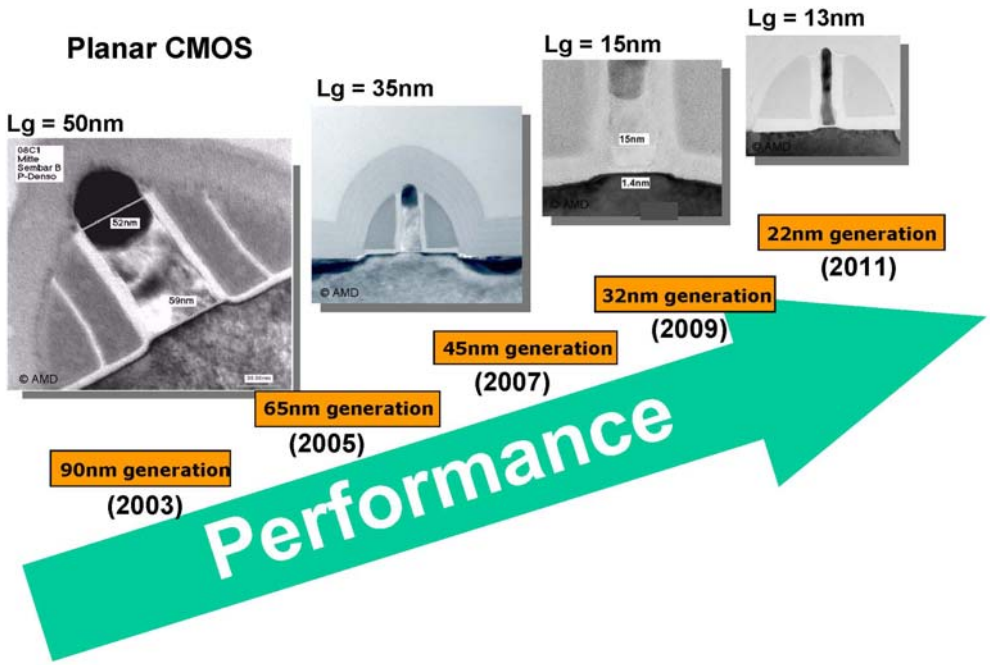

Figure 1.1: Roadmap for planar CMOS device shrinking at AMD. TEM (transmission electron microscopy) cross-section images from test devices. Adapted from Ref. [1.3].

The Semiconductor Industry Association determines periodically the targets for the production of future devices in the International Technology Roadmap for Semiconductors (ITRS) [1.5]. It identifies the technical capabilities and technology needs that still have to be developed and in particular those technical areas where no “manufacturable solutions” are known for further shrinking of the IC chips. The ITRS, resulting from a worldwide collaboration, is the guideline for semiconductor research in industries, universities and other institutions.

An exhaustive report about the technological issues of semiconductor industry is beyond the aims of this work and the reader can refer to the wide specific literature on the subject for further information ([1.1, 1.2, 1.4] and references therein). In the next section, the focus will be, instead, on the role ion implantation plays in the fabrication of CMOS transistors.

1.1.2. CMOS transistors and ion implantation

The production of metal-oxide semiconductor (MOS) IC's is the dominant technology in semiconductor industry. It allows the fabrication of devices with millions of transistors on a single IC chip with the best cost-to-performance ratio [1.2]. The most common families of MOS field effect transistor are the n-channel MOS (NMOS), the p-channel MOS (PMOS) and the CMOS, which combines a PMOS and a NMOS transistor. The CMOS transistor is the basic component of a microprocessor. In a chip, e.g. AMD Athlon XP^{TM} for the 130nm technology node, shown in Fig. 1.2, 54 millions CMOS are assembled in a chip area of 101mm^2. The AMD most advanced product has currently 210 millions transistors.

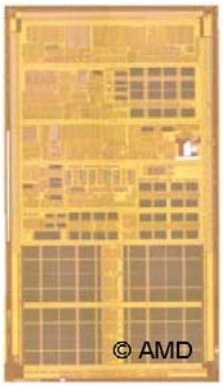

Figure 1.2: 130nm technology node transistor AMD Athlon XP^{TM} Barton from AMD. Adapted from Ref. [1.3].

A TEM cross-section view of a MOS transistor is presented in Fig. 1.3(a) and its basic elements are schematically illustrated in Fig. 1.3(b). A MOS transistor is composed by source, drain and gate. The source and the drain can be considered respectively as emitter and collector of charge carriers (holes or electrons) and must be electrically insulated from one another. The region between the source and the drain is referred to as channel region. If the channel is p-type Si, then source and drain are n-type Si, thus creating a PMOS transistor. The gate is insulated and may be thought as one electrode of a parallel-plate capacitor with a dielectric, usually SiO_2, separating it from another electrode, i.e. the substrate. By applying an appropriate voltage to the gate, a conductive layer of charge is formed in the channel region, which is removed when changing the voltage. Therefore, the transistor acts like a switch controlled by the gate voltage.

The charge in the source, drain and channel region is created by locally adding dopant ions to the silicon lattice. In the substrate, Si atoms are arranged in diamond structure forming four covalent bonds with their neighbours. When Si is doped with atoms containing five

valence electrons, like arsenic and phosphorous, the extra electron is free to move in the lattice, becoming an additional charge carrier. This is called n-type Si. Analogously, when the doping atoms have three valence electrons, like boron, the carriers are holes and p-type Si is formed [1.7]. The border region between a p-type and an n-type Si area is called junction.

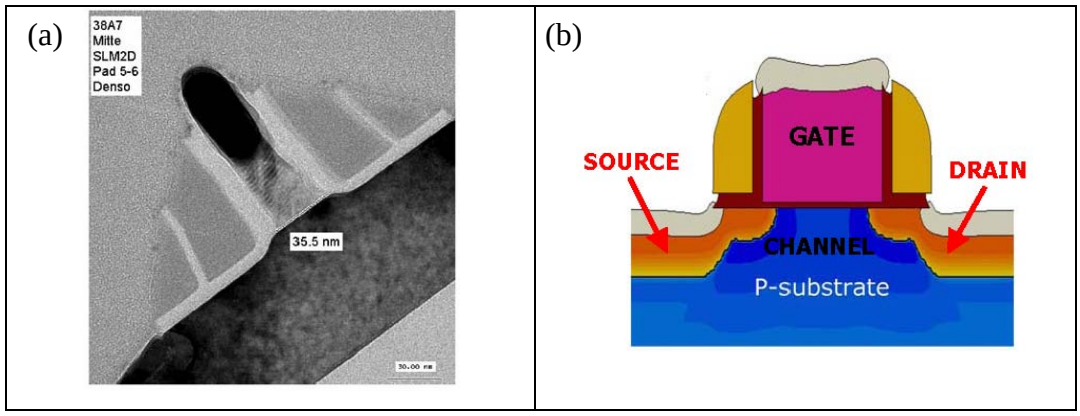

Figure 1.3: (a) Cross section TEM image from an optimised transistor, featuring optimised gate length of 35 nm. Adapted from Ref. [1.6]; (b) Schematic view of a MOS transistor structure showing source, gate and drain. See details in the text.

An IC incorporates both p-type and n-type junctions and their properties are of paramount importance for the device performance. The tailoring of the dopant profile, both in vertical and lateral directions, together with the concomitant carriers and field distributions, is among the main responsibles for the electrical properties of the device. Measurements of electrical properties, such as overlap capacitance, drive current, saturation current, threshold voltage roll-off, sheet resistance [1.2, 1.8] are used to optimise the transistor performance. All of the properties finally depend on the CMOS design and architecture, e.g. on the proper scaling and doping of source/drain areas. In order to process devices in the deep sub-μm range and meet the ITRS targets, an aggressive junction engineering and the extremely accurate control on the dopant concentration and profile are mandatory.

The Si doping is commonly done using ion implantation. Discovered in 1952 [1.9], ion implantation is one of the most important processing tools in Si-based IC's industry. The advantages of the use of ion implantation over other doping techniques (e.g. chemical vapour deposition, molecular beam epitaxy or thermal diffusion of dopant atoms) include accurate dose control, high purity of the dopant species, reproducibility of the impurity profiles, lower process temperature -even if subsequent annealing is required-. Ion implantation selectively dopes the Si and tailors the doping profile in a processing time scale compatible with industrial throughputs. In order to fabricate such small features, as those needed for current

devices, implantation protocols have become rather complex counting as many as 20 different implantations [1.10].

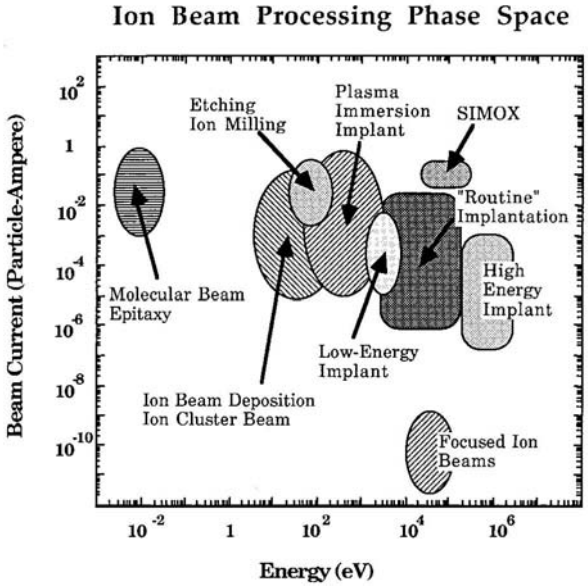

Figure 1.4: Schematic map of the range of ion energy and beam currents used in semiconductor industry. Adapted from Ref. [1.10].

Ion implantation is performed using a wide range of energies (1 keV-5MeV) and doses (10^{11}-10^{15} cm^{-2}). A variety of dopant (B, P, As, …) and non-dopant (Ge, Si, Xe, F,…) ions can be implanted. Figure 1.4 schematically represents a panorama of the ion implantation processing used in semiconductor manufacturing. The lowest energies are used for junction formation, while the highest for substrate and well doping [1.2].

1.1.3. Ultra-low energy ion implantation for ultra-shallow junctions

The fine tailoring of the dopant profile close to the MOS channel dramatically affects the electrical performance of the device, because of the complex interactions between lateral and vertical junction depth and abruptness. For very deep sub-μm technologies, down scaling and transistor performance are strongly connected with the design of appropriate doping profiles close to the Drain Extension Channel Junction (DECJ) under the gate, as illustrated in Fig. 1.5. The doping is realised via different ion implantation steps and finally the DECJ is created. DECJ governs the dopant distribution in the area of the drain junction elongating towards the channel. Due to its reduced thickness, below 100 nm, this typology of junction is called ultra-shallow junction.

The 2003 edition of the ITRS Roadmap [1.5] gives a guideline for junction depth scaling for high performance processes during the next few years. A summary of key parameters for ultra-shallow drain extensions is given in Table 1.1 [1.6].

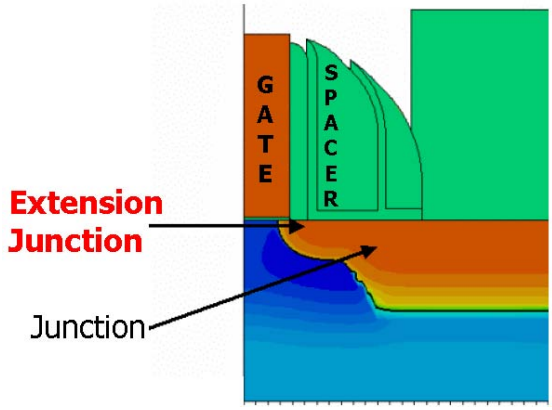

Figure 1.5: Simulation of the dopant profile in the region close to the channel of a MOS transistor. The dopant profile from the extension junction is elongating into the channel. The gate, spacer and junction areas are indicated for easier localisation of the extension junction. Figure by courtesy of T. Feudel.

The extension junctions, both of n- and p-type, are currently fabricated by ultra-low energy (< 5 keV) ion implantation. The need for increasingly thinner USJ's creates new challenges for the semiconductor technology processing and the ion implantation tools. The tuning of the final dopant profile (i.e. after implantation and annealing) requires not only an appropriate control on implant and annealing conditions, but also a deeper understanding of the interaction among the dopant atoms and the implantation-induced defects.

Table 1.1: ITRS Roadmap 2003, drain extension junction specifications. HP node="half pitch" technology node, HP Lgate= "half pitch" gate length, Xj Drain Extension= junction depth of the drain extension [1.5, 1.6].

	2003	2004	2005	2006	2007
HP node		HP90			HP65
HP Lgate (nm)	40	37	32	28	25
Xj Drain Extension (nm)	24.8	20.4	17.6	15.4	13.8

When the dimensions of the device were in the micrometer range, it was not crucial to deeply understand these dopant-defect interactions. At present, when the CMOS features are of the same order of magnitude of the dopant diffusion path during rapid thermal processing [1.2], the physics of dopant-defect interactions is a real challenge for a further evolution of the semiconductor devices.

1.2 Material science issues

Ion implantation has been used in Si MOS technology starting from the early 70s. Since then specific physics and engineering challenges have been faced that are strictly related to its application in Si processing. A brief review of the major materials science issues connected to ion implantation is given in this section. First, the features of the crystalline regrowth of an amorphous layer on a Si substrate will be explained. The section will continue with a discussion of the diffusion of dopant atoms in Si. The description of the types of defect present in Si after ion-implantation and annealing will conclude Sec. 1.2.

1.2.1 Damage creation and solid phase epitaxial regrowth

Doping Si by ion implantation introduces different degrees of damage in the substrate, depending on the implanted ions and the process conditions. The implantation process has a considerable physical complexity and its full microscopic understanding is not yet achieved [1.4]. Monte Carlo simulation methods are used to model the energy loss and damage/dopant distribution in the substrate for the as-implanted samples. SRIM (Stopping and Range of Ions in Matter) is a software, which calculate the distribution of the dopant atoms into matter and the damage cascade they produce, using quantum-mechanical treatment of the interaction between the ion and the atom of the substrate [1.11]. One example of such calculations, produced by TRIM (software belonging to the SRIM package), is given in Fig. 1.6.

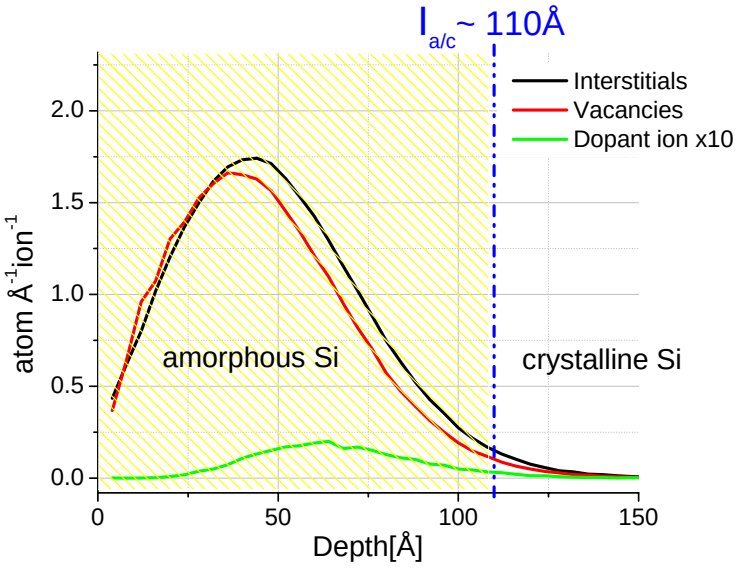

Figure 1.6: Simulated depth distribution of damage and dopant ions following As implant in Si at 3keV, angle of incidence 0 deg. The displacement energy per Si atoms used for computing the recoils distribution is 13 eV. The calculation is performed using TRIM 2003 [1.12].

In this case, the depth distribution of interstitials, vacancies and dopant atoms are calculated for arsenic ion implantation at 3keV with an ion beam normal to the Si substrate surface. The As ions will stop in a fraction of picosecond forming a Gaussian distribution [1.2] centred on the mean projected range (R_p) of the ions. Simultaneously a damage cascade is produced. The depth distributions of vacancies and interstitials can be shifted from each other, depending on the process parameters. For high implanted doses (e.g. $\geq 4x10^{14}$ cm^{-2} for As in Si at 2.5 keV), the substrate damage is so enhanced that the Si gets amorphised. For As ions at a dose $2x10^{15}$ cm^{-2} implanted at 3 keV, the amorphised layer extends up to ~115 Å below the surface (Sec. 4.5), as measured by Medium Energy Ion Scattering (MEIS) and shown in Fig. 1.6. Thus, the Si amorphous phase exists in direct contact with crystalline one. The abruptness of the amorphous to crystalline (a/c) interface is determined by the implanted atomic species. Heavier atoms (e.g. Ge, Xe) produce sharper interfaces [1.13].

The recrystallisation of the amorphous Si takes place to minimise its free energy, starting from a temperature around 500 °C [1.14]. The process begins at the a/c interface and continues up to the total recrystallisation of Si. This kind of recrystallisation is called solid phase epitaxial regrowth (SPER) as it consists of the growth of an oriented film on a crystalline substrate. SPER after amorphising ion implantation was first reported in Ref. [1.15] in 1967.

The crystalline quality after the regrowth depends on the orientation of the substrate. Müller *et al.* [1.16] demonstrated that, while the regrowth on a (111)-oriented substrate results in high residual damage, the regrowth on (001)- and (110)-oriented Si crystals leave behind much less residual disorder. Further investigations [1.17] proved that undoped layers on (001)-oriented substrates regrow about 2.5 times faster than for similar layers on (110)-oriented Si crystals. For both (001)- and (110)-oriented crystal, the SPER is linear with time, indicating a layer-by-layer mechanism. This is not the case for the (111)-oriented crystals where non-planar interfaces were observed.

The temperature dependence of SPER was accurately investigated and it was generally observed that the activation energy of SPER does not depend on the substrate orientation. Finally, Olson [1.18] reported, in relation (1.1), the SPER velocity v for layers amorphised by As implantation to a dose $2x10^{14}$ cm^{-3} over a wide temperature range.

$$v = 3.68x10^{15}\exp\left(-(2.76 \pm 0.05)\text{eV/kT}\right) \text{ nm/s} \qquad (1.1)$$

Dopants and other impurities affect the SPER rate and several studies and models are reported in literature ([1.13] and references therein). Atoms of diverse chemical species may either slow down or accelerate the regrowth, depending on their nature and dose. In the

models proposed, SPER rate variations are justified by the presence of different kind of defective sites at the amorphous to crystalline interface, like Si dangling bonds, kinks or fivefold-coordinated Si atoms in amorphous Si. No final solution to this question has been found so far also due to lack of numerical implementation of the models. For implants of arsenic, antimony, indium and other elements, the concentration of which exceeds the dopant-dependent maximum solubility, Williams and Elliman [1.19, 1.20, 1.21] reported a sharp decrease in the epitaxial regrowth. The authors speculated that the retardation of the regrowth might be attributed to local stress caused by the dopants in the crystalline phase.

In order to obtain electrically active dopants, the implanted ions must occupy substitutional positions in Si. In this case only, shallow donor energy levels are created, close to the Si conduction band. The electrons that occupy these states are, then, free to move in the crystal becoming electrically active. The main property of SPER is that it makes the dopant atoms become substitutional and electrically active in concentrations well exceeding their solid solubility limit. Crowder [1.25] already pointed out this phenomenon in 1971 and several investigations confirmed it for dopants like antimony, arsenic, boron, gallium, indium and other impurities. For example, Ref. [1.26] reports about an activation of about 90% for As doped to a dose 10^{15} cm^{-2} annealed in a temperature range from 450°C to 650°C. The high concentration of substitutional impurities can be attributed to their trapping by the rapidly moving interface.

Because of the high rate of the recrystallisation, the redistribution of the dopant after SPER is usually negligible, especially when (001)-oriented substrates are used. This is not the case when considering USJ's formation. Due to their sub-μm size, the dopant atoms diffusion during SPER can be significant (see Sec. 1.2.2) in such systems. Nevertheless, SPER is currently considered as potential solution to meet the specifications for USJ's in the 65 and 45 nm technology node [1.5].

1.2.2. Conventional and transient enhanced diffusion of dopant atoms in Si

A thermal treatment after ion implantation is needed in order to recover the crystalline structure and activate the dopant atoms. In order to get the maximum dopant activation (i.e. > 95%), the annealing has to be performed in a temperature range between ~900°C and 1200°C. The dopant activation may be accomplished during a classical thermal procedure (e.g. furnace annealing) or a rapid thermal process (RTP). A clever engineering of the annealing step is needed to achieve the best dopant profile. RTP is normally used because it has the advantage of minimising the dopant redistribution effect [1.2]. The annealing process not only activates

the dopant, but also accelerates the undesired dopant atoms diffusion into the Si substrate. Therefore the control of the dopant profile after ion implantation and annealing is strictly connected to a detailed knowledge of the atomic diffusion mechanisms in Si.

The diffusion of an element A in a solid, such as Si, can take place following different mechanisms that can be either direct or indirect. Small impurities, like hydrogen or *3d* transition metals, are known to diffuse via direct interstitial mechanism (A on interstitial position, i.e. A_i). Also direct diffusion of substitutional impurities (A_s) via substitutional sites can occur, but more rarely. The most common diffusion mechanisms are indirect, where intrinsic point defects, such as interstitials (I's) and vacancies (V's) are involved. These mechanisms [1.27] can be expressed by point defect reactions:

$$A_s + V \Leftrightarrow AV \tag{1.2}$$

$$A_s + I \Leftrightarrow AI \tag{1.3}$$

$$A_s + I \Leftrightarrow A_i \tag{1.4}$$

$$A_s \Leftrightarrow A_i + V \tag{1.5}$$

and are schematically illustrated in Fig. 1.7. Reactions (1.2) and (1.3) represent the vacancy and interstitial mechanisms, respectively. Isolated intrinsic defects approach substitutional impurities and form nearest-neighbour AV and AI defect pairs due to Coulomb attraction and/or minimisation of local strain. For long-range migration of A_s, the AV pair partially dissociates and the vacancy diffuses to at least a third nearest-neighbour site in the diamond lattice before returning along a different path. The diffusion step is thereby completed.

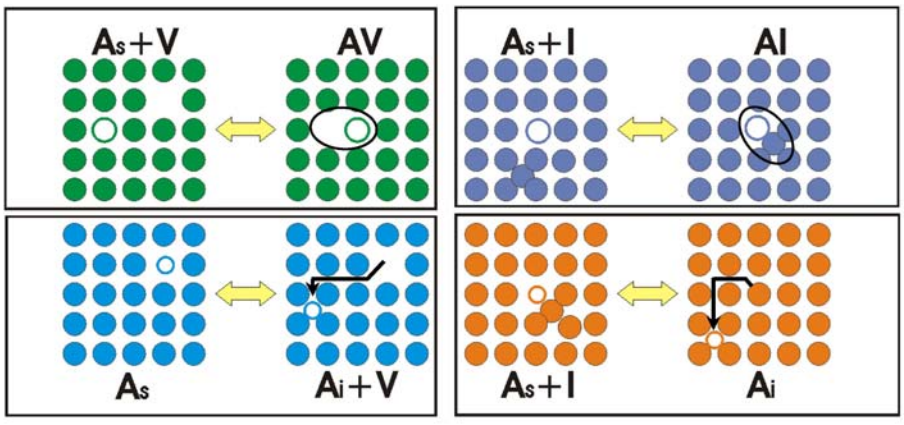

Figure1.7: Schematic two-dimensional representation of diffusion mechanisms of an element A in a solid. A_i, A_s, V, I denote interstitially and substitutionally dissolved foreign atoms, vacancy and Si self-interstitials, respectively. AV and AI are defects pairs of the corresponding defects.

In contrast, the dopant diffusion via the interstitial mechanism only occurs if the AI pair does not dissociate. Reactions (1.4) and (1.5) are the kick-out and the dissociative (or Frank-

Turnbull) mechanisms, respectively. They describe the diffusion behaviour of hybrid elements, like gold, sulphur, zinc and platinum that are mainly dissolved on substitutional sites, but move as interstitial defects.

Mass transport in solid can be treated on the basis of the Fick's law for diffusion in one dimension, Eq. (1.6).

$$\frac{\partial C_A}{\partial t} = \frac{\partial}{\partial x}\left(D_A \frac{\partial C_A}{\partial x} \right) + G_A \tag{1.6}$$

where C_A and D_A are , respectively, the concentration and the diffusion coefficient of a point defect A as a function of time *t* and position *x*. Possible reaction between A and other defects are accounted for by the term G_A. If no reaction takes place, it is $G_A = 0$.

The diffusion of isolated vacancies and self-interstitials in Si can be described by the Eq. (1.6), with $G_{V,I} = 0$. Taking into account all possible contributions to self-diffusion, the coefficient for Si self-diffusion D_{Si} is given by Eq. (1.7),

$$D_{Si} = D_{Si}^{V} + D_{Si}^{I} + D_{ex} \tag{1.7}$$

where D_{Si}^{V} is the contribution from the vacancy mechanism, D_{Si}^{I} the contribution from the interstitial mechanism and D_{ex} the exchange between two neighbouring atoms. The D_{Si} can be measured indirectly from samples containing heterostructures of tagged Si atoms, e.g. [1.28, 1.29].

The diffusion of common dopants, like boron, phosphorous, arsenic and antimony, is always faster than Si self-diffusion irrespective of whether the atoms have a smaller or larger atomic radius than Si. This is an indication that dopant diffusion, as well as Si self-diffusion, is mediated by vacancies and self-interstitials. The diffusion of dopants can be described using reaction (1.2) and (1.3), that are equivalent to the kick-out reaction (1.4). The dopant diffusion coefficient D_A is then given by Eq. (1.8).

$$D_A = D_A^{AV} + D_A^{AI} = \frac{C_{AV}^{eq} D_{AV}}{C_{A_s}^{eq}} + \frac{C_{AI}^{eq} D_{AI}}{C_{A_s}^{eq}} \tag{1.8}$$

C_{AV}^{eq} and C_{AI}^{eq} denote the equilibrium concentration of AV and AI. The pair diffusivities D_{AV} and D_{AI} are complex quantities that include dissociation and correlation effects. Eqs. (1.7) and (1.8) show that both vacancies and self-interstitials are involved in self- and dopant-atom-diffusion.

Defining the so called fractional interstitial component of dopant diffusion as Eq. (1.9),

$$f_A^{AI} = \frac{D_A^{AI}}{D_A^{AI} + D_A^{AV}} = \frac{D_A^{AI}}{D_A^{'}} \tag{1.9}$$

the ratio between the dopant-diffusion coefficient under nonequilibrium ($D_A^{'}$) and equilibrium condition (D_A) is given by Eq.(1.10) [1.30].

$$\frac{D_A^{'}}{D_A} = \left(1 - f_A^{AI}\right)\frac{C_V}{C_V^{eq}} + f_A^{AI}\frac{C_I}{C_I^{eq}} \tag{1.10}$$

This equation describes the impact of a super- or under-saturation of intrinsic point defects on dopant diffusion. Fig. 1.8 shows germanium diffusion measured by secondary ion mass spectrometry (SIMS), as an example of diffusion under equilibrium and nonequilibrium conditions. The broadening of the Ge-doped buried epitaxial Si layer increases both by vacancy and self-interstitials injection, thus confirming the leading role of intrinsic point defects in diffusion.

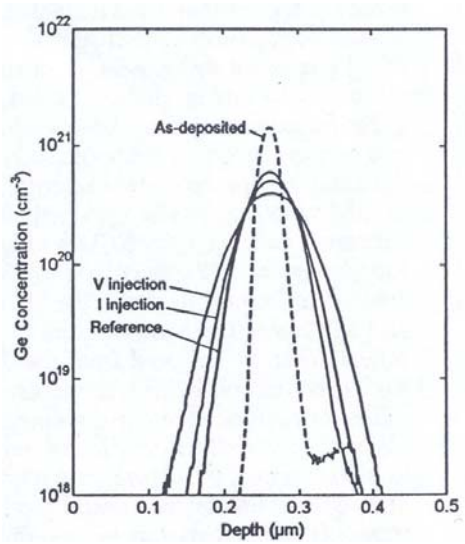

Figure 1.8: Concentration profiles of a buried Ge epitaxial layer in Si, measured by SIMS (dashed curve), and after (solid curve) diffusion at 1050°C for 80 min. under boundary conditions that cause either vacancy (V), or self-interstitial (I) injection, or no injection of intrinsic point defects. Adapted from [1.31].

Table1.3: Fractional interstitial component f_A^{AI} of dopant diffusion in Si [1.29] See text for details.

Element [A]	f_A^{AI}	Temperature [°C]
B	≥0.94	810, 860
Ga	≥0.95	1050
P	≥0.93	1100
As	≈0.4	1100
Sb	≤0.02	790, 1050

The main diffusion mechanism, being interstitial- or vacancy- mediated, depends on the dopant chemical species. Table 1.3 illustrates the fractional interstitial component, f_A^{AI}, for some of the most common dopants. Accordingly, boron diffuses almost entirely via interstitial mechanism, like gallium and phosphorous, while antimony is rather insensitive to interstitials injection. The fractional component for arsenic appears to be lower than for phosphorous, indicating a higher vacancy component. For more detailed information about diffusion phenomena in Si, the reader is referred to Ref. [1.30, 1.32].

A major challenge related to dopant diffusion in USJ's fabrication is the so-called dopant transient enhanced diffusion (TED). TED is a transient effect observed during post-implantation annealing, when the diffusion coefficient of implanted atoms increases temporarily up to 10 times its typical value. The first experimental study of time-resolved TED in Si after B implantation was performed by Michel *et al.* in 1987 [1.33]. An example from their results is reported in Fig. 1.9.

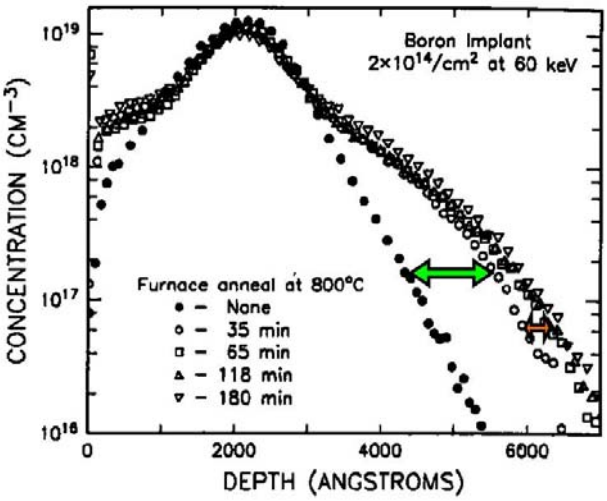

Figure 1.9: Boron profiles for several annealing times at 800 °C. Adapted from Ref. [1.33].

It is well established ([1.34] and references therein) that TED takes place in early stages of the annealing process, when ion-implantation-induced damage is present in the Si substrate. The central role of defects in the diffusion of dopant atoms is now known and much work has been done for understanding TED and the key parameters of this phenomenon [1.35, 1.36]. The TED is driven by the diffusion of Si self-interstitials, which are present in the damaged area of ion-implanted Si. This issue will be discussed in more detail in Sec. 1.2.3. Currently, understanding and modelling of residual defects evolution coupled with dopant diffusion equations is a priority [1.37, 1.38]. This is crucial especially for B diffusion ([1.39],

[1.40] and references therein), because it has been shown that $f_B^{BI} \geq 94$ (see Table 1.3). Arsenic experiences TED too, as discussed in Ref. [1.41, 1.42].

1.2.3 Residual defects after ion-implantation and annealing

As already mentioned in Sec. 1.2.1, ion implantation leads to the generation of interstitials and vacancies via collisional displacements of lattice atoms. The majority of Frankel pairs (interstitial + vacancy) recombine during ion-implantation and/or early stage of the annealing, while the remaining ones aggregate to form different kind of defects. Figure 1.10 illustrates the scheme of a Si wafer after ultra-low energy ion implantation and annealing. Below a 2-3 nm layer of amorphous material, whose characteristics will be described in Secs. 4.3 and 5.2, the crystalline region develops a layered structure. Distinct typologies of residual defects can be identified. The most important disorder is the End-Of-Range (EOR) damage located below the original a/c interface, where the vast majority of defective crystalline sites are concentrated. EOR defects strongly influence the diffusion of the dopant atoms, especially when the dopants are located in the defects proximity. Therefore, the characterisation of such defects is of major relevance in this work and their properties will be deeply discussed in Sec. 1.2.4.

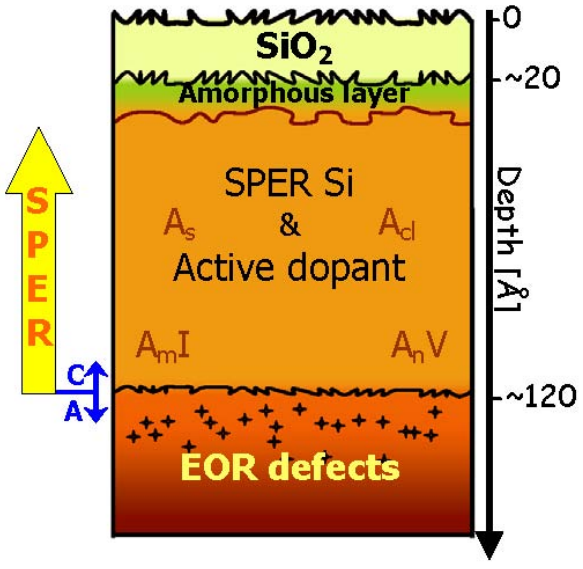

Figure 1.10: Scheme of the structure of the Si substrate after implantation of the ion species A and annealing (see text for details).

In the SPER area, where the junction is located, the crystalline quality is very high; nevertheless, several types of small defects may be present. Electrically active dopant atoms (A) must be located on substitutional positions, consequently the most common defect is A_s,

the substitutional dopant atom. Clusters of electrically inactive dopant are present, A_{cl}, together with several defects that cooperate in the diffusion of the dopant atoms. Concerning arsenic implantation, for instance, which is the most common dopant studied in this work, A_nV, dopant-vacancy aggregates are found. Such aggregates impede the As atoms to occupy a substitutional position, thus, decreasing the level of electrical activation and simultaneously promote TED. The most stable clusters are As_2V, As_3V and As_4V [1.41]. When boron is implanted, the stabilised clusters are the so-called BIC's (boron-interstitial clusters), indicated, in Fig. 1.10, as A_nI [1.37, 1.43-1.45]. Moreover, intrinsic defects are present in the SPER region, namely equilibrium concentrations of interstitials (I's) and vacancies (V's)). The concentration and evolution of A_nV's and A_nI's is strongly affected by the variations in intrinsic point defect concentration (see Eq. (1.10)).

1.2.4 "Excess interstitial" model for EOR damage

After amorphising implant and annealing in Si, EOR defects condense below the original a/c interface. The mechanism of EOR damage formation is well known [1.46]. As shown in Fig. 1.6 and Fig. 1.11 (dashed area) [1.47], the region below the a/c interface is heavily supersaturated with Si self-interstitials (SiI's). During the annealing, simultaneous defect growth and SPER occur. As a consequence of the fast rate of SPER (Sec. 1.2.1) and of the Si self-diffusivity being smaller in the amorphous layer than in the crystalline one, the SiI's supersaturation is confined to its original position and the EOR defects are formed. The total number of Si atoms bonded into the defects is approximately equal to the number of excess SiI's left behind the interface [1.48]. This model is known as "excess interstitial" model [1.49].

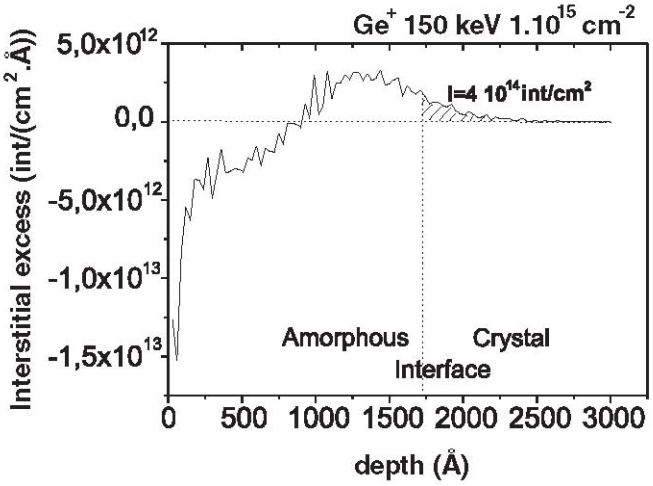

Figure1.11: Depth profile of the interstitials excess after Ge^+ implant (150KeV, $1*10^{15}cm^{-2}$) using Monte Carlo simulation. Adapted from Ref. [1.47]

Previously, another model, known as "+1" model [1.50], was used to describe the ion-implantation-induced damage. Valid for non-amorphising implants done using light atoms and low fluences, this model predicts that the defects form at the projected range of the implanted ions (Sec. 1.2.1). In both models, the defects contain a number of SiI's equal to the implanted dose, i.e. the SiI's supersaturation is created by the activation of the dopant via ejection of Si atoms due to dopant incorporation on substitutional sites. Provided that the total amount of dopant atoms occupies substitutional sites, the SiI's supersaturation is obtained by integrating over the implanted depth the difference between the remaining vacancies and the SiI's. The difference between the two models is that, in the "excess interstitial" model, such integral is non-zero only in the crystalline region below the a/c interface, implicitly assuming that no point defect is left within the amorphous phase.

Depending on the experimental conditions, up to five types of defects can be detected in the EOR damage region. They are all of extrinsic nature, i.e. formed by the supersaturation of excess SiI's, and the number of SiI's they contain determines their size and structure. Immediately following implantation and/or in the early stage of the annealing, the excess interstitials are stored as di-interstitials, i.e. clusters of two SiI's [1.51]. When the clusters grow during moderate thermal annealing (e.g. 600 - 700 °C), the formation of very small aggregates of SiI's becomes energetically favoured. Following Ref. [1.52], the most stable clusters are made of 4 and 8 atoms and are named "magic clusters". Their existence has been detected via indirect measurements, i.e. studying the diffusion of delta-doped-layers of boron in Si. The delta-layers were grown by molecular beam epitaxy and investigated by SIMS after annealing [1.52].

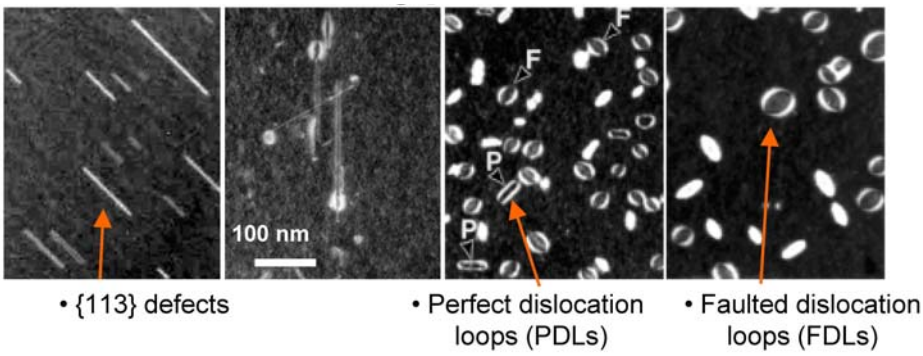

Figure 1.12: TEM images of the types of defect present in the EOR damage area of ion-implanted Si. Adapted from Ref. [1.53].

For higher temperatures and/or longer annealing times, the "excess interstitial" population condenses into extended defects, so-called because they are visible by

transmission electron microscopy (TEM). Defects such as {113}-defects (113's), faulted dislocation loops (FDL's) and perfect dislocation loops (PDL's) belong to this class. Fig. 1.12 presents a TEM overview of the typical defects for the EOR damage, which will be discussed hereafter.

1.2.4.1 Structure of {113}-defects

113's are a peculiar class of defects that is present only in silicon and in germanium after ion implantation and annealing. The existence of such defects is known from the late 70's based on TEM observations [1.54, 1.55]. They were called {113}-stacking faults and/or rod-like defects, due to their particularly elongated shape. The determination of their origin and structure has been rather controversial in literature, although it is now agreed [1.56, 1.57] that these defects are agglomerate of <110>-oriented rows of SiI's, as already suggested by early investigations [1.54, 1.55]. The controversy in literature arises from the existence of at least two different morphological types of 113's: the linear or planar {113}-defects and the zig-zag or rod-like {113}-defects. A wide literature is available ([1.47], [1.58] and references therein) where the structure of 113's is discussed.

In this work, the structure for 113's is taken from Ref. [1.58] by Parisini and Bourret. The authors discuss the crystallographic features of 113's as well as the results from the total energy calculations for several configurations of such defects. The outcome is the identification of two most stable defect configurations that are described in the following.

Among the linear 113's, the so-called Improved model for Rectilinear Defect (IRD) [1.59], shown in Fig. 1.13, results in the most stable configuration. The chains of additional Si atoms extend in the <110> direction. They are sandwiched by two {113} reconstructed interfaces without dangling-bonds in the {110} cross-section. The main chain is constituted of wurtzite (hexagonal)-type rings (i.e. 6-membered rings). The remaining SiI's aggregate in units of 5-, 7- and 8-membered rings, needed to release the strain along the main chain. Therefore, the core of the defect presents a different structure from the usual diamond-structure of Si. The observed sequence of rings is not strictly periodic, and the interstitial density of the planar 113's in Si varies around 5 nm^{-2} [1.47]. It should be noticed that the two extra {113} planes are not fully occupied. For this reason, the IRD does not posses a true stacking fault, even if a fault vector $\boldsymbol{R}$ (i.e. the relative displacement vector of planar defects) can be determined as $\boldsymbol{R} = a/25\langle 116\rangle$, $|\boldsymbol{R}| = 0.132$ nm from high resolution TEM (HRTEM) [1.60].

For zigzag-shaped {113}-defects, the energetically favoured configuration is the {1Hex}ZD, i.e. the zigzag defect containing one hexagonal ring. Details on the {1Hex}ZD structure are shown in Fig. 1.14. The habit plane of the defect is periodically changing from (113) to $(\bar{1}\bar{1}3)$ [1.61]. The net effect is that {1Hex}ZD plane is on average perpendicular to the <100> direction. The wurtzite-type rings in this structure appear to be less deformed than in IRD, indicating that almost all the strain caused by the introduction of these units has been released.

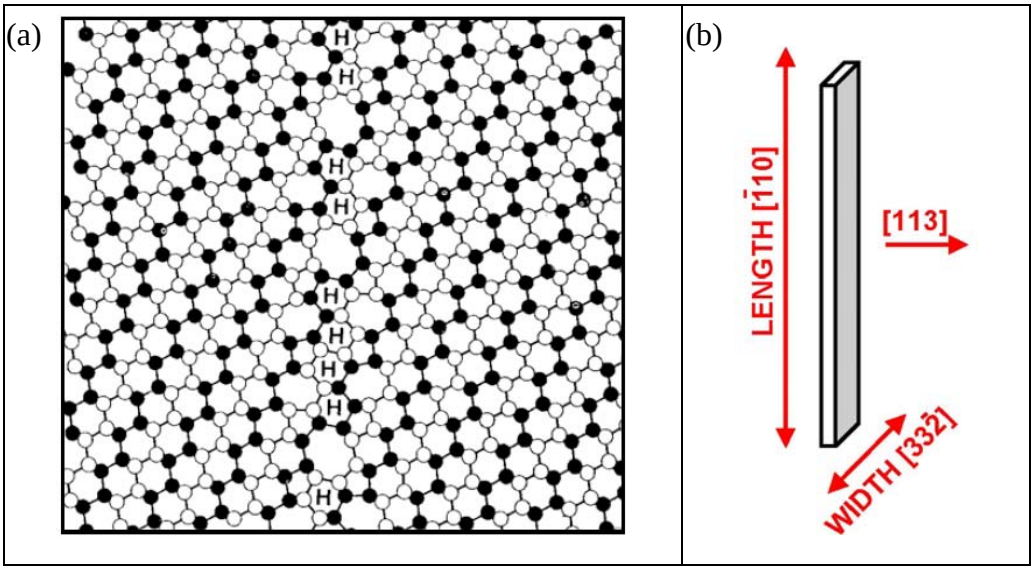

Figure 1.13: (a) <011> projection of the structure of the IRD. Note the presence of 8-membered atom rings inside the chain of wurtzite-type rings (H). Adapted from Ref. [1.58]. (b) Scheme of the same defect showing the crystallographic directions useful for its characterisation using x-ray scattering.

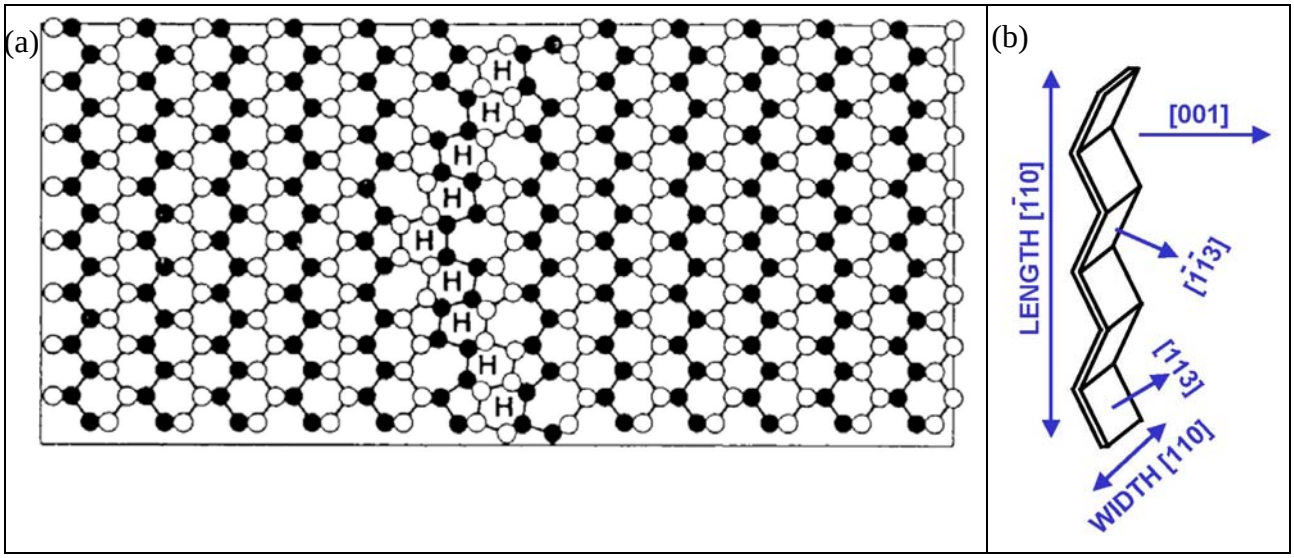

Figure 1.14: (a) <011> projection of the structure of the {1Hex}ZD. The wurtzite-type rings (H) lie in two intersecting {113} planes. Adapted from Ref. [1.58]. (b) Scheme of the same defect structure showing the crystallographic directions useful for its characterisation using x-ray scattering.

For both IRD and {1Hex}ZD, the direction of the defect "length" is a $[\bar{1}10]$ crystal direction. The direction of the defect "width" is different: $\left[33\bar{2}\right]$ and [110], for IRD and {1Hex}ZD, respectively [1.62].

In ion-implanted Si, the long narrow zig-zag defects are by far more often observed than the linear ones [1.47]. However, unlike the periodic and symmetric models presented in this section, the exact shape of 113's defects is rather irregular and depends on the sample processing conditions. Therefore these types of model can only represent a fraction of the total 113's present in real samples [1.47].

Eaglesham *et al.* [1.35] systematically studied rod-like defects in Si-implanted Si by TEM. They concluded that the mean width of 113's does not depend on the annealing conditions and it has a constant value of about 4 nm. Only recently Venezia *et al.* [1.63] have shown that significantly larger defects may appear for different annealing conditions. Nevertheless, direct measurements of 113's width with high statistics have not been published so far and recent models of extrinsic defects evolution in ion-implanted Si continue to assume a fixed width for 113's [1.64].

1.2.4.2 Structure of dislocation loops

In all crystal structures, dislocation loops form in the most densely packed crystal planes for reasons of energy minimisation. The {111} faulted circular Frank loops (FDL's) are typical for Si crystals and are the type of EOR defects most extensively studied by TEM. Among the numerous publications on this subject, one example is given in Ref. [1.65]. These loops consist of two circular extra {111} planes of SiI's with a stacking fault and a planar density of SiI's d = 15.66 nm^{-2}. The fault is bounded by a Frank partial dislocation with Burger's vector $\boldsymbol{b} = a/3\langle 111\rangle$, where a is the constant of the Si lattice. Four equivalent crystallographic variants of FDL exist.

The {111} perfect loops (PDL's) have {111}-habit planes and are elongated along <110> directions, perpendicular to their Burger's vector $\mathbf{b} = a/2\langle 110\rangle$. They present no stacking fault and exist in twelve crystallographic variants. The SiI's planar density in PDL's is the same as that for FDL's. As the other extended EOR defects, PDL's have been extensively studied via TEM imaging [1.67]. The structure of FDL's and PDL's is illustrated in Fig. 1.15 (a) and (b), respectively.

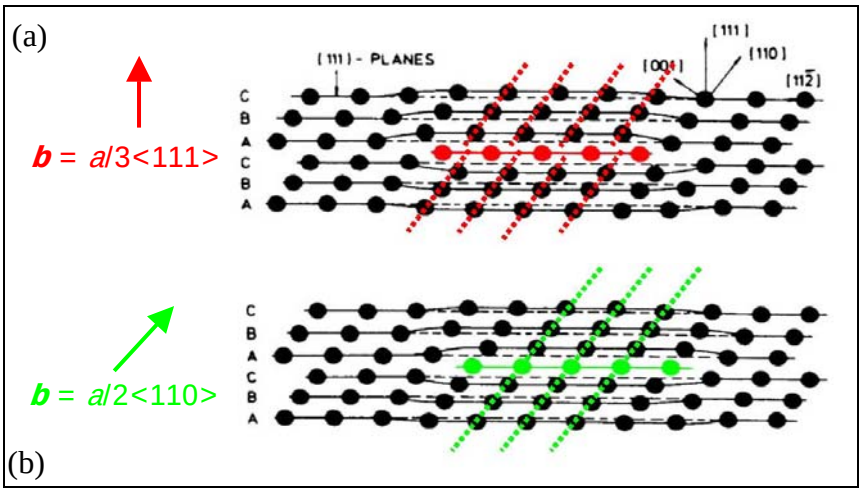

Figure 1.15: Crystallographic structure of faulted dislocation loops (a) and perfect dislocation loops (b), in silicon. The crystallographic orientations shown in (a) are valid for (b) too. Note that FDL's contain a {111} stacking fault, whereas PDL's do not. Adapted from Ref. [1.66].

1.2.4.3 Evolution of EOR defects

The EOR defects transform from type to type during the annealing. The mechanism responsible for their thermal evolution is the interchange of SiI's between defects of different size following an Ostwald ripening process [1.67]. The bigger defects grow at the expense of the smaller; the size of the latter reduces up to their complete dissolution. This theory relies on the Gibbs-Thompson equation, which states that every defect is surrounded by a supersaturation S of free interstitials directly related to its formation energy E_f. E_f is the energy needed to add an extra atom to the defect. Eq. (1.11) defines S.

$$S = \frac{C_i}{C_i^*} e^{E_f / kT} \tag{1.11}$$

where C_i^* is the equilibrium concentration of SiI's and C_i the dynamic concentration in equilibrium with the defect. E_f decreases with increasing defect size. Therefore, a gradient ΔS exists in the supersaturation between defects of different size, which induces the evolution of the defect population. The flux of SiI's, J, between defects of different formation energy is a function of their distance d, as shown in Eq. (1.12).

$$J = D_i C_i^* \frac{\Delta S}{d}, \tag{1.12}$$

where D_i is the diffusion coefficient for the Si self-interstitial atoms. In addition, the continuous interchange of SiI's maintains, in the EOR region, a certain "mean supersaturation", whose magnitude depends on the size distribution of the defects.

The diagram of formation energy of the EOR defects, reported in Fig. 1.16, mirrors the hierarchy of their evolution. Starting from the "magic clusters", stable for a number of SiI's n

< 10, the EOR damage evolves by forming {113}-defects. 113's formation energy, $\gamma_{\{113\}}$, approaches 0.65eV when the FDL's structure becomes more stable, for $n \sim 400$. At the end of the evolution process ($n \sim 10^5$), PDL's are the final structures with the lowest formation energy $\gamma_{PDL} = 0.027$eV.

The surface may play a crucial role in the damage evolution, acting as a strong sink (E_f ~0) for the SiI's involved in the defect ripening [1.69]. The flux of SiI's towards the surface J_{surf} is described in Eq. (1.13).

$$J_{surf} = D_i C_i^* \frac{\Delta\left(S_{EOR} - S_O\right)}{R_P} \tag{1.13}$$

where S_{EOR} and S_O are the average interstitial supersaturation in the defect layer and at the surface, respectively; R_p is the distance of the EOR damage from the surface.

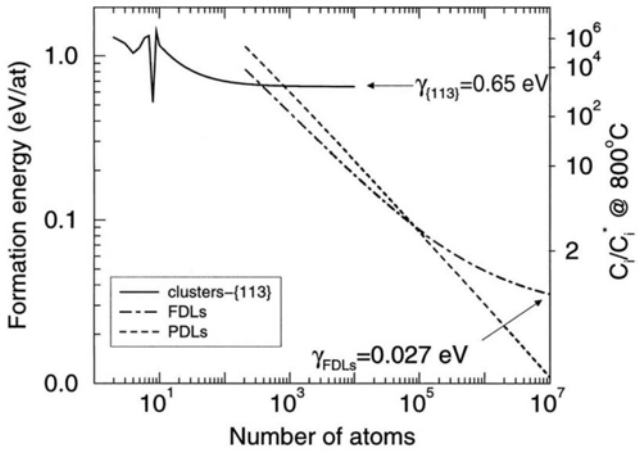

Figure 1.16: Formation energy (left axis) of the different types of extrinsic defects as a function of their size and corresponding values of Si interstitials supersaturation (right axis). Adapted from Ref. [1.68].

The recombination length, L_{surf}, gives the capture efficiency of the surface-sink and is determined by the implant and temperature conditions. Fig. 1.17(a) represents the surface proximity effect in the early stage of the annealing process for a shallow implant. A strong supersaturation gradient, S_{EOR} - S_O, exists between the region where the EOR defects are located, R_p, and the surface. Therefore, the latter competes with the defect growth in the total energy minimisation. An important flux of SiI's towards the surface is created. In Fig. 1.17(b) and (c), further evolution steps of the annealing process are presented, with the formation of 113's and DL's. The supersaturation S_{EOR} reduces and approaches the equilibrium concentration of SiI's, C_i^*. There are two reasons for this reduction. On one side, the formation of energetically more stable defects lowers the total energy in the EOR region. On the other side, the SiI's partially recombine at the surface. The supersaturation gradient, S_{EOR} -

S_O, decreases up to stopping the flux of SiI's, J_{surf}. In the example shown, this happens when DL's are formed, in the final stage of the annealing. The evolution of EOR defects may be blocked before the formation of DL's, if the supersaturation gradient S_{EOR} -S_O is so small that the flux of SiI's towards the surface is negligible $J_{surf} \approx 0$.

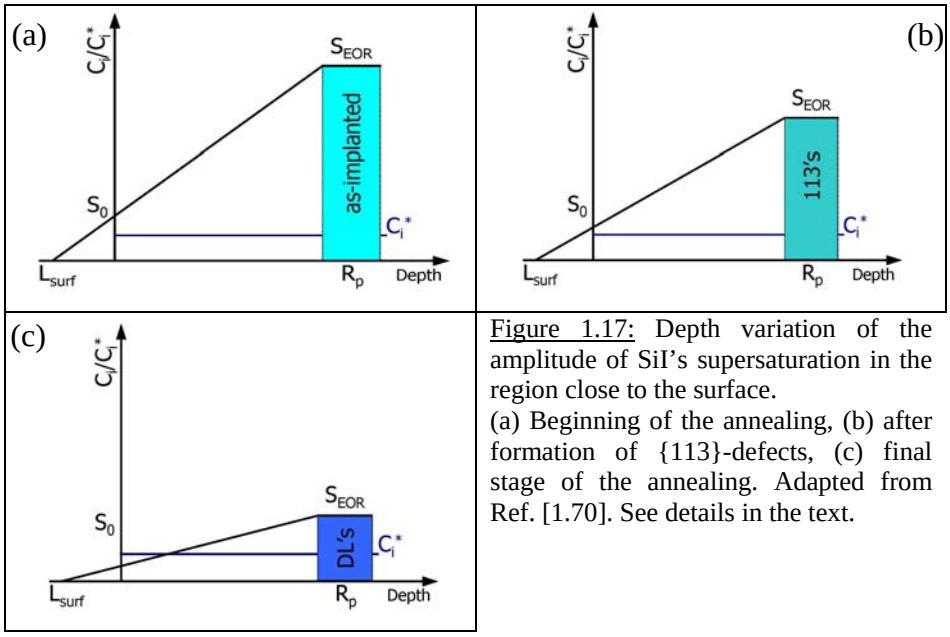

Figure 1.17: Depth variation of the amplitude of SiI's supersaturation in the region close to the surface.
(a) Beginning of the annealing, (b) after formation of {113}-defects, (c) final stage of the annealing. Adapted from Ref. [1.70]. See details in the text.

For a value of R_p large enough, corresponding to high implantation energy, the flux of SiI's towards the surface is negligible from the beginning of the annealing and the EOR damage evolves following a conservative Ostwald ripening mechanism, i.e. the number of SiI's in the EOR region is constant. When the flux of SiI's towards the surface is non-negligible, the Ostwald ripening is non-conservative, because a fraction of the SiI's supersaturation is captured by the surface. Other phenomena may give rise to a non-conservative evolution of the EOR damage. For instance, the annealing in oxidising ambient causes the injection of SiI's, which increases the supersaturation and affects the EOR behaviour [1.67].

The EOR damage behaviour has been extensively studied by TEM or by combining TEM and SIMS measurements, as reported in literature [1.47, 1.49, 1.52, 1.53, 1.65, 1.67-1.70].

1.3 Structural characterisation of ion-implanted Si

The continuous reduction of the p/n junction depth, required by front-end CMOS manufacturing, is intimately linked to the possibility of characterising such junctions. Therefore, the technological interest in deep sub-μm devices is the driving force of the development and up-grade of analytical techniques able to investigate the reproducibility of the implantation and annealing process on such reduced scale. The final aim is a detailed understanding of the physical mechanisms that govern doping and dopant activation processes. Since the structure of a CMOS transistor is too complex for being studied after the full process flow, all the issues related to ion implantation and annealing are investigated using bare wafers, i.e. Si wafers on which ion implantation and annealing only have been performed, avoiding all the other manufacturing steps.

A variety of techniques are traditionally used to provide information on the structural properties of ion-implanted Si. As indicated by the examples shown before, SIMS is the main experimental technique used to study the chemical profile of the dopant atoms in Si and in semiconductors in general. SIMS is an analytical technique based on ion sputtering. A primary ion beam with an impact energy varying from 0.2 to 15 keV is focused on the sample surface eroding it by sputtering. A little fraction of the emitted particles (electrons, atoms, photons) is represented by ions that can be extracted and discriminated by their mass, either by a magnetic field or a quadrupole or a time-of-flight system. [1.71]. The very good detection limit (usually between ppm and ppb), the reproducibility and the excellent depth resolution, which can be as low as 2 nm/decade, are the main strengths of SIMS.

The introduction of USJ's in the recent technological nodes has represented a challenge for SIMS applications [1.72, 1.73]. Being confined in the first tens of nanometers, with extremely abrupt distributions and high level of concentration, USJ dopant distributions require ultimate accuracy in terms of depth resolution, depth calibration, sensitivity and reduction of matrix and initial transient effects [1.71]. The traditional approach to meet such requirements is the reduction of the impact energy and the use of more grazing incidence angles for the ion beam. As a consequence, the penetration depth of primary ions decreases together with the ion-mixing effects. Unfortunately, several artifacts can hinder this approach. The roughness evolves during sputtering by sub-keV O_2^+ and Cs^+ and the depth resolution deteriorates quickly. Also the sputtering rate decreases, producing an inaccurate shift of the measured distributions to the surface when a constant sputtering rate is employed to convert the time into depth [1.74]. Moreover, several accuracy problems arise for the quantification of

the near-surface distributions, because of the variations of ion yield when the sputtering process starts.

Another ion-based technique extensively used to investigate damage formation and annealing in Si is the Rutherford Backscattering Spectrometry in Channeling geometry (RBS-C) and more recently its low energy variant, the Medium Energy Ion Scattering (MEIS) technique [1.75, 1.76]. MEIS measurements require that the ions, normally H^+ or He^+, are accelerated to around 100 keV and scattered from the crystalline sample. After aligning the ion beam along the major crystal directions, the scattered ions are collected as a function of their exit energy and scattering angle. On the basis of the collected ion yield vs. energy spectrum, quantitative compositional and depth analysis can be done. MEIS is thus able to provide simultaneous information about the disorder in the Si lattice and the dopant atoms taking up substitutional positions. The use of medium ion energy, in combination with high resolution energy analyser ($\Delta E/E < 0.5\%$), results in a sub-nm depth resolution that is the main advantage of this technique with respect to RBS-C.

In the field of crystalline defects characterisation, TEM and HRTEM are the traditional analytical techniques, as confirmed by the majority of the cited references [1.47, 1.49, 1.52, 1.53, 1.65, 1.67-1.70].

Recently, x-ray scattering techniques based on synchrotron radiation [1.78, 1.79] became available, which offer new possibilities for a non-destructive study of ion-implanted Si. The main aim of this work is to develop a combination of different x-ray scattering methods, such as grazing-incidence diffuse x-ray scattering, high-resolution x-ray diffraction and specular reflectivity, sensitive to the structural properties of USJ's. The results from the x-ray scattering investigation will be compared with those obtained by SIMS, MEIS and TEM in order to identify the corresponding advantages and drawbacks.

2. Theoretical background

Grazing incidence diffuse x-ray scattering (GI-DXS) is the main experimental technique used in this thesis for the investigation of the structural properties of ion-implanted Si. In this chapter, the theoretical background of this method is described on the basis of the specific literature available on this subject. Sec. 2.1 contains the explanation of the origin of the defect-induced diffuse x-ray scattering (DXS) and a summary of the theory of the DXS for point and extended defects applied to bulk crystals. The use of the grazing-incidence scattering geometry enables the near-surface sensitivity of the x-rays. For this reason, it is needed in order to study the structure of ultra-low energy ion implanted Si. The physics related to this aspect is briefly reported in Sec. 2.2. Finally, in Sec. 2.3, the results from the theory of the GI-DXS technique are discussed.

2.1 Theory of the defect-induced diffuse x-ray scattering

The first calculations of the diffuse x-ray scattered (DXS) intensity from defects in a crystal were published by Huang [2.1] in 1947. The publications by Krivoglaz and co-workers, during the 60's, were the foundations of a fundamental work, which was recently reedited [2.2]. The experimental investigation of the defect structure in crystals, using the DXS technique, was first developed for defects in metals [2.3, 2.4]. The reader is addressed to the review papers from Dederichs [2.5] and Ehrhart [2.6] for more detailed references on the early history of DXS. A summary of the fundamental results from the theory of the diffuse x-ray scattering is provided in the following. The basic principles of x-ray scattering will not be explained in this section and the interested reader is addressed to Refs. [2.7, 2.8, 2.9] for further information.

2.1.1 Origin of the defect-induced diffuse x-ray scattering

The results from the diffuse x-ray scattering theory discussed in this and in the following section (Sec. 2.1.2) are based on Ref. [2.5] and [2.9].

For elastic scattering of x-rays, the frequencies ω of the primary and scattered waves are equal. Therefore, their wave vectors, $\boldsymbol{k}_i$ and $\boldsymbol{k}_f$, respectively, show the same modulus, defined as $k = |\boldsymbol{k}_i| = |\boldsymbol{k}_f| = \omega/c = 2\pi/\lambda$, where λ is the x-ray wavelength.

The primary wave is assumed to be planar and monochromatic and it reads

$$\boldsymbol{E}_i(\boldsymbol{r}) = E_i e^{i\boldsymbol{k}_i \boldsymbol{r}} \tag{2.1}$$

where $\boldsymbol{r}$ is the vector of the space coordinates. The scattered wave is a coherent superposition of plane waves with equal frequencies, but different directions,

$$\boldsymbol{E}_f(\boldsymbol{r}) = \int d\Omega E_f(\Omega) e^{i\boldsymbol{k}_f \boldsymbol{r}} \tag{2.2}$$

where $d\Omega = d\phi d\theta \sin\theta$ and the spherical coordinate angles θ and ϕ determine the direction of $\boldsymbol{E}_f$. In the Fraunhofer or far-field approximation, used in the following, the direction of the exit wave is determined by the position of the detector.

Any scattering process can be described by the scalar wave equation in (2.3).

$$\left(\Delta + k^2\right)\boldsymbol{E}_f(\boldsymbol{r}) = \hat{\boldsymbol{V}}(\boldsymbol{r})\boldsymbol{E}_f(\boldsymbol{r}) \tag{2.3}$$

where $\hat{\boldsymbol{V}}(\boldsymbol{r})$ is the operator of the scattering potential. In a non-magnetic material (i.e. where the magnetic permeability of the sample is $\mu = \mu_o$), the scattering potential is defined as,

$$\hat{\boldsymbol{V}}(\boldsymbol{r}) = graddiv - k^2 \chi(\boldsymbol{r}) \tag{2.4}$$

where $\chi(\boldsymbol{r}) = \varepsilon_{rel}(\boldsymbol{r}) - 1$ is the polarizability of the material; ε_{rel} is the relative permittivity.

Within the kinematical (i.e. single scattering) approximation, the intensity of the scattered wave can be expressed by the differential cross-section in Eq. (2.5) written using the bra-ket notation.

$$\frac{d\sigma}{d\Omega} = \frac{1}{16\pi^2}\left|\left\langle \boldsymbol{k}_f \left| \hat{\boldsymbol{V}} \right| \boldsymbol{k}_i \right\rangle\right|^2 \tag{2.5}$$

The differential cross-section determines the flux of the scattered photons into an elementary solid angle $d\Omega$ pointing towards the detector. Since $div\left|\boldsymbol{k}_i\right\rangle = 0$, in the kinematical approximation the matrix element $\mathcal{T}$ can be expressed as in Eq. (2.6) and it is proportional to the Fourier transform of the electron density.

$$\mathcal{T} \approx \left\langle \boldsymbol{k}_f \left| \hat{\boldsymbol{V}} \right| \boldsymbol{k}_i \right\rangle \approx 4\pi r_e C \int d^3\boldsymbol{r}\, \rho_{el}(\boldsymbol{r}) e^{-i(\boldsymbol{k}_f - \boldsymbol{k}_i).\boldsymbol{r}} \tag{2.6}$$

where $r_e = 2.814 \times 10^{-5}$ Å is the classical radius of the electron and C is the linear polarization factor. Two limiting cases exist for the polarization of the primary wave with respect to the scattering plane. In the S-polarization, the polarization vectors of the primary and of the scattered waves are perpendicular to the scattering plane and $C = 1$. In the P-polarization, both the polarization vectors lay in the scattering plane and $C = \cos(2\theta)$, where 2θ is the scattering angle. In the case of synchrotron radiation, the x-rays are linearly polarized in the horizontal plane [2.8]. Therefore, the S-polarization holds for the experiments performed in this work (see Sec. 3.1.2). $\rho_{el}(\boldsymbol{r})$ in Eq. (2.6) is the electron density.

If the illuminated sample is randomly distorted, due to the presence of defects, and the scattered wave is averaged over a statistical ensemble of all the microstructure configurations of such defects, the random fluctuation of the defect concentration can be neglected. This is called ergodic hypothesis and based on it, Eq. (2.7) is valid.

$$\left|\mathcal{T}\right|^2 = \left|\left\langle \boldsymbol{k}_f \left| \hat{\boldsymbol{V}} \right| \boldsymbol{k}_i \right\rangle\right|^2 \tag{2.7}$$

Hence, the differential cross-section in Eq. (2.5) can be rewritten as

$$\frac{d\sigma}{d\Omega} = \frac{1}{16\pi^2}\left\langle \left|\mathcal{T}\right|^2 \right\rangle \tag{2.8}$$

with $\left\langle \left|\mathcal{T}\right|^2 \right\rangle = \left|\left\langle \mathcal{T} \right\rangle\right|^2 + Cov(\mathcal{T},\mathcal{T})$

(The covariance of two random quantities *a* and *b* is defined as $Cov(a,b) = \left\langle ab^* \right\rangle - \left\langle a \right\rangle \left\langle b \right\rangle^*$.)

Following Eq. (2.8), the scattered wave contains two components. A coherently scattered wave, corresponding to $\left|\left\langle \mathcal{T} \right\rangle\right|^2$, and a diffusely scattered wave that originates from $Cov(\mathcal{T},\mathcal{T})$.

In a deformed lattice, the polarizability coefficients are a function of the spatial coordinates and $\chi^{def}(\boldsymbol{r})$ can be expressed as a "distorted" Fourier series, as shown in Eq. (2.9).

$$\chi^{def}(\boldsymbol{r}) = \sum_g \left[\chi_g + \delta\chi_g(\boldsymbol{r}) \right] e^{i\boldsymbol{g}.(\boldsymbol{r}-\boldsymbol{u}(\boldsymbol{r}))} \equiv \sum_g \chi_g(\boldsymbol{r}) e^{i\boldsymbol{g}.(\boldsymbol{r}-\boldsymbol{u}(\boldsymbol{r}))} = \sum_g \chi_g(\boldsymbol{r}) e^{i\boldsymbol{g}_{def}.(\boldsymbol{r}-\delta\boldsymbol{u}(\boldsymbol{r}))} \tag{2.9}$$

where the index *g* indicates a sum over all the reciprocal lattice points, because the periodicity of the polarizability $\chi(\boldsymbol{r})$ is the same as the one of the crystal. The factor $\delta\chi_g(\boldsymbol{r})$ represents the change of the polarizability due to the displacement of the atoms into the elementary unit cell. In addition, the polarizability in Eq. (2.9) depends on ***u(r)*** that is the random displacement field induced by the presence of the defects. The displacement field can be divided into two parts: $\boldsymbol{u}(\boldsymbol{r}) = \langle \boldsymbol{u}(\boldsymbol{r}) \rangle + \delta\boldsymbol{u}(\boldsymbol{r})$; i.e. ***u(r)*** results from the averaged displacement $\langle \boldsymbol{u}(\boldsymbol{r}) \rangle$ and a random deviation $\delta\boldsymbol{u}(\boldsymbol{r})$ from the new average lattice sites. The presence of defects in a perfect lattice induces a shift in the position of the Bragg peaks, which is accounted for by $\boldsymbol{g}_{def.}$ Defined as $\boldsymbol{g}_{def} = \boldsymbol{g} - \nabla\left(\boldsymbol{g}\left\langle \boldsymbol{u}(\boldsymbol{r}) \right\rangle\right)$, $\boldsymbol{g}_{def}$ is the vector of the averaged reciprocal lattice. In the following the subscript "$_{\text{def}}$" will be omitted for sake of brevity.

Using the two-beam approximation, i.e. selecting only one $\boldsymbol{g} = \boldsymbol{h}$ from the series in Eq. (2.9), the diffuse part of the differential cross-section can be rewritten as,

$$\left(\frac{d\sigma}{d\Omega}\right)_{diff} = \frac{k^4}{16\pi^2}\int_V d^3\boldsymbol{r} \int_V d^3\boldsymbol{r}' M_h\left(\boldsymbol{r},\boldsymbol{r}'\right) e^{-i\boldsymbol{q}.(\boldsymbol{r}-\boldsymbol{r}')} \tag{2.10}$$

where $\boldsymbol{q} = \boldsymbol{k}_f - \boldsymbol{k}_i - \boldsymbol{h} = \boldsymbol{Q} - \boldsymbol{h}$ is the reduced scattering vector, V is the sample volume and $M_h(\boldsymbol{r},\boldsymbol{r}') = Cov\left(\chi_h(\boldsymbol{r})e^{-i\boldsymbol{h}.\delta\boldsymbol{u}(\boldsymbol{r})}, \chi_h(\boldsymbol{r}')e^{-i\boldsymbol{h}.\delta\boldsymbol{u}(\boldsymbol{r}')}\right)$ is the covariance of the lattice deformation in point ***r*** and ***r'***. In conclusion, the diffusively scattered intensity originates from the covariance *M* of the deformation. Therefore, a sample would not produce any incoherent scattered wave, if its deformation in point ***r*** and ***r'*** would not be correlated, i.e. if $M_h(\boldsymbol{r}, \boldsymbol{r'}) = 0$.

Summarising, the scattered intensity ***I(Q)*** as a function of the scattering vector ***Q*** for a perfect undistorted crystal, Fig. 2.1(a), is shown in Fig 2.2, red curve. ***I(Q)*** is zero except for the node of the reciprocal lattice, where the Bragg's law, $\lambda = 2d_{hkl}\sin\Theta_B$, is satisfied. d_{hkl} is the characteristic distance of the family of planes *hkl* and Θ_B is the Bragg angle. Narrow Bragg peaks are expected at the reciprocal lattice vectors $\boldsymbol{h}_{hkl}$.

Figure 2.1(b) shows the scheme of a distorted crystal containing point defects.

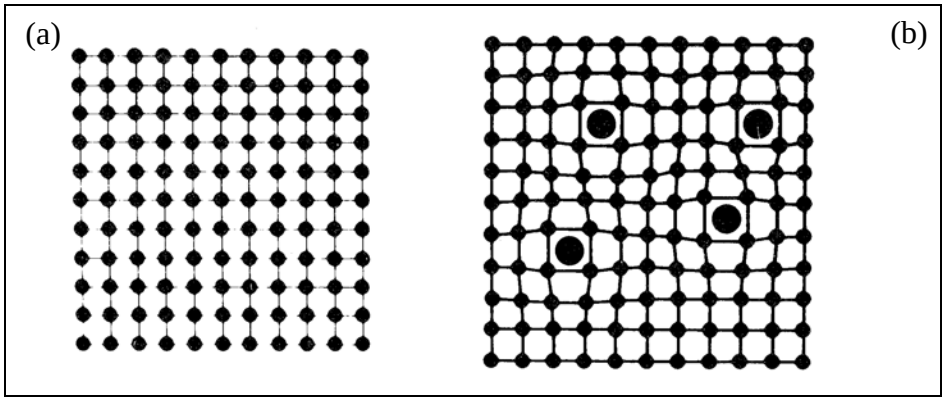

Figure 2.1: Schematic view of a crystal without (a) and with (b) defects. The presence of defects originates a distortion field in the crystalline matrix. Adapted from Ref. [2.10].

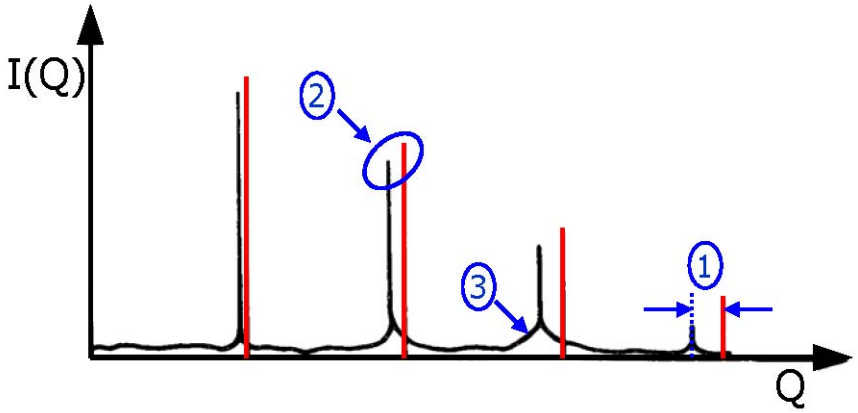

Figure 2.2: Schematic representation of the scattered intensity $I(\boldsymbol{Q})$ as a function of the scattering vector ***Q***. From perfect crystals (red line) and from crystals containing lattice-expanding defects (black line). The numbers visualise the three effects predicted by the theory for a crystal containing defects. See details in the text. Adapted from Ref. [2.10].

For the kinematical scattering from a lattice containing defects, the following changes of distribution of the scattered intensity are predicted [2.10].

1) The position of the Bragg peaks is shifted, due to the change Δa of the average lattice parameter induced by $\langle \boldsymbol{u(r)} \rangle$. Therefore, $\boldsymbol{g}$ is redefined as $\boldsymbol{g}_{def}$.
2) The Bragg coherent intensity is attenuated, due to deviations $\delta \boldsymbol{u(r)}$ from this new average lattice. Such reduction is described by a static Debye-Waller factor D^2. D is defined as $D = \left\langle \exp\left(-i\boldsymbol{h}_{hkl}.\delta \boldsymbol{u}\right)\right\rangle$. The value of the attenuation yields the average number of atoms that are no longer contributing to the Bragg scattering.
3) The intensity, lost in the coherent Bragg peaks, appears as diffuse scattering (DXS) intensity in the neighbourhood of the reciprocal lattice points, as described by Eq. (2.10).

The scattering pattern from a lattice containing defects is shown schematically in Fig. 2.2, black curve.

2.1.2 Diffuse x-ray scattering from point defects and defect clusters in bulk crystals

In the Krivoglaz's classification of defects [2.2], point defects and defect clusters are considered as weak defects, i.e. they are finite defects in an infinite crystal matrix. Different areas compose such defects, as schematically represented in Fig. 2.3. The defect core is the region where the structure differs appreciably from the structure of the matrix, Fig. 2.3(a). Moreover, a deformed crystalline area surrounds the defect core.

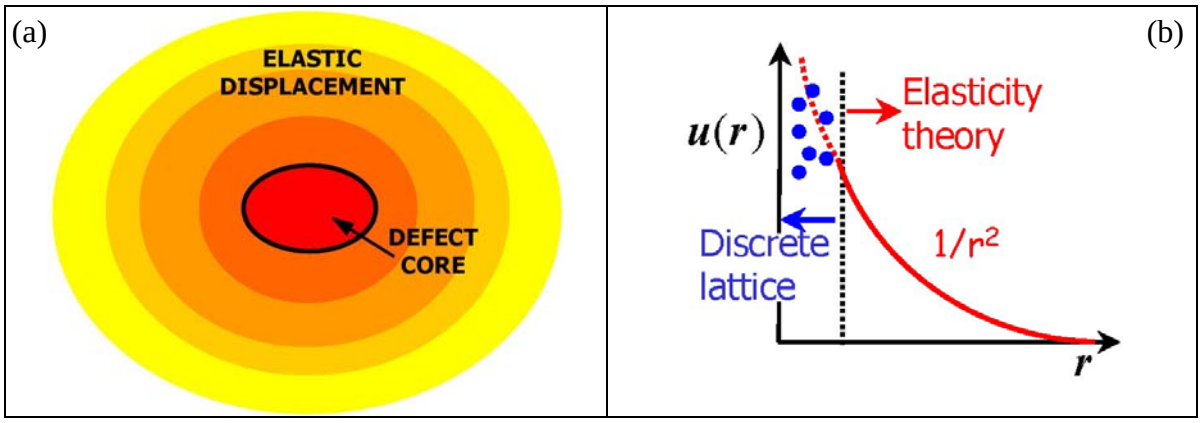

Figure 2.3: (a) Scheme of the structure of a defect formed by a defect core and its distortion field. (b) Schematic view of the distortion field, which is formed by two zones. Close to the defect core, atomistic models only can describe the distortion field because of the strong distortion. Far from the defect core, the elasticity theory is valid and $\boldsymbol{u}(\boldsymbol{r}) \propto r^{-2}$.

In this deformed region, two zones can be further distinguished. Close to the defect core, the lattice distortion is strong. Therefore, only calculations performed using a discrete atomistic model for the distortion field can be applied to calculate the DXS from this area. Outside this region, the distortion is weaker and the asymptotic displacement field can be described using the elasticity theory (i.e. $\boldsymbol{u}(\boldsymbol{r}) \propto r^{-2}$).

The total displacement field of the *n*-th atom in the defect neighbourhood is defined as

$$\boldsymbol{u}(\boldsymbol{r}_n) \equiv \boldsymbol{u}_n = \sum_{\alpha} \sum_{m} c_m^{\alpha} \boldsymbol{v}_{nm}^{\alpha}, \tag{2.11}$$

where α is the type of defect, *m* are the different lattice sites and c_m^{α} is the random occupation number (if a defect of type α occupies the position *m*, the value of c_m^{α} is 1, otherwise is 0). $\boldsymbol{v}_{nm}^{\alpha}$ is the component of the displacement at the *n*-th atom, due to the presence of a defect of type α on the lattice site *m*.

The polarizability of the core differs from the matrix following Eq. (2.12).

$$\chi_h(\boldsymbol{r}_n) \equiv \chi_{hn} = \chi_h + \sum_{\alpha} \Delta\chi_h^{\alpha} \sum_{m} c_m^{\alpha} s_{nm}^{\alpha} \tag{2.12}$$

where $\Delta\chi_h^{\alpha}$ is the difference between the polarizability in the core of a defect of type α and the polarizability of the surrounding matrix. s_{nm}^{α} is the shape function of the core for a defect of type α. The value of s_{nm}^{α} is unity if both points *n* and *m* belong to the core, otherwise it is zero.

The density of the defects of type α is defined as $c^{\alpha} = \left\langle c_m^{\alpha} \right\rangle$ and, in the assumption that $c^{\alpha} << 1$ and the defect positions are not correlated, the covariance function $M_h(\boldsymbol{r}_n, \boldsymbol{r}_m)$ can be rewritten as in Eq. (2.13).

$$M_h(\boldsymbol{r}_n, \boldsymbol{r}_m) = \sum_{\alpha s} c^{\alpha} \Psi_{ns}^{\alpha} \left(\Psi_{ms}^{\alpha} \right)^* \tag{2.13}$$

where $\Psi_{ns}^{\alpha} = \left\langle \chi_{\boldsymbol{h}} \right\rangle \left(e^{-i\boldsymbol{h}.\boldsymbol{v}_{ns}^{\alpha}} - 1 \right) + \Delta\chi_{\boldsymbol{h}}^{\alpha} s_{ns}^{\alpha} e^{-i\boldsymbol{h}.\boldsymbol{v}_{ns}^{\alpha}}$.

The effective defect size D_e is defined as the size of the defect core and the corresponding displacement field (Fig. 2.3). If D_e is much smaller than the thickness of the layer where the defect is located, then $\Psi_{ns}^{\alpha} = \Psi_{n-s}^{\alpha} \equiv \Psi^{\alpha}(\boldsymbol{r}_n - \boldsymbol{r}_s)$ and depends only on the distance between the *n*-th and the *s*-th atoms. Under this condition, the diffuse cross section has the form

$$\left(\frac{d\sigma}{d\Omega} \right)_{diff} = \frac{k^4}{16\pi^2} V \sum_{\alpha} n^{\alpha} \left| \Psi^{\alpha FT}(\boldsymbol{q}) \right|^2 \tag{2.14}$$

with $n^{\alpha} = c^{\alpha} / a^3$, being the density of the defect of type α per unit cell. $\Psi^{\alpha FT}(\boldsymbol{q})$ is the Fourier transform $\Psi^{\alpha FT}(\boldsymbol{q}) = \int d^3\boldsymbol{r}\, \Psi^{\alpha}(\boldsymbol{r})\, e^{-i\boldsymbol{q}.\boldsymbol{r}}$.

Following the definition of Ψ^{α}_{ns} in Eq. (2.13), the diffusely scattered signal is composed by the coherent superimposition of two contributions. The first one is the diffuse scattering from the deformed area in the defect neighbourhood and it is represented by the term

$$\Psi^{\alpha}_{Huang} = \chi_{\boldsymbol{h}} \left(e^{-i\boldsymbol{h}.\boldsymbol{v}^{\alpha}} - 1 \right) \overset{\substack{for\ small \\ \boldsymbol{h}.\boldsymbol{v}^{\alpha}}}{\approx} i\chi_{\boldsymbol{h}} \boldsymbol{h}.\boldsymbol{v}^{\alpha}(\boldsymbol{r}) \tag{2.15}$$

for defects of type α. The expression in the third term is valid, provided that the displacements of the atoms around the defect core are much smaller than the distance $2\pi/|\boldsymbol{h}|$ of the diffracting crystal planes. This scattering contribution is usually called Huang diffuse scattering (HDS) and the HDS intensity is given by Eq. (2.16).

$$I_{Huang}(\boldsymbol{Q}) \propto \left|\chi_{\boldsymbol{h}}\right|^2 \sum_{\alpha} n^{\alpha} \left| \boldsymbol{h}.\boldsymbol{v}^{\alpha FT}(\boldsymbol{q}) \right|^2 \tag{2.16}$$

The second contribution to Eq. (2.13) is the core scattering, expressed as

$$\Psi^{\alpha}_{core} = \Delta\chi^{\alpha}_{\boldsymbol{h}} s^{\alpha}(\boldsymbol{r}) e^{-i\boldsymbol{h}.\boldsymbol{v}^{\alpha}(\boldsymbol{r})} . \tag{2.17}$$

The corresponding intensity is proportional to the square of the Fourier transform of the shape function of the defect α. This term is also known as “Laue scattering”.

If the defect distortion is weak, it can be described by means of the elasticity theory. In this case, the expression of the HDS intensity can be simplified as shown in Eq. (2.18).

$$\left| \boldsymbol{h}.\boldsymbol{v}^{FT}(\boldsymbol{q}) \right|^2 = \left| 4\pi P \frac{\boldsymbol{h}.\boldsymbol{q}}{q^2} \right|^2 \tag{2.18}$$

where P expresses the defect “strength” as $P = \frac{\delta}{4\pi} \frac{1+\nu}{1-\nu}$. δ is the lattice mismatch between the defect core and its matrix and ν is the Poisson ratio. Eq. (2.18) is valid exactly for isotropic defects in an isotropic matrix only.

Due to the inversion symmetry of the elastic displacement field $\boldsymbol{u}(\boldsymbol{r}) = \text{-}\boldsymbol{u}(\boldsymbol{r})$, the HDS is symmetric with respect to the Bragg peak and presents a nodal plane through the reciprocal lattice point. A nodal plane is plane of zero scattered intensity. Its existence is related to the symmetry of the displacement field, so the nodal plane may vanish if such symmetry disappears.

As mentioned above, the total DXS is the coherent superimposition of the Huang scattering term and of the core scattering term. If the exact formula is used, instead of the so-

called Huang approximation, i.e. $\exp(-i\boldsymbol{h}.\boldsymbol{v})-1 \approx -i\boldsymbol{h}.\boldsymbol{v}$, the symmetry of the HDS is broken. Hence, an asymmetric component of DXS is observed, which depends on the sign of the displacement field $\boldsymbol{u}(\boldsymbol{r})$, which is the same as the sign of δ.

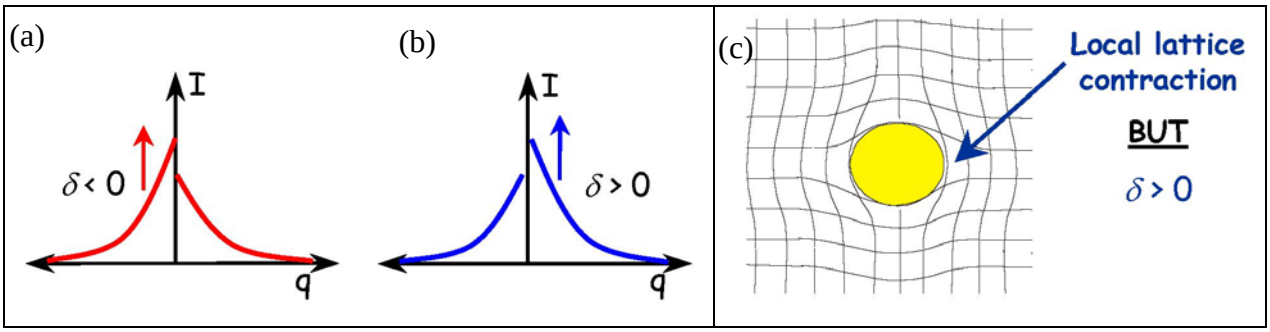

Figure 2.4: Schematic representation of diffuse intensity as a function of q: (a) diffuse scattering intensity from a defect contracting the lattice (e.g. vacancy); (b) same as (a) for a defect expanding the lattice (e.g. interstitial); (c) scheme of a defect expanding the lattice showing local lattice contraction.

The scattering from lattice expanding defects with positive δ, like SiI's, is illustrated in Fig. 2.4(b). It results in local lattice compression, as shown in Fig.2.4(c), and exhibits a higher diffuse intensity for positive values of q. On the contrary, for defects that contract the average lattice, the DXS intensity is stronger for negative values of q, as shown in Fig. 2.4(a). In conclusion, the shift of the DXS intensity appears in the opposite direction with respect to the shift of the Bragg peak (Sec. 2.1.1), because the local lattice distortion dominates DXS. As the DXS intensity is proportional to the square of the defect-induced distortion field $\boldsymbol{v}^{\alpha}(\boldsymbol{r})$, the DXS contribution from contracting and expanding defects cannot cancel each other resulting is zero DXS intensity, when both types of defects are present. For example, for vacancy with $\delta_V < 0$ and interstitials with $\delta_I > 0$, in a Si lattice, the HDS intensity will be: $I_{HDS,V\&I}(\boldsymbol{Q}) \propto n^V \delta_V{}^2 + n^I \delta_I{}^2$.

Point defects may aggregate to form clusters. The theory of the DXS from defect clusters relies on the assumption that a defect cluster can be treated like a new bigger point defect, as schematised in Fig. 2.5(a). For a random distribution of point defects of type α, the HDS component is $I^1_{HDS,\alpha}(\boldsymbol{Q}) \propto n^{\alpha}\boldsymbol{v}^{\alpha}(\boldsymbol{r})^2$. In the hypothesis that the long-range displacement fields of N_d point defects of type α superimpose linearly when they aggregate to form a cluster, i.e. $\boldsymbol{v}^{N_d}(\boldsymbol{r}) = N_d\boldsymbol{v}^{\alpha}(\boldsymbol{r})$, the superposition model is valid. This would be the case for a cluster of weakly interacting defects. The HDS intensity component $I^{N_d}_{HDS,\alpha}(\boldsymbol{Q})$ of the total scattered intensity from a cluster containing N_d point defects can be written as Eq. (2.19) [2.4].

$$I^{N_d}_{HDS,\alpha}(\boldsymbol{Q}) \sim n^{N_d}\left(\boldsymbol{v}^{N_d}(\boldsymbol{r})\right)^2 \sim \frac{n^\alpha}{N_d}\left(N_d{}^2\boldsymbol{v}^\alpha(\boldsymbol{r})^2\right) \sim n^\alpha N_d \boldsymbol{v}^\alpha(\boldsymbol{r})^2 \sim N_d I^1_{HDS,\alpha}(\boldsymbol{Q}) \qquad (2.19)$$

The scattered intensity increases by a factor N_d, compared to the signal arising from the same number of separate point defects of type α. As a consequence of the clustering process, the point defects are no longer scattering independently, as assumed when considering $n^\alpha << 1$, but they scatter coherently. Therefore, an increase in the total scattered yield is observed, when point defects aggregate.

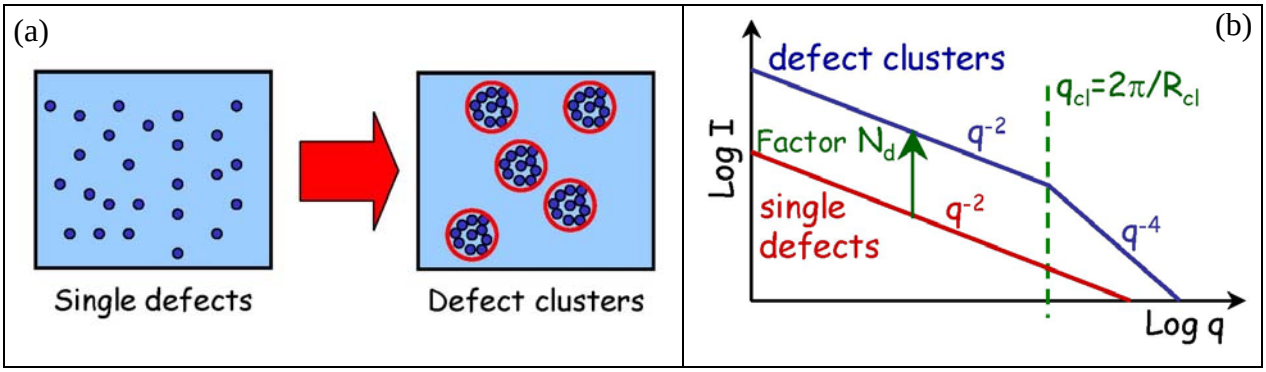

Figure 2.5: (a) Scheme of the aggregation of defect clusters from point defects. (b) q-dependence of the DXS intensity close to the Bragg peak for point defects and defect clusters. See text for details.

In the region close to the cluster, the displacement field $\boldsymbol{v}^{N_d}(\boldsymbol{r})$ is strong and the Huang approximation is no longer valid. Another asymptotic expression can be applied in this region of larger $\boldsymbol{q}$ that is known as Stokes-Wilson scattering (SWS) [2.5]. Following this approximation, the DXS intensity, $I_{SW}(\boldsymbol{Q})$, is expressed by Eq. (2.20).

$$I_{SW,N_d}(\boldsymbol{Q}) \sim n^{N_d}\frac{P_{N_d}{}^2}{q^4} \qquad (2.20)$$

The main properties of the SWS are its linearity with the concentration of the clusters n^{Nd} and its q^{-4} dependence. The SWS is proportional to the square of the cluster "strength", P_{Nd}. In conclusion, the q-dependence of the DXS from defect clusters presents two different behaviours. First, a q^{-2} decay is observed close to the Bragg peak, where the HDS approximation for weak distortions is valid. In addition, a q^{-4} decrease characterises the region with higher values of q, where the SWS model can be applied. The average size of the clusters, $R_{cl}=2\pi/q_{cl}$, is evaluated by the position in q_{cl} of the change in the slope of the DXS intensity from q^{-2} to q^{-4}, as illustrated in Fig. 2.5(b).

For even larger q values, the displacement field in the core of the cluster determines the scattering cross-section. Therefore, the decay of the DXS intensity can be even faster than q^{-4}

[2.5] and lattice statics simulations have to be used to predict the defect-induced DXS intensity, as it will be explained in the following section.

Experimentally, a q^{-2} decay of the scattered intensity, typical for the Huang diffuse scattering, is found for point defects and small defects cluster, which distort the lattice weakly (e.g. “magic clusters” and di-interstitials in ion-implanted Si, see Sec.1.2.4).

2.1.3 Diffuse x-ray scattering from extended defects

It has been shown in Sec. 1.2.4 that extended defects, such as dislocation loops and {113}-defects, are present in Si after ion implantation and annealing. In this section, the features of the DXS signal typical for this class of defects are discussed.

The properties of the scattering from faulted dislocation loops (FDL’s) are explained hereafter, based on the theory developed by Larson [2.11] and Krivoglaz [2.2]. It has been shown in Sec. 1.2.4.2 that FDL’s contain an extrinsic stacking fault (SF) in the {111} directions. The predicted DXS intensity from this kind of defect extends with a rod shape in the [111] direction, which is the direction of the Burger’s vector of the SF. This rod-shape DXS intensity distribution is usually called “streak”. The distortion field induced by the SF, $\boldsymbol{v}^{SF}(\boldsymbol{r})$, lies parallel to the Burger’s vector, $\boldsymbol{b}$, and hence its Fourier transform $\boldsymbol{v}^{SF,FT}(\boldsymbol{q})$ also possesses this direction. In conclusion, $\boldsymbol{v}^{SF}(\boldsymbol{r}) // \boldsymbol{v}^{SF,FT}(\boldsymbol{q}) // \boldsymbol{b} // [111]$. The width of the streak along the direction of the Burger’s vector $\boldsymbol{b} // [111]$ is constant, while its intensity shows a q^{-2} decay typical for HDS. According to Ref. [2.11], the scattering cross-section of the FDL in the Huang approximation is given by Eq. (2.21).

$$I_{HDS}^{SF} \propto n^{\alpha,SF} \left| \boldsymbol{h}.\boldsymbol{v}^{SF,FT}(\boldsymbol{q}) \right|^2 \left(2\frac{J_1(hR_{SF})}{hR_{SF}} \right)^2 \tag{2.21}$$

where $n^{\alpha,SF}$ is the concentration of the atoms α bonded to the SF’s. The form factor of the disc-shaped extrinsic SF is determined from the first-order Bessel function $J_1(hR_{SF})$ of the radius of the SF, R_{SF}. In Ref. [2.11], Eq. (2.21) is derived for {111}-FDL’s in an Al crystal of fcc structure, nevertheless it is applicable also for Si crystals, because the Si diamond structure is the combination of two shifted fcc lattices. In conclusion, the analysis of the [111]-oriented DXS intensity streaks enables to determine experimentally both the average radius of the SF perpendicular to the Burger’s vector, from the full width half height of the DXS streak, and the total number of atoms tied up in the SF, from the integrated intensity of the streak.

Calculations of the DXS intensity, based on atomistic simulations, are currently available, as pioneered by K. Nordlund *et al.* [2.12]. They constitute a powerful tool for calculating the DXS intensity from any defect configuration in most of the crystalline solids, provided that reliable models for the interatomic potential are available for the crystalline matrix. This is indeed the case for Si. Therefore, these atomistic calculations are used successfully to model the DXS from extended defects in ion-implanted Si samples.

The calculated DXS pattern for FDL's in Si has been published in Ref. [2.13] and is shown in Fig. 2.6.

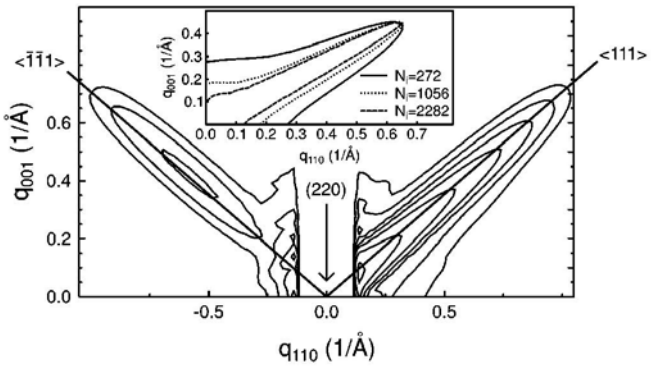

Figure 2.6: Simulated DXS pattern around the 220 surface Bragg peak for a FDL with a stacking fault formed by 1000 interstitial atoms. The pattern is averaged over the four different crystallographic orientations. The inset shows one iso-intensity line from the positive side of the 220 for three stacking faults with different number of SiI's, N_i . Adapted from Ref. [2.13].

The calculated DXS patter consists, as expected, in intensity streaks elongating in the [111] and $[\bar{1}\bar{1}1]$ directions. The asymmetric distribution of the streaks intensity with respect to the Bragg peak an indication of the stacking fault, being intrinsic or extrinsic. In case of intrinsic SF's, one {111} plane is added in the Si stacking and the asymmetry is positive, i.e. the DXS intensity is higher for positive q, as shown in Fig. 2.6. In case of intrinsic SF's, one {111} plane is missing and the DXS intensity is higher for negative q. As expected, the number of SiI's in the FDL, N_i, affects the width of the streak in the direction perpendicular to the [111]. As it is clearly visible in the inset Fig. 2.6, the streak becomes narrower for bigger defects. Experimental observations of [111]-oriented DXS intensity streaks, indicating the presence of FDL's is Si have been first published in Ref. [1.77].

During annealing, the FDL's present in ion-implanted Si transform into perfect dislocation loops (PDL's). The DXS intensity map induced by the presence of such PDL's in fcc crystals has been calculated and published by Ehrhart *et al.* [2.14]. Figure 2.7 shows the results of this calculation for both FDL's and PDL's. As for the calculation shown in Fig. 2.6, [111]-oriented intensity streaks are observed for FDL's, because of the presence of the SF in

their structure (part (a) of the figure). In the calculated DXS map for PDL's, part (b), no intensity streak is found, which makes it difficult to detect the presence of PDL's by DXS methods. Nevertheless, the transformation of FDL's into PDL's is characterised by a progressive decrease of the [111]-streak intensity, as experimentally observed by Sztucki *et al.* [1.78] for ion-implanted Si samples.

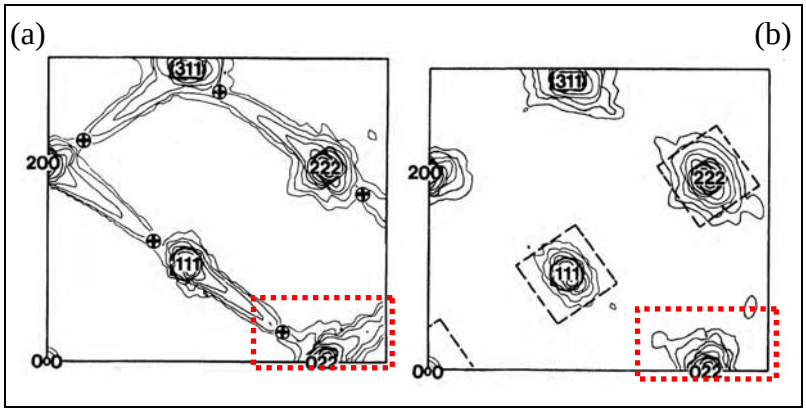

Figure 2.7: Calculated isointensity curves for the diffuse x-ray scattering in the $(01\bar{1})$ plane for interstitial loops in the close-packed {111} planes of an elastically isotropic fcc lattice. (a) FDL's and (b) PDL's. The reciprocal space area that has been measured in the present work (Ch. 3) is indicated. Adapted from Ref. [2.14].

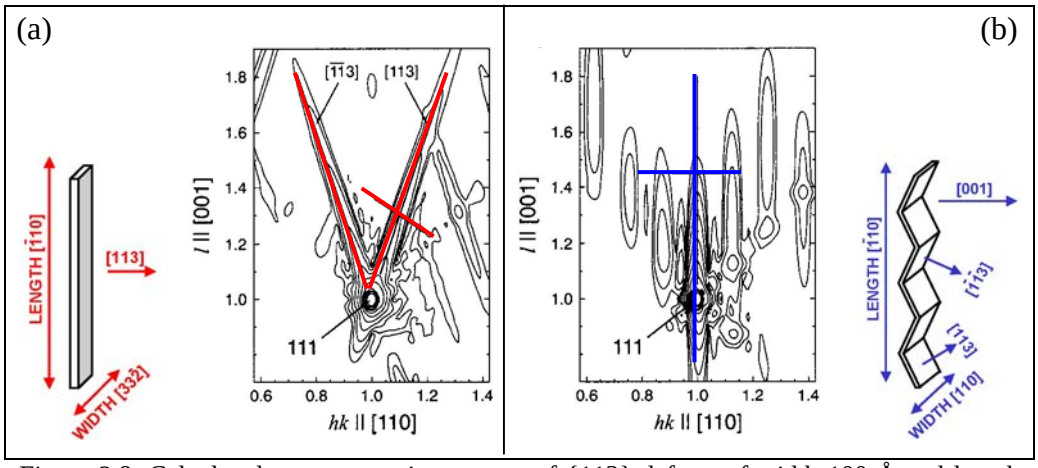

Figure 2.8: Calculated x-ray scattering pattern of {113}-defects of width 100 Å and length 100 Å around the 111 Bragg peak. The lines are iso-intensity curves with a difference of one order of magnitude in scattering intensity. Thick lines indicate the directions of the main streaks, as well as the scan directions corresponding to the defect width. (a) IRD defect; (b) {1Hex}ZD. Adapted from Ref. [1.62]. The corresponding defect structures are shown in the inserts. See Sec. 1.2.4.1 for further details on the defect structure of IRD and {1Hex}ZD.

Other type of extended defects may be present in the EOR damage region of ion-implanted Si, namely the {113}-defects (113's). The DXS pattern from 113's has been calculated by Nordlund [1.62] for two selected crystallographic types: the IRD and the

{1Hex}ZD {113}-defects, described in Sec. 1.2.4.1. Close to the Bragg peaks, the DXS distribution differs significantly for the two types of defects, as shown in Fig. 2.8. The IRD originates a streaked intensity in the <113> directions, because it contains a pseudo- stacking fault on the corresponding plane. The features of this streaked intensity are similar to those mentioned above for the FDL-induced streaks. The structure of {1Hex}ZD is, in average, perpendicular to [001], thus inducing intensity streaks in this direction.

The peculiar feature that makes unique the scattering pattern from 113's is a DXS intensity created far from the Bragg peaks. The signal is located close to the position h, k, l = (1.3, 1.3, 0) in reciprocal space, where an intensity hump is expected in case 113's are present in the lattice. As no other defect gives rise to a DXS signal at this position in reciprocal space, the measurement close to (1.3, 1.3, 0) is especially sensitive to 113's. In particular, the calculated DXS distribution in the $(1\bar{1}0)$ plane, shown in Fig. 2.9, is characteristic for the predominant type of 113. The maximum of the DXS signal is located at $h = k = 1.25$, for the {1Hex}ZD type, (a), or at $h = k = 1.35$, for the IRD type, (b).

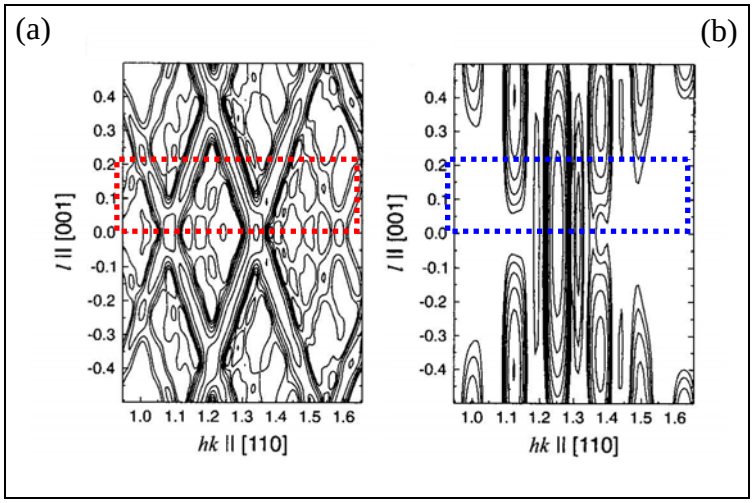

Figure 2.9: X-ray scattering pattern of {113}-defects of width 100 Å and length 100 Å around the 1.3 1.3 0 position in reciprocal space. (a) IRD; (b) {1Hex}ZD. Adapted from Ref. [1.62]. The reciprocal space area that has been measured in the present work is indicated by a dotted curves.

Following the Ref. [1.62], the width and length of the 113 defects can be determined by performing scans through the (1.3, 1.3, 0) position. For both 113's configurations, the defect length can be determined from a measurement in the $[\bar{1}10]$ direction. The width is evaluated from a scan in the [110] direction, for {1Hex}ZD defects, and from a scan in the $[33\bar{2}]$, for the IRD defects.

In conclusion, the evolution of the different defect types typical for the post implantation annealing can be studied, investigating the appropriate regions in the reciprocal space. Small clusters of SiI's and dopant atoms are detectable based on their Huang diffuse scattering, close to the Bragg peaks. In the same region, dislocation loops and {113}-defects induce characteristic DXS intensity streaks. Moreover, the presence of 113's generates a diffusely scattered intensity close to (1.3, 1.3, 0) position in reciprocal space.

2.2. X-ray scattering from thin films

In ultra-low energy implanted Si, the ion-implanted layer and the related defects occupy the near-surface region As a consequence, the use of x-ray scattering methods sensitive to such shallow layers is mandatory to study the structure of these samples. In this section, the x-ray scattering from thin films is described according to Refs. [2.8, 2.15 and 2.16].

2.2.1 X-ray interaction with matter

The x-rays are electromagnetic waves; therefore, they undergo refraction phenomena at interfaces between different media. To describe such refractive phenomena, matter is taken to be homogeneous with sharp boundaries between the media. Each medium is characterised by an index of refraction *n*. By definition the refractive index for vacuum is one. The index of refraction for electromagnetic waves displays resonant behaviour at frequencies corresponding to electronic transitions in atoms and molecules. On the low frequency of a resonance, *n* increases with ω. Immediately above the resonance frequency, it decreases, and as more and more resonance frequencies are passed, the magnitude of the index of refraction decreases. X-ray frequencies are usually higher than all transition frequencies with the exception of inner shell K- or L- electrons. As a result, in the x-ray region, for condensed matter *n* turns out to be less than unity. The refractive index $n(\boldsymbol{r})$ can be expressed as

$$n(\boldsymbol{r}) = 1 - \delta(\boldsymbol{r}) + i\beta(\boldsymbol{r}), \tag{2.22}$$

where $\boldsymbol{r}$ represents the spatial coordinates, $\delta(\boldsymbol{r})$ and $\beta(\boldsymbol{r})$ are the dispersion and the absorption, respectively. For x-ray energies far from any absorption edge,

$$\delta(\boldsymbol{r}) = \lambda^2 / 2\pi \, r_e \rho_{el}(\boldsymbol{r})$$

and

$$\beta(\boldsymbol{r}) = \lambda / 4\pi \, \mu(\boldsymbol{r}),$$

where λ is the wavelength of the impinging wave, r_e is the classical radius of the electron. $\rho_{el}(\boldsymbol{r})$ is the electron density and $\mu(\boldsymbol{r})$, the linear absorption coefficient of the material. In the

x-ray region, δ is always positive and its value is $\delta \approx 10^{-5}$. β is usually one or two orders of magnitude smaller than δ [2.16].

As $\delta(\boldsymbol{r})$ is proportional to the product of the r_e with electron density $\rho_{el}(\boldsymbol{r})$, the deviation of n from unity is related to the scattering properties of the medium, as shown in Eq. (2.6). The relation of the atomic scattering form factor with the index of refraction will be made explicit hereafter. The atomic form factor is defined in Eq. (2.23), as a function of the x-ray wavelength λ and of the scattering vector $\boldsymbol{Q}$ [2.8].

$$f(\boldsymbol{Q},\lambda) = f^0(\boldsymbol{Q}) + f'(\lambda) + if''(\lambda) \tag{2.23}$$

where *f'* and *f"* are the real and the imaginary part of the dispersion correction, respectively. The energy dependence of the dispersion corrections presents discontinuities at the absorption edges and is dominated by the binding energy of the inner-shell electrons of the atom. In the limit for $\boldsymbol{Q} \to 0$, $f_0(\boldsymbol{Q}) = Z$, the number of electrons Z in the atom, whereas, for $\boldsymbol{Q} \to \infty$, $f_0(\boldsymbol{Q}) = 0$.

Based on Eq. (2.23), the index of refraction can be rewritten as

$$n = 1 - \frac{2\pi\rho_{el} r_e}{k^2}\left\{ f^0(0) + f' + f'' \right\}, \tag{2.24}$$

with $\beta = -\left(\frac{2\pi\rho_{el} r_e}{k^2}\right) f''$. The properties of the dispersion corrections of the atomic form factor *f'* and *f"* can be exploited to perform anomalous scattering experiments, as described in Sec. 3.3.2.

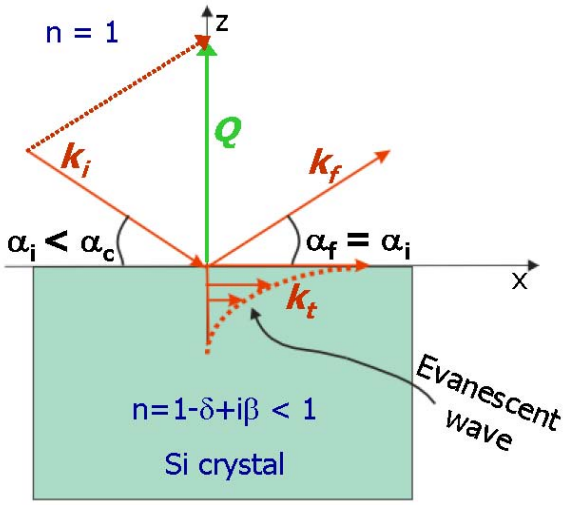

Figure 2.10: An x-ray wave with wavevector $\boldsymbol{k}_i$ hits a surface under a grazing angle α_i smaller than α_c. The wave splits into a reflected wave of wavevector $\boldsymbol{k}_f$ at $\alpha_f = \alpha_i$ and a transmitted (or refracted) wave with wavevector $\boldsymbol{k}_t$ travelling parallel to the surface. $\boldsymbol{Q} = \boldsymbol{k}_f - \boldsymbol{k}_i$ represents the total momentum transfer of the scattering process.

The Snell's law relates the incident grazing angle α_i to the refracted angle α_i' in the matter, as shown in Eq. (2.25).

$$\cos\alpha_i = n\cos\alpha_i' \tag{2.25}$$

As the index of refraction is smaller than 1 for x-rays, the phenomenon of the total external reflection occurs for incident angles α_i smaller than the critical angle, α_c. Starting from Eqs. (2.23) and (2.25) and setting $\alpha_i' = 0$, the critical angle for total external reflection is obtained as

$$\alpha_c = \sqrt{2\delta} = \lambda\sqrt{r_e\rho_{el}} \tag{2.26}$$

Being $\delta \approx 10^{-5}$, α_c is in the order of the tenth of a degree (e.g. α_c = 0.22 deg, for Si at 8 keV). For α_i smaller than α_c, an evanescent wave is created, which travels parallel to the surface with an amplitude decaying rapidly in the material on the nm-scale. The phenomenon of the total external reflection is schematically shown in Fig. 2.10.

2.2.2 The evanescent x-ray wave

The amplitudes of the transmitted and reflected waves are calculated, based on the continuity of the electric and magnetic fields at the interface (z = 0). The z-components of the incoming and transmitted waves are $k_{i,z}$ and $k_{t,z}$, respectively. The well-known Fresnel's coefficients R_F , for the reflected wave, and T_F , for transmitted one are thereby obtained.

$$R_F = \frac{k_{i,z} - k_{t,z}}{k_{i,z} + k_{t,z}} \overset{\alpha_i \ll 1}{=} \frac{\alpha_i - \alpha'_i}{\alpha_i + \alpha'_i} \tag{2.27}$$

$$T_F = \frac{2k_{i,z}}{k_{i,z} + k_{t,z}} \overset{\alpha_i \ll 1}{=} \frac{2\alpha_i}{\alpha_i + \alpha'_i} \tag{2.28}$$

where α'_i is the refracted beam angle that is defined by

$$\alpha'_i = \sqrt{\alpha_i^2 - \alpha_c^2} \tag{2.29}$$

For incident angles smaller than the critical angle, $\alpha_i < \alpha_c$, $k_{t,z}$ becomes imaginary and the transmitted electrical field is described by

$$E_t \sim e^{ik_{t,z}z} \sim e^{-kz\sqrt{\alpha_i^2 - \alpha_c^2}} = e^{z/L_i} \tag{2.30}$$

The amplitude of the transmitted wave is exponentially dumped in the less dense medium and its penetration depth L_i is defined when its amplitude reaches 1/e in Eq. (2.31) [2.15].

$$L_i = \lambda \big/ 2\pi l_i \tag{2.31}$$

with $l_i = 2^{-1/2}\left\{\left(2\delta - \sin^2\alpha_i\right) + \left[\left(\sin^2\alpha_i - 2\delta\right)^2 + 4\beta^2\right]^{1/2}\right\}^{1/2}$, which has the asymptotic value for $\alpha_i \to 0$ of $L_{i0} = \lambda/2\pi\alpha_c \approx 50$ Å for Si at 8 keV.

2.2.3 The Distorted Wave Born Approximation for grazing incidence scattering

The diffraction theory for small crystals [2.7] is inadequate to describe the diffraction pattern produced by an x-ray beam striking the surface of a crystal with an angle of incidence in the order of the critical angle for total external reflection. The reason is that it relies on the first Born approximation, i.e. no multiple scattering phenomena are considered. On the contrary, the essence of the grazing incidence scattering methods is in the total external reflection, which is a multiple scattering phenomenon. The demand for a theoretically simple model for the description of grazing incidence scattering phenomena was satisfied by Vineyard [2.17] with the Distorted Wave Born Approximation (DWBA) in 1982. Sinha *et al.* [2.18] completed the DWBA theory and its application to near-surface structure investigation is described in Ref. [2.9, 2.15, 2.19-2.21].

The DWBA is a combination of dynamical and kinematical treatment of the scattering process. The refraction by smooth interfaces is exactly taken into account, while the scattering at lateral inhomogeneities of the crystal is treated kinematically, i.e. without including the multiple scattering effects [2.16]. In the conventional theory of diffraction, a sample containing near-surface scatterers is assumed to be illuminated by a single plane wave, $\boldsymbol{E}_i = E_i e^{i\mathbf{k}_i\mathbf{r}}$ and interact with it in a dynamical scattering process to result in an outgoing wave, $\boldsymbol{E}_f = E_f e^{i\mathbf{k}_f\mathbf{r}}$. In the DWBA, the real scattering sample is first replaced by a simpler distribution of material, the scattering from which can be calculated exactly (e.g. a semi-infinite crystal). The electric field thereby created, namely the evanescent ("distorted") wave, $\boldsymbol{T}_i = T_i e^{i\mathbf{k}'_i\mathbf{r}}$, is used to illuminate each element of the real scatterer. The interaction of $\boldsymbol{T}_i$ with the sample is treated in the kinematical approximation, resulting in $\boldsymbol{T}_f = T_f e^{i\mathbf{k}'_f\mathbf{r}}$. The interaction of $\boldsymbol{T}_f$ with the model system on its outgoing path originates $\boldsymbol{E}_f$. (The mark " ' ", like in $\boldsymbol{k}'_i$, indicates the quantities inside the semi-infinite crystal.)

In the previous section, it was explained how the incoming beam $\boldsymbol{E}_i$ experiences the trasmissivity of the interface between the vacuum and the matter. The formation of an evanescent wave $\boldsymbol{T}_i$ is the first step of the application of the DWBA. Following Helmholtz's reciprocity principle [2.15],

"if the source and the point of observation are interchanged the same amplitude would result", the same process holds for the beam exiting the sample and creating $\boldsymbol{T}_f$. The scattered intensity, $I(\boldsymbol{Q}')$, results then in Eq. (2.32) [2.16].

$$I(\boldsymbol{Q}') \propto I_0 \left|T_{i,z}\right|^2 \left|T_{f,z}\right|^2 S(\boldsymbol{Q}') \tag{2.32}$$

where the incoming transmitted amplitude is $T_{i,z} = \dfrac{2k_{i,z}}{k_{i,z} + k'_{i,z}}$ and the exiting transmitted amplitude is $T_{f,z} = \dfrac{2k_{f,z}}{k_{f,z} + k'_{f,z}}$. The z-component of the wavevectors of the transmitted beams are defined as $k_{i,z} = k \sin\alpha_i$, $k_{f,z} = k \sin\alpha_f$, $k'_{i,z} = nk \sin\alpha'_i = k\left(n^2 - \cos^2\alpha_i\right)^{1/2}$ and $k'_{f,z} = nk \sin\alpha'_f = k\left(n^2 - \cos^2\alpha_f\right)^{1/2}$. $S(\boldsymbol{Q}')$ is the kinematic structure factor of the scatterer with $\boldsymbol{Q}'$ denoting the complex scattering vector in the crystal, $\boldsymbol{Q}' = \boldsymbol{k}'_f - \boldsymbol{k}'_i$.

The scattering depth Λ depends both on α_i and on the exit angle, α_f, and is given by Eq. (2.33) [2.15].

$$\Lambda = \mathrm{Im}\{Q_z'\}^{-1} = \frac{\lambda}{2\pi\left(l_i + l_f\right)}, \tag{2.33}$$

where $l_{i,f}$ are calculated from Eq. (2.31), for both indices i and f. As an example, Figure 2.11 shows the results from the calculation of the scattering depth Λ for Si at 8 keV. A wide range of Λ from 45 to 4000 Å is accessible with an appropriate setting of α_i and α_f.

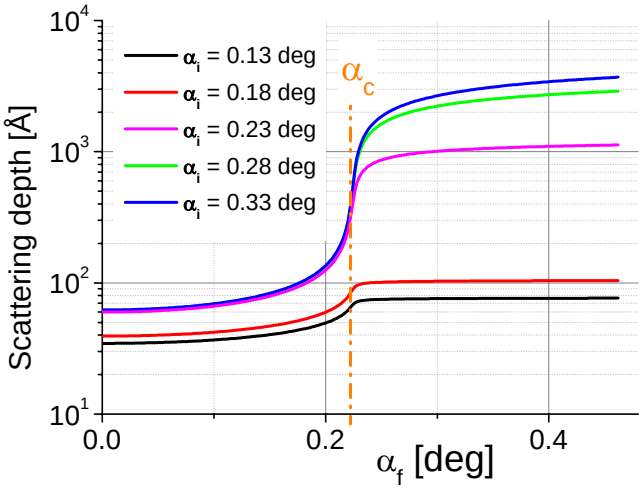

Figure 2.11: Calculated scattering depth Λ from Eq. (2.33) for Si at 8 keV as a function of the incidence, α_i, and exit angles, α_f. The location of the critical angle is indicated at α_c = 0.22 deg.

The main advantage of the use of grazing incidence scattering methods is the enhancement of the experimental signal from the scatterers located in the near-surface layer. The scattering signal arising from the substrate is suppressed. The evanescent scattering enables to study the structural properties from layers of nanometric thickness, provided that a brilliant enough x-ray beam is available. This condition dictates the preferential application of grazing-incidence scattering methods using synchrotron radiation.

2.3 Grazing-incidence diffuse x-ray scattering

In Secs. 1.2.3 and 1.2.4, it has been shown that several types of residual defects are expected in the near-surface region, as a consequence the ion implantation at ultra low energy. Due to the shallow location of such defects, the use of grazing incidence scattering methods (Sec. 2.2.3) is needed in order to detect their structural properties. In Sec. 2.1, the capabilities of the diffuse x-ray scattering technique for the detection of the defect structure have been described. The grazing incidence diffuse x-ray scattering technique combines the depth sensitivity of the evanescent x-ray wave with the diffuse x-ray scattering method. For this reason, the GI-DXS method is the main experimental technique used for the structural characterisation performed during this PhD thesis.

Examples of the use of the GI-DXS technique applied to Si structural characterisation can be found in Refs. [1.77, 1.78, 2.22-2.24].

2.3.1 Theory of the diffuse x-ray scattering for weak defects in thin layers

In this section, the theory of defect-induced scattering from weak defects located in thin layers is reported as a sequel of Sec. 2.1.2 and following Ref. [2.9].

Within the DWBA, the differential cross-section of the diffusely scattered intensity can be written in the form

$$\left(\frac{d\sigma}{d\Omega}\right)_{diff} = A\left|T_i T_f\right|^2 S(\boldsymbol{Q}') = A\left|T_i T_f\right|^2 \sum_{\alpha} \int d^3\boldsymbol{r}'' n^{\alpha}(\boldsymbol{r}'') \left|\Psi^{\alpha}(\boldsymbol{q}', \boldsymbol{r}'')\right|^2 \qquad (2.34)$$

where A is a constant and T_i and T_f are the Fresnel's transmission coefficients of the free surface corresponding to the primary and scattered wave, respectively. $\boldsymbol{q}' = \boldsymbol{k}_f' - \boldsymbol{k}_i' - \boldsymbol{h}$ is the complex reduced scattering vector in the material, including refraction and absorption. The sum $\sum_{\alpha}$ is over the defect types, $n^{\alpha}(\boldsymbol{r}'')$ is the profile of the defects of type α. The

integration is calculated over the volume V of the semi-infinite substrate, i.e. $z \leq 0$. The function $\Psi^{\alpha}(\boldsymbol{q}', \boldsymbol{r}'')$ is the structure factor of the scatterers and is defined as

$$\Psi^{\alpha}(\boldsymbol{q}', \boldsymbol{r}'') = \int d^3\boldsymbol{r} \Psi^{\alpha}(\boldsymbol{r}, \boldsymbol{r}'') e^{-i\boldsymbol{q}'.\boldsymbol{r}} \tag{2.35}$$

and $\Psi^{\alpha}(\boldsymbol{r}, \boldsymbol{r}'') = \langle \chi_h \rangle \left(e^{-i\boldsymbol{h}.\boldsymbol{v}^{\alpha}(\boldsymbol{r}, \boldsymbol{r}'')} - 1 \right) + \Delta\chi_h^{\alpha} s^{\alpha}(\boldsymbol{r} - \boldsymbol{r}'') e^{-i\boldsymbol{h}.\boldsymbol{v}^{\alpha}(\boldsymbol{r}, \boldsymbol{r}'')}$.

The displacement of the atom in point ***r*** due to a defect of type α in point ***r***" is denoted as $v^{\alpha}(\boldsymbol{r}, \boldsymbol{r}'')$. $\langle \chi_h \rangle$ is the average polarizability of the crystal with defects, $\Delta\chi_h^{\alpha} = \chi_h^{\alpha} - \langle \chi_h \rangle$, where χ_h^{α} is the polarizability of the core of a defect of type α. $s^{\alpha}(\boldsymbol{r} - \boldsymbol{r}'')$ is the shape function of the core of a defect of type α. This function is unity, if both point ***r***' and ***r***" lay in the same core, otherwise is zero.

The Eqs. (2.34) and (2.35) have been derived assuming that the positions of the defects are completely non-correlated. The Huang approximation for the displacement field around the defect (see Eq. (2.15)) has been assumed to be valid.

As a further simplification, the surface relaxation of internal stresses can be neglected, which will be discussed in the next Sec. 2.3.2. Based on this simplification,

$$\boldsymbol{v}^{\alpha}(\boldsymbol{r}, \boldsymbol{r}'') = \boldsymbol{v}^{\alpha}(\boldsymbol{r} - \boldsymbol{r}'') \tag{2.36}$$

i.e. the displacement v^{α} does not depend on the absolute positions of the points ***r*** and ***r***", but on their distance only, leading to Eq. (2.37)

$$\Psi^{\alpha}(\boldsymbol{q}', \boldsymbol{r}'') = e^{-i\boldsymbol{q}'.\boldsymbol{r}''} \left[-i \langle \chi_h \rangle \boldsymbol{h}.\boldsymbol{v}^{\alpha FT}(\boldsymbol{q}') + \Delta\chi_h^{\alpha} s^{\alpha FT}(\boldsymbol{q}') \right], \tag{2.37}$$

where $\boldsymbol{v}^{\alpha FT}(\boldsymbol{q}') = \int d^3(\boldsymbol{r} - \boldsymbol{r}'') \boldsymbol{v}^{\alpha}(\boldsymbol{r} - \boldsymbol{r}'') e^{-i\boldsymbol{q}'.(\boldsymbol{r} - \boldsymbol{r}'')}$

and $s^{\alpha FT}(\boldsymbol{q}') = \int d^3(\boldsymbol{r} - \boldsymbol{r}'') s^{\alpha}(\boldsymbol{r} - \boldsymbol{r}'') e^{-i\boldsymbol{q}'.(\boldsymbol{r} - \boldsymbol{r}'')}$.

In Eq. (2.37) the first term corresponds to the Huang scattering and the second term to the Laue or core scattering. Eqs. (2.34) and (2.37) are used to describe the scattering from weak defects in a thin layer and they will be used in this work in order to simulate the distribution of the defect-induced diffuse x-ray scattering as it will be explained in Sec. 3.2.3.

2.3.2 Effect of the surface relaxation on the defect-induced DXS

The results from the theory of DXS reported in Sec. 2.1 were obtained assuming defects randomly distributed in an infinite, elastically isotropic crystal. In reality, the defects are located in a finite crystal. Therefore, the defect-induced strain field may be influenced by the finite dimensions, e.g. the surface, and deviate from its characteristic r^{-2} behaviour. Barabash and Krivoglaz derived the general expression for the DXS from defects close to a surface

[2.25]. According to their work, the thickness of the sub-surface layer, in which the surface relation of internal stresses remarkably affects the DXS, is small. The DXS from defects close to the surface will be similar to the bulk value, if $D_e \gg 1/q$, where D_e is the effective depth of the defect (Sec. 2.1.2). For a value of $q \sim 0.1 Å^{-1}$, only defects very close to the surface, i.e. ~10 Å, would be affected by the surface relaxation.

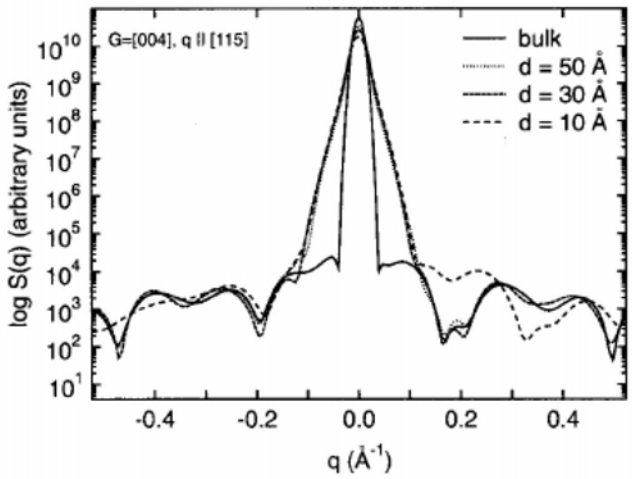

Figure 2.12: Calculated diffuse x-ray scattering from an out-of-plane 004 peak and close-to-normal [115] scanning direction for the damage produced by a 2 keV-recoil in Si placed at different depth in the simulation cell. The diffuse scattering outside the truncation rod region is similar to the bulk value except for the damage depth $\leq$ 30 Å. Figure adapted from Ref. [2.12].

Therefore, only for the defects located in this thin layer the simplification expressed in Eq. (2.36) cannot be performed. The theory of the DXS from weak scattering defects in the subsurface region is treated in details in Refs. [2.9] and [2.2].

Atomistic-based simulations of defect-induced DXS were applied to investigate the effects of the surface relaxation on the DXS intensity calculated for the typical defects, which are created by an ultra-low energy ion implantation in Si [2.12].

Figure 2.12 shows the results, obtained for the defects present in the damaged region of a Si implantation in Si at 2keV. For defects located deeper than 30Å, the surface effects are negligible. The author concludes that “the small surface effect found for defects very close to the surface will rarely be of significance” in ultra-low energy ion implantation damage, even when studied by grazing-incidence diffuse x-ray scattering.

Accordingly, the surface relaxation effect is neglected in present work. The depth of the studied defects is such that the relaxation of internal stresses at the surface does not affect the GI-DXS intensity.

3. Methods and experimental details

In the first part of this chapter, the main features of the beamline ID01 at the European Synchrotron Radiation Facility (ESRF), where all the experiments were carried out, will be described. Later, the set-up for grazing incidence experiments will be explained in detail due to its importance for the use of near-surface sensitive x-ray scattering techniques.

In the second part of the chapter, the GI-DXS data acquisition will be discussed and one example of GI-DXS data analysis will be given. The combination of GI-DXS, specular reflectivity (SR) conventional x-ray diffraction (XRD) and grazing incidence diffraction (GID) for the complete structural characterisation of ion-implanted Si will be the subject of the final section of this chapter.

3.1 Beamline ID01 at the European Synchrotron Radiation Facility

All the x-ray measurements presented in this work have been performed using synchrotron radiation at the ESRF in Grenoble (F). The ESRF is a “third generation” synchrotron. Its storage ring for the electron beam has a circumference of 844 m and more than 40 beamlines. Details on the structure of the ESRF can be found in Ref. [3.1]. Figure 3.1 shows an aerial view of this large-scale facility, where the main components of the ESRF have been indicated, such as the linear accelerator, the booster synchrotron, the storage ring and a beamline.

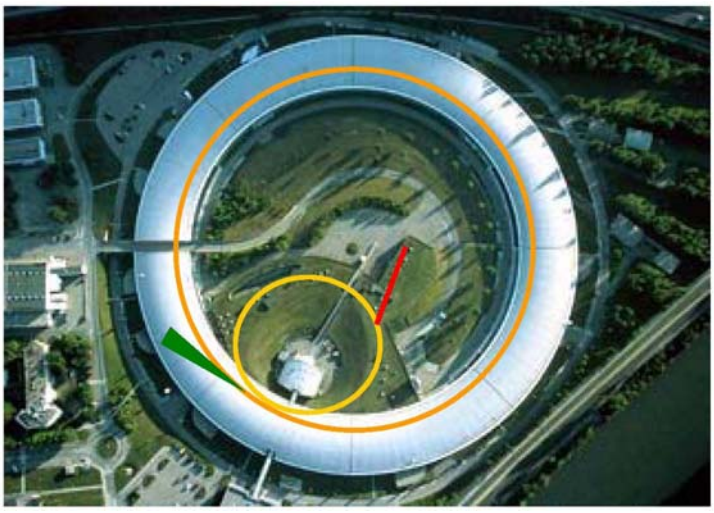

Figure 3.1: Aerial perspective of the European Synchrotron Radiation Facility. The main components of this large-scale facility have been highlighted. In red, the linear accelerator, where the electrons are produced and first accelerated, in yellow, the booster synchrotron, where the electrons are accelerated to relativistic speeds before being injected into the storage ring (orange line). A green line indicates the location of the beamline ID01. Adapted from [3.1].

Many remarkable properties characterise the synchrotron radiation, such as energy tunability, high photon flux, low x-ray beam divergence, coherence and pulsed emission [2.8]. In order to apply grazing incidence x-ray scattering techniques, the most important characteristic of the synchrotron radiation is its brilliance. The brilliance is defined as:

$$\text{Brilliance} = \frac{\text{Photons/second}}{\text{mrad}^2\text{mm}^2(0.1\%\ \text{bandwidth})}.$$

It depends on the number of photons emitted per second and the collimation of the beam, expressed in mrad, both for the horizontal and the vertical directions. Moreover, the area of the x-ray source is considered, which is expressed in mm^2. The spectral distribution of the source is taken into account by defining the photon energy with a determined bandwidth, i.e. $\Delta E/E = 0.1\%$.

The parameter of the brilliance can be used to compare different x-ray sources. The brilliance is a function of the photon energy and its value, in a third generation undulator, is about 10 orders of magnitude higher than for a conventional rotating anode [2.8, 3.1]. For grazing-incidence x-ray scattering experiment, the high brilliance of synchrotron radiation is needed in order to obtain sufficiently high signal-to-background ratio. The reader is referred to Refs. [2.8, 3.2] for an extended discussion of the physics of synchrotron radiation.

3.1.1 Beamline ID01

The beamline ID01 at the ESRF has been designed to combine small- and wide-angle x-ray scattering techniques with anomalous dispersion [3.3, 3.4]. To this end, a widely tunable energy range is needed to reach the K and L absorption edges of a large number of elements. The layout of the beamline is schematically shown in Fig. 3.2.

3.1.1.1 ID01 optics hutch

On the beamline ID01, two insertion devices, a wiggler and an undulator [2.8, 3.1], select an x-ray beam with an energy variable from 2.5 to 35 keV. The wiggler is used for low energies ($E < 5$ keV), while the undulator for the high energies. In the present work, the undulator was used.

The energy of the x-ray beam produced by an undulator is tuned by changing the gap between its magnets and by selecting one of its harmonics. The double-crystal monochromator, Si (111) in our case, allows for the fine tuning of the desired energy with an energy resolution $\Delta E/E$ of 10^{-4}. This allows accurate scanning of the x-ray energy around the absorption edge of an element with an absolute resolution of ~ 1 eV. For example, if an x-ray

energy of 8 keV is chosen on the 1st harmonic of the undulator, I_λ, and reflected by the 111 Bragg peak of the Si monochromator, the x-ray beam will contain as well photons with an energy of 24 keV, $I_{\lambda/3}$, originating from the 3rd harmonic of the undulator and selected by the 333 Si reflection at the same Bragg angle as the 111 Si reflection. In the optics hutch of ID01, two Si mirrors [3.3], located before and after the monochromator, are used to reject these harmonics ($I_\lambda/I_{\lambda/3} < 10^{-4}$) and maintain the focal spot fixed at the sample position, during the tuning of the energy. This is called "fixed exit geometry".

In order to increase the photon flux at the sample position, the x-ray beam can be focussed both in horizontal and vertical directions. The horizontal focussing is achieved by sagittally bending the second crystal of the monochromator, while the vertical focussing is obtained by bending the second mirror along the direction of the beam. The expected flux of photons at the sample position is ~10^{13} ph s^{-1} in $\Delta E/E = 10^{-4}$, at a storage ring current of 0.2 A at 8 keV, in a spot of 0.2 x 0.08 mm^2.

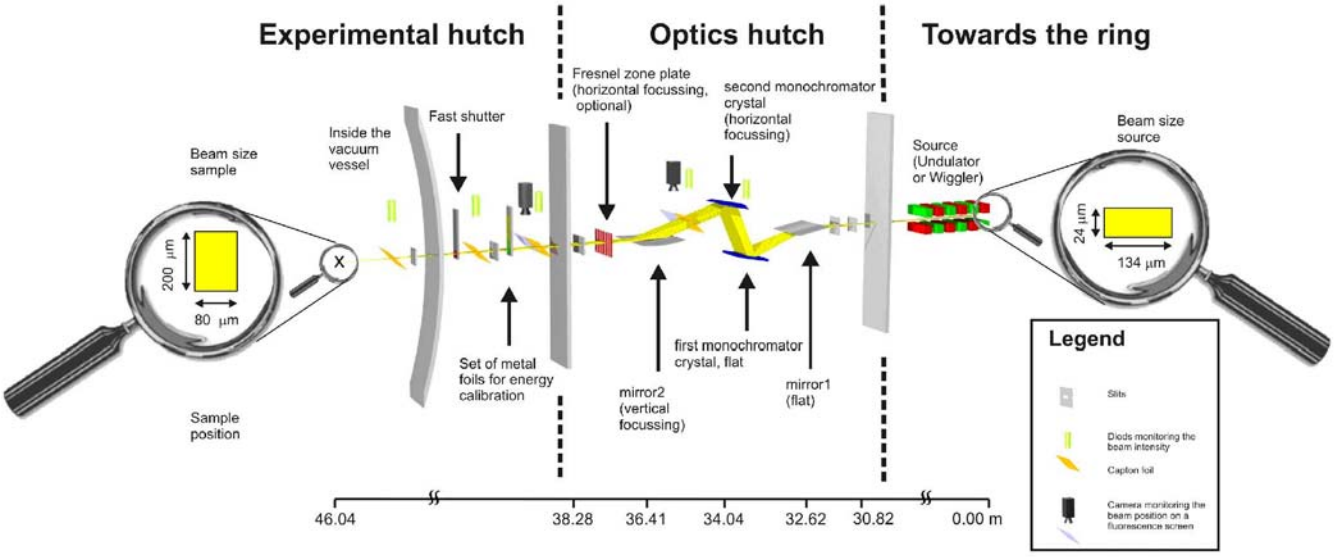

Figure 3.2: Scheme of optics elements of the beamline ID01 from the x-ray source to the sample position. The insertion devices from ID01 (a wiggler and an undulator) are located in the storage ring. The main components of the optics hutch are the double-crystal monochromator and the two Si mirrors. The distance of the elements from the x-ray source is indicated. Note that the sample is located at ~ 46 m from the x-ray source. Courtesy of B. Krause.

3.1.1.2 ID01 experimental hutch

At lower x-ray energies, absorption and scattering by air play an increasingly important role. In order to avoid these effects, ID01 beamline has been designed to operate under vacuum and without any beryllium window from the storage ring to the x-ray detector.

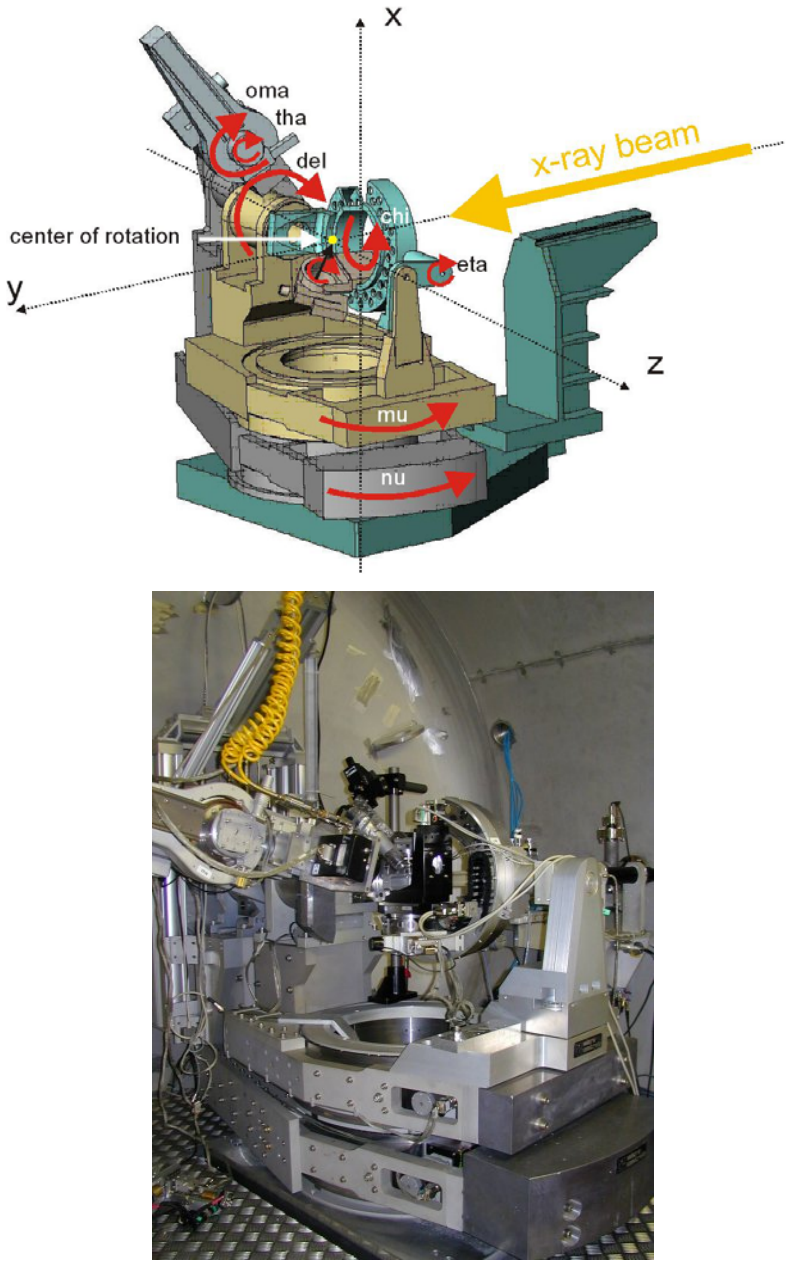

Figure 3.3: The 4+2 diffractometer of the beamline ID01. Upper part: Scheme of the diffractometer. The axes of the four circles (*del*, *eta, chi*, *phi*) and the two independent horizontal circles (*mu* and *nu*) are indicated. The motors *oma* and *tha* are used only when an analyser crystal is mounted. The centre of rotation of the diffractometer is indicated by a yellow dot. The beam enters from the right, along the y-axis in this scheme. Bottom part: Photograph of the diffractometer in the vessel of the experimental hutch. Adapted from Ref. [3.3].

To this end, the 4+2 circle diffractometer of ID01 is located in a huge vessel with a diameter of 2.8 m that can be evacuated to a pressure of P_{min} = 5x10^{-3} Torr. A four circles diffractometer (*eta*, *chi*, *del* and *phi*) is combined with two additional horizontal rotations (*nu* and *mu*). Figure 3.3 shows a scheme and a photograph of the ID01 diffractometer. The axes of rotation of the diffractometer motors are indicated together with the direction of the incoming x-ray beam and the centre of rotation.

3.1.2 Experimental set-up for grazing incidence x-ray scattering techniques

The scattering set-up shown in Fig. 3.4 is used to perform grazing incidence diffuse x-ray scattering experiments. The incident beam with wavevector $\boldsymbol{k}_i$ impinges on the surface under a grazing incident angle α_i. The scattered beam leaves the surface under the angle α_f with a wavevector $\boldsymbol{k}_f$. The angles α_i and α_f determines the scattering depth of the x-rays Λ, according to Eq. (2.33). In this geometry, the Bragg condition is fulfilled only for the reciprocal lattice nodes with crystallographic vector parallel to the surface (i.e. $hk0$ for Si (001)), $\boldsymbol{Q}_{//} = \boldsymbol{h}_{hk0}$. This is called "lateral diffraction condition" [2.9] and the scattering planes are perpendicular to the sample surface.

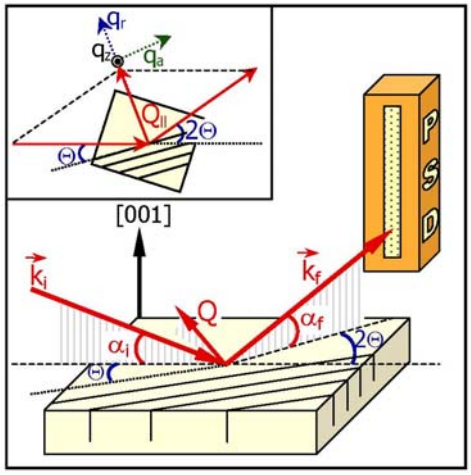

Figure 3.4: Scattering geometry used to measure the diffuse x-ray scattering at grazing incidence α_i and exit angles α_f. The Bragg condition $\boldsymbol{Q}_{//} = \boldsymbol{h}_{hk0}$ is satisfied by lattice planes perpendicular to the surface. The linear position sensitive detector is mounted with an orientation perpendicular to the sample surface. In the insert: top view of the scattering geometry showing the reduced scattering vectors q_r, q_a and q_z. See details in the text.

In this work, the 220 surface Bragg reflection is selected. The reciprocal space surrounding the 220 is probed in three different crystallographic directions: q_r, radial, q_a, angular and q_z, azimuthal, as shown in the inset of Fig. 3.4. The reduced scattering vector, $\boldsymbol{q}$, points in [110] direction for a radial scan q_r, and along the $[1\,\bar{1}0]$ direction in the case of an angular scan q_a. The small q_z component is given by selecting α_i and α_f. The intensity along q_z (i.e. [001] direction) is recorded for each q_r and q_a position, resulting in reciprocal space maps in the $(1\,\bar{1}0)$ and (110) plane, respectively.

The set-up for grazing incidence x-ray scattering experiments used on ID01 is described hereafter. The sample is mounted on a sample holder and fixed on a motorised goniometer head. The head, Fig. 3.5(a), is positioned in the centre of rotation of the diffractometer. A

kapton cone, flushed with He, covers the sample and reduces the air scattering by a factor 20 [3.3]. Simultaneously it protects the sample surface from ozone, which would otherwise be formed by x-ray-induced ionisation of the air. Figure 3.5(b) shows the He cone mounted on the sample holder with an indication of the sample location and of the directions of the incoming and outgoing x-ray beam.

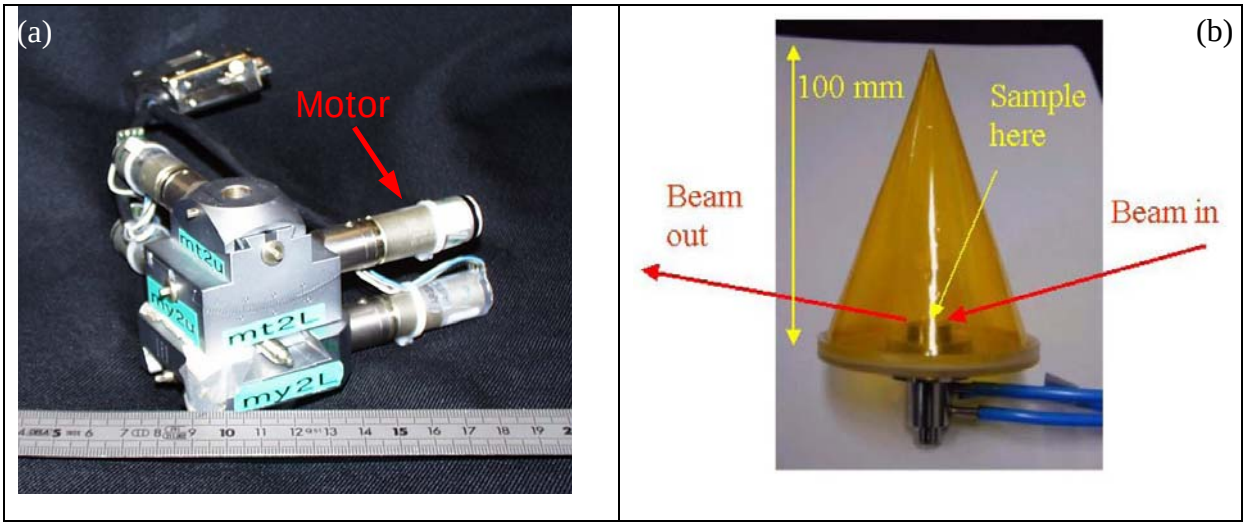

Figure 3.5: (a) Picture of the goniometer head. The green labels indicate the four motorised movements of the head: two translations and two rotations. The rotations are used to align the sample surface perpendicularly to the *phi* circle. The translation stage enables the sample translation in the beam. An arrow indicates the location of one of the motors and a ruler is shown as a reference for the size. (b) Picture of the sample holder covered by a kapton cone. The blue hoses in the bottom are needed as input and output for the He gas, which flushes the sample environment. The directions of the incoming and outgoing beam and the sample location are shown for clarity. Adapted from [3.3].

The standard energy used for the experiments reported in this PhD thesis is 8 keV. At this energy, there is no need for evacuating the whole diffractometer vessel. In order to reduce the air scattering and absorption, the use of flight tubes, shown in Fig. 3.7, is sufficient, if associated with the He-flushed cone as sample environment.

As shown in Fig. 3.6, the sample surface is oriented vertically (i.e. *chi* = 90 deg). As already mentioned, the crystalline planes that diffuse the x-ray beam are perpendicular to the sample surface and, therefore, are horizontal in this geometry. This configuration enables to perform the experiment using a vertical scattering plane, which is defined as the plane that contains the scattering vector $\boldsymbol{Q}$. This is advantageous, because the x-ray beam divergence is smaller than in the horizontal direction allowing for the highest angular resolution. In addition, the polarisation factor of the synchrotron radiation is $P = 1$ in the vertical scattering plane (Sec. 2.1.1).

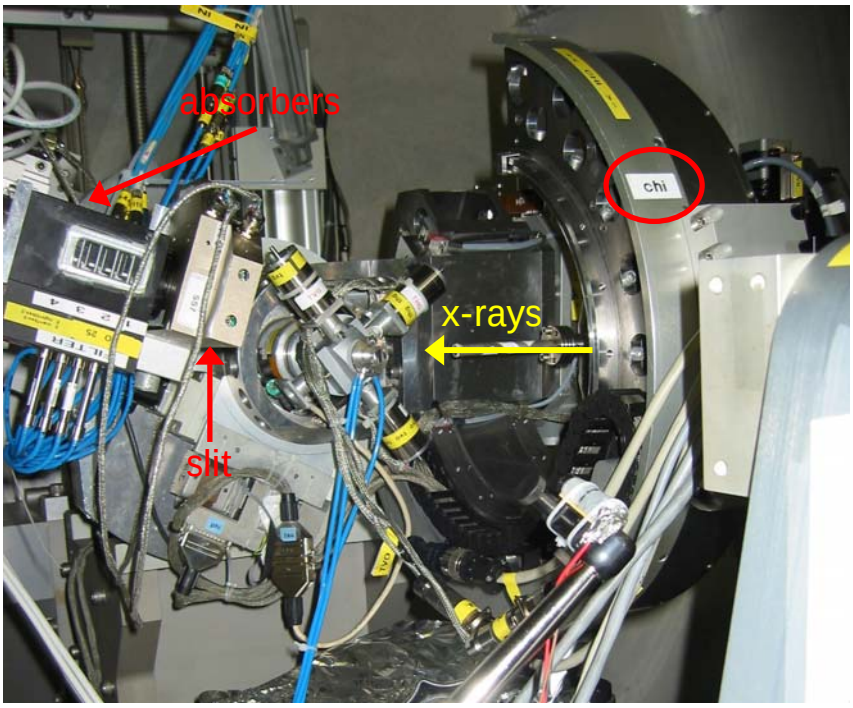

Figure 3.6: Picture of the ID01 diffractometer showing the sample mounted on the sample holder and on the motorised goniometer head in the position corresponding to *chi* = 90 deg. This scattering set-up is used to perform grazing incidence scattering experiments. The box containing the dynamical absorbers is visible on the left side of the picture together with the slit located after the sample. The *chi* circle of the diffractometer is highlighted for clarity. Adapted from [3.3].

The size of the x-ray beam at the sample position is defined by a slit located as close as possible to the sample with an aperture of 0.5 x 0.2 mm^2, vertically and horizontally, respectively. In the horizontal direction, the aperture is small in order to illuminate only the sample. In the vertical direction, SS5 is open to about twice the FWHM of the focussed beam impinging on the sample. The intensity of the x-ray beam is monitored between the slit and the sample to enable the normalisation of the scattered intensity, which is useful for the data analysis, and to check the correct alignment of the beamline optics.

The Bragg condition for the 220 Si lattice node is fulfilled when the Bragg angle Θ_B and the scattering angle $2\Theta_B$ are set using motors *phi* (i.e. sample rotation) and *del* (i.e. detector arm vertical rotation), respectively. In reciprocal space, the scans in the radial direction q_r are carried out by maintaining the Θ-to-2Θ condition between the detector and sample rotation moving both motors *del* and *phi*. The angular (or transversal) scans in the q_a direction are performed by rotating the sample only (motor *phi*), while keeping the detector position fixed at the $2\Theta_{220}$ value selected for the 220 Bragg peak. The α_i angle is defined with an accuracy of 0.001 deg. The equations used to calculate the reciprocal space position during the scans will be discussed in Sec. 3.2.2.

After the interaction with the sample, the scattered photons are collected by a linear position sensitive detector (PSD), which is mounted perpendicularly to the sample surface at a distance of ~ 1 m from the sample, as shown in Fig. 3.7. This orientation of the detector is well suited to record α_f-resolved spectra.

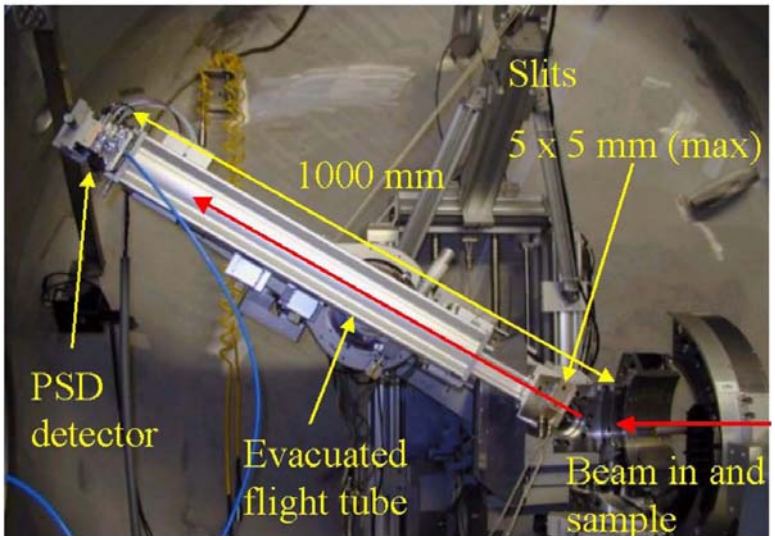

Figure 3.7: View of the experimental set-up for grazing incidence scattering experiments centred on the detector arm. The linear position sensitive detector (PSD) is mounted at the end of the detector arm. The evacuated flight tube is located in front of the detector in order to reduce scattering and absorption by air. The slit located after the sample is indicated. The one located in front the detector is integrated to the PSD support box and it is, therefore, not visible. Adapted from [3.3].

The PSD, fabricated by Braun, has a sensitive area of 50 x 10 mm^2 and a spatial resolution of ~100 μm over 512 channels. The PSD is a gas filled detector based on the ionisation of a mixture of $Ar_{0.9}(CH_4)_{0.1}$. A scheme of the functional principle of this detector is shown in Fig. 3.8(a) and a picture of the counting tube in part (b) of the same figure.

The gas pressure is 7 bar. The anode counting wire is located in the centre of the PSD tube, while the cathode at the back of the tube. The operating voltage is 3700 V. The x-ray photons enter the counting tube via a beryllium window (400 μm thick) and ionise the gas. The electrons thereby created are accelerated towards the anode, whereas the ions reach the cathode. The spatial resolution is achieved by the peculiar geometry of the silver cathode, which is made by two sets of triangular teeth electrically insulated from each other. The position of the ion beam spot on the cathode (blue spot in the figure) is determined through the ratio of the current $(I_A-I_B)/(I_A+I_B)$, as indicated in the scheme. The resulting distribution of the peak height of the output current is read out and transform into channel number by a multi channel analyser.

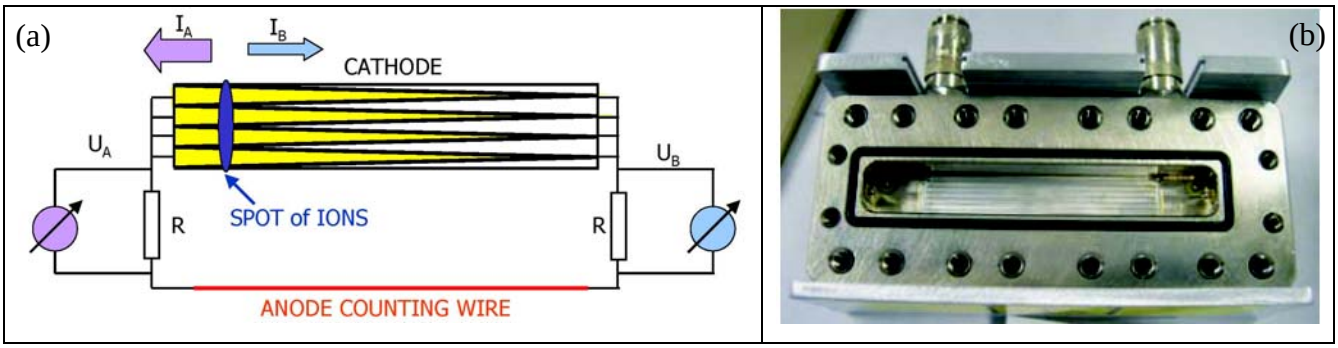

Figure 3.8: Position sensitive detector. (a) Scheme of the functional principle of the PSD showing the triangular structure of the cathode and the anode counting wire. (b) Photograph of the PSD counting tube. The beryllium window has been removed and the cathode on the backside is visible. Photograph by courtesy of T. Schülli.

The PSD response is linear until ~5000 ct/s of integrated intensity over all the channels within a dead time loss of ~5%. The linearity of the detector response is crucial when measuring both Bragg diffraction and diffuse scattering in the same scan, because the dynamic range of the measured signal can be of many orders of magnitude (see Sec. 3.2.3). Moreover, the linear detector response is needed for comparing absolute scattering intensities from different scans. In order to avoid the saturation of the detector and the consequent lost of linear response, the dynamic range of the detector is enhanced by using dynamical absorbers. At an energy of 8 keV, the absorbers consist of an arrangement of Al foils with an individual thickness of 100 μm. The thickness of the needed absorber is automatically calculated and the metal foils are inserted in the scattered beam path on the basis of the intensity of the x-rays that reach the detector.

Two sets of slits, one just after the sample and the other just before the detector, define a collimation path for the scattered beam and a small footprint (~1 mm^2) of the x-ray beam on the sample surface. This configuration allows for an angular resolution of ~ 0.1 deg, achieved with an opening of the detector slit of 2 mm. Such resolution is sufficient for measuring the GI-DXS intensity distribution in reciprocal space, which spreads over an angular range of about ± 7 deg in $2\Theta_B$ from the Bragg peak position. The position of these two slits is shown in Fig. 3.7.

As already discussed, for the grazing-incidence scattering geometry, used for GI-DXS experiment, the vertical scattering plane is obtained by orienting the sample surface vertically, i.e. the motor *chi* = 90 deg, Fig. 3.6. When SR and conventional wide-angle XRD experiments are performed the sample surface has to be oriented horizontally, to have a vertical scattering plane. This scattering configuration is set by rotating the *chi* circle of the diffractometer to the position *chi* = 0 deg.

The possibility of a quick change of the experimental set-up between grazing-incidence-angle (*chi* = 90 deg) and wide-angle scattering (*chi* = 0 deg) allows to perform GI-DXS, GID, SR and conventional XRD using the same set-up without remounting of the sample. Therefore, both the lateral and vertical structure of the sample can be studied simultaneously by combining the results obtained from all these x-ray scattering techniques, as it will be explain in details in the following sections.

3.2 The grazing-incidence diffuse x-ray scattering experiment

3.2.1 The "double-structure" sample

As introduced in Sec. 2.1.4, the Huang Diffuse x-ray Scattering (HDS) component of the DXS intensity indicates point-defect-induced distortions in the crystal. Starting from Eq. (2.16), for a radial measurement close to the 220 Bragg reflection, the features of the HDS component of the DXS can be summarised by:

$$I_{HDS,radial} \propto \sum_{\alpha} \frac{n_\alpha \delta_\alpha^2}{\left(c_{11}+c_{12}+c_{44}\right)^2} \left| \frac{\boldsymbol{h}.\boldsymbol{q}}{q} \right|^2 \tag{3.1}$$

The intensity I_{HDS} is proportional to the sum $\sum_{\alpha}$ over the different types of defect of n_α, the density of the defects of type α, and of the square of the defect-induced lattice parameter change, δ_α, defined according to Eq. (2.18). c_{ij} are the elastic constants of the crystalline matrix [2.7]. In addition, I_{HDS} is proportional to h^2, the reciprocal space vector corresponding to the Bragg peak, indicating that the I_{HDS} increases with the order of the Bragg reflection. The reduced scattering vector, $\boldsymbol{q}$, give rise to the typical intensity decay of the HDS proportional to $\boldsymbol{q}^{-2}$. The theory of the defect-induced DXS, summarised in Ch. 2, has been derived assuming a static crystalline lattice.

The presence of defects in a crystal is not the only origin for diffuse scattered intensity. The atomic thermal vibrations give rise to the thermal diffuse x-ray scattering (TDS), which is the dynamic analogous of the static HDS. The first-order TDS [2.7] is described in Eq. (3.2).

$$I_{TDS,radial} \propto \frac{T}{c_{11}+c_{12}+c_{44}} \left| \frac{\boldsymbol{h}.\boldsymbol{q}}{q} \right|^2 \tag{3.2}$$

The TDS, in the high temperature approximation, is proportional to the temperature *T.* As the HDS, the TDS is proportional to h^2 and to $\boldsymbol{q}^{-2}$.

As a consequence, for the investigation of the defect-induced DXS, the DXS background caused by the TDS must be subtracted from the total DXS intensity. To this end, the intensity collected on the implanted and the non-implanted areas on the same Si wafer are used to obtain the pure defect-induced DXS intensity: $I_{defect-induced\ DXS} = I_{total\ DXS} - I_{TDS}$.

The DXS intensity measured on the non-implanted area of the wafer is an estimation of the TDS, in the assumption that this DXS component is not affected by the implantation and annealing treatments. Hence, the residual DXS intensity arises only from the crystalline defects created by the ion-implantation.

In order to have implanted and non-implanted areas on the same Si crystal, the wafers are patterned with photo-resist in stripes of 10 mm before the implantation and stripped prior to the annealing. Samples of size 10 x 20 mm^2 are cleaved from the wafers, as shown in Fig. 3.9(a), and consist of an implanted and a "virgin" non-implanted half. A schematic view of the sample is given in Fig 3.9(b). All the samples studied are (001)-oriented Si wafers because this crystallographic orientation is used in industrial applications due to the very high quality of its SPER (Sec. 1.2.1).

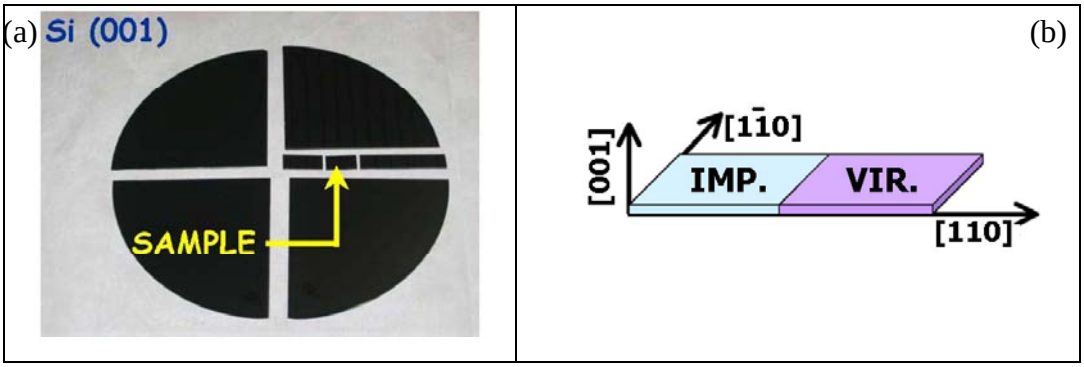

Figure 3.9: (a) Photograph of a Si wafer showing the cleavage of a sample for x-ray scattering experiments. (b) Scheme of the (001) Si "double-structure" sample with an implanted and a "virgin" non-implanted area.

The double structure of the sample is needed for all x-ray techniques as a reference background. The DXS intensity is collected on both regions by translating the sample, while keeping all other experimental conditions unchanged. In addition, the use of the "double-structure" sample enables to minimise the effects of scattered intensity variations caused by the miscut of the Si crystal, i.e. the misalignment of the (001) crystal planes with respect to the nominally (001)-oriented surface. In the present work, the samples miscut is ≤ 0.005 deg i.e. smaller than α_c. Therefore, the miscut negligibly affects the scattered intensity and is not considered in the present work.

3.2.2 The GI-DXS experiment: data acquisition

GI-DXS measurements were carried out with an 8 keV x-ray beam. Starting from the 220 surface Bragg reflection, the reciprocal space is probed in three different crystallographic directions: q_r, q_a and q_z, as depicted in Fig. 3.4. The values of q_r, q_a and q_z are calculated following Eqs. (3.3), (3.4) and (3.5), respectively.

$$q_r = \frac{4\pi}{\lambda}\left(\sin\Theta - \sin\Theta_{220}\right) \approx Q\cot\Theta_{220}\Delta\Theta, \tag{3.3}$$

where Θ_{220} is the Bragg angle for the 220 lattice node, Q is the modulus of the momentum transfer and λ is the x-ray wavelength. $\Delta\Theta$ is defined as $\Delta\Theta = \Theta_{220}-\Theta$.

$$q_a = \frac{4\pi}{\lambda}\sin\Theta_{220}\sin\left(\Theta - \Theta_{220}\right) \approx Q\Delta\Theta \tag{3.4}$$

$$q_z = \frac{2\pi}{\lambda}\left(\sin\alpha_i + \sin\alpha_f\right) \approx \frac{2\pi}{\lambda}\left(\alpha_i + \alpha_f\right) \tag{3.5}$$

As pointed out before, the grazing incidence scattering geometry is well suited for depth-resolved measurements, because the x-ray penetration depth can be tuned by the incident and exit angles, α_i and α_f, according to Eq. (2.33). In the GI-DXS experiment, two values of α_i are used. With α_i smaller than the critical angle for total external reflection, α_c, i.e. $\alpha_i = 0.68\alpha_c$, the x-rays are scattered from a depth Λ of ≈ 10 nm, which is comparable with the USJ depth and enables the study of the near surface layer. For $\alpha_i = 1.32\alpha_c$, Λ ≈ 400 nm and the end-of-range damage region can be reached. Experimentally, the value of Λ is determined by means of the calibration of the critical angle α_c from the optical surface of the Si crystal. As a consequence, Λ is independent on the sample being crystalline or amorphous. This may affect the scattered intensity in presence of an amorphous non-scattering layer at the surface, as it will be discussed in Ch.4.

The zero of the α_f scale is given by the sample horizon on the PSD. The resolution in α_f is calculated from the channels of the PSD and the distance between the sample and the detector, resulting in ~ 0.005 deg. The intensity recorded by the PSD (i.e. along q_z) is used in different ways. After subtraction of the TDS component, the defect-induced DXS intensity integrated along q_z is exploited to study the $q_{//}$ dependence of the DXS. As introduced in Sec. 2.1.2, this results in the characterisation of the defect type. $q_{//}$ corresponds to q_r or q_a, depending on the direction of the measurement. The PSD can be used for mapping the reciprocal space in the $q_{//}$-q_z plane to detect the presence of DXS intensity streaks from extended EOR defects (Sec. 2.1.3). In addition, q_z-resolved intensity measurements are performed at fixed $q_{//}$ using a long integration time to improve the statistics. The latter's are

exploited to provide the depth distribution of the defects. The selected positions are q_a = 0.06 Å^{-1}, for the angular direction, and q_r = 0.14 Å^{-1}, for the radial one. These positions are chosen, because they are far enough from the Bragg peak to avoid eventual coherent scattering contributions centred on the Bragg peak, e.g., arising from small crystallites, as it will explained in Sec. 5.3. At the same time, these positions are close enough to the 220 reciprocal space node to record the HDS component of the DXS and to detect the presence of DXS intensity streaks arising from extended EOR defects, especially concerning the radial direction.

3.2.3 The GI-DXS experiment: data evaluation

In this section, one example of data evaluation is given for an arsenic-implanted sample annealed at low temperature. The details on the sample preparation are not discussed, because they are not important at this stage of the data analysis.

The first step in the data evaluation is the subtraction of the background DXS intensity acquired on the non-implanted side of the sample (i.e. the TDS) from the DXS measured on the implanted area. The defect-induced DXS is thereby obtained. Figure 3.10 shows an example of a radial measurement performed at $\alpha_i = 1.32\alpha_c$ on the implanted and virgin side of the sample together with the resulting defect-induced DXS. The maps of the distribution in reciprocal space of the measured DXS intensity in the $(1\bar{1}0)$ plane are plotted in parts (a) and (b) for the implanted and virgin areas of the sample, respectively. The PSD acquisition that contains the Bragg peak has been removed to enhance the contrast of the DXS signal. The DXS signal measured below $q_{z,critical}$ = 0.039 Å^{-1}, where $q_{z,critical}$ is value of q_z for the critical angle α_c, is weak. This is due to the grazing incidence geometry, where all scattered intensities are multiplied by the transmission functions T_i and T_f (Secs. 2.2 and 2.3). The defect-induced DXS obtained from (a) and (b) is plotted in Fig. 3.10(c). As expected, the defect-induced DXS increases as the Bragg peak position approaches. Part (d) of the same figure shows the DXS intensity integrated over the q_z-direction for the data plotted in part (a), (b) and (c). The maximum of the q_z-integrated DXS intensity close to the Bragg peak is ~4.5 orders of magnitude smaller than the Bragg peak intensity.

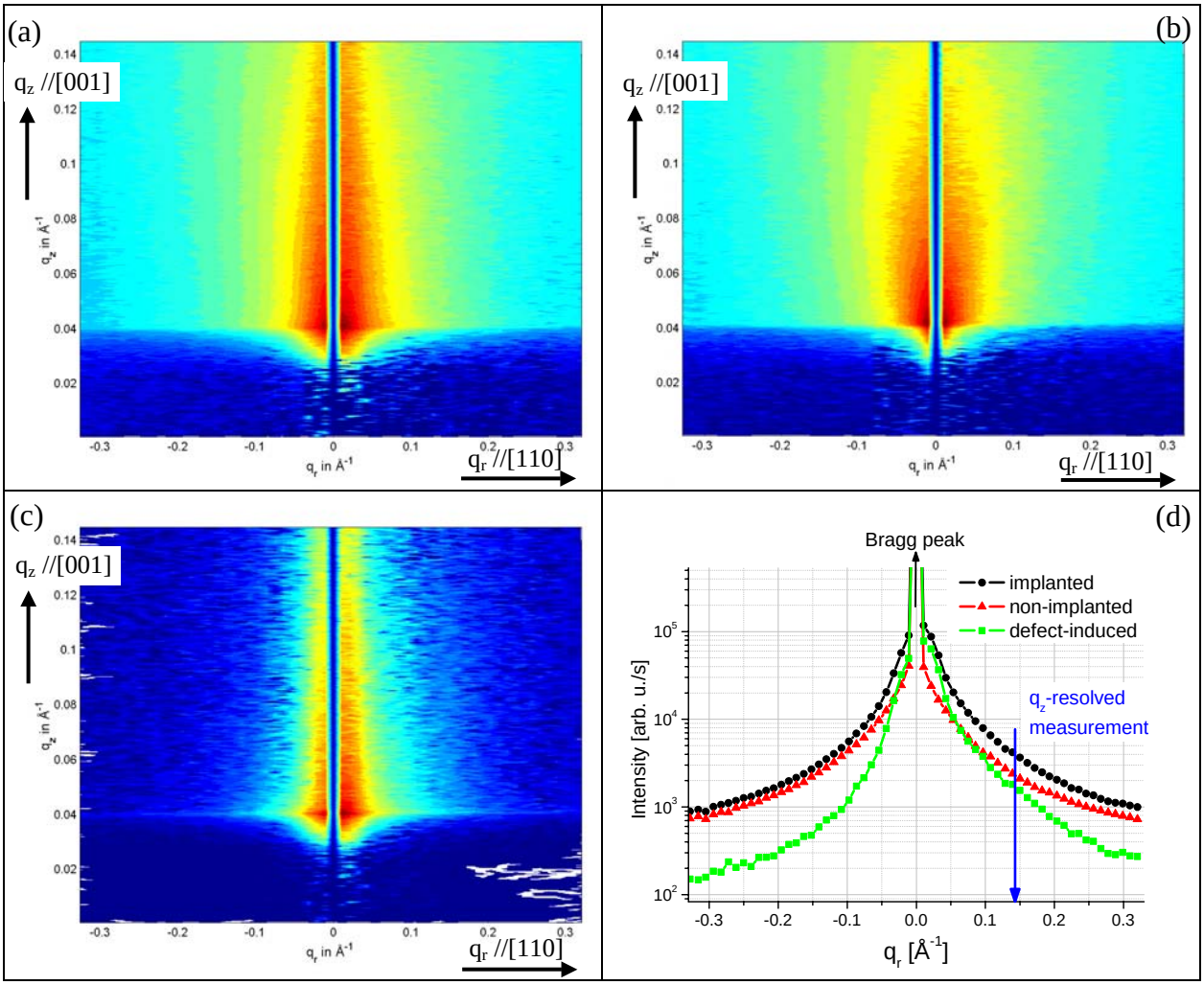

Figure 3.10: Reciprocal space maps of the diffuse x-ray scattering close to the 220 surface Bragg reflection at $\alpha_i = 1.32\alpha_c$ for an As-implanted Si wafer. (a) DXS from the Si implanted area. (b) DXS from the Si non-implanted area. (c) Defect-induced DXS. The PSD measurement corresponding to the Bragg peak position has been removed for all the maps. (d) DXS intensity integrated along q_z from the maps shown in (a), (b) and (c). The blue arrow indicates the radial position for the q_z-resolved measurement with long integration time.

For the analysis of the $q_{//}$ dependence, the q_z-integrated intensity of the defect-induced DXS is symmetrised by

$$I_{sym} = \frac{I(q_{//,+}) + I(q_{//,-})}{2}, \tag{3.6}$$

where $I(q_{//,+})$ is the defect-induced DXS intensity for $q_{//} > 0$ and $I(q_{//,-})$, for $q_{//} < 0$. Figure 3.11 shows the symmetric component of the DXS for the measurements plotted in Fig. 3.10. A q^{-2} decay typical for the HDS is found, indicating that weakly distorting defects are present in the sample. The deviation from q^{-2} in the region close to the Bragg peak will be explained in Ch. 5. The HDS intensity is plotted as a function of the reduced scattering vector q, where $q = \sqrt{q_r^2 + q_z^2}$ [2.24].

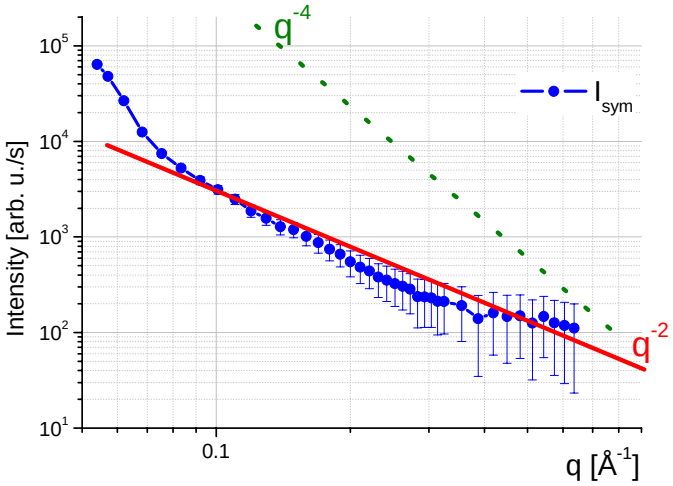

Figure 3.11: Double logarithmic plot of the symmetric part of the defect-induced DXS in radial direction obtained from the raw data shown in Fig. 3.10 (blue dots with corresponding error bars). The q^{-2} and q^{-4} decays of the intensity are shown for comparison (red and green lines).

The analysis of the $q_{//}$ dependence is done for both angular and radial scans. However, the asymmetric contribution of the defect-induced DXS is present only in the strain sensitive radial direction, where the variation of the modulus of the total momentum transfer is $\Delta|\boldsymbol{Q}| \neq 0$. The asymmetric contribution of the DXS, I_{asym}, is obtained by:

$$I_{asym} = \frac{I(q_{r,+}) - I(q_{r,-})}{2} \tag{3.7}$$

and yields information on the sign of the distortion field around the defect (i.e. $\delta > 0$ or $\delta < 0$, Fig. 2.4). As discussed in Sec. 2.1.2, the scattering from lattice expanding defects, like SiI's, results in local lattice compression and exhibits a higher diffuse intensity for positive q_r, while the opposite happens for lattice contracting defects. The asymmetry of the defect-induced DXS is visible in Fig. 3.11(d), green line. In the example, $I(q_{r,+}) > I(q_{r,-})$ indicates that the defects are expanding the Si lattice. By combining the information from I_{sym}, I_{asym} and the known depth from which the DXS signal originates, the defect-induced DXS signal is attributed to the presence of SiI's "magic clusters" in the EOR region of the sample. The presence of an intensity hump in the region close to the Bragg peak will be explained in Sec. 5.3. In the DXS map shown in Fig. 3.10(c) no intensity streaks are observed (Sec. 2.1.3). Therefore, the presence of extended defects, like FDL's and 113's, can be excluded. The interpretation of DXS intensity streaks from extended defects will be reported in Chs. 5-7.

The depth distribution of the defects is obtained using the q_z-resolved DXS measurements combining the α_i and α_f angles. When keeping α_i fixed (i.e. the penetration depth, Eq. (2.31)), the scattering depth can be tuned as a function of α_f, according to Eq.

(2.33). The scattering depth increases with increasing α_f. One example of DXS distribution along q_z is given in Fig. 3.12 for $q_r = 0.14$ Å^{-1} and $\alpha_i = 0.32\alpha_c$ from the same sample shown in Fig. 3.10. The TDS is measured on the virgin sample (red symbols) and subtracted from the DXS of the implanted sample (black symbols). The curve obtained is the defect-induced DXS (green symbols).

A peak at $q_z = (0.039 \pm 0.001)$ Å^{-1} is found for the defect-induced DXS, which is not observed for the TDS measurement. The presence of this peak indicates that the defects are located in a layer close to the surface. In this case, the DXS is enhanced by the peak of the transmission function, which occurs at the critical angle $\alpha_f = \alpha_c$, corresponding to $q_{z\,\mathrm{critical}} = 0.039$Å^{-1}.

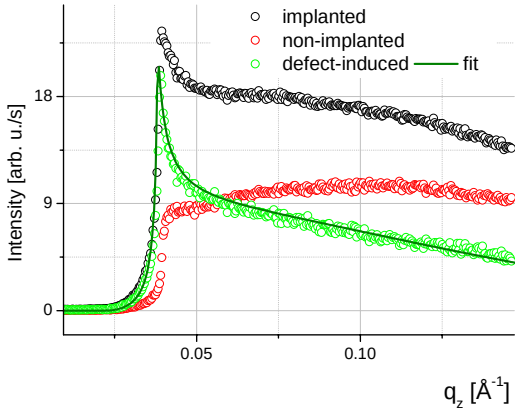

Figure 3.12: Diffuse intensity distribution along q_z measured at $q_r = 0.14$ Å^{-1} and at $\alpha_i = 0.32\alpha_c$ for an As-implanted Si wafer (same sample as in Fig. 3.10).

The q_z-resolved intensity of the defect-induced DXS was simulated using a code written by V. Holy, starting from the theory of the defect-induced DXS developed in Ref. [2.9] and summarised in Sec. 2.3.1. The code is based on the following assumptions:

- ✓ The matrix is an isotropic elastic semi-infinite continuum.
- ✓ The defects are crystalline spherical inclusions of radius R_z. The lattice inside the defects is cubic with a mismatch δ with the lattice parameter of the matrix.
- ✓ The depth distribution of the defect density is Gaussian, as shown in Eq. (3.8).

$$n(z) = n_{\max} \exp\left(\frac{-(z - z_{\max})^2}{(2\Delta z)^2}\right) \tag{3.8}$$

where $z_{\max}$ is the centre of the defect distribution and Δz its FWHM.

- ✓ The density of the defects is uniform in the directions parallel to the sample surface.

In addition, for the simulations performed in this work, the defect cores have been considered empty, i.e. the difference of the polarizability of the matrix with respect to the defect core is $\Delta\chi_h = -\chi_h$.

The simulations show a significant dependence of the shape of the DXS distribution along q_z as a function of z_{max}, as shown in Fig. 3.13(a). In particular, the presence and height of the transmission function-enhanced peak of the DXS signal changes with z_{max}. Also the variations of the defect size R_z, as in Fig. 3.5(b), strongly affect the distribution of the DXS along q_z. The strongest variations are observed for $q_z > q_{z,critical}$. The q_z distribution of the DXS is not much affected by changes of Δz, in Fig. 3.5(c), especially for $q_z > q_{z,critical}$, and by variations of δ, in Fig. 3.5(d). The intensity of the simulated DXS is proportional to the defect concentration n_{max}. However, this parameter cannot be used for fitting the data, because the DXS intensity is measured on a relative scale only. Therefore, all the simulations plotted in Fig. 3.13 have been normalised to 1.

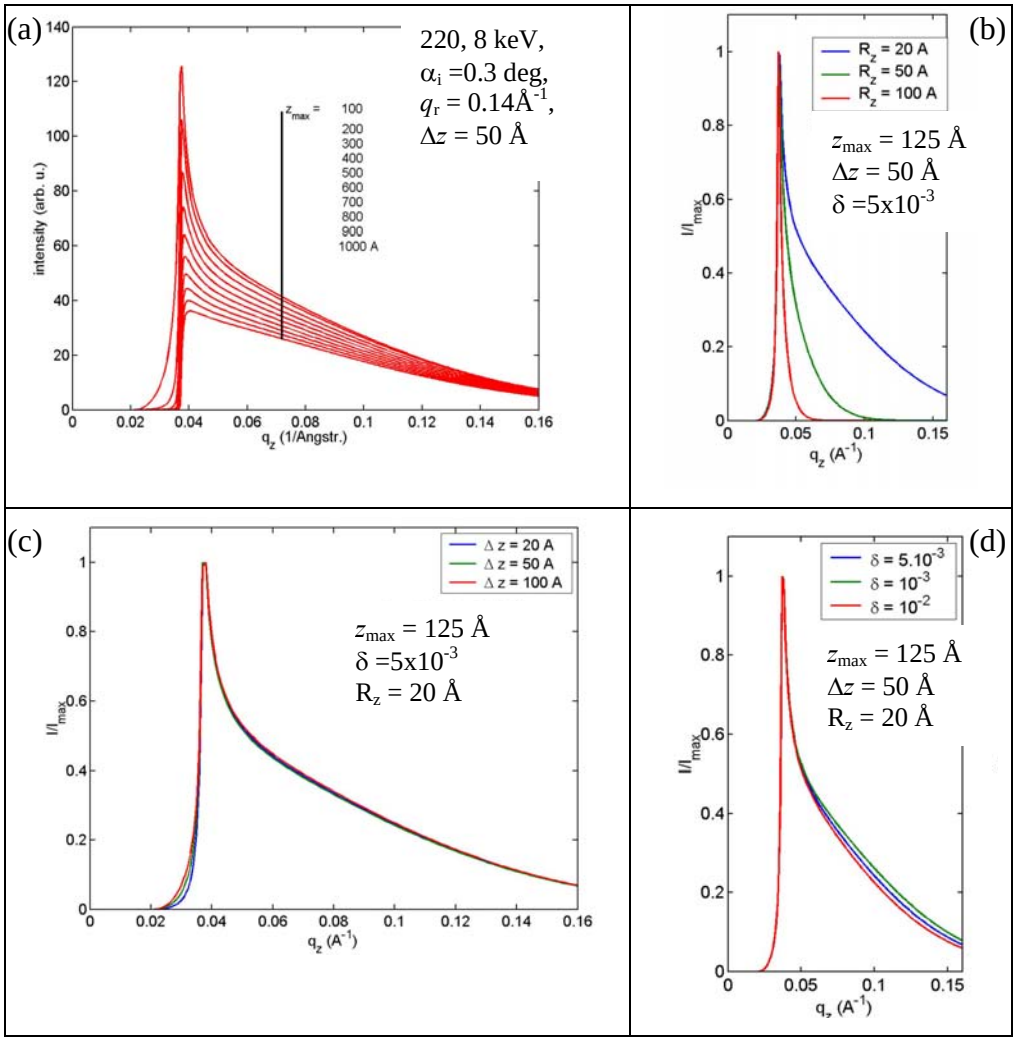

Figure 3.13: Calculated defect-induced DXS as a function of: (a) z_{max}, (b) R_z, (c) Δz and (d) δ (see details in the text). Courtesy of V. Holý.

The defect-induced DXS from Fig. 3.12 is fitted using α_i = 0.3 deg at 8 keV (i.e. the experimental conditions), R_z = (15 ± 5) Å, δ = (1.0 ± 0.5) x 10^{-4}, Δz = 50 Å and z_{max} = (125 ± 10) Å. Due to the low sensitivity of the q_z DXS distribution to δ variations, the accuracy on its determination is poor. Δz has been set fixed to 50 Å, which is a reasonable value as deduced by TRIM simulations [1.12]. R_z is in agreement with the expected radius of "magic clusters", i.e. ~20 Å (Sec. 1.2.4). In conclusion, the most reliable and important information obtained from the fit is the location of the centre of the defect distribution, z_{max}, in this case, 125 Å below the surface.

3.3 Combining the x-ray scattering methods

The structural characterization obtained from GI-DXS only was not complete, because of the layered sample structure and of the different types of defect present after ion implantation and annealing. Therefore, a combination of scattering techniques, such as conventional x-ray diffraction (XRD) and specular reflectivity (SR), grazing incidence diffraction (GID) and GI-DXS, has to be applied.

3.3.1 Conventional x-ray diffraction

Conventional x-ray diffraction (XRD) is sensitive to the strain distribution of the crystalline part of the Si wafer in the direction perpendicular to the SPER (i.e. perpendicular to the sample surface). The scattering contrast is obtained from the interference of the scattering amplitudes from the stack of deformed crystalline layers in the sample. The interference fringes appear on both sides of the Bragg peak. The position, periodicity and contrast of such fringes are determined by their strain and thickness [3.5, 2.7].

A detailed report on the theory of this characterisation method is beyond the aims of this work. The technique is widely discussed in the literature, e.g. Ref. [3.5] and references therein.

For the samples studied in this thesis, the XRD intensity was measured along the q_z direction [001] in the reciprocal space region close to the 004 Bragg reflection of Si, as schematically shown in the inset of Fig. 3.14. The energy used was 8 keV. One example of XRD measurements performed on an As-implanted Si sample is shown in Fig. 3.14(a).

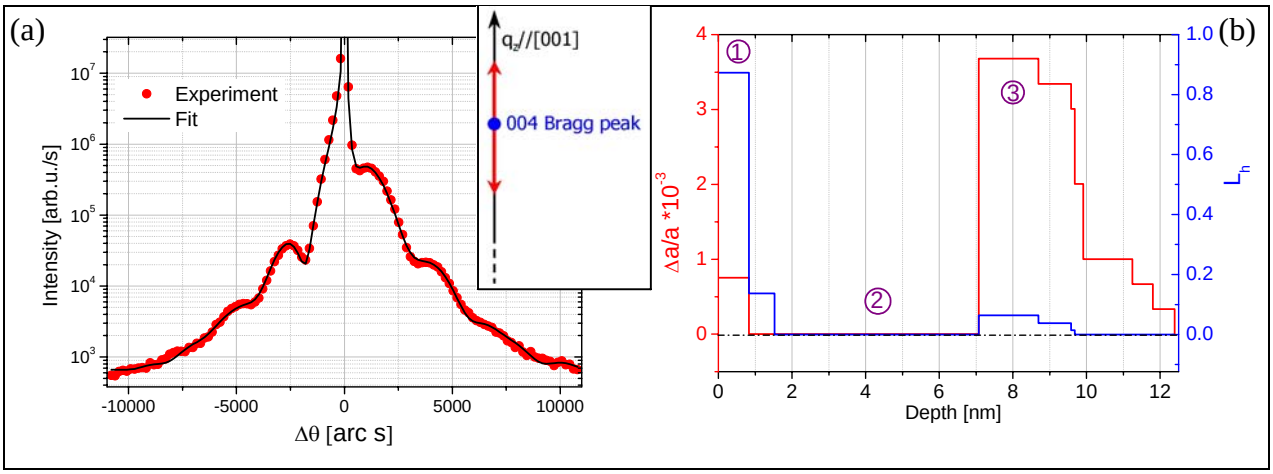

Figure 3.14: (a) XRD scan close to the 004 Bragg reflection ($\Delta\Theta = 0$) measured on an As-implanted Si wafer (red symbols). The best fit is shown as a black line. (b) Profiles of the lattice distortion, $\Delta a/a$, (red curve, left axis) and the static Debye-Waller factor, L_h, (blue curve, right axes) obtained from the fit of the experimental curve shown in (a). The numbers indicate the three characteristic regions of the profile. Inset: the red arrow explains where the scan has been performed close to the 004 Si Bragg peak.

Two parameters can be extracted by simulating the XRD curves. The depth distribution of the lattice strain, $\Delta a/a$, in the direction perpendicular to the sample surface (a is the Si lattice parameter). The second quantity is the exponent of the static Debye-Waller factor (L_h). In the approximation of a Gaussian distribution of the atomic displacements from the ideal sites of the deformed lattice, L_h is defined as $L_h = \left[\pi \sin \theta_B / \lambda\right]^2 \left\langle w^2 \right\rangle$, where $\left\langle w^2 \right\rangle$ is the mean square displacement and θ_B, the Bragg angle [3.5, 3.6].

The XRD measurements have been fitted using the RELP software, which is a recursive model based on dynamical diffraction [3.5, 3.6]. M. Servidori, from IMM-CNR, Bologna (Italia) performed the simulations. One example is plotted in Fig. 3.14(a) as a black line, the results from which are shown in part (b) of the same figure. The "zero" of the depth scale is located at the a/c interface.

Three main regions with different distortion features exist in the profile. The first layer is ascribed to the a/c interface, the second region to the SPER layer and the third to the EOR damage. The physical model for their interpretation will be discussed in detail in Ch. 4.

3.3.2 X-ray specular reflectivity

Specular reflectivity (SR) measurements are sensitive to the electron density distribution $\rho_{el}(z)$ perpendicular to the sample surface, independent of the sample being crystalline or amorphous [2.9, 2.16]. The scattering contrast is provided by the difference in the polarizability between the layers and the substrate. In this work, the SR technique has

been used to study the amorphous layer present close to the surface of the Si wafer (refer to Fig. 3.17).

The Fresnel's reflectivity coefficient, R_F, has been defined in Eq. (2.27). Experimentally, the SR is measured in the plane of incidence when the condition $\alpha_i = \alpha_f$ is satisfied. All the SR curves were measured using an 8 keV-beam. In order to separate the specular from the diffuse off-specular component of the reflectivity, an off-specular scan, with $\Delta\alpha_i$ = 0.3 deg, was measured for each sample both for the implanted and non-implanted sides. The inset of Fig. 3.15 schematically visualises the specular and off-specular scans in reciprocal space. The off-specular scan was used as a background signal and its intensity was subtracted following the procedure described in Ref. [2.9]. In addition, the illumination correction was performed on the measured intensity I_{meas} in order to obtain the corrected intensity, I_{cor}.

$$I_{cor} = \frac{b}{L \sin \alpha_i} I_{meas}, \tag{3.9}$$

where b is the beam size, L is the sample length in the direction of the beam. The illumination correction is applied for all $\alpha_i < \alpha_{i,\max}$, with $\sin\alpha_{i,\max} = b/L$ [2.9].

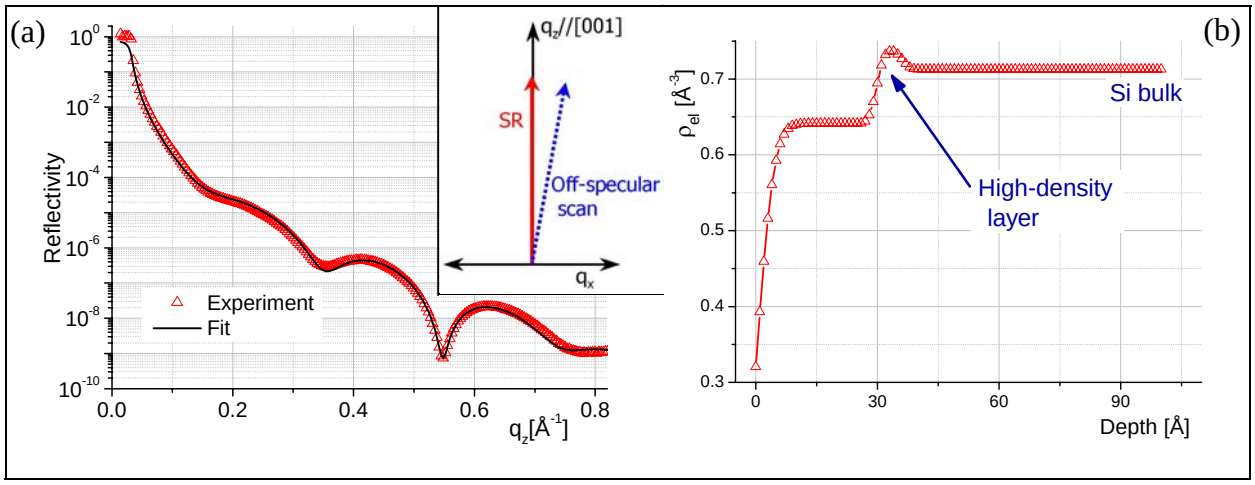

Figure 3.15: (a) SR curved measured on an As-implanted Si wafer (red symbols) and corresponding fit (black line). (b) Profile of the electronic density ρ_{el} obtained from the fit of the experimental curve shown in (a). Inset: Reciprocal space scheme of the specular (SR) and off-specular reflectivity scans. q_x is the in plane component of the scattering vector $\boldsymbol{Q}$.

One example of SR curve, obtained after background subtraction and illumination correction, is plotted in Fig. 3.15(a). The presence of intensity oscillations is observed. The period Δq_z of the oscillation is $\Delta q_z \approx \frac{2\pi}{\Delta d}$ and it is inversely proportional to the thickness Δd of the layer that induces the oscillations.

The SR curves were simulated using the Parrat formalism [3.7] to obtain the corresponding electronic density profiles. As an example, the density profile from the SR curve plotted in Fig. 3.15(a) is given in Fig. 3.15(b). In this case, the "zero" of the depth scale is located at the surface of the sample, differently from the profile derived from the XRD measurement, shown in Fig. 3.14(b). The density of the Si substrate is kept fixed during the fitting procedure. The simulation results consist in the thickness and roughness of the layers. For the example reported in Fig. 3.15(b), the surface roughness is ~0.3 nm. In addition, two layers are identified on top of the Si substrate. The first one is characterised by a density lower than the bulk and a thickness of (3.00 ± 0.05) nm. The thickness of the second layer is only (0.7 ± 0.2) nm and its density is ρ_{el} ~ 0.74 Å^{-3}, higher than for the bulk. The physical model explaining the presence of these layers will be discussed in Ch. 4.

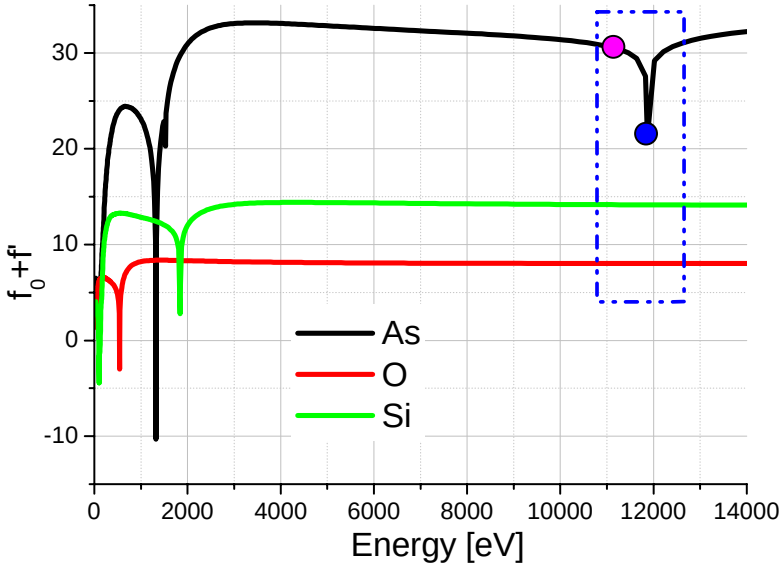

Figure 3.16: f_0+f' components of the atomic form factor for silicon, oxygen and arsenic as a function of the energy. Data from Ref [3.8], "Henke factors".

Anomalous SR measurements were performed to gain chemical information on the amorphous sub-surface layer. The energy dependence of the dispersion corrections of the atomic form factor $f(\boldsymbol{Q},\lambda)$, defined in Eq. (2.23), is exploited. Close to the absorption edge of an element, f' and f'' change dramatically, thus influencing the total $f(\boldsymbol{Q},\lambda)$, as shown in Fig. 3.16.

The anomalous SR technique consists in measuring the SR intensity at two energies: near the absorption edge of an element and some tens of eV below it. As many of the studied samples were implanted by arsenic atoms, the K-edge of As, located at E_{EDGE} = 11867 eV, was chosen

to perform anomalous SR measurements. In the measurement carried out with an energy close to the K-edge of As (blue dot), the form factor of this element is attenuated by ~ 30% with respect to its form factor below the edge ($E_{OUT\text{-}EDGE}$, magenta dot). For the other elements in the sample, such as oxygen and silicon, the atomic form factor is constant in the energy range close the As K-edge. One example of anomalous SR measurement will be discussed in details in Sec. 5.2.

Further information on the theory of the SR technique can be found in Refs. [2.9] and [2.16].

3.3.3 Grazing-incidence diffraction

It has been shown in Sec. 3.3.1 that the XRD technique provides the depth profile of the lattice strain in the SPER direction, perpendicular to the sample surface, by means of a scan through the 004 reciprocal lattice point along the [001] direction. Grazing-incidence diffraction (GID) provides the corresponding strain information for the lattice parameter in the lateral direction. Using the non-coplanar scattering geometry described in Sec. 3.1.2, the position of the in-plane Bragg peaks (i.e. *hk0*) is measured, thus determining the level of relaxation of the crystalline structure of the thin implanted layer with respect to the Si bulk. In all the samples studied by GID, no shift of the in-plane Bragg peak positions was observed by performing a radial scan at the 220 surface Bragg reflection with a resolutionon the lattice parameter of $\Delta a/a \leq 10^{-4}$. Therefore, the lattice of the implanted layer is pseudomorphically strained by the defects located in the near-surface region. The lateral lattice parameter is the same as for the Si bulk, while the implantation-induced stress is accommodated by a strained lattice parameter in the SPER direction.

If defects are present, they create a distortion field $\boldsymbol{u}(\boldsymbol{r})$, as discussed in Sec. 2.1.1. In a pseudomorphically strained lattice, no change of the lattice parameter is observed in the lateral direction, thus the average defect-induced distortion field in the lateral direction is $\langle \boldsymbol{u}(\boldsymbol{r})_{//} \rangle = 0$. Nevertheless, the deviations from $\langle \boldsymbol{u}(\boldsymbol{r})_{//} \rangle$, $\delta \boldsymbol{u}(\boldsymbol{r})_{//} \neq 0$ and give rise to the diffuse x-ray scattering signal that is measured with the GI-DXS technique.

3.3.4 Complete structural characterisation by combined x-ray scattering techniques

The combination of x-ray scattering methods described above is used to provide the details of the structure for ion-implanted Si samples. The scheme in Fig. 3.17 shows an

overview of the experimental techniques specifically applied for the investigation of different layers in the sample.

The layering of the wafer is determined by performing conventional XRD and SR measurements. In this way, the depth distributions of the lattice strain and of the electronic density are obtained. The GID technique is sensitive to the lateral lattice parameter and gives evidences that the implanted layer is pseudomorphically strained. The GI-DXS method provides the information on the lateral distortion field in the Si lattice induced by the presence of the defects. From this information it is possible to identify the types of defect present in the probed layer. The glancing angle scattering geometry allows for a resolution in depth exploited for the determination of the defect distribution from the DXS distribution along q_z.

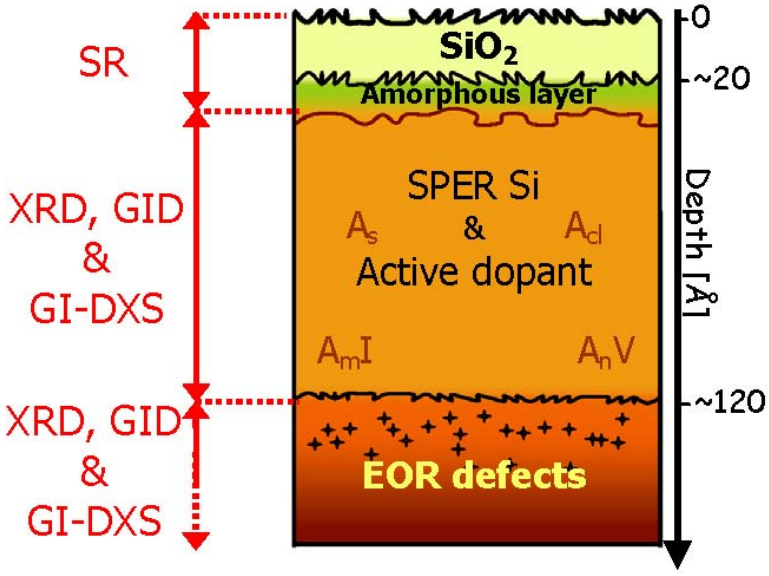

Figure 3.17: Scheme of the sample after ion implantation and annealing showing the experimental techniques used to investigate its layered structure. (The same sample scheme has already been show in Ch. 1, Fig. 1.10, where all the types of defect shown in the scheme are discussed.)

It will be shown that only the combination of the results from GI-DXS, GID, SR and XRD provide a complete understanding of the Si structure after implantation and annealing. As already mentioned, all techniques can be performed on the beamline ID01 using the same experimental set-up (Sec. 3.1).

In Secs. 3.2 and 3.3, it has been explained how the data acquisition and the subsequent analysis were performed. This same experimental approach was used for all the samples whose structural properties will be discussed in the following chapters.

For the samples described in Chs. 4-6, the dopant-ion implantation was carried out with arsenic ions. Arsenic is commonly used in industrial applications for the fabrication of CMOS

transistors (Sec. 1.1.2). In particular, ultra low energy As implantation is used for manufacturing the n-type drain extension channel junctions described in Sec. 1.1.3.

For sake of brevity, only a selection of the relevant experimental curves will be shown and discussed for each sample series.

4. Solid phase epitaxial regrowth of Si amorphised by As implantation

4.1 Motivation and samples description

A study of the evolution of the structural properties of Si during solid phase epitaxial regrowth (SPER) at low temperature (≤ 700 °C) after As ion implantation is presented in this chapter. Simultaneously, the influence of impurity atoms in Si is investigated.

Impurity atoms, such as oxygen, iron and copper, are known to be present in Cz-grown Si substrates in concentration as high as, e.g., $1x10^{18}$ cm^{-3} for O [1.2]. These concentrations are too low to be directly detected by GI-DXS, but the heteroatoms could play a role in the defect structure of Si after ion-implantation and annealing, e.g., by forming aggregates with the SiI's or the dopant atoms. In this way, they could create additional diffuse scattering components, thus influencing the investigation of the implantation-induced defects. In order to evaluate to impurity effect, two different Si substrates were used for the sample preparation: Cz p-type (001) Si wafers, the typical industrial substrate for n-type DECJ's, and impurity-free epitaxially grown (001) Si.

Table 4.1: Samples characterised using GI-DXS, XRD and SR techniques. All samples were implanted with As ions to a dose of $2x10^{15}$ cm^{-2} at 3 keV. RTA means Rapid Thermal Annealing.

Sample	Substrate	Processing conditions
Epi 550	Epi Si	RTA 550ºC; 200s
Epi 600	Epi Si	RTA 600ºC; 20s
Epi 650	Epi Si	RTA 650ºC; 10s
Epi 700	Epi Si	RTA 700ºC; 10s
Cz 550	Cz Si	RTA 550ºC; 200s
Cz 600	Cz Si	RTA 600ºC; 20s
Cz 650	Cz Si	RTA 650ºC; 10s
Cz 700	Cz Si	RTA 700ºC; 10s

The samples were prepared using the procedure described hereafter. First, the Si wafers were cleaned from the native oxide by APM chemical treatment (Ammonium Peroxide Mixture). Such processing step is meant to avoid the influence of native oxide on the outcome of the ion implantation. Subsequently, As^+ ions were implanted at 3 keV to a dose of $2x10^{15}$ cm^{-2}, producing a typical ultra-low energy implant. The dopant implantation results in an 11nm-thick amorphous layer, as evidenced by MEIS spectra, reported in Sec. 4.5, Fig. 4.10 for the as-implanted sample. The implantations were performed on an ultra-low-energy ion implanter (Applied Materials Quantum LEAP) by AMD, Dresden (D). Low annealing temperatures from 550°C to 700 °C were chosen to capture the end of the SPER and on-set of

defect annihilation. The samples were annealed in a Mattson AS10 RTP system at the University of Salford (UK) in an inert atmosphere (N_2). A total of 8 samples were characterised, which are described in Table 4.1. In the following, the sample batches will be referred to as Epi and Cz series, depending on the implanted Si substrate.

4.2 Solid phase epitaxial regrowth monitored by XRD

In this section, the layered structure of the implanted Si is discussed, based on the results from the XRD technique. The XRD measurements on the 004 Bragg peak were performed both on the Epi and Cz samples series. The evolution of the parameters extracted from the simulation of the XRD curves from both the Cz and Epi series look very similar, in spite of some minor differences in the SPER layer thicknesses. Therefore, for sake of brevity, only the data concerning one series, namely the Epi series, are discussed in this section.

The XRD curves measured on the Epi series are shown in Fig. 4.1. The same measurement performed on a non-implanted Si wafer is plotted as a reference (bottom curve). For sake of clarity, the curves are plotted using an arbitrary intensity offset.

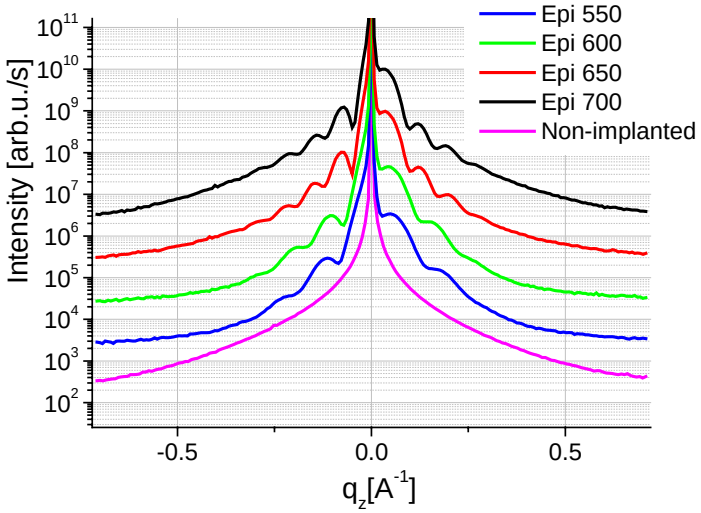

Figure 4.1: XRD measurements on 004 Bragg reflection for the Epi sample series. The same acquisition performed on a non-implanted Si substrate is shown for comparison. An intensity offset of one decade is applied for clarity.

All the curves from the implanted Si samples show intensity oscillations characterised by a period that decreases with increasing annealing temperature. The decay of the intensity with $|q_z|$ for the implanted Si is faster than for the virgin sample. Such difference between

the implanted and non-implanted Si samples decreases with the increase of the thermal budget (this feature is not clearly visible in Fig. 4.1, due to the intensity offset). These variations in the $|q_z|$ gradient of the scattered intensity from the implanted Si are associated with disorder and/or roughness at the a/c interface. The scattering contrast giving rise to the oscillation is related to the interference between the a/c interface and the distorted lattice in the EOR defects region.

The XRD curves in Fig. 4.1 were simulated and the resulting profiles are shown in Fig. 4.2(a) and (b) for the lattice strain, $\Delta a/a$, and static Debye-Waller factor, L_h, respectively. The "zero" of the depth scale is set at the a/c interface.

The strain profile can be divided in three characteristic regions as a function of the depth. The zone close to the a/c interface from 0 to 1.5 nm is characterized by an expansion of the lattice parameter, $\Delta a/a \sim (0.4 - 0.7) \times 10^{-3}$, and by a high disorder, $L_h \sim 0.6 - 0.9$. In the second region, starting from ~ 1.5 nm until a depth variable in the range of 6-10 nm depending on the sample, the strain is either negative or zero ($-0.75\times10^{-3} < \Delta a/a < 0.00$) with $L_h = 0$, indicating a well-ordered crystalline layer.

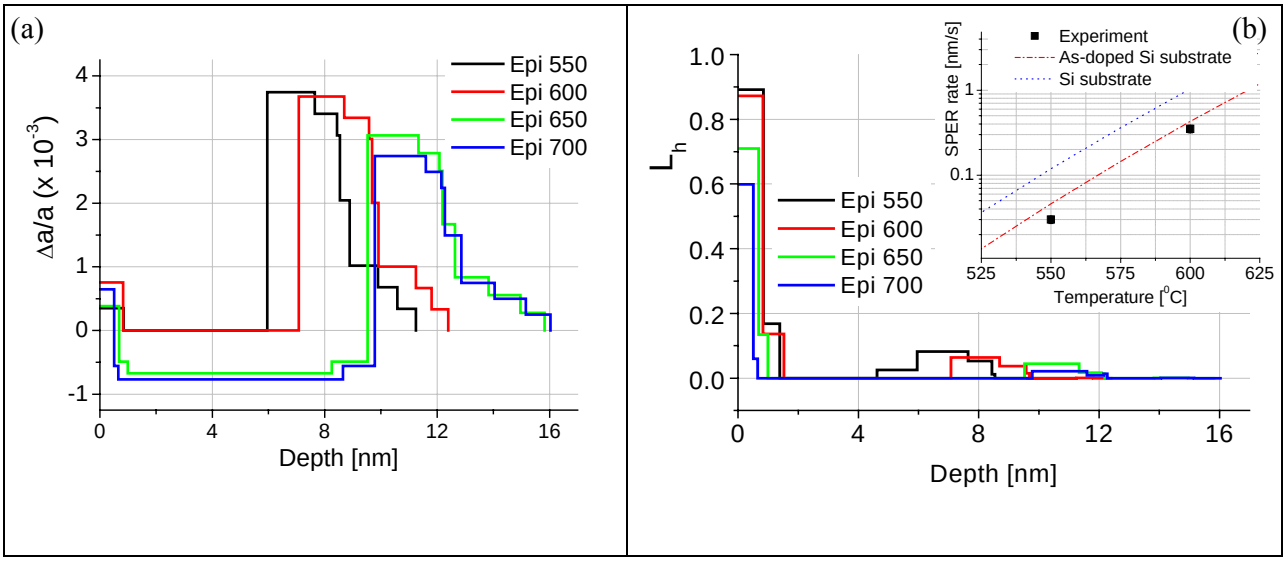

Figure 4.2: Epi sample series: (a) Depth profile of the lattice distortion, $\Delta a/a$, and (b) of the static Debye-Waller factor, L_h. Both profiles are obtained from the fit of the experimental curves shown in Fig. 4.1. Inset of Part (b): SPER rate for Epi 550 and Epi 600 compared with calculated SPER for As-doped Si (Eq. (1.1) by Olson) and pure Si [1.13].

The third layer is located in the deepest region at about 6-10 nm and is ~ 4 nm thick. It is characterised again by positive $\Delta a/a$ from 2.75×10^{-3} to 3.75×10^{-3} with L_h from 0.02 to 0.1, which are one order of magnitude higher and lower, respectively, than the corresponding values observed for the sub-interface layer. The first region is attributed to the interface between amorphous and crystalline part of the sample. The second area is ascribed to the

SPER layer. The deeper layer is attributed to the EOR damage region. This structure is typical for ion-implanted Si [4.2].

When the profiles are compared through the series, the main effect of the annealing is the progressive recrystallisation of the original amorphous layer above the EOR defects region. The thickness of the SPER area increases as a function of the annealing time and temperature. It is 6.0 nm, for the Epi 550, 7.0 nm, for the Epi 600, 9.6 nm, for the Epi 650 and 9.8 nm, for the Epi 700. The SPER process can be considered complete for Epi 650 and Epi 700. The measured regrowth rates for Epi 550 and Epi 600 are lower than foreseen by Olson's Eq. (1.1) (Sec. 1.2.1, [1.18]), as shown in the inset of Fig. 4.2(b). For the dopant profile of the as-implanted Epi sample, the maximum As concentration is ~$2x10^{21}$ cm^{-3}, as measured by SIMS. Therefore, the SPER is further inhibited with respect to Olson's calculation, due to the higher concentration of As in the measured samples. The As concentration was $2x10^{14}$ cm^{-3} for Olson's equation. This result confirms that high As doses slow down the regrowth rate of amorphous Si. The calculated SPER rate of pure amorphous Si is plotted in the same inset for comparison.

In the SPER layer, the lattice parameter is contracted for Epi 650 and Epi 700. Following [4.1], the lattice parameter change caused by As doping consists of two components. Locally, due to the size of the As electronic core bigger than for Si, an expansion of the lattice parameter is expected, $(\Delta a/a)_{size} > 0$. In addition, the hydrostatic deformation potential of the electronic band edge, occupied by the free electrons *e* of the As, induces an average contraction of the lattice parameter, $(\Delta a/a)_e < 0$. This second component is stronger, leading to an average negative lattice strain when As becomes electrically active by occupying substitutional positions in the Si lattice. This is the case for Epi 650 and Epi 700. For Epi 550 and Epi 600, the thermal budget is too low to induce As electrical activation, thus resulting in no negative strain. From the profiles reported in Fig. 4.2(a), the electrical activation takes place only when the SPER is complete. It has to be emphasised that, despite the average lattice contraction for Epi 650 and Epi 700, the corresponding L_h value remains unchanged at $L_h = 0$, indicating that the variation of the average lattice parameter does not affect the perfect local ordering of the SPER layer.

Moreover, upon increasing annealing temperature, the reduction of the strain in the EOR region is observed. This indicates that the SiI's confined in this area begin to rearrange into lower energy (i.e. strain) configurations and/or annihilate at the surface [1.47]. This behaviour is observed for Epi 650 and Epi 700.

Finally, the reduction of the $\Delta a/a$ and L_h values for the a/c interface with the increasing thermal budget indicates an improvement of the crystalline quality of the a/c interface, as it will be discussed in Sec. 4.5.

4.3 Evolution of the structure of the near-surface layer by SR

The complementary information on the amorphous region of the layered structure of the samples is obtained using the SR technique. The SR curves measured for Epi series are shown in Fig. 4.3(a) together with a measurement on a reference non-implanted Si. The SR signal from the low-temperature annealed samples (up to 600°C) is very similar to the non-implanted one. The broad intensity hump indicates the presence of a thin SiO_2 layer of a thickness of 1.5-2 nm. For the samples Epi 650 and Epi 700, an intensity oscillation appears, that becomes more marked for high temperatures. The period of the oscillation gets shorter with increasing temperature.

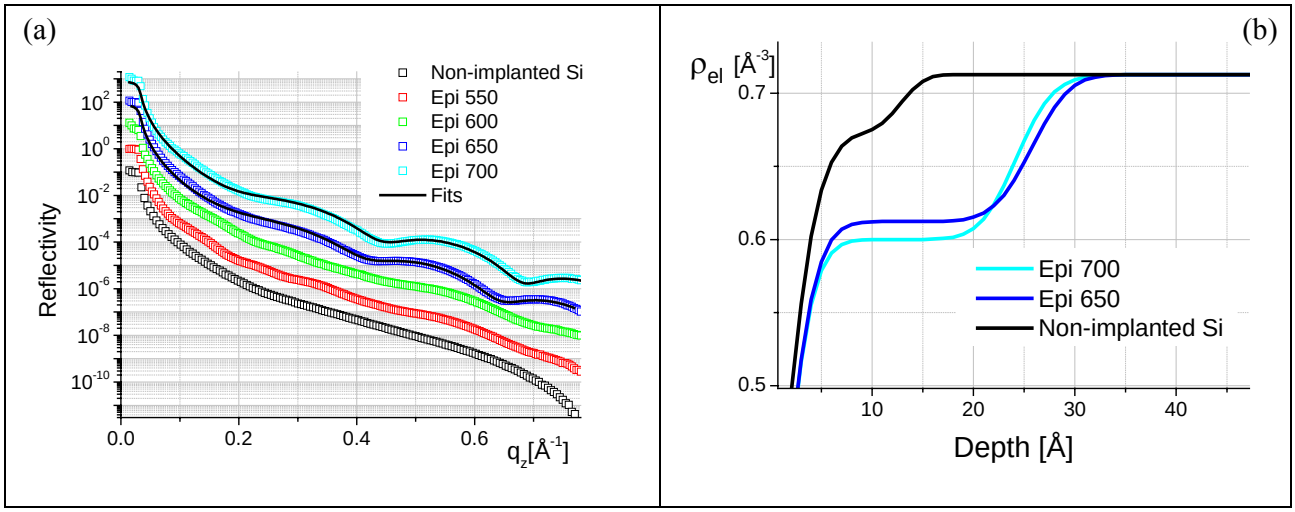

Figure 4.3: (a) Specular reflectivity curves for the Epi sample series and non-implanted Si (open symbols) with corresponding fits (full line). An intensity offset is applied to the measured intensity for clarity. (b) Corresponding depth profile of the density as derived from the fits for Epi 650, Epi 700 and non-implanted Si.

The curves with intensity oscillations (i.e. Epi 650 and Epi 700) have been fitted and the resulting simulations are shown in Fig. 4.3(b). For the annealing performed at 650°C and 700°C only, the SiO_2/Si interface becomes sharper and the contrast increases, thus resulting in intensity oscillations. The increased contrast has two origins: the formation of a layer with higher density below the SiO_2 layer, attributed to a partial As segregation, and a SiO_2 layer of a density lower than for the natural oxide of the virgin sample. When the oscillations are present, their period is an accurate measure for the oxide thickness after annealing: (2.6 ± 0.1)

nm, for Epi 650, and (2.5 ± 0.1) nm, for Epi 700. The thickness of the As-rich layer is (0.7 ± 0.3) nm for both samples and its density is about 0.5% higher than the Si bulk. Note that the accuracy of the thickness of the As rich layer is much poorer than for the SiO_2 layer. Despite its low density-contrast and reduced thickness, the accurate fit of the curves is obtained only if the As-rich layer is taken into account in the layer stack used for the modelling. For higher annealing temperature, the interface between the As-rich and the SiO_2 layers becomes even sharper and the As density higher. As a consequence, the As-rich layer results better visible by SR, as it will be explained in Sec. 5.2.

The SR curves measured on the Cz series presents the same behaviour and, therefore, they are not reported for brevity.

4.4 Characterisation of the residual defects by GI-DXS

The samples were investigated by GI-DXS to study the defect structure. Radial and angular scans close to the 220 surface Bragg reflection were performed, as described in Ch. 3. The analysis of the defect-induced DXS from a radial scan at $\alpha_i = 1.32\alpha_c$ ($\Lambda \sim 400$ nm) shows that the diffuse signal is strongly asymmetric with higher intensity for positive q_r values, similar to the example shown in Fig. 3.10(b). This asymmetry arises from the presence of defects expanding the Si lattice. The defect-induced DXS was symmetrised in order to study its $q_{//}$ dependence, as shown in Fig. 4.4(a). The analysis of the I_{sym} shows a q^{-2} decay typical for HDS from point-like defects or small clusters.

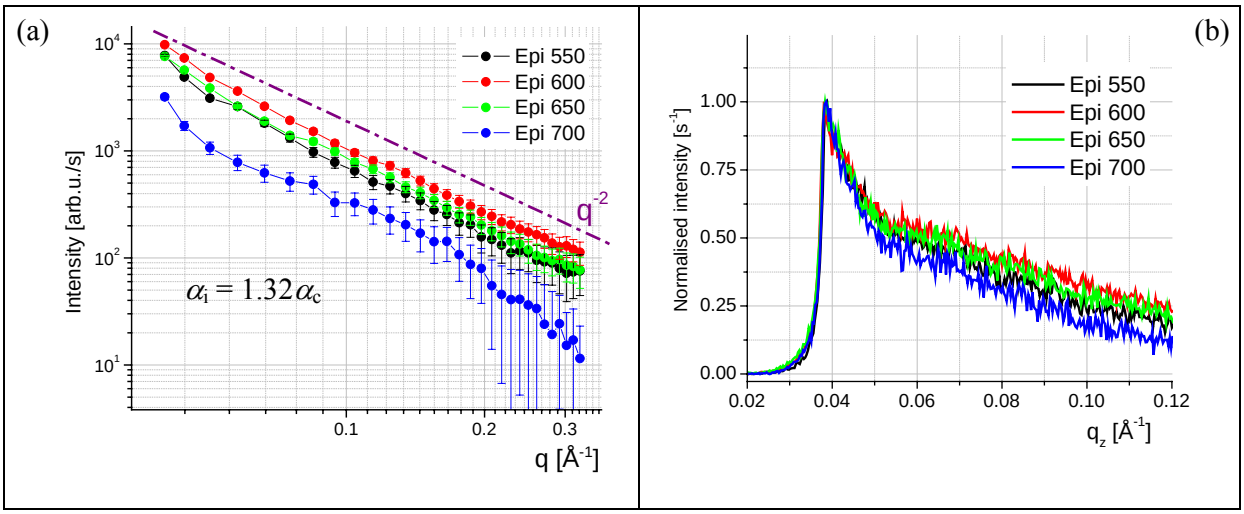

Figure 4.4: Epi sample series: (a) Symmetric component of the defect-induced DXS from the radial measurement close to the 220 surface Bragg reflection at $\alpha_i = 1.32\alpha_c$. The q^{-2} decay of the intensity is shown for comparison. (b) Defect-induced DXS along q_z measured at $q_r = 0.14$ Å^{-1} for the same scans reported in (a).

These experimental features are ascribed to the presence of EOR damage in form of small SiI's "magic clusters". The HDS intensity does not change significantly, when the sample from this series are compared, except for Epi 700. In the latter, the lower DXS intensity indicates a reduction of defect density with respect to the other samples.

The normalised distribution of the DXS along q_z is shown in Fig. 4.4(b). The intensity profile is constant upon annealing, indicating that the depth distribution of the EOR defect do not change through the sample series. The presence of the intensity peak close to $q_z = 0.039$ Å^{-1} is due to the enhancement of the defect-induced DXS caused by the peak of the transmission function (see Sec. 3.2.3).

No experimental evidence of the formation of extended defects in the EOR region is observed, as expected from the " excess interstitial" model (Sec. 1.2.4) for this type of implantation and annealing processing. Due to low energy of the As implant and, therefore, to the low depth of the EOR damage (~12 nm), the annihilation of small SiI's "magic clusters" at the surface is the energetically favoured path for the evolution of the EOR damage. As indicated by the GI-DXS results and confirmed by reduction of the lattice strain in the EOR region observed by XRD, at 700ºC the annealing of the EOR defects is in progress.

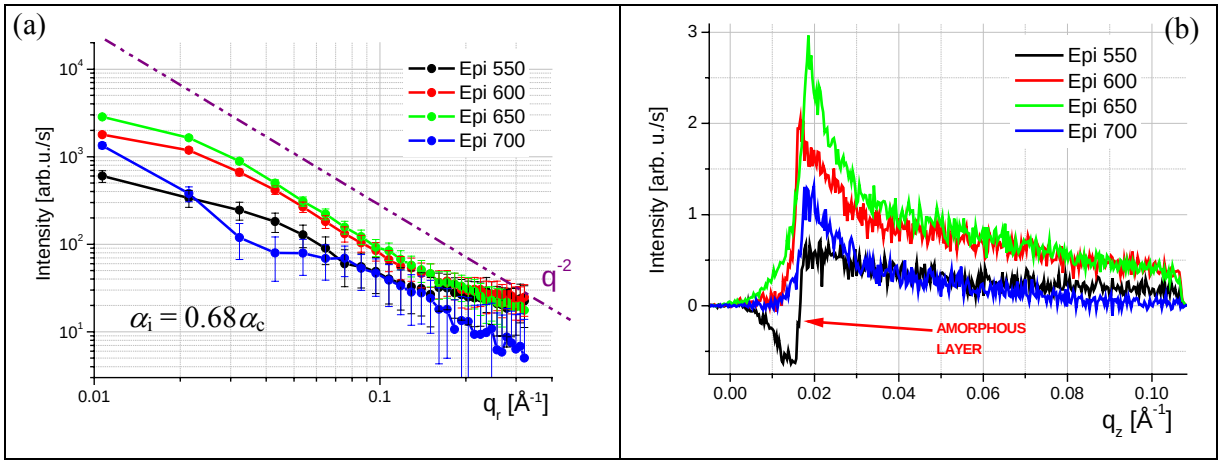

Figure 4.5: Epi sample series: (a) Symmetric component of the defect-induced DXS from a radial measurement around the 220 surface Bragg reflection at $\alpha_i = 0.68\alpha_c$. The q^{-2} decay of the intensity is shown for comparison. (b) Defect-induced DXS along q_z measured at $q_a = 0.06$ Å^{-1} at $\alpha_i = 0.68\alpha_c$.

The GI-DXS data measured at $\alpha_i = 0.68\alpha_c$ ($\Lambda \sim 10$ nm) will be discussed hereafter. In these experimental conditions, two major contributions determine the measured defect-induced DXS intensity: the thickness of the crystalline regrown region that is probed in the scattering depth, as explained in Sec. 3.2.3, and the defect-induced scattering, which is proportional to the defect type and concentration. For the investigation of this sample series,

the thickness of the SPER layer is crucial, because it has been shown by the XRD measurements that the SPER is not complete for Epi 550 and Epi 600.

The analysis of the data from the radial measurement shows that the defect-induced DXS is asymmetric with $I_{asym} > 0$, as for $\Lambda \sim 400$ nm. The symmetric part of the defect-induced DXS, I_{sym}, shows q^{-2} dependence typical for HDS, which is plotted in Fig. 4.5(a). When the HDS intensity is compared through the series, the samples Epi 600 and Epi 650 show a higher intensity with respect to Epi 550 and Epi 700. The reduced scattered intensity on Epi 700 is explained, if we consider that it originates from the decreased defect concentration in the EOR damage region, located at a depth of about ~11 nm. Indeed, even if the scattering depth is set to $\Lambda \sim 10$ nm, the tail of the evanescent x-ray wave reaches the depth of the EOR region, thus giving rise to a DXS intensity from the corresponding defects. The reduced DXS intensity observed for Epi 700 is then partly justified by the annealing of these EOR defects, which has been observed from the analysis of the GI-DXS measurement at $\Lambda \sim 400$ nm. The remaining DXS intensity is induced by the residual defects trapped in the regrown layer and mainly at the a/c interface, which are point defects expanding the lattice too. In the regrown region, a mixture of point defects is expected, like As on substitutional sites, As_xV clusters and SiI's. From all of these small defects an average q^{-2} decay of the DXS is observed, indicating that they distort the lattice weakly. As the same $q_{//}$-behaviour has been observed for the "magic clusters" in the EOR area, it is not possible to separate the contributions of the different kind of defects. In the measured q_r range, the DXS intensity decreases for Epi 700 by a factor of 5, when $\Lambda \sim 400$ nm is used, i.e. when both the complete EOR defect band and defects in the near-surface area are illuminated. The defect-induced DXS reduction is limited to only 2.5, when $\Lambda \sim 10$ nm is used, i.e. when only a fraction of the EOR defects is probed.

In the case of Epi 550, the reduced intensity is due to an amorphous surface layer, the presence of which was detected by XRD. In this case, the crystalline part of the probed volume is reduced as compared to the other samples. For Epi 550, the thickness of the crystalline SPER layer is ~4 nm less than for Epi 650 or Epi 700. The reduction in the scattered intensity due to the increased x-ray absorption from the additional 4 nm of amorphous material is estimated to ~10%, which does not justify the observed reduction of the measured intensity. Therefore, the reduced intensity for Epi 550 is explained by the smaller scattering volume of this sample compared to the completely regrown ones.

This interpretation is confirmed when looking at the q_z-resolved acquisitions performed at an angular position q_a = 0.06 Å^{-1},[a], shown in Fig. 4.5(b). The diffuse intensity measured below the critical angle, i.e. for $q_z < q_{z\,critical}$, is lower on the implanted area of the sample than on the virgin sample. This results in negative values when the two intensities are subtracted to calculate the defect-induced DXS. Such mathematically "negative" contribution is included in the calculation of the q_z-integrated defect-induced DXS intensity, in Fig. 4.5(a), thus decreasing its total value. The presence of "negative defect-induced DXS" intensity for $q_z < q_{z\,critical}$ is a clear indication that an extended, non-scattering layer is located in the sub-surface area of Epi 550 sample.

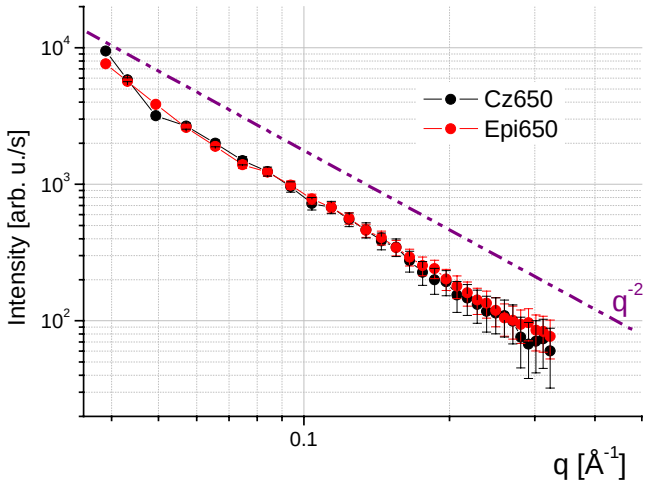

Figure 4.6: Epi 650 and Cz 650. Symmetric component of the defect-induced DXS from a radial measurement around the 220 surface Bragg reflection at $\Lambda \approx$ 400 nm. The q^{-2} decay of the intensity is shown for comparison.

To conclude, the comparison between the defect-induced DXS from the Epi series and from the Cz series is shown in Fig. 4.6 by one example of the data acquired on Cz 650 and Epi 650. The choice of two samples is motivated by their complete SPER. The two measurements exhibit the same $q_{//}$-dependence and intensity. Although the impurities concentration (mainly oxygen) is higher in the Cz Si wafer, the presence of contaminant atoms does not affect the DXS pattern from the implantation-induced defects.

[a] The data from the angular position are shown in Fig. 4.5(b), because their signal-to-noise ratio is better than for the corresponding acquisitions in radial direction. This choice does not affect the discussion of the related physical properties.

4.5 Comparison with MEIS

The MEIS technique has been applied for the characterisation of both the Epi and Cz sample series. Our IMPULSE project partners from Salford University (UK) (see Appendix) performed the measurements at the CLRC Daresbury facility (UK). The measurements were performed using a 100 keV beam of He^+ ions, incident along the $[\bar{1}\bar{1}1]$, so-called channeling direction, and detected along the [311] and [111], so-called blocking directions. The details concerning the use of the MEIS technique for the analysis reported in this work are given in Ref. [4.3]. In this section, the comparison between the results from MEIS and x-ray-based techniques is reported for the Epi sample series.

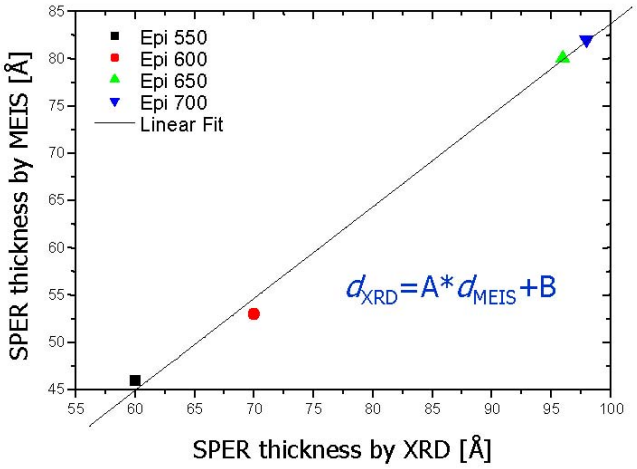

Figure 4.7: Thickness of the regrown layer: comparison between MEIS (d_{MEIS}) and XRD (d_{XRDS}) results. The constant offset (B ~ 16 Å) is due to the different definition of the depth origin for the two techniques. See text for details

Both XRD and MEIS techniques are sensitive to the regrowth of the amorphised Si during the annealing. MEIS measures, with depth resolution, the scattering yield from all of the atoms that are not occupying the Si lattice positions. XRD is sensitive to the crystalline part of the Si sample. In this sense, the two techniques give complementary information on the regrowth. Figure 4.7 shows a plot of the thickness of the SPER layer measured by MEIS and by XRD. All data points lay on a straight line with a constant offset (B ~ 1.6 nm) between the two measurements. This depends on the fact that, as a consequence of the different sensitivity of the two techniques, the criterion for setting the zero for the depth scale changes. MEIS sets its "zero" at the surface, where disordered Si is always visible, mainly due to the

presence of native SiO_2. On the other hand, XRD measures the regrown layer starting from the a/c interface that moves upon annealing towards the surface. In order to allow a direct comparison to the MEIS spectra, the strain profiles obtained from XRD measurements have been rescaled by a shift of each profile using the procedure described hereafter. The EOR damage region, which causes the strongest contrast in XRD curves, is located at the back edge of the as-implanted Si amorphous layer and its position is maintained fixed during annealing, as justified by the GI-DXS measurements shown in Fig. 4.4(b) and expected for EOR defects in this temperature range. Figure 4.8 shows the results of this rescaling of the depth. The disordered Si profile from MEIS is superimposed by the lattice strain profile from the fit of the XRD curves (see Fig. 4.2(a)). All the EOR damage is located at a constant depth (between 13.5 and 16.5 nm) and the a/c interface from XRD always aligns with the back edge of the Si hump in MEIS (i.e. the area of strong lattice disorder corresponds to highest yield). This procedure demonstrates that an excellent agreement of the SPER thickness measured by the two techniques is reached. The systematic decrease of the static disorder parameter L_h from XRD with the increasing temperature shows that the crystalline quality of the a/c interface layer improves.

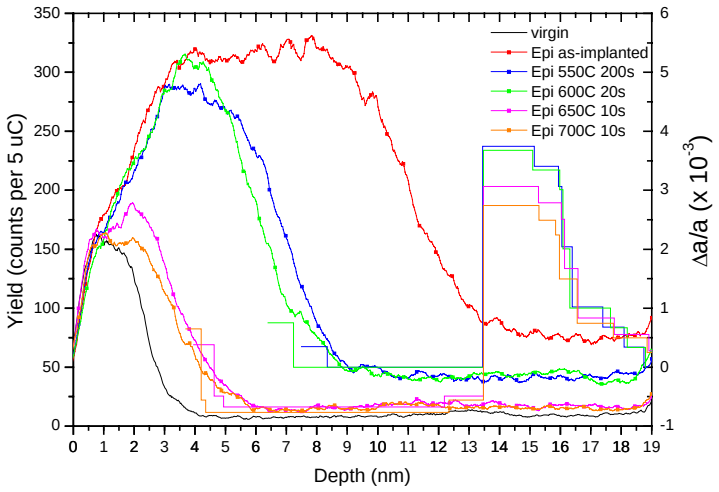

Figure 4.8: Epi sample series. Comparison between the MEIS depth profile for Si atoms and the strain profile from XRD measurements after rescaling of the depth (see text for details). Figure courtesy of M. Werner.

The rescaled profile of the static Debye-Waller factor (Fig. 4.2(b)) is plotted in Fig. 4.9 for the Epi sample series. For the a/c interface layer, L_h decreases from $L_h = 0.9$ for Epi 550 to $L_h = 0.6$ for Epi 700. The improvement in the quality of the crystalline layer is also borne out by MEIS, where for higher anneal temperatures a reduction in the background count is observed, which is due to more perfect reordering.

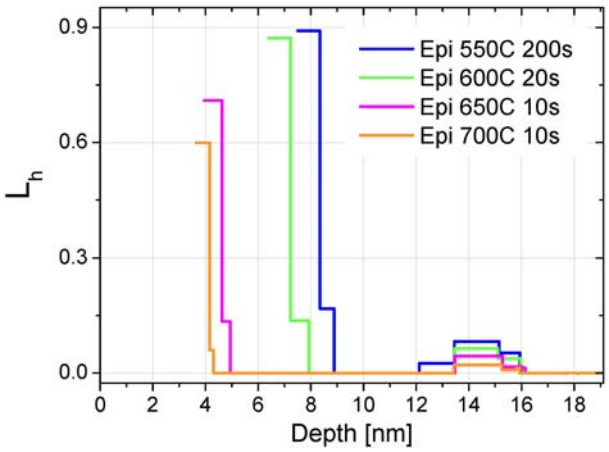

Figure 4.9: Epi sample series. Depth profile of the static Debye-Waller factor from the fit to XRD measurements after rescaling of the depth (see text for details).

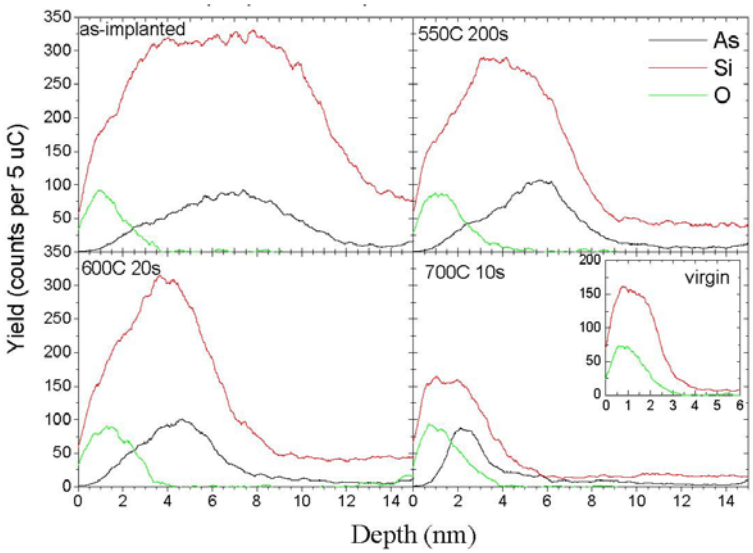

Figure 4.10: Epi sample series. MEIS depth profiles for As, Si and O, for as-implanted and annealed samples. The same profiles for a virgin non-implanted Si wafer are shown for comparison in the inset. Courtesy of M. Werner.

The SR results can be compared to MEIS for the measurement of the oxide layer thickness. The corresponding values are in agreement, as confirmed by the MEIS profiles shown in Fig. 4.10 for oxygen, arsenic and silicon. In the MEIS measurements, the layer thickness is estimated from the position of the half-high of the front and back edges of the element specific peaks [4.3]. SR shows a segregated As near-surface layer, which is buried under the oxide, for the 650 °C and 700 °C samples (Sec. 4.3). However, the MEIS sensitivity for the As layer is much higher than compared to SR where the detection is limited to

variations in the electron density. Further comparison between MEIS and SR and the corresponding detection of the segregated dopant layer will be presented in Sec. 5.5.

4.6 Conclusions

The results obtained for the characterisation of the SPER of Si amorphised by As implantation have been summarised in this chapter. The measurements provided useful information about the SPER rate of doped Si, confirming the presence of As at high doses reduces the regrowth rate of amorphised Si. The formation of a segregated dopant-rich layer below the native oxide was observed. XRD and SR proved to be the most suitable techniques for SPER investigation of the Epi and Cz sample series, because of their sensitivity to the Si layered structure.

The results of the regrowth study have important implications for the interpretation of GI-DXS measurements for all sample series studied within this work. Due to the variable thickness of the regrown layer at low temperatures, a quantitative interpretation of the GI-DXS intensity is possible only after complete SPER. The change of the DXS intensity is strongly affected by the increase of the crystalline volume during the regrowth, while the DXS contribution, induced by the rearrangement of the point defects during annealing, is much weaker. Therefore, in order to investigate the point defect evolution during annealing by GI-DXS, a fully epitaxial regrowth is mandatory and a detailed study of the regrowth behaviour at low temperatures was indispensable.

The defect-induced DXS originating from the residual implantation defects after full regrowth is negligibly affected by the presence of contaminant atoms in Cz-Si. Accordingly, only investigations performed on industrial Cz-Si substrates will be reported in the following.

Finally, the comparison between the results from MEIS and x-ray based techniques for the Epi sample series demonstrates the excellent complementarity of the information provided by the techniques, resulting in an clear model of the evolution of the sample structure during SPER.

5. Influence of the preamorphisation on the structural properties of ion-implanted Si

5.1 Motivation and samples description

In this chapter, the influence of the amorphisation of the Si substrate before the dopant-implantation (preamorphisation) on the final structural properties of the implanted samples is investigated. This study was used as a test for the development of the experimental method. The advantages and drawbacks of the use of x-ray scattering techniques with respect to other experimental methods, such as TEM and MEIS, will be discussed, in the final sections.

The implantation of dopant atoms in the ultra-low energy (ULE) regime may easily give rise to ion-channeling phenomena. The implanted ions, driven by the interatomic potential, penetrate the substrate through the channels of its crystalline structure, despite the titled orientation of the crystal with respect to the ion beam during implantation. As a result, the implanted dopant profile is shifted deeper inside the matrix. Obviously, such shift has to be avoided, because it leads to an increase of the junction depth after annealing. To prevent the ion-channeling, industrial ULE implants are performed in amorphised Si substrates. The amorphisation is produced by a processing step called pre-amorphising implant (PAI), which is performed before the dopant implant using high implantation energy (≥ 30 keV) and heavy ions (e.g. Ge, Xe) in order to produce a sharp a/c interface (i.e. high quality SPER) [1.13].

In addition to limiting the dopant ion channeling, the PAI affects the defect structure and, in particular, the EOR damage. When the ULE dopant implant is the only processing step, provided that the implanted dose is high enough to amorphise the substrate, the EOR defects are located below the a/c interface it creates. For PAI samples, the EOR damage is created by the PAI, because of their higher mass and implantation energy. In this case, the EOR defects are located much deeper inside the substrate, depending on the PAI parameters. As explained in Sec. 1.2, the defects present after ion implantation and annealing give rise to TED phenomena important for the device performance. For this reason, the investigation of preamorphisation effects is relevant, especially for the fabrication of USJ's.

To investigate the influence of PAI, a sample series containing a set of varying annealing conditions for both preamorphised and not-preamorphised wafers was prepared. Following the findings of Ch. 4, this sample batch was produced taking care of the full SPER

of Si. The "double-structure" with implanted and non-implanted areas on the same wafer was necessary for the x-ray techniques used.

For both samples series Cz p-type (001) Si wafers were implanted, which were previously cleaned from native oxide by APM treatment. The Si wafers used to prepare the preamorphised samples (PAI series) were implanted with Xe ions at 130 keV to a dose of $2x10^{14}$ cm^{-2}. TEM shows that an amorphous layer, about 100 nm thick, is thereby created, as it will be explained in Fig. 5.9 of the corresponding section. Subsequently, As^+ ions were implanted at 3 keV to a dose of $2x10^{15}$ cm^{-2}. For the non-preamorphised (NoPAI) sample series, only the As^+ implantation was performed, thus producing a typical ULE implant. In this case, the dopant implant results in an 11 nm-thick amorphous layer, as evidenced by MEIS spectra and already discussed in Ch. 4. The implantations were performed on an ultra-low-energy, high-current ion implanter (Applied Materials Quantum LEAP) by AMD, Dresden (D). Both series were subsequently annealed using two different conditions: a low temperature furnace treatment at 600°C for 20 minutes, to study the defects after solid phase epitaxial regrowth (SPER), and a spike annealing performed on an Applied Materials RTP Radiance system at 1130°C, close to the processing conditions for industrial devices. Both annealing treatments were performed in an atmosphere of 5% O_2 and 95% N_2 to reduce dopant loss. A total of 6 samples was characterised, whose preparation conditions are summarised in Table 5.1.

Table 5.1: (001) Si samples characterised using GI-DXS, XRD and SR techniques. When indicated, a PAI treatment was performed with Xe ions at 130 keV to a dose of $2x10^{14}$ cm^{-2}. All samples were implanted with As ions to a dose of $2x10^{15}$ cm^{-2} at 3 keV.

Sample	PAI treatment	Annealing conditions
PAI as-implanted	Yes	No annealing
NoPAI as-implanted	No	No annealing
PAI 600	Yes	Furnace at 600 ºC for 20 min.
NoPAI 600	No	Furnace at 600 ºC for 20 min.
PAI spike	Yes	RTA spike annealing at 1130 ºC
NoPAI spike	No	RTA spike annealing at 1130 ºC

5.2 Si layered structure by SR and XRD

As described in Ch. 4, the samples develop a layered structure after implantation and annealing. SR enables to study the depth profile of the electronic density of the layer stack, if the density contrast is sufficiently high. The layering is expected to consist of a SiO_2 cap layer, an amorphous sub-surface region and a SPER crystalline part containing the dopant atoms.

The SR measurements on the PAI series, performed with a x-ray energy of 8 keV, are reported in Fig. 5.1(a) together with the measurement of a non-implanted wafer. The SR curves relative to the annealed samples show an intensity oscillation, which is more pronounced in the case of spike annealing. The period of the oscillations is attributed to the interference between the surface and the interface between the SiO_2 layer and the high-density subsurface layer, to which the As and SiI's are swept by the regrowing crystalline front. For the as-implanted sample, the As depth distribution is broad and without sharp interfaces (see MEIS results in Fig. 5.8(a)). As a consequence, the corresponding SR curve is quite similar to the non-implanted wafer. From this sample, only one long-period oscillation is observed, caused by the thin native oxide. The curves have been simulated and the best fits are also shown in Fig. 5.1(a) as black lines. The resulting electronic density profiles are reported in Fig. 5.1(b) for the implanted wafers. The surface roughness is around 3Å for all the samples. The SiO_2 layer thickness increases from (14 ± 1) Å, for the as-implanted, to (21.7 ± 0.5) Å, for the 600°C-annealed, and to (29.8 ± 0.5) Å, for the spike-annealed sample.

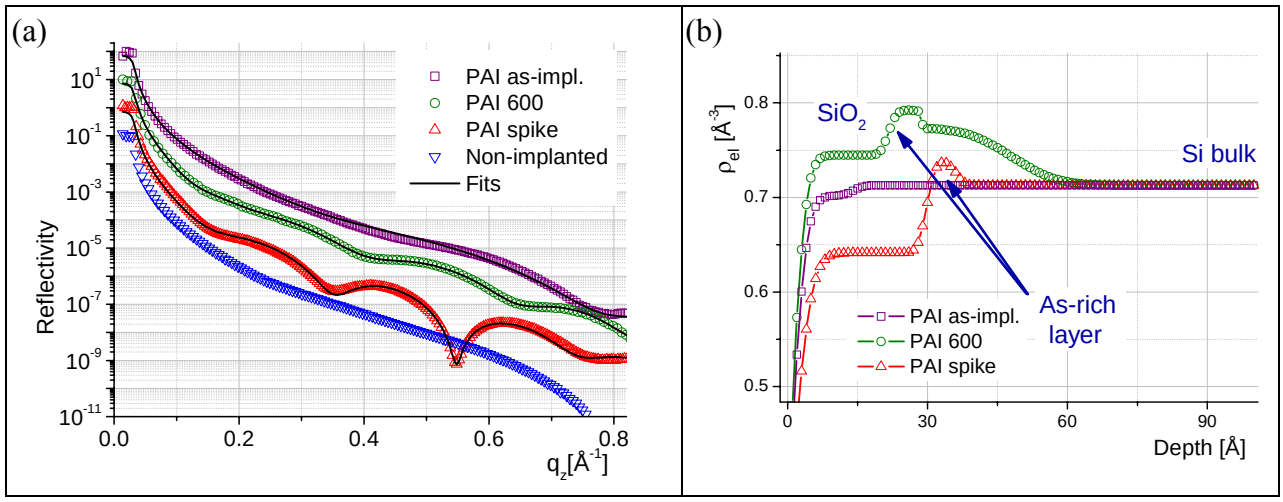

Figure 5.1: (a): Specular reflectivity curves for the PAI sample series and non-implanted Si with corresponding fits. (An intensity offset of one decade is applied.) (b): Depth profile of the density as derived from the fits.

The thickness of the high-density layer located below the SiO_2 layer is the same for the two annealed-samples: (7 ± 2) Å with a roughness of about 1.5 Å. The fit on sample PAI 600 indicates the presence of a third layer with higher density, characterised by a thickness of (19 ± 2) Å and a density gradient of 8 Å, which extends into the SPER part.

The increase of the SiO_2 thickness with annealing is explained by the presence of 5% O_2 in the annealing atmosphere. The higher oxide density for PAI 600 is most likely due to the long annealing time (20 min.). Further discussion on the SiO_2 growth upon annealing will be reported in Sec. 6.2. The increase of the density in the layer below SiO_2 is due to the

accumulation of excess As and SiI's atoms pushed towards the surface by the SPER front. The higher density stems mainly from the higher number of electrons of the As atoms. The third layer on PAI 600 contains a decaying density profile of As atoms. For the PAI spike sample, the contrast of the interference oscillations in SR is higher than for PAI 600, because the density contrast between SiO_2 and the As-rich layer is stronger and the interface sharper. The same evolution of the SR curves is observed for NoPAI samples (not reported here): only minor differences in layers thickness are noticed.

Anomalous SR measurements have been performed on these samples to prove that the scattering contrast in the SR curves is mainly due to the As atoms. For this experiment, x-rays of energy close to the K-edge of As, at E_{EDGE} = 11.866 keV, were used.

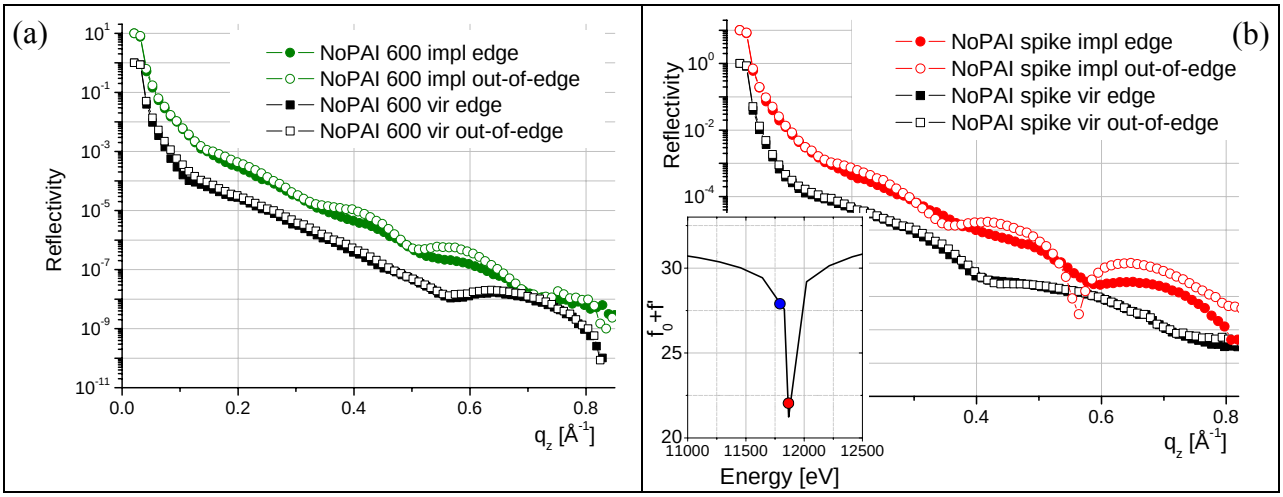

Figure 5.2: Specular reflectivity curves measured using 11.864 keV (full symbols) and 11.804 keV (open symbols). (a): NoPAI 600 sample and corresponding virgin non-implanted Si. (b) NoPAI spike sample and corresponding virgin Si. An intensity offset of one decade is applied for the data acquired on the implanted Si for clarity. Inset of part (b): Atomic form factor of As close to K absorption edge at 11.866 keV. The energy used for the SR measurements is indicated by coloured dots.

In particular, measurements close to the As K-edge were performed using an x-ray energy of 11.864 keV (i.e. E_{EDGE} -2eV), whereas out-of-the edge at 11.804 keV (i.e. E_{EDGE} -60eV), as shown in the inset of Fig. 5.2(b). The corresponding SR curves are shown in Fig. 5.2(a) and (b), for the samples NoPAI 600 and NoPAI spike, respectively. The corresponding curves for the virgin non-implanted region of the same samples are plotted for comparison. As expected for the As-free Si, the SR signal of the virgin samples (square symbols) does not change with the annealing. As shown in Sec. 3.3.2, Fig. 3.16, the atomic form factor of Si and O is constant in this energy range.

On the other hand, when the measurements on the implanted region are considered (dot symbols), an significant reduction in the contrast of the SR signal is observed for the curves measured close to the As K-edge, compared to the out-of-edge measurements. Such decrease

is ascribed to the reduced atomic form factor of the As atoms present in the implanted region, in particular, those As atoms segregated in the sub-oxide region. The As atoms contain 33 electrons each and, as a consequence, their form factor is higher than for Si (14 electrons) even at the As K-edge, as shown in Fig. 3.16. Therefore, the residual scattering contrast measured on the implanted samples close to the As K-edge is partly attributed to the remaining scattering from the As atoms and partly to the Si atoms confined into the sub-oxide layer. In conclusion, the main outcome from the anomalous SR curves is the evidence that the high-density layer is indeed created by the segregation of the As dopant atoms below the oxide cap-layer. The concentration of the As atoms in the segregated layer is variable in a range close to ~ 40% of the implanted dose for this sample series, as determined by MEIS measurements [4.3].

A quantitative evaluation of the percentage of As and Si atoms in the segregated layer should be possible as a result of the simulation of the anomalous SR curves measured. Such fit relies the known atomic form factor of the elements as a function of the x-ray energy. In Table 5.2, the values of the dispersion corrections *f*' and *f*" to the atomic form factor are shown for As and Si, for the energies of 8 and 11.865 keV. *f*' and *f*" have been defined in Eq. (2.24).

Table 5.2: Dispersion corrections *f*' and *f*" of the atomic form factor of As and Si for 11.865 and 8 keV. ITC=International Table of Crystallography, H=Henke factors, BC=Brenner-Cowern factors. The data are taken from the x-ray server of S. Stephanov, see Ref. [5.1].

Element, Energy	Source	*f*'	*f*"
As at 11.865 keV	ITC	$0.105*10^{-4}$	$-0.122*10^{-5}$
	H	$0.668*10^{-5}$	$0.832*10^{-5}$
	BC	$0.795*10^{-5}$	$-0.426*10^{-6}$
As at 8 keV	ITC	$0.022*10^{-4}$	$-0.712*10^{-6}$
	H	$0.222*10^{-4}$	$-0.732*10^{-6}$
	BC	$0.222*10^{-4}$	$-0.705*10^{-6}$
Si at 11.865 keV	ITC	$0.346*10^{-5}$	$-0.337*10^{-7}$
	H	$0.346*10^{-5}$	$-0.073*10^{-7}$
	BC	$0.346*10^{-5}$	$-0.339*10^{-3}$
Si at 8 keV	ITC	$0.765*10^{-5}$	$-0.179*10^{-6}$
	H	$0.767*10^{-5}$	$-0.177*10^{-6}$
	BC	$0.767*10^{-5}$	$-0.179*10^{-6}$

The values reported in this table are taken from three different sources: the International Table of Crystallography (ITC), the Henke factors (H) and the Brenner-Cowern factors (BC) [5.1]. For Si atoms, the values of *f*' and *f*" are very similar for the three different references used. On the contrary, while the agreement on the dispersion corrections for As is excellent for the energy of 8 keV, the variations are non-negligible for the As K-edge energy. The simulation of the anomalous SR curves based of the values of the dispersion corrections *f*' and

f" taken from the literature would not enable the quantification of the As concentration in the segregated dopant layer. The further quantitative analysis of the anomalous SR curves would require the experimental calibration of the dispersion corrections to the As form factor in the energy range close to the As K-edge. For example, this could be made by measuring the SR of samples containing As with a known stoichiometry. At the current stage, such calibration has not been performed yet. Nevertheless, the presence of segregated As atoms in the high-density layer is qualitatively confirmed by the anomalous SR measurements.

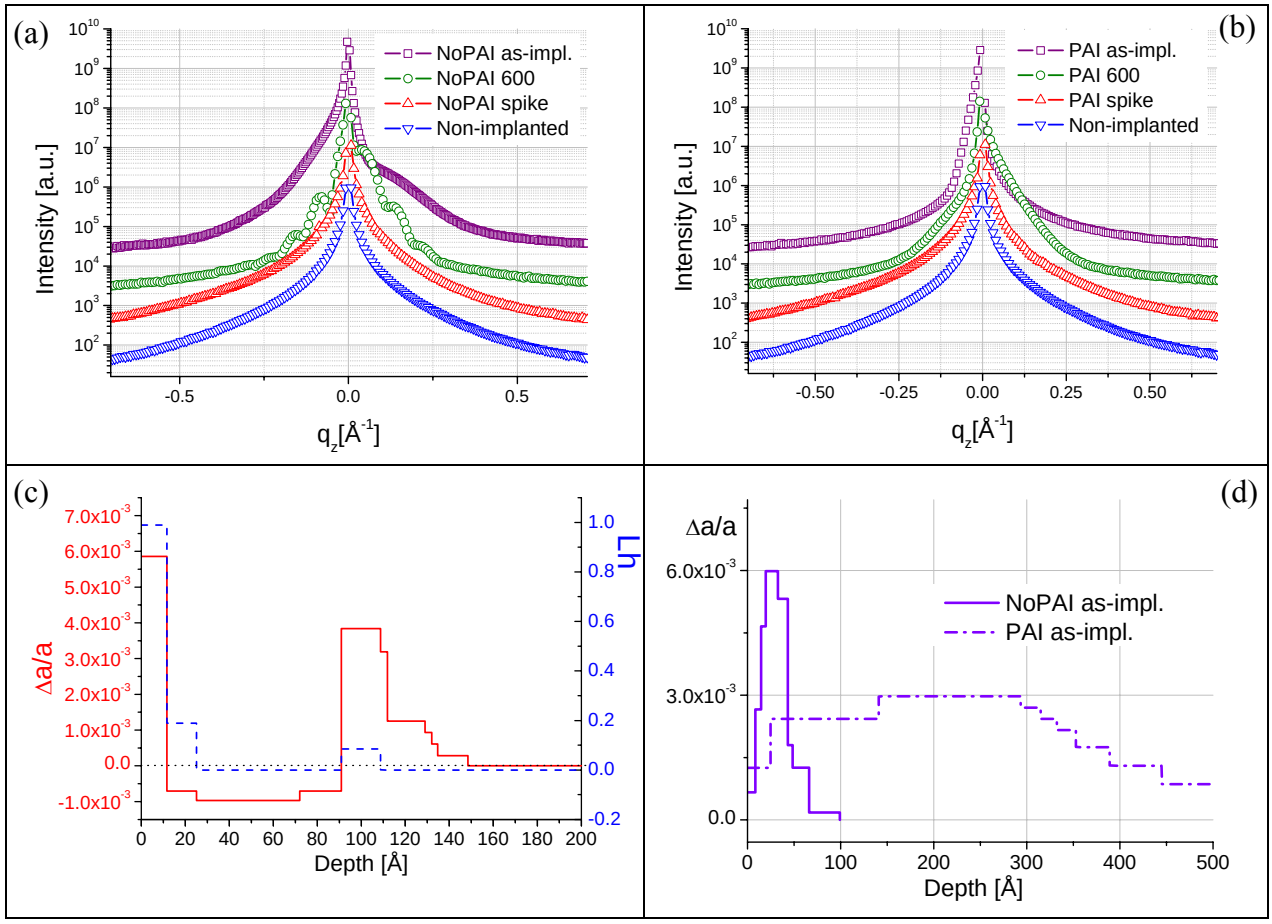

Figure 5.3: XRD curves for the NoPAI (a) and PAI (b) sample series. An intensity offset of one decade each is applied. The experimental points corresponding to the Bragg peak have been removed for clarity. (c) Depth profile of the lattice distortion, $\Delta a/a$ (red full line), and of the static Debye-Waller factor, L_h (blue dashed line), obtained from the fit of the experimental curves from sample NoPAI 600. (d) Depth profile of the $\Delta a/a$ from the as-implanted samples PAI (dash-dotted line) and NoPAI (full line). The "zero" of the depth scale is located at the amorphous to crystalline interface.

The measurement of the depth distribution of the lattice strain along the SPER direction using conventional XRD technique completes the investigation of the layered structure of the samples. The XRD curves measured at the 004 Bragg reflection of Si are shown in Fig. 5.3(a) and (b), for NoPAI and PAI series, respectively. The measured XRD intensity from the as-implanted and the 600 °C-annealed samples decays much faster with $|q_z|$ than for the virgin Si (bottom curves). For both as-implanted samples, the intensity is higher for negative q_z,

while for the 600 °C-annealed wafers the asymmetry is on the other side. For the spike-annealed samples, the $|q_z|$ decay is the same as for the non-implanted wafers. The "fast" decay of the scattered intensity observed for the implanted samples is due to the rough interface between the regrown and the amorphous layer. For the spike-annealed samples the high quality of the a/c interface enables to recover the original $|q_z|$ decay as for the non-implanted Si. The asymmetry in the XRD curves is an indication of the sign of the lattice strain. The lattice is expanded, for the as-implanted samples, and compressed, for the 600 °C-annealed samples. In the case of the NoPAI 600, the q_z decay is superimposed to intensity oscillations, originating from the interferometric behaviour of the distorted layers.

Figure 5.3(c) shows the results from the simulation of the measurement of NoPAI 600. Two parameters are extracted as a function of the depth: $\Delta a/a$, i.e. the strain of the lattice parameter, and L_h, the static Debye-Waller factor. The "zero" of the depth scale is set at the a/c interface. For this sample, as for the Epi series, the resulting strain profile can be divided in three main regions. The sub-interface layer with 12 Å thickness is ascribed to the a/c interface. It is characterized by an expansion of the lattice parameter ($\Delta a/a = 6.0\text{x}10^{-3}$) and L_h is high (also due to the presence of the "dendrites", see Sec. 5.3). In the SPER layer, from 12 to 90 Å, the strain is negative, $\Delta a/a = -1.0\text{x}10^{-3}$, and $L_h = 0$, which indicates a well-ordered layer. The negative strain is typical for As on substitutional sites, as discussed in Sec. 4.3. At a depth from 90 Å to 130 Å, the lattice is expanded ($\Delta a/a = 4.0\text{x}10^{-3}$) by the EOR defects composed of a supersaturation of SiI's.

The period of the oscillations measured on the non-PAI sample is inversely proportional to the thickness of SPER layer. In the PAI sample, the original amorphous to crystalline interface is located about 10 times deeper below the surface (depth ≈ 100 nm). Experimentally, the correspondent oscillation could be resolved, but the contrast between the a/c interface and the EOR region is too weak due to the broad profile of the SPER-to-EOR interface, as it is observed from the strain profile of the as-implanted PAI sample in Fig. 5.3(d). Therefore, only the 'envelope' of these oscillations is observed.

The fit of the XRD curves from the as-implanted samples, shown in Fig. 5.3(d), gives information on the EOR damage layer. The thickness of the distorted layer below the a/c interface is evaluated to be 90 Å, for the NoPAI, accompanied by $\Delta a/a = 6.0\text{x}10^{-3}$. For the PAI sample, the thickness of the EOR damage layer is 450 Å with $\Delta a/a = 3.0\text{x}10^{-3}$. For both the PAI and NoPAI samples, the profiles of the lattice distortion that results from the XRD curves are in agreement with the corresponding TRIM calculations [1.12]. The location of the a/c interface was done according to MEIS and TEM measurements, for NoPAI and PAI

samples, respectively. The TRIM calculation for the NoPAI implant (i.e. As at 3 keV) is shown in Fig. 1.6.

The disappearing of the interface between the SPER and EOR layers, due to the annealing of the EOR defects band, explains the absence of relevant oscillation for NoPAI spike. In PAI spike, FDL's are present at a depth around 100 nm from the surface in the EOR region (Sec. 5.4). They are not detected, because the strain they induce in the SPER direction is not sufficient considering that they distributes in the whole EOR depth range (~45 nm) and are located deep below the surface.

5.3 Defects in the near-surface layer: GI-DXS at $\alpha_i < \alpha_c$

To investigate the defect structure in the near surface layer, GI-DXS measurements were performed close to the 220 surface Bragg reflection at $\alpha_i = 0.68\alpha_c$ ($\Lambda \approx 10$ nm). The defect-induced DXS intensity measured along the angular direction for PAI 600 and NoPAI 600 is plotted in Fig. 5.4(a). The measurement for a non-implanted Si, dotted line, is shown as reference for the q^{-2} behaviour. The decay of the intensity as a function of $|q_a|$ follows a q^{-2} behaviour typical for HDS for $|q_a| > 0.05$ Å^{-1}. A broad intensity hump is found in the central part of the scan. In addition, the scattered intensity for the NoPAI sample is larger than for the PAI. To explain the presence of the hump, we assume a partial regrowth of the amorphous sub-surface layer by formation of crystalline "dendrites" at the a/c interface, as schematically shown in Fig. 5.4(b). The presence of these islands of nanometre size results in a form-factor-induced scattering contribution close to the Bragg peaks [2.7]. The intensity hump was fitted using a Gaussian curve. The width of the form factor-induced scattering measured in q-space (i.e. the FWHM of its Gaussian fit), w, was used to determine the lateral size, d, of the crystalline "dendrites" following $w = \frac{2\pi}{d}$. The solid line in Fig. 5.4(a) shows the fit to the measured intensity resulting from two contributions: form factor induced Bragg diffraction (Gaussian curve) and the HDS intensity from point-like defects. The two contributions have been added incoherently. The average diameter of the islands d is (14.5 ± 0.5) nm and (16.0 ± 0.5) nm in the non-PAI and PAI sample, respectively. The HDS stems mainly from defects located in a layer of about 10 nm (penetration of the x-rays) where a complex variety of defects are expected, such as vacancies, SiI's, As on substitutional sites, As_4V clusters (Sec. 1.2.3). Since, an overall q^{-2}-dependent DXS is found, the predominant defects are distorting the lattice only weakly.

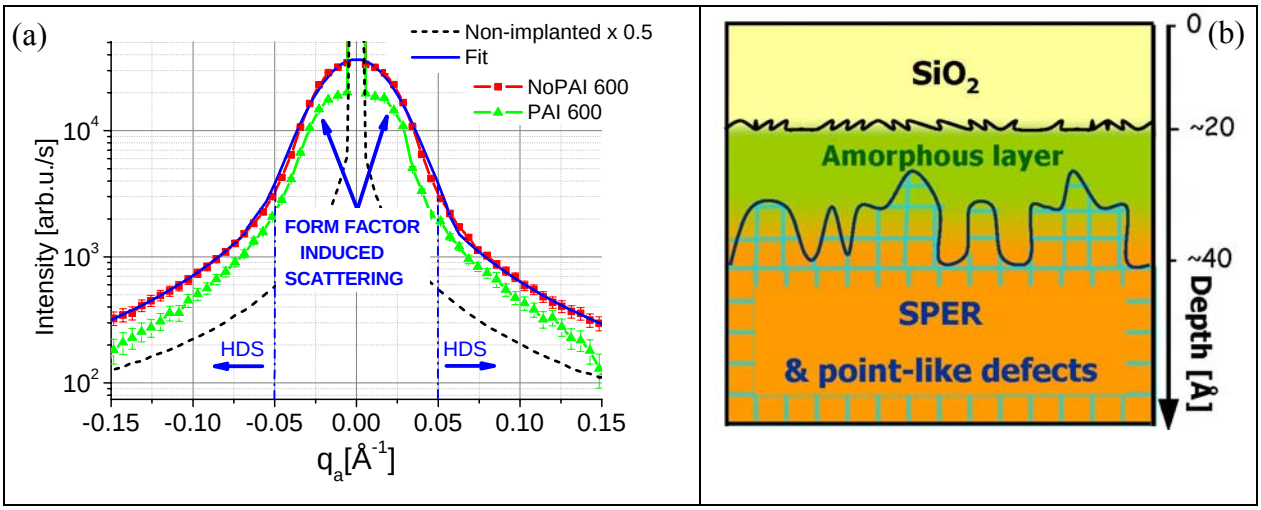

Figure 5.4: (a) q_z-integrated defect-induced DXS intensity in angular direction, q_a, through 220 at $\Lambda \approx 10$ nm for samples NoPAI 600 and PAI 600. The fit to the experimental curve from NoPAI 600 is the solid line (see details in the text). The DXS from a non-implanted sample is shown for comparison (black dashed curve). (b) Schematic sample structure showing the near-surface region of the 600°C-annealed samples with "dendritic" regrowth.

The GI-DXS measurements in the radial direction, not shown here, present an asymmetric intensity distribution with higher intensity for positive q_r values, similar to the curve shown in Fig. 3.11(d). Therefore, the defects are expanding the Si lattice. In the NoPAI 600 sample, the HDS is higher than for the PAI because the EOR defects (located at a depth of ~11 nm) contribute to the HDS as they are still detected by the evanescent x-ray wave (see Sec. 4.4 for Epi 700). In contrast, for the PAI 600 sample, the EOR defects are located far beyond the x-ray penetration depth at ~ 100 nm, thus not contributing to the HDS.

The GI-DXS data from the spike-annealed samples show a very weak HDS, which is close to the detection limit, for both the PAI and NoPAI wafers (not shown here). This evidence confirms that the high temperature spike-anneal succeeds in inducing nearly perfect recrystallisation of Si, as prescribed for a high electrical performance of the final device. The asymmetric component of the defect-induced DXS is higher for positive q_r, indicating lattice expanding defects. For the NoPAI sample, such asymmetric contribution can originate from some residual EOR defects. For PAI spike, the influence of the EOR defects can be excluded, due to the deep location of this defect band (~ 100 nm).

When a probed depth of $\Lambda \sim 10$ nm is used, the USJ region is illuminated, where the main defect expected is the electrically active substitutional As. Therefore, the PAI spike sample, which has the highest substitutional fraction of As (~ 65% of the implanted dose) and no EOR defects in this depth range, is ideally suited to investigate the distortion field $\boldsymbol{u}(\boldsymbol{r})$ induced by this defect. However, experimentally only a very weak signal from point defects expanding the lattice is found, which is ascribed to the defects in the a/c interface. The DXS signal from the substitutional As cannot be detected. This is explained exploiting the results

from the XRD characterisation of As-implanted samples. It is known [4.1], that As atoms induce a hydrostatic contraction of the Si lattice by affecting the electronic band structure. As a result the average displacement field $\langle \boldsymbol{u}(\boldsymbol{r}) \rangle$ is $\langle \boldsymbol{u}(\boldsymbol{r}) \rangle \propto \Delta a/a < 0$, as observed from the $\Delta a/a$ profile of PAI 600 and discussed in Sec. 4.2 for the Epi sample series. This contraction of the average lattice parameter does not affect the local order of the SPER layer, where the static Debye-Waller factor is always $L_h = 0$. Therefore, the presence of substitutional As does not originate deviations from the average contracted lattice, i.e. $\delta \boldsymbol{u}(\boldsymbol{r}) \approx 0$. In As-implanted Si, the average contraction of the lattice parameter is observed only in the SPER direction, because the lateral lattice parameter of the implanted layer is pseudomorphically strained (Sec. 3.3.3). Therefore, the average defect-induced distortion field in the lateral direction is $<\boldsymbol{u}(\boldsymbol{r})_{//}> = 0$. For substitutional As, the deviations from $<\boldsymbol{u}(\boldsymbol{r})_{//}>$, $\delta \boldsymbol{u}(\boldsymbol{r})_{//} = 0$ and, as a consequence, this crystalline defect does not give rise to DXS intensity, because $I_{HDS} \propto \left(\delta \boldsymbol{u}(\boldsymbol{r})\right)^2 \approx 0$. This justify that the measured HDS at $\Lambda \approx 10$ nm is ascribed to defects trapped in the thin a/c interface for completely regrown samples containing electrically activated As. In the interface layer, we expect to find SiI's and inactive As atoms. For the latter, the size-effect is predominant, resulting in an expansion of the lattice, as discussed in Sec. 4.2.

Both the as-implanted samples were not measured using $\Lambda \approx 10$ nm, because, for the GI-DXS measurements, crystalline samples are needed (Sec. 4.6).

5.4 Defects in the EOR damage region: GI-DXS at $\alpha_i > \alpha_c$

By increasing the incident angle α_i to $1.32\alpha_c$, the scattering depth is set to $\Lambda \approx 400$ nm. In this experimental condition, the x-ray beam reaches the EOR damage layer and GI-DXS technique can be used to study the evolution of the SiI's present in this region. The characteristics of the EOR defects have been discussed in Sec. 1.2.4.

The I_{sym}, symmetric component of defect-induced DXS, is evaluated for the two sample series as a function of q and shown in Fig. 5.5(a). The I_{sym} from sample NoPAI as-implanted decays with q^{-2} typical for the HDS from point defects located in the EOR damage region, most likely di-interstitials [1.52]. The PAI as-implanted sample was not measured because a 100 nm-thick amorphous cover layer.

The 600 °C-annealed samples shows a q^{-2} decay of I_{sym} for $q > 0.09$ Å^{-1}, which is attributed to the presence of small "magic" clusters [1.47] that have formed during the regrowth. The increase of intensity for q smaller than 0.09 Å^{-1} is caused by the presence of the

crystalline "dendrites" at the amorphous to crystalline interface, as explained in the previous section. The I_{sym} for sample PAI and NoPAI 600 is reduced by a factor of 2 as compared to NoPAI as-implanted indicating a partial annihilation of the defects. Note that an intensity offset of one decade is applied in the figure. The DXS from the two 600 °C samples shows the same intensity except for the q-range from 0.08 to 0.22 Å^{-1}, where the intensity for PAI 600 is higher. The additional scattering contribution on the PAI 600 is explained by the analysis of the corresponding intensity distribution along q_z, as discussed later in this section.

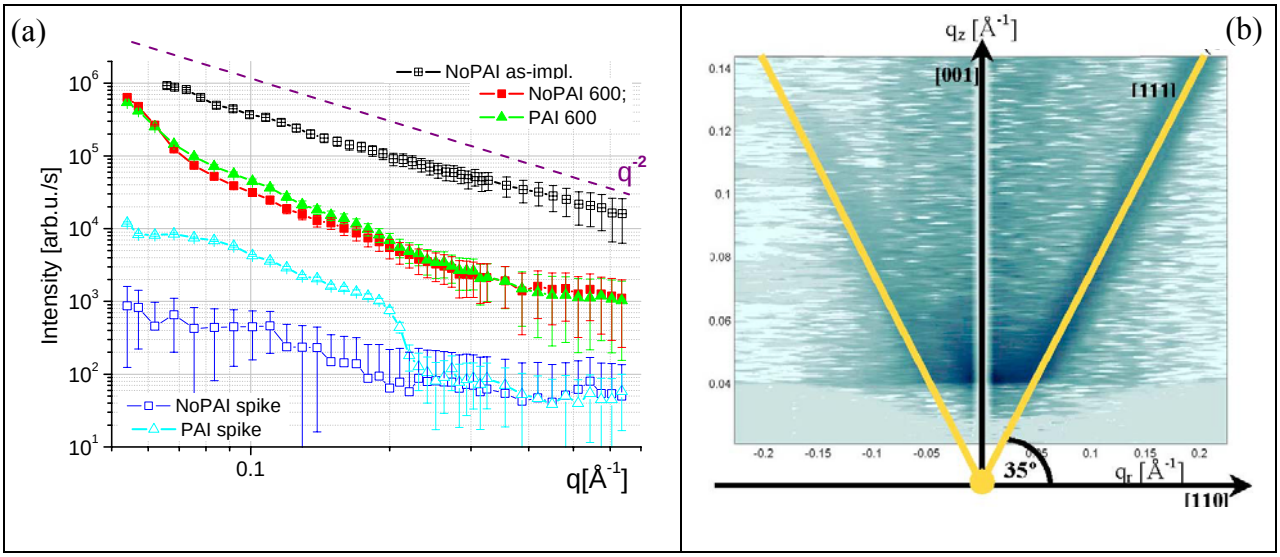

Figure 5.5: (a): Symmetric part of the diffuse intensity in radial direction through 220 at $\alpha_i = 1.32\alpha_c$. The dashed line indicates the q^{-2} decay expected for the HDS. An intensity offset was applied for the signal from the different annealing treatments. (b): Reciprocal space map of defect-induced DXS intensity in the q_r-q_z plane close to the 220 Bragg reflection for sample PAI spike. The intensity streak points in the [111] direction with an angle of 35 deg with respect to the radial direction [110] (note the different scales for q_z and q_r).

For the spike-annealed samples, a strong reduction of the DXS intensity, I_{sym}(NoPAI spike) ≈ 10% I_{sym}(NoPAI as-impl.), indicates the annihilation of the defects. For PAI spike, the main feature is the presence of an intensity hump located in the q-range between 0.04 to 0.22 Å^{-1}. The origin of this hump is understood from the reciprocal space map in the q_r-q_z plane reported in Fig. 5.5(b). The hump-effect in the integrated intensity is due to the presence of DXS intensity streaks along the [111] directions, with an inclination of 35 deg with respect to q_r // [110] direction. As discussed in Sec. 2.1.3 and references therein, these diffuse intensity streaks are typical for extrinsic stacking faults (SF's) and proves that SiI's in the EOR region have aggregated to form FDL's.

Depth-resolved information on the defect structure is obtained from the DXS distribution as a function of q_z. The "q_z-slices" acquired at $q_r = 0.14$ Å^{-1} for the whole sample set are reported in Fig. 5.6. Comparing the two 600 °C-annealed samples (Fig 5.6(b)), the q_z slices of the DXS show a different intensity distribution along q_z. For the NoPAI 600 only, a

peak at $q_{z,critical}$ = (0.039 ± 0.001) Å^{-1} is found, indicating that the EOR defects are located in a layer close to the surface and the DXS is enhanced by the peak in the transmission function. The same behaviour has been reported for the Epi sample series in Sec. 4.4. For the PAI sample, this intensity enhancement at $q_{z,critical}$ is missing and the broad intensity distribution along α_f is dominated by the increase of the penetration depth with q_z. The x-rays first have to pass through the weakly scattering SPER region, before the EOR defects are reached and contribute significantly to the DXS.

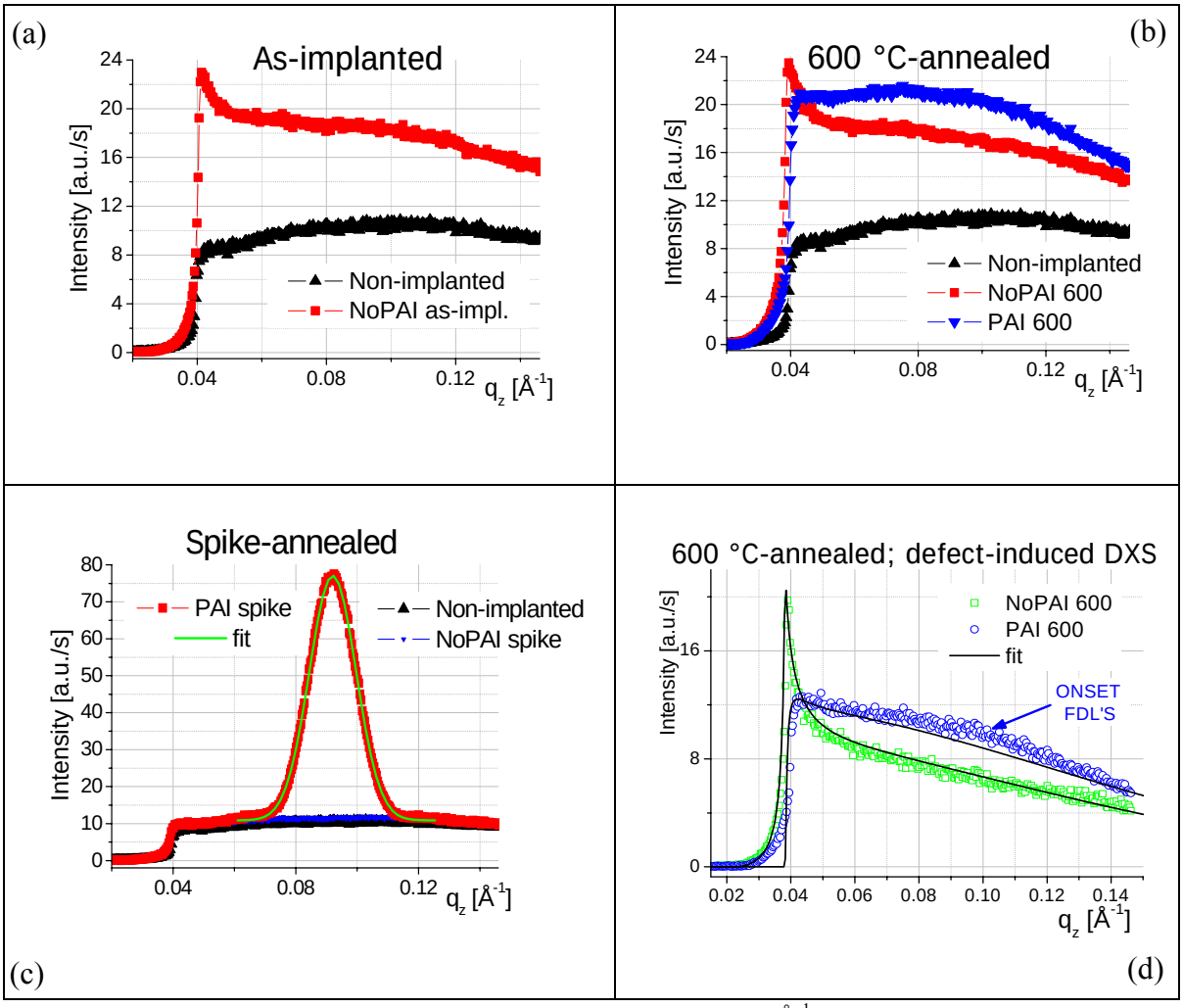

Figure 5.6: Diffuse intensity distribution along q_z measured at q_r = 0.14 Å^{-1} $\alpha_i = 1.32\alpha_c$ for non-implanted Si in comparison with NoPAI as-implanted (a), 600°C-annealed samples (b), spike annealed samples (c).(d): Simulation of the defect-induced DXS for the 600°C-annealed samples.

The defect-induced DXS from PAI 600 and NoPAI 600 has been simulated using the code from V. Holý, described in Sec. 3.2.3, and the fits are shown in the part (d) of the figure together with the measured data. The simulations has been obtained using the same parameters that characterise the defects, namely, an inclusion radius R_z = (15 ± 5) Å and lattice mismatch δ = (1.0 ± 0.5) x10^{-4} (Sec. 3.2.3). The two simulations differ in the depth of

the density maximum: z_{max}= (125 ±10) Å, for NoPAI 600, and z_{max} = (1000 ± 200) Å, for PAI 600. In addition, for PAI 600, a broad hump-like DXS distribution is observed in the range from q_z = 0.065 to 0.125 Å^{-1} indicating the onset of FDL's formation (Sec. 2.1.3). The DXS distribution along q_z measured for sample NoPAI as-implanted, Fig. 5.6(a), shows similar features to sample NoPAI 600, Fig. 5.6(b), because the two samples have the same depth distribution of interstitial type defects, which are located below the original amorphous to crystalline interface present after the implantation (~125 Å).

In the intensity distribution for the PAI spike, the presence of an intensity hump centred at 0.09 Å^{-1} dominates the DXS in the q_z-slice, Fig. 5.6(c). It is a section of the intensity streak shown in Fig. 5.5(b) and caused by FDL-induced DXS. The hump is fitted using a Gaussian curve to derive quantitative information on the FDL's. The area below the fit curve is a measure of the relative number of SiI's forming the SF. The Gaussian FWHM gives the diameter of the SF, d_{SF} according to $d_{SF} = 2\pi/(\Delta q_z \cos 35\,\mathrm{deg})$. The diameter of the SF is found as (505 ± 5) Å for the PAI spike. For q_z values outside the SF-induced hump, the DXS intensity is comparable with the non-implanted sample. This is the evidence that all excess SiI's are aggregated into extended defects. A complete study of the formation of FDL's in the PAI series during isothermal annealing at 900 °C will be reported in Ch. 6. For the NoPAI spike sample, the DXS intensity in the q_z-slice, Fig. 5.6(c), is the same as for the non-implanted Si. The excess SiI's are annihilated by diffusion to the surface and no FDL's are formed.

The "excess interstitial" model, discussed in Sec. 1.2.4, can be used to describe the evolution of EOR damage during annealing. For high-energy implants, the defects are far from the surface, which then does not act as a sink for the excess interstitials. In this case, the total number of excess SiI's in the EOR region remains constant during the annealing. The defects transform and grow by conservative Ostwald ripening according to the calculated energy of formation for the different defect configurations as a function of the number of aggregated SiI's (see Fig. 1.16). First, they form small "magic clusters" of 4 and 8 atoms, then {113}-defects, faulted dislocation loops until the most stable form, the perfect dislocation loops, is reached. The rate of the evolution and the relative fraction of defect types depend on the implant and annealing conditions.

In the PAI sample series, the EOR defects are deeply buried after the Xe implantation at 130 keV. Following the TRIM calculation [1.12] and the determination of the a/c interface via TEM (see Fig. 5.9(a)), the SiI's supersaturation in the EOR damage region is calculated according to the "excess interstitial" model (Sec. 1.2.4) in S_{EOR} ~ 1.5x10^{15}cm^{-2} with an

accuracy of ~20%. S_{EOR} distributes over a range of 45 nm starting from ~100 nm. The surface is far from the EOR defects, i.e. the SiI supersaturation at the surface is $S_0 \approx 1$, following the formalism from Sec. 1.2.4.3. Therefore, the SiI supersaturation in the EOR damage region S_{EOR} evolves with an Ostwald ripening mechanism. For the PAI spike sample, the EOR damage consists of 50 nm-diameter FDL's, as a consequence of the high thermal budget. The density of SiI's in a FDL is ρ = 15.66 nm^{-2} (Sec. 1.2.4.2). As a result, the FDL's of the PAI spike sample contain n = (307 ± 6) x10^2 SiI's atoms. For 4x10^4 < n < 10^5, the FDL is the most stable configuration for the excess SiI-based defects. This result from the GI-DXS is in agreement with the outcome from the calculations of the formation energy for EOR defects in Si, shown in Fig. 1.16. Sample PAI 600 represents an intermediate step in the growth process of EOR defects. Therefore, diffuse intensity from "magic clusters" and the onset of FDL's formation are measured simultaneously from GI-DXS close to the 220 Bragg peak.

With decreasing implantation energy, the EOR defects are expected in a region closer to the surface. For shallow implants, the surface proximity affects the evolution of the EOR damage during annealing. The surface, acting as strong sink for the excess SiI's, competes with the formation of extended defects during Ostwald ripening. The growth of more stable extended defects is no longer the favourite path for energy minimisation in the EOR region. Due to the surface proximity, the maximum size the defects can reach before dissolution reduces as the implant energy decreases. The surface traps the free SiI's at the very beginning of the clusters growth, which explains that no extended defects are expected in the EOR region for low energy implants.

For the NoPAI sample series, the supersaturation of SiI's in the EOR defects, S_{EOR} , was calculated according to the "Si interstitial model" by combining the information obtained from TRIM (Fig. 1.6) with the thickness of the amorphised layer from MEIS. The result is S_{EOR} ~ 1x10^{15} cm^{-2} distributing over a range of 4.5 nm from a depth ~11 nm. Due to the surface proximity, no formation of extended defects was observed in the EOR region. After the 600°C treatment only point defects, like "magic clusters", are observed, while after spike annealing nearly no defects are left and in particular no FDL's are present.

As shown in Eq. (1.13), the flux of SiI's atoms towards the surface is $J_{surf} \propto D_i C_i^*$, where $D_i C_i^*$ is the product of the diffusion coefficient with the equilibrium concentration of SiI's and can be calculated using Eq. (5.1) from [1.67].

$$D_i C_i^* = 2 * 10^{24} \exp\left(\frac{-4.52}{kT}\right) \text{cm}^{-1}\text{s}^{-1}, \tag{5.1}$$

with k = 8.6173x10^{-5} eV/K, the Boltzman's constant. As a result, the number of SiI's that recombine at the surface, n_{surf}, can be compared between NoPAI spike and NoPAI 600.

$\frac{n_{surf}(spike)}{n_{surf}(600)} = \frac{D_i C_i^*(spike) t_{spike}}{D_i C_i^*(600) t_{600}} \approx 10^8$, where t is the annealing time.

It is clear that after the high thermal budget of the spike annealing process nearly no residual defects are detected by GI-DXS.

The limiting parameter of the application of the "excess interstitial" model to the GI-DXS data analysis is that the gradient of the SiI's supersaturation between the EOR defects region and the surface cannot be calculated. Recently, Lamrani *et al.* measured the gradient of the SiI's supersaturation between the EOR defects region and the surface by a combined SIMS and TEM analysis [5.2]. They provided the first experimental evidence of the role of the surface in the SiI's recombination process and indicated an upper depth limit for the surface recombination of SiI's of about 200 nm for annealing at 850 °C. In conclusion, all the results from the defect characterisation in the PAI *vs.* NoPAI sample series are in agreement with the "excess interstitial" model.

5.5 Comparison with MEIS

The results from the x-ray scattering experiments were compared with those from the MEIS obtained on the same samples to achieve a detailed and comprehensive picture of the reordering processes occurring by combining the capabilities of the different techniques.

5.5.1 Results from MEIS

The MEIS measurements were performed using the same experimental condition discussed in Ch. 4 for the Epi sample series. The details on the MEIS experiment conditions and analysis are found in Ref. [4.3].

MEIS energy spectra for both PAI and NoPAI sample series are shown in Fig. 5.7. A spectrum from a virgin Si sample and a spectrum taken from an amorphous Si sample are plotted as references. The measured energy spectra have been converted into depth profiles using a standard procedure described in [4.3] and applying the stopping powers from TRIM 2003 [1.12]. The resulting depth profiles are plotted in Fig. 5.8(a) and (b) for As and Si, respectively.

Figure 5.8(b) shows that the 3 keV As implant produces a ~11 nm deep amorphous layer, as evidenced by the extra Si scattering yield behind the surface peak that reaches the

random level and extends to a depth of 11 nm (half height). The depth profiles of the As implantation for the PAI and NoPAI implants are in close agreement. This is expected since Si is amorphised after a As dose of 10^{14} cm^{-2} [5.3]. MEIS shows that the peak of the As distribution is at 6.3 nm depth, in close agreement with TRIM calculations (results not shown). Following a 600 °C, 20 min annealing, the amorphous layer has recrystallised by SPER. The regrowth is not perfect, leaving a surface damage peak of larger width (5 nm) than the surface peak of the virgin sample (2.5 nm) and larger height.

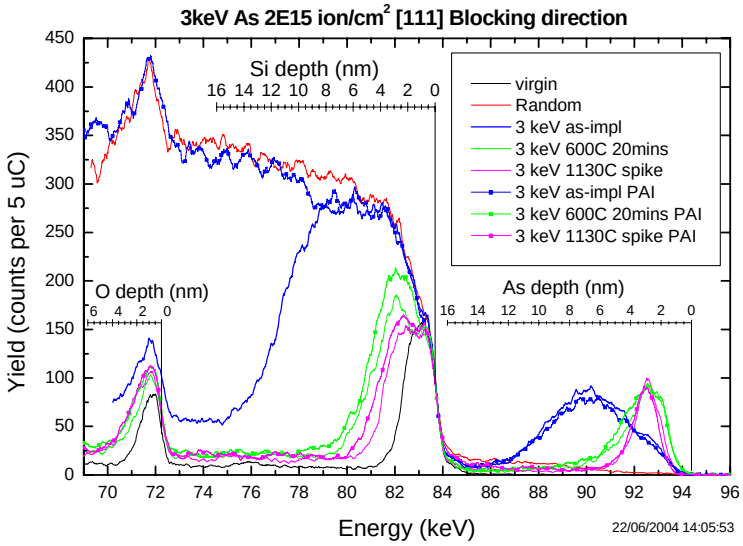

Figure 5.7: MEIS spectra collected along the [111] blocking direction for all the annealed samples. The non implanted Si sample and an amorphous Si spectrum are shown for comparison. Courtesy of M. Werner.

The As profile too has undergone considerable change with the corresponding signal strongly reduced in the implanted profile and the appearance of a very narrow, segregated As peak at a depth of 3 nm.

The former is due to As taking up substitutional positions within the regrown Si, where it is no longer visible to the beam. The latter is due to the As that is "snowploughed" ahead of the advancing a/c interface and forms the narrow segregated surface peak. The integration of the electron yield of the peak and its subsequent calibration shows that ~ 40 - 46 % of the dopant is no longer visible to the beam. From previous SIMS studies it is known that no As has been lost from the matrix [5.4].

The spike annealing to 1130 °C produces more perfect regrowth. The segregated As peak is sharper and the surface damage layer for this anneal condition is reduced to ~ 4 nm. The latter includes a substantial component from the silicon in the oxide layer, which has

grown in thickness to ~ 3 nm as a result of the spike RTA. The anneal conditions also affect the percentage of the dopant atoms taking up substitutional positions. The 1130 °C spike anneal produces the highest substitutional fraction with ~ 60 % of the implanted ions taking up substitutional lattice positions.

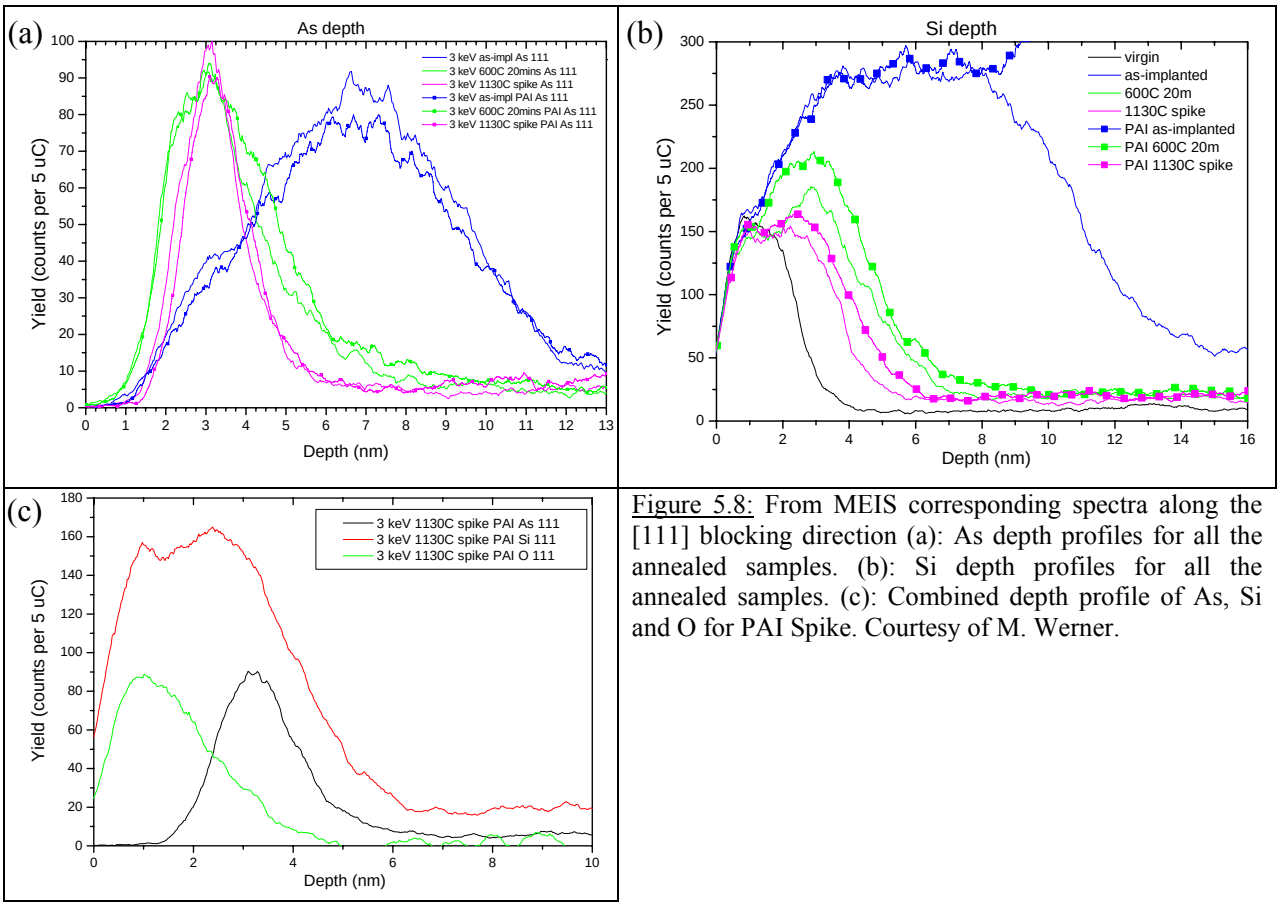

Figure 5.8: From MEIS corresponding spectra along the [111] blocking direction (a): As depth profiles for all the annealed samples. (b): Si depth profiles for all the annealed samples. (c): Combined depth profile of As, Si and O for PAI Spike. Courtesy of M. Werner.

A comparison of MEIS spectra for implants in the PAI samples with the NoPAI samples shows the general annealing behaviour remains similar for both. However, the PAI samples show a higher amount of residual damage after annealing, as evidenced by the higher background level, caused by dechannelled particles. Marginally thicker oxide layers for the PAI As implant are also observed.

The precise nature of the interaction between the oxide layer and the segregated As layer is more clearly visualised by overlaying the As and O depth profiles with the dechanneling background removed under the O peak, Fig. 5.8(c). Although the effects of energy resolution and straggling broaden the peaks it is clear that the segregated As is situated under the oxide. The down slope of the oxide peak indicates the existence of suboxides, as discussed in [5.5]. The Si depth profile extends over the range of the O and the As peaks, as

shown in the figure, further demonstrating that disordered Si is present in both the oxide and segregated As regions.

5.5.2 Comparison with x-ray experiments

The layered structure of Si after implantation has been investigated by XRD and SR. In the case of the PAI sample series (see Fig. 5.1), the fit to the SR curves shows a SiO_2 layer growing in thickness with increasing thermal budget and the formation of an As rich layer underneath. MEIS is depth and element sensitive. From the MEIS results, the As segregated layer is found to be below the oxide layer. This information has to be used in the modelling of the SR curves because the sequence of the different layers in the stack is not unique in SR, due to the well known "phase problem" in x-ray scattering. Table 5.2 shows the layer thicknesses from the PAI sample series obtained combining the MEIS and the SR results. For SR, the SiO_2 thickness is given by the period of the oscillation (see Fig. 5.1(a)) and thus can be determined with an accuracy of 0.05 nm especially for PAI 600 and PAI spike where several well-pronounced oscillations are observed. As already discussed in Sec. 5.2, the SiO_2 layer thickness increases from (14.2 ± 1) Å, for the as-implanted, to (21.7 ± 0.5) Å, for the 600°C-annealed, and to (29.8 ± 0.5) Å, for the spike-annealed sample. For MEIS, the SiO_2 thickness is derived with less accuracy (± 0.2 nm) from the half width height of the O peak. The measurements of the SiO_2 thickness are in agreement, if the corresponding accuracy is considered.

The MEIS sensitivity for As is much higher than for SR, due to its chemical selectivity. For the as-implanted sample, SR detects only the electronic density contrast arising from the SiO_2 layer. The As distribution is smeared out too much to give a significant contribution to the SR signal. MEIS, on the contrary, has enough sensitivity to detect the as-implanted As profile directly. Agreement on the As layer thickness is found for the PAI 600 sample: 2.8 nm, from the MEIS data, and 0.7 + 1.9 = 2.6 nm from SR, where both As-rich and "third layer" have to be taken into account (Fig. 5.1 (b)).

For the spike annealed sample, a significant difference between the As layer thickness for MEIS and SR is observed, thickness = 0.7 nm from SR and thickness = 1.7 nm from MEIS. Such difference can be explained considering that the MEIS values are affected by an instrumental resolution broadening (effectively around 0.8 nm) that has not been corrected for. For layers of sub-nanometre thickness, this widening of the peak may affect the measurement. Theoretical studies [5.6] suggest that the excess dopant cumulates in a layer of 1 ML ($7x10^{14}$ As atoms/cm^2) only. This is supported by the SR result for PAI spike, where

the As-rich layer formed is thinner than 1 nm. The same thickness has been observed by SR for all As implanted samples annealed at high temperature.

Table 5.2: Comparison of layer thicknesses of the PAI sample series obtained from MEIS and SR experiments.

Sample	As depth [ii] [nm]	As peak FWHM [nm]	As atoms in peak [%]	Si peak width [i] [nm]	O thickness [iii] [nm]	SiO_2 thickness; [nm]	"As-rich layer" thickness [nm]	"Third layer" thickness [nm]
Method	MEIS	MEIS	MEIS	MEIS	MEIS	SR	SR	SR
PAI as-impl	6.8	5.5	100	--	1.8	1.4	--	--
PAI 600	3.6	2.8	60	4.9	2.3	2.2	0.7	1.94
PAI spike	3.3	1.7	46	4.2	2.4	2.9	0.7	--

[i] estimated from the back edge half height.
[ii] depth of the As peak centre.
[iii] estimated from integrated area of the O peak

To conclude this section, MEIS and SR give comparable results on the near-surface layered structure of implanted Si. The two techniques are complementary with respect to their specific sensitivity. In fact, the layered element-specific sequence of the sample as obtained from MEIS is needed as a starting point for an unambiguous modelling of the SR curves. While MEIS is element specific and sensitive to disordered material, SR needs electronic density contrast between the layers, independent of the atoms being in a disordered or crystalline structure. The nature of the defects in ion implanted Si has been studied using GI-DXS which turned out to be mainly sensitive to the EOR defects. MEIS cannot detect these defects because they are located in the crystalline part of the sample and the disorder they induce is not sufficient for their detection. Therefore, no direct comparison between MEIS and GI-DXS results on extended EOR defects can be made.

5.6 Comparison with transmission electron microscopy

Transmission electron microscopy (TEM) is traditionally used for the characterisation of residual defect after ion-implantation and annealing. In this section, some TEM and HRTEM cross-section images will be discussed, which were acquired using a JEOL JEM 2010F field emission microscope at 200kV accelerating voltage, with a point resolution of 0.19 nm. The sample preparation before the analysis is needed to reduce the sample thickness to 100 nm using mechanical polishing and a precision ion polishing system. The images were carried out at the microscopy laboratory of the IMM-CNR Institute of Catania (I) by our Impulse project co-workers. The details on the realisation of the TEM experiment are reported in Ref. [5.7].

Figure 5.9 shows the TEM cross-section images for the PAI sample series. In part (a) of the figure, the as-implanted PAI sample is illustrated. The Xe PAI has amorphised the Si up to ~ 100 nm (bright area) and a band of EOR defects is observed (dark grey) below the a/c interface. Such interface is abrupt (roughness ~ 10 nm) and well defined due to the high mass of the implanted Xe atoms [1.13].

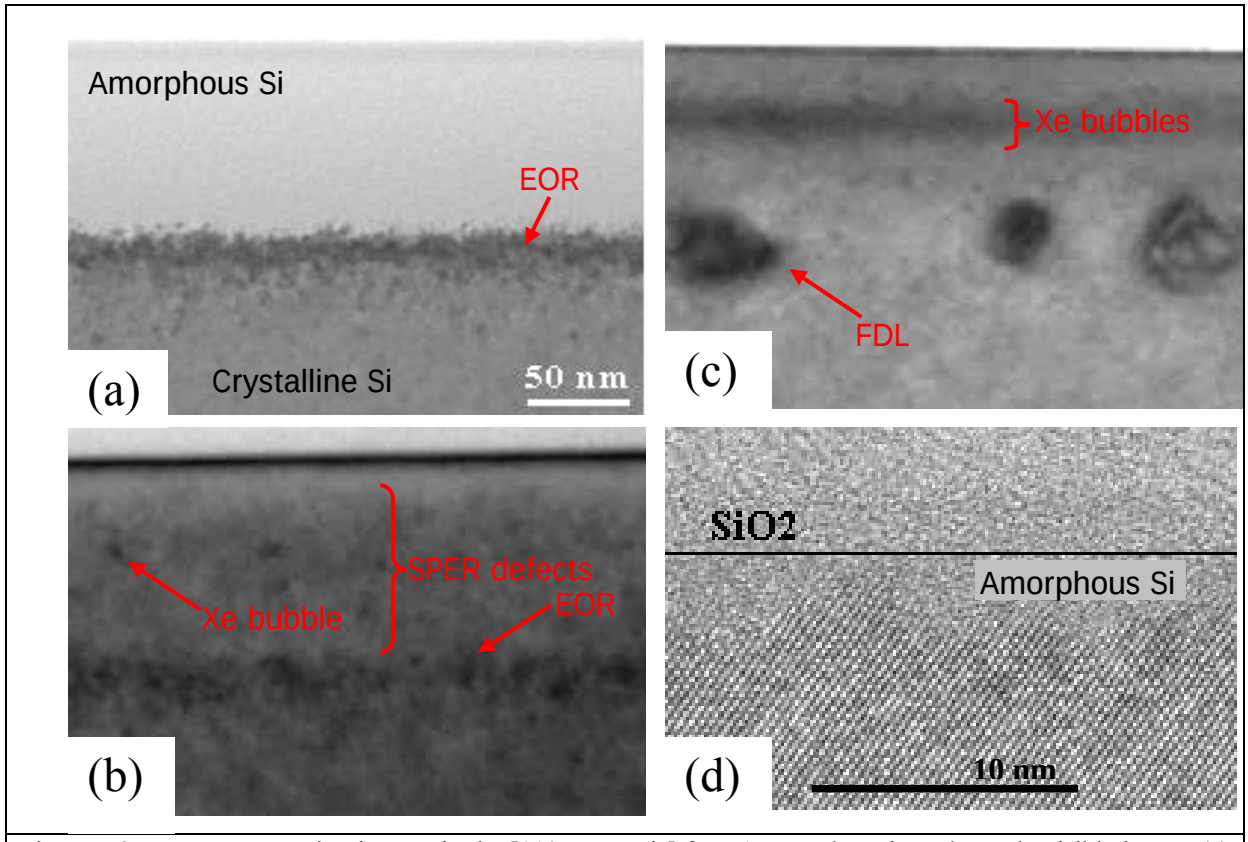

Figure 5.9: TEM cross-section images in the [110 zone axis] for PAI sample series. The scale visible in part (a) is valid for parts (b) and (c) as well. (a) PAI as-implanted; (b) PAI 600; (c) PAI spike. (d) HRTEM cross-section image of the a/c interface of PAI 600 showing the "dendritic" regrowth. Courtesy of L. Ottaviano.

The structure of the sample after the 600 °C-annealing is shown in part (b). The SPER is complete and the band of the EOR defects is visible -mainly very small defects- in a depth of about 100 nm. No FDL's are observed. In the regrown area, a small concentration of residual defects is visible uniformly distributed in the SPER layer, as indicated in the figure. The darker spots are ascribed to the formation of Xe bubbles in the depth range of ~30 nm [5.7]. The black line at the surface is induced by the tilt of the sample and it is not related to the defect structure. The structure of the PAI spike sample is shown in Fig. 5.9(c). The SPER is complete and the main feature is the formation of FDL's that appear as darker circles at the depth of the Xe EOR defects. The size of the FDL's is in the 50nm-range. The darker band at a depth of about 30 nm is again ascribed to the presence of Xe bubbles.

The structural characterisation from TEM is in agreement with the results from the GI-DXS method for the evolution and localisation in depth of the EOR damage.
The presence of Xe bubbles has not been detected using the combined x-ray scattering method [a].

Figure 5.9(d) is a HRTEM image from the a/c interface region of sample PAI 600. The crystalline region can be recognised by the ordered structure of the pattern, whereas the amorphous one, in the upper part of the figure, appear more randomly organised. At the interface between the crystalline and amorphous phases, the presence of crystalline "dendrites" is observed, which show a maximum thickness of about 3 nm and a maximum width of about 6 nm. Therefore, the TEM characterisation corroborates the presence of a "dendritic" regrowth at the interface for PAI 600, as detected by GI-DXS. Using the GI-DXS method, only the lateral properties of such "dendrites" can be investigated. It has been shown in Sec. 5.3, that the average dendrite lateral size is (16.0 ± 0.5) nm, which is about two times the size measured by TEM. This can be explained by considering the smaller area investigated by TEM, 0.04 μm^2 *vs.* ~ 1 mm^2 investigated by GI-DXS. In addition, atomic force microscopy measurements performed in the surface characterisation laboratory of the ESRF (not reported here) have shown that the density of the "dendrites", visible also at the surface, is non-uniform on the implanted sample.

The XRD technique has been used to investigate the lattice strain in the SPER direction. The measurements for PAI 600 and NoPAI 600, where the "dendrites" have been detected by GI-DXS, have been shown in Fig. 5.3. In particular, the results from the simulation of the XRD measurement for NoPAI 600 are shown in Fig. 5.3(c). No direct information of the average vertical size of the "dendrites" is obtained from the XRD data. However, when the results from NoPAI 600 are compared with the ones for Epi 600, annealed at the same temperature, but for a shorter time (20 s), a remarkably higher value for the lattice distortion $\Delta a/a$ is obtained for the interface layer of NoPAI 600. $\Delta a/a = 6.0 \times 10^{-3}$, for NoPAI 600, and $\Delta a/a = 0.8 \times 10^{-3}$, for Epi 600. The corresponding values of the static Debye-Waller factor L_h are $L_h = 0.97$ and $L_h = 0.88$, for NoPAI 600 and Epi 600, respectively. The presence of the "dendrites" at the a/c interface increases the strain and the disorder in the interface layer, where the layer-by-layer regrowth is of poorer quality. In conclusion, a good agreement is found between x-ray techniques and TEM imaging on the PAI sample series.

[a] A grazing incidence small angle scattering experiment was performed to investigate the Xe bubbles, but the structural contrast they induce was not sufficient for their detection.

TEM is mostly used to study the evolution of extended EOR defects in Si, because of their well-defined crystallographic properties and size suited for TEM. This technique presents advantages and disadvantages with respect to GI-DXS.

The major drawback of the TEM is the long and destructive sample preparation, which is not needed for the x-ray methods. The evaluation of the defect structure (i.e. defect size and density) by TEM is straightforward, even if based on a poor statistics. Only the defects present in the very small probed area (~1.5 μm^2) are studied. For GI-DXS, the illuminated area is larger (~1mm^2) and the properties of a statistical ensemble of defects are investigated. The TEM sensitivity is higher than for GI-DXS. The lowest defect density detectable by TEM is of ~ 10^8 defects/cm^2, but limited to extended defects. Complementarily, GI-DXS is able to detect also point defects. The detection limit of the GI-DXS technique depends on the strain induced by each particular type of defect and, thus, it can vary on a wide range. GI-DXS is not destructive and this is another big advantage in the use of this technique. On the other hand, its main drawback with respect to the TEM technique is the lack of an absolute scale for the DXS intensity, which impedes the evaluation of the absolute defect density.

5.7 Conclusions

In this section, the results from the structural characterisation on the PAI and NoPAI sample series have been reported and a further understanding of the influence of the PAI process on the final structure of the implanted Si has been gained. The layered structure of the samples was studied by SR and XRD. Experimental evidences were found for the segregation of As dopant atoms below the oxide layer located at the surface and for the presence of strained Si regions, especially in the EOR damage area. For PAI 600 and NoPAI 600, the presence of "dendritic" regrowth was found at the a/c interface.

The GI-DXS technique showed to be particularly well suited for the characterisation of the evolution of the defects in the EOR damage region upon annealing. For the PAI spike sample, the formation of FDL's was observed and their size quantified. On the contrary, the formation of extended defects was not observed for the NoPAI series, where the surface acts as a strong sink for the excess SiI's present in the EOR area.

In the near surface SPER region, several defect types are present and their individual fetures cannot be distinguished. It has been shown that As atoms on substitutional sites do not give rise to DXS contribution, because they create no deviations from the average lattice.

The current industrial process (by AMD) for the fabrication of n-type drain extension channel junctions (DECJ) uses pre-amorphisation and spike annealing processing. The corresponding "PAI Spike" sample was investigated in detail. It was shown that the influence of the EOR defects on the ultra-shallow junction (USJ) structure can be excluded, due to the deep location of this defect band (~ 100 nm). In the USJ region (depth < 30 nm), nearly no residual defects were observed, confirming the high crystalline quality of the solid phase epitaxial regrowth.

The results from the x-ray investigation were compared with MEIS and TEM findings, showing an agreement within the error bars. TEM and GI-DXS only are sensitive to the EOR defects. They provide complementary information, making the combination of them both the most powerful tool for defect characterisation [2.24].

Based on the results from the characterisation of the PAI *vs.* NoPAI test samples, the main topic reported in the next chapters will be the investigation of the defects present in the EOR damage region using the GI-DXS method.

6. Evolution of the structural properties during isothermal annealing

6.1 Motivation and sample preparation

Once established the sensitivity and strengths of the combined x-ray scattering methods, namely GI-DXS, XRD and SR, the structural properties of a PAI sample series during isothermal annealing were studied to investigate and model their evolution.

Cz p-type (001) Si wafers were cleaned from native oxide and preamorphized using a Xe implant at 130 keV with a dose of $2x10^{14}$ cm^{-2}. Subsequently, As^+ ions were implanted at 3 keV to a dose of $2x10^{15}$ cm^{-2}. The implantation conditions are the same as for the PAI sample series, described in Ch. 5. Afterwards, rapid thermal annealing (RTA) was performed at 900 ºC using an atmosphere of 95% N_2 and 5% O_2 at AMD, Dresden (D). The samples were prepared in order to be completely regrown and with the "double-structure" composed by implanted and non-implanted areas. The industrial processing equipment by AMD was used for the samples preparation, as described in Sec. 5.1 for the PAI sample series. A series of five wafers were annealed for 5, 10, 20, 40 and 80 seconds, respectively, as summarised in Table 6.1.

Table 6.1: Samples characterised using GI-DXS, XRD and SR techniques. A PAI treatment was performed with Xe ions at 130 keV to a dose of $2x10^{14}$ cm^{-2} followed by an As ions implantation to a dose of $2x10^{15}$ cm^{-2} at 3 keV. The samples were annealed using the conditions in the Table. RTA means Rapid Thermal Annealing.

Sample	Annealing conditions
5S	RTA 900°C, 5s
10S	RTA 900°C, 10s
20S	RTA 900°C, 20s
40S	RTA 900°C, 40s
80S	RTA 900°C, 80s

The samples will be referred to as 5S, 10S, 20S, 40S and 80S or 900 sample series.

6.2 As segregation and SiO_2 growth by SR

SR measurements were performed to study the evolution of the amorphous layers that occupies the surface of the Si wafers after implantation and annealing. Figure 6.1 shows the curves measured for the 900 sample series along with the corresponding SR simulations performed using the Parrat formalism [3.1]. The main feature is the presence of an oscillation,

the period of which shortens with the annealing time. Such oscillation is ascribed to the interference between the electronic density of the SiO_2 and the As-rich layer. The results from the simulations are plotted in Fig. 6.2(a). The electronic density profile consists of two layers on the Si substrate: the oxide layer and the As-rich layer. The thickness of the As-rich layer is constant at (8 ± 2) Å and its density is ~0.76 $Å^{-3}$. The SiO_2 layer is growing with the annealing time from (27.3 ± 0.5) Å, for 5S, to (37.5 ± 0.5) Å, for 80S. The oxide thickness increases as $\sqrt{t}$, where t is the annealing time. Following the random walk model for diffusion [6.1], the mean path $\langle x(t) \rangle$ of a particle, whose probability of moving is isotropic with respect to the direction of the movement x, is given by Eq. (6.1).

$$\langle x(t) \rangle = \sqrt{\frac{t}{\tau}}(\Delta s) \tag{6.1}$$

where τ is the time needed to perform a single diffusion step and Δs is the step length.

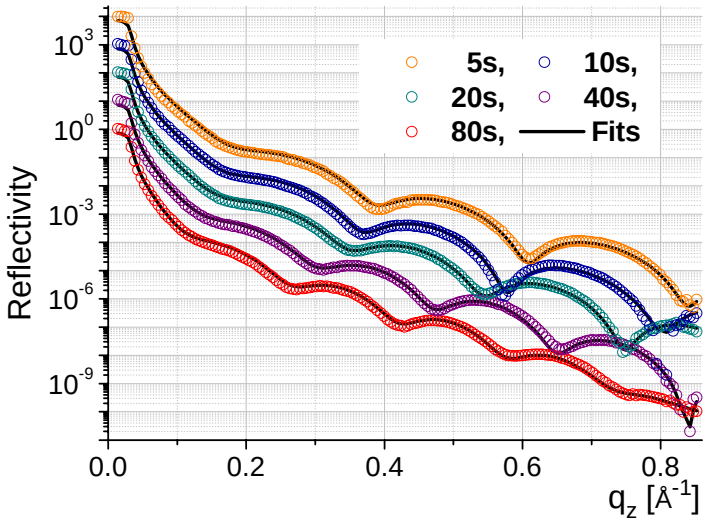

Figure 6.1: 900 sample series. Specular reflectivity curves measured at 8 keV. An intensity offset is applied for better visualisation.

Therefore, the oxide growth is diffusion limited. The oxygen, which is present in the annealing ambient, penetrates through the surface and diffuses through the already grown oxide. It reacts to form fresh SiO_2 at the interface with the As segregated layer, which results in a shift of the latter to greater depth upon annealing. The source for Si atoms is constituted by the disordered Si present in the high-density layer and by the flux of SiI's towards the surface-sink. This growth mechanism is known to affect the oxide stoichiometry with formation of suboxides [5.5]. In the assumption of a fixed absolute position of the surface, the segregated As layer would be shifted to greater depth by the oxide growth. This mechanism for the oxide growth is less

probable, because it would imply the movement of a high concentration of As towards a Si region, in which this element is already present in concentrations above its solid solubility limit. However, SR cannot give a final answer to this question, because the depth of the layers is measured with respect to the sample surface.

The XRD measurements were performed on the 900 sample series (not shown here). As expected from the high-energy of the Xe PAI, the oscillations fringes were not visible due to the deep location of the EOR damage. Only an asymmetry of the intensity distribution with respect to the Bragg peak was observed. This asymmetry presents the same features as those discussed for the sample PAI 600 in Sec. 5.2. No change of the XRD curves is observed upon annealing. Due to the lack of structured intensity distribution, no XRD simulation has been possible for these samples.

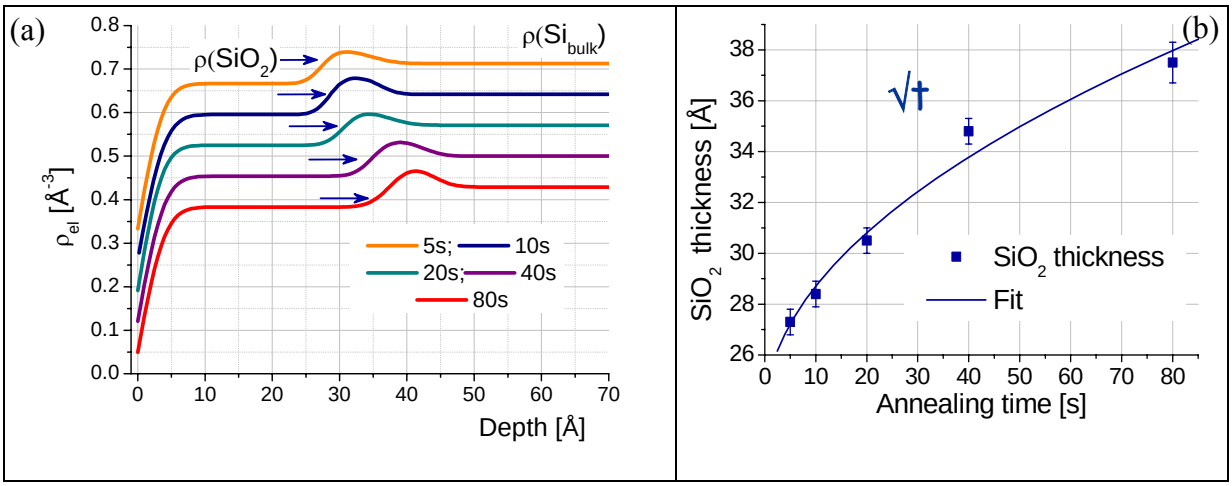

Figure 6.2: 900 sample series.(a) Depth profile of the electronic density. An intensity offset is applied for better visualisation. (b) SiO_2 thickness as a function of the annealing time.

6.3 Point and extended defects monitored by GI-DXS

The characterisation of the EOR defects for the 900 series was performed using GI-DXS technique with a probed depth of $\Lambda \sim$ 400nm. The study reported in this section has been published in Ref. [6.2].

The reciprocal space map of the defect-induced DXS in the q_z-q_r plane close to the 220 Bragg reflection is shown in Fig. 6.3(a) and (b), for sample 5S and 80S, respectively. In the insets, the intensity distribution along q_z at $q_r = 0.14$ Å^{-1} is displayed, both for the implanted and the virgin part of the sample. In the main panel of Fig. 6.3, we observe that the most remarkable change of the DXS distribution in reciprocal space after annealing is the appearance of an intensity streak oriented in the [111] direction for 80S sample, emphasised by a yellow line in the

figure. The analysis of the DXS distribution along q_z at a fixed q_r enables a deeper understanding of the features of the defect structure.

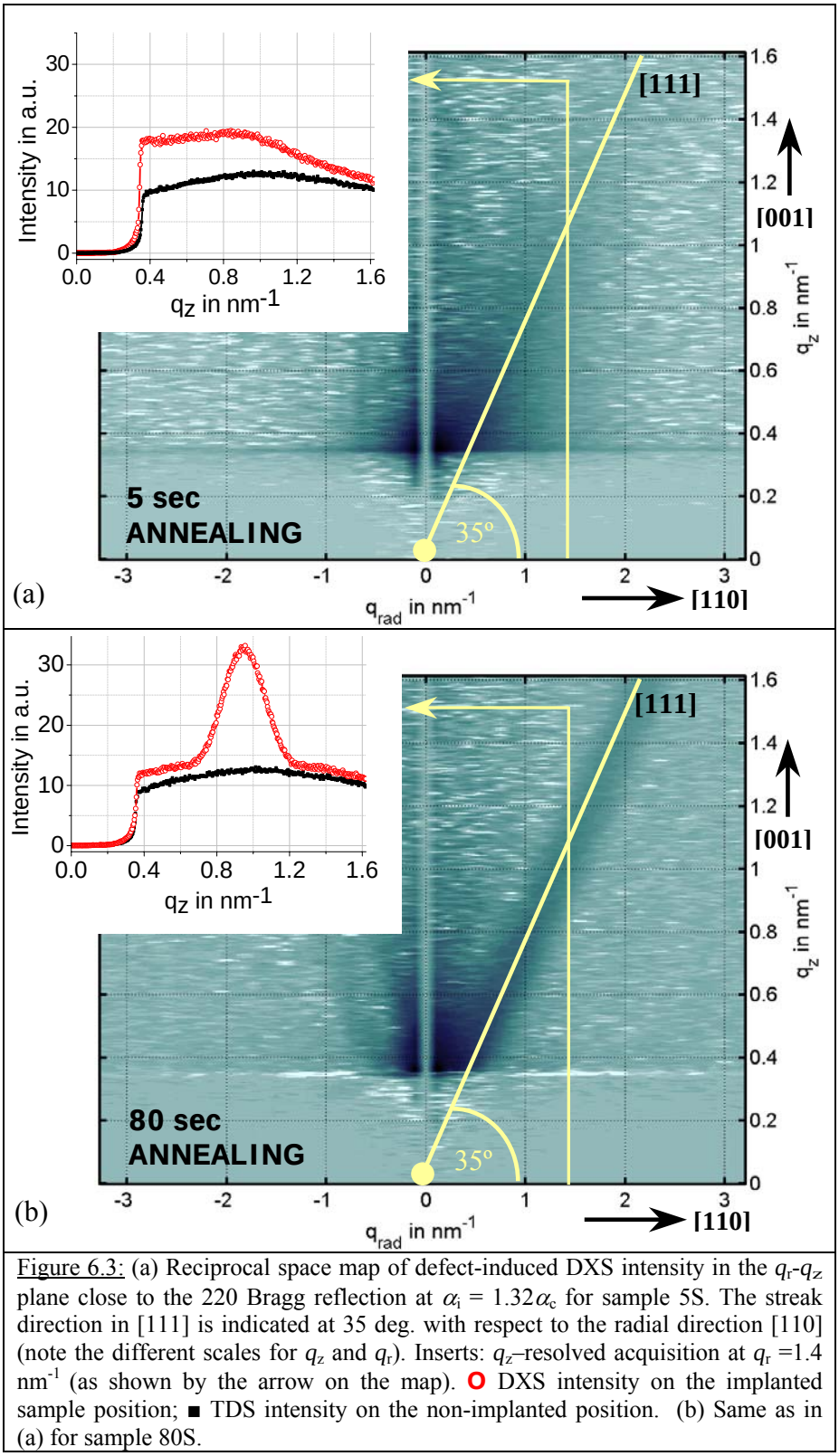

Figure 6.3: (a) Reciprocal space map of defect-induced DXS intensity in the q_r-q_z plane close to the 220 Bragg reflection at $\alpha_i = 1.32\alpha_c$ for sample 5S. The streak direction in [111] is indicated at 35 deg. with respect to the radial direction [110] (note the different scales for q_z and q_r). Inserts: q_z–resolved acquisition at q_r =1.4 nm^{-1} (as shown by the arrow on the map). **O** DXS intensity on the implanted sample position; ■ TDS intensity on the non-implanted position. (b) Same as in (a) for sample 80S.

For both S5 and S80 samples, two independent contributions give rise to the DXS distribution along q_z. A hump-like intensity centred at ~0.88 nm^{-1} sits on a broad DXS distribution. With increasing annealing time, the hump gets narrower and the area underneath increases. Simultaneously, the broad intensity on which it sits is reduced after 80s of annealing almost to the level of the thermal diffuse scattering (TDS) background of the non-implanted sample. As expected, the annealing process does not affect the TDS intensity. From the main panel of Fig. 6.3, it is clear that the hump-like intensity follows exactly the <111> directions, indicated by the 35-deg angle between the [110] and [111] direction. The intensity streak is more pronounced on the positive q_r side, [111]. The intensity at the Bragg peak position (q_r = 0) has been omitted from the map to emphasize the much weaker DXS contribution. The streak width was found to be almost constant along [111] and the streak intensity decays as q^{-2} (as expected from Ref. [1.78], but not shown here). The intensity concentrated in streaks along <111> is characteristic for the presence of FDL's (Sec. 2.1.3). The asymmetric intensity distribution of the streaks with higher scattering signal for q_r positive proves the extrinsic nature of the SF contained in the FDL's. The area under the hump, which can be analysed and fitted by a Gaussian, is proportional to the number of SiI's forming the FDL's. This feature will be used later on to investigate the redistribution and evolution of these extended defects.

The broad scattering contribution underneath the hump-like structure is attributed to point defects expanding the Si matrix, most likely the SiI's "magic clusters". Their presence induces HDS intensity, which is more evident for sample 5S than for 80S indicating a reduction of the concentration of these small defects during the annealing.

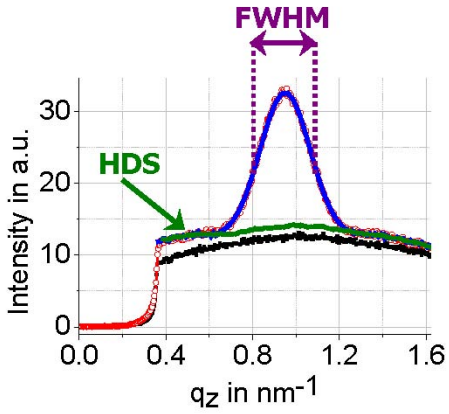

Figure 6.4: q_z–resolved acquisition at q_r = 1.4 nm^{-1} for sample 80S. O DXS intensity on the implanted sample position; ■ TDS intensity on the non-implanted position. The green line separates the HDS from the FDL-induced scattering contribution. The blue line is the Gaussian fit to the FDL-induced scattering contribution.

After subtraction of the TDS, the two scattering contributions induced by the presence of residual defects from the implantation process were separated, as shown in Fig. 6.4. The area below the green line was attributed to the HDS component, whose presence is confirmed by the DXS intensity decay in the q_a direction (not shown here). The HDS intensity was approximated by a linear decay of the signal along q_z on which the streaked intensity sits. The latter can be fitted by a Gaussian distribution, as shown in Fig. 6.4. The mean diameter of the SF's was determined using the q-space width of the streak perpendicular to the [111] direction (FWHM of the Gaussian fit). The total number of SiI's bound in the SF's was deduced from the integrated intensity, i.e. the area A_{SF} under the Gaussian curve. The results obtained from this data treatment of the whole sample series are shown in Fig. 6.5 as a function of the annealing time.

The mean diameter of the SF's, Fig. 6.5(a), increases from 20 nm to 34 nm after an annealing time of 5 to 80 s, respectively. The solid line shows that the SF's grow in size following a $\sqrt{t}$ behaviour, indicating that the rate-determining step of the process is the diffusion of the SiI's [6.3].

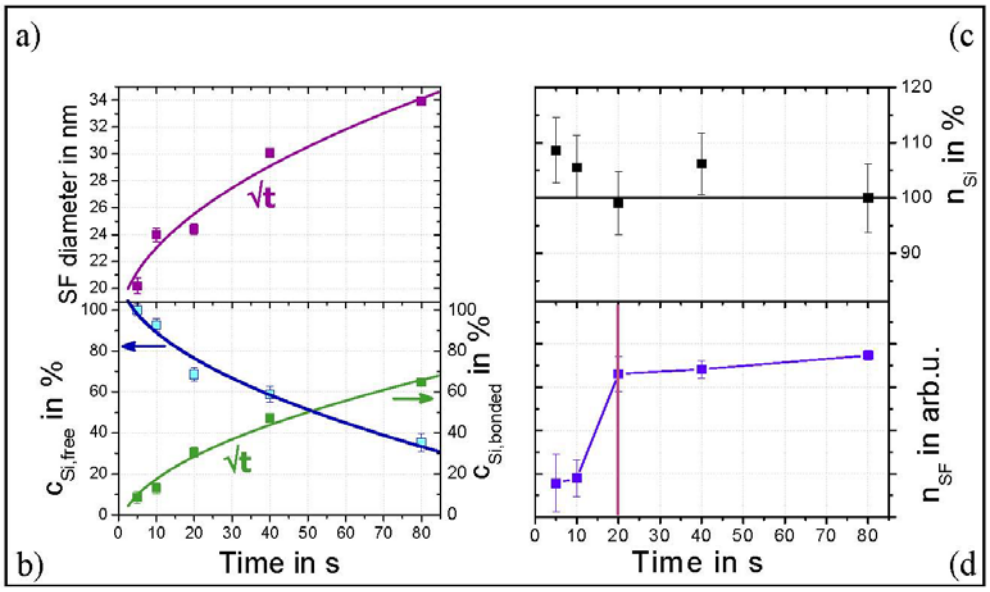

Figure 6.5: Results extracted from DXS distribution along q_z as a function of annealing time. (a) Average diameter of the stacking faults. The solid line gives the $\sqrt{t}$ fit to the experimental data. (b) Relative change of the number of free and bonded Si interstitials (in %, left and right scale, respectively). (c) Total number of excess Si interstitials n_{Si} in % present as SiI's clusters or bonded to the SF's. (d) Relative change of the number n_{SF} of SF's. See text for details.

The HDS intensity is proportional to the number of SiI's forming the small clusters, $c_{Si,\,free}$. Since we cannot normalise the intensity into absolute units, only relative changes can be considered. Setting the starting concentration of the SiI's at 5 seconds to 100% (for sample 5S,

$c_{Si,\,free}^{5S} \equiv 100$), the relative decrease of the SiI's concentration with the annealing time is found from the decay of the HDS intensity, as shown in Fig. 6.5(b). The decrease of the SiI's concentration is accompanied by an increase of the scattering from the SF's, which is measured by the area A_{SF} underneath the Gaussian curve (the fit obtained for 80S is shown in Fig. 6.4, blue solid line). Again there is no absolute scale and A_{SF} was normalised by $c_{Si,bonded}^{80S} = 100 - c_{Si,\,free}^{80S}$ and plotted in the same graph (Fig. 6.5(b)). If during the annealing treatment, the total number of SiI's, free or bound in the extended EOR defects does not change, the sum of the normalised $c_{Si,\,free}$ and $c_{Si,bonded}$ should stay constant. This behaviour is found and displayed in Fig. 6.5(c). This result confirms unambiguously that, for these implant and annealing conditions, the surface plays no role as a sink for self-interstitials, as predicted and discussed in Sec. 1.2.4.3. The SiI's supersaturation evolves following conservative Ostwald ripening.

Assuming a disk shape for the FDL's, the relative change of the total number of SF's can be determined from the relation:

$$n_{SF} \propto A_{SF} \Big/ \pi \left(d/2 \right)^2 \tag{6.2}$$

Eq. (6.2) is justified because A_{SF} is proportional to the total number of the bonded SiI's

$$c_{Si,bonded} \propto \rho\pi \left(\frac{d}{2} \right)^2, \tag{6.3}$$

where ρ is the known density of the interstitials in the FDL's (planar density of interstitials = 15.66 nm^{-2}, see Sec. 1.2.4.2). From the measured relative changes of A_{SF} and the diameter, d, the resulting evolution of the number of SF's, n_{SF}, is given in Fig. 6.5(d). Two different steps characterise the annealing process. In the beginning of the thermal treatment or during the ramp up of the temperature, the small SiI's "magic clusters" are the predominant defects and coexist with small FDL's. During the first 20 s of annealing, we observe a strong reduction of the HDS and, therefore, of the concentration of clusters. At the same time, A_{SF} increases, indicating the creation of a large number of new SF's with an average diameter around 20-24 nm. In conclusion, the SiI's "magic clusters" condense into small FDL's via SiI's diffusion.

For annealing times above 20 s, the density of free SiI's is depleted and the number of SF's, n_{SF}, remains almost constant, while the size of the SF's (Fig. 6.5(a)) still increases considerably. In the range from 20 to 80 s of annealing time, the big aggregates grow on the expense of the small ones, which is typical for Ostwald ripening (Sec. 1.2.4). A second source for the size-increase of the large SF's comes from the residual SiI's belonging to the clusters, which decrease in density with increasing time even after 20 s of annealing. The number of

atoms bound in the biggest SF's can be calculated:

$$n_{Si,bonded} = \rho\pi\left(\frac{d_{S80}}{2}\right)^2 = (142 \pm 4)*10^2 \text{ atoms}.$$

Using the relation between the formation energies and the number of atoms, as given in Fig. 1.16, it is evident that the FDL's are expected to be the dominant extended defect at 80 s and the number of excess SiI's clusters is small. It is foreseen that for annealing times longer than 80 s or higher temperatures, the FDL's will grow in size to the maximum predicted (about 80 nm diameter corresponding to 10^5 atoms) and subsequently transform into PDL's. Since PDL's are not visible by DXS in the $(1\bar{1}0)$ plane a decrease of the streak intensity is expected as found by Sztucki *et al.* [1.78].

6.4 Comparison with MEIS and SIMS

The 900 sample series was investigated also using the MEIS and SIMS experimental techniques. As for the other samples series, our co-workers from the University of Salford carried out the MEIS measurements. The SIMS profiles were performed by our IMPULSE partners from the ITC-Irst of Trento, I (see Appendix). Because neither MEIS nor SIMS can detect the EOR defects, only a comparison with SR results will be reported in the following.

The MEIS measurements were performed using the same experimental conditions as for the other sample series (Sec 4.5). The details of the MEIS experimental method can be found in Ref. [4.3]. The SIMS spectra were acquired using a CAMECA SC-ultra instrument, which is a magnetic sector instrument with floating primary column and a field-free region at the sample surface. The new arrangement of the magnetic sector implemented in this SIMS instrument allows the detection of negative secondary ions, which was previously possible only for quadrupole SIMS instruments. The ion beam was composed of Cs^+ at 0.5 keV and an angle of incidence of ~45 deg. The sputtering rate was 0.37 Å/s and the monitored ions were $^{28}Si^-$ and $^{28}Si^{75}As^-$. These experimental conditions are particularly suited for the investigation of shallow As profiles [6.4]. Nevertheless, the accuracy of the analysis of the first 2 nm from the surface is usually influenced by SiO_2-induced artefacts, which may affect also the dopant dose determination.

The MEIS energy spectra for the different annealing times are shown in Fig. 6.6 together with an as-implanted sample. The spectra from a virgin and an amorphous Si samples are given

for reference. The depth scales calibrated for As, Si and O are added to facilitate the direct conversion of the energy into depth. The spectrum of the as-implanted sample (blue line) shows the complete amorphisation caused by the 130 keV Xe PAI by the fact that the Si peak reaches the random level until a depth (i.e. energy) that exceeds the range of the acquisition. The As distribution has a peak at a depth of ~ 6.3 nm, which is in agreement with TRIM simulations [1.12]. For such implantation, the mean projected range of the As ions is R_p = 6.3 nm (Fig.1.6).

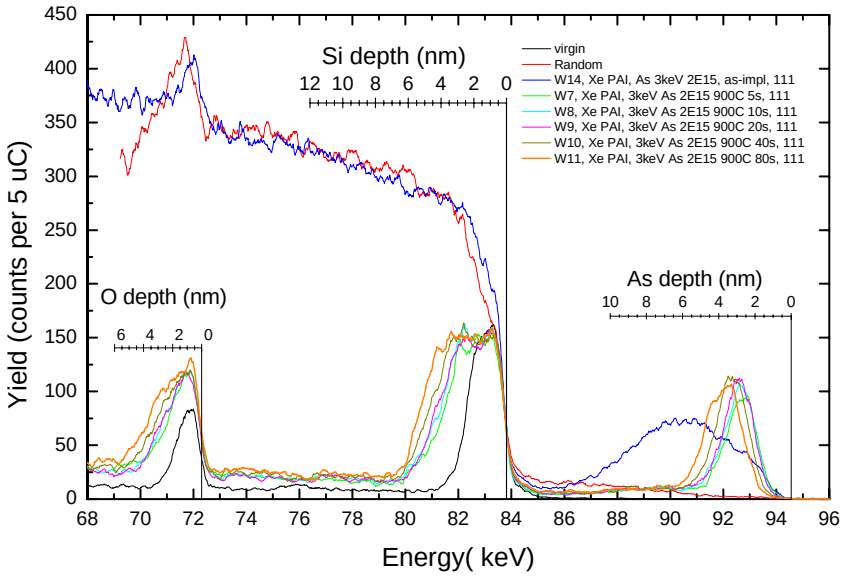

Figure 6.6: 900 sample series. MEIS spectra collected along the [111] blocking direction. The spectra from a non-implanted Si and an amorphous Si are shown for comparison. Courtesy of M. Werner.

Following the annealing at 900 °C, the SPER process is complete, as evidenced by the dramatic decrease of the Si yield in the 73 –80 keV energy range and by the fully regrown Si surface peak in the energy interval between 80 and 83.5 keV. However, the Si surface peaks are broader than for the virgin sample. This is due to the increased thickness of the oxide layer that will be discussed below.

During the regrowth process, the As that exceeds the solid solubility at the anneal temperature forms the segregated peak trapped at depths between 2-5 nm underneath the oxide layer. Assuming a perfect SPER process, As atoms in substitutional sites are invisible in the MEIS spectra.

Several effects can be observed with increasing annealing time. The first is the growth of the thickness of the oxide layer. This is visible from the increased height and width of the O peak that extends to lower energies (i.e. greater depth) with respect to the shorter annealing times. The growth of the oxide affects both the Si and As peaks. The segregated As peak is trapped underneath the SiO_2 layer. This is confirmed by the observation that the depth of the

segregated As peak increases with the increasing oxide thickness resulting from the longer annealing times. The depth profiles of the As atoms from the whole sample series are shown in Fig. 6.7(a).

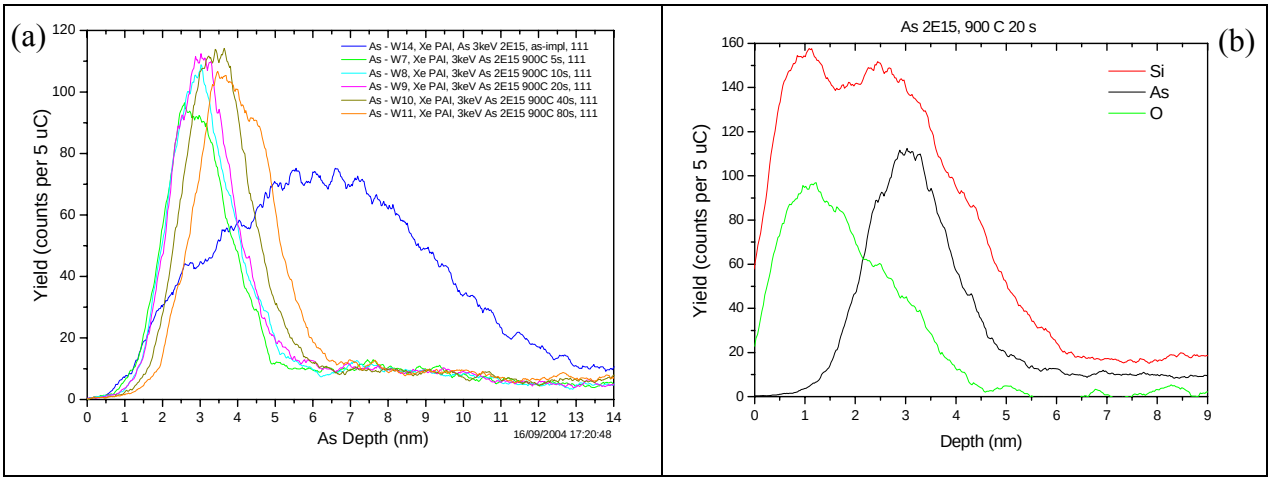

Figure 6.7: (a) Depth profile of the As atoms. (b) Depth profiles of As, O and Si atoms for sample 20S extracted from the MEIS spectra in Fig. 6.6. Figure courtesy of M. Werner.

The increased Si peak width with respect to the virgin sample (see Fig. 6.6) is accounted for by the increased oxide thickness. Moreover, this Si peak contains the scattered yield from the displaced Si at the depth of the segregated As layer. The detailed behaviour of the interaction between the oxide layer and the snowploughed As layer is more clearly visualised by overlaying the As and O depth profiles with the dechanneling background removed under the O peak, as shown in Fig. 6.6(b). Although the convolution effects (energy resolution & energy straggling) broaden the peaks, the segregated As is clearly situated under the oxide. The Si depth profile, also shown in the figure, further demonstrates the fact that the Si surface peak contains both scattering off Si in the oxide layer and disordered Si at the depth of the segregated As peak. With increasing annealing time, the peak corresponding to the segregated As moves to greater depths due to the oxide growth. MEIS shows that the As concentration in the surface peak increases with the annealing time.

The comparison between the layer thicknesses measured by MEIS and by SR is shown in Table 6.2. For the as-implanted sample, the electronic density contrast of the broad implanted As distribution on the Si bulk is not strong enough to enable its detection by SR. For the annealed samples, the MEIS values for the thickness of the segregated As layer are affected by instrumental resolution broadening, as discussed in Sec. 5.5.2. Therefore, the agreement with the SR is still satisfactory.

Table 6.2: Comparison of the layer thicknesses between MEIS and SR on the 900 sample series.

Sample	As depth [i] [nm]	As peak FWHM [nm]	As atoms in peak [%]	As atoms in peak [cm^{-2}]	Si peak width [ii] [nm]	O thickness [ii] [nm]	SiO_2 thickness; [nm]	"As segregated layer" thickness; [nm]
Method	**MEIS**	**MEIS**	**MEIS**	**MEIS**	**MEIS**	**MEIS**	**SR**	**SR**
as-impl.	6.3	6.2	100	1.96×10^{15}	--	--	--	--
5S	2.9	1.8	43	8.35×10^{14}	3.8	2.4	2.73	0.75
10S	3.0	1.8	46	8.97×10^{14}	4.0	2.8	2.84	0.76
20S	3.1	1.8	48	9.42×10^{14}	4.4	2.8	3.05	0.69
40S	3.5	1.9	51	9.99×10^{14}	4.8	3.2	3.48	0.76
80S	3.9	2.1	52	1.03×10^{15}	5.4	3.7	3.75	0.64

[i] estimated from the back edge half height.
[ii] depth of the As peak centre.
SR: The error σ(SiO_2) on the SiO_2 thickness is ~0.05 nm; σ(As-rich)~0.2 nm.

The results concerning the oxide thickness are in agreement within the accuracy of the MEIS and SR measurements. The error on SiO_2 thickness measurement is 0.05 nm for the SR, and 0.2 nm for the MEIS. It has been shown that MEIS gives evidences of increasing concentration of As atoms in the segregated peak with increasing annealing time. SR observed no systematic increase of the electron density from the As segregated peak, probably due to the lower sensitivity of this technique.

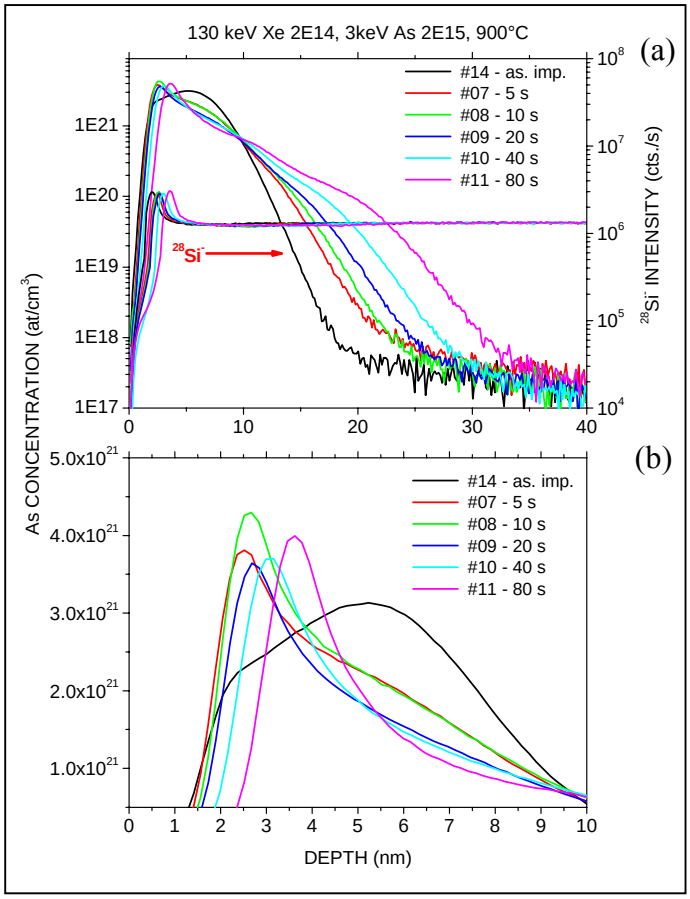

Figure 6.8: 900 sample series and as-implanted Si. (a) SIMS profiles of Si and As atoms. (b) Zoom of the data shown in (a) in the near-surface region from 0 to 10 nm. Courtesy of D.Giubertoni.

The SIMS profiles corroborate the migration of the segregated As peak to greater depths, as evidenced in Fig. 6.8(b), where the depth of As segregated peak increases with the annealing time. Moreover, the SIMS profiles show an enhanced diffusion of the tail of the As profile into the bulk upon annealing, which is plotted in Fig. 6.8(a). The junction depth X_j, evaluated at 10^{18} ats./cm^3, increases from (22.1 ± 1.5) nm, for 5S, to (31.2 ± 1.5) nm, for the sample 80S. The total measured As dose is ~$1.8x10^{15}$ ats./cm^2 for all of the 900 sample series, slightly lower than the nominal implanted dose of $2x10^{15}$ ats./cm^2. The accuracy of the SIMS profiles is poor for the near-surface region, especially concerning the dose evaluation. Therefore, SIMS neither confirm nor confute the MEIS observation concerning the increase of the As concentration in the segregated peak upon annealing. The profile of the Si measured by SIMS, in Fig. 6.8(a), shows a shift of the peak of the Si concentration upon annealing, thus confirming the growth of the oxide in agreement with SR and MEIS.

A further comparison between SR and SIMS is not possible, because of the radically different sensitivity of the two analytical methods. While the strength of the SIMS is its chemical sensitivity, the SR detects only the electronic density profile.

6.5 Conclusions

The GI-DXS technique was employed to investigate the evolution of the EOR defects in Si after PAI with Xe and annealing at 900°C. It has been demonstrated that this method provides simultaneously information on point-like and extended EOR defects in a non-destructive way. The results show that the dynamic exchange between point-defect, such as “magic clusters” of SiI’s, and FDL’s can be quantified. The annealing process takes place in a time-limited window of the evolution of the EOR damage where the conservative Ostwald ripening mechanism describe the growth of the FDL’s, because no annihilation of the SiI’s at the surface is observed. The studied thermal budgets of the annealing are too low to result in energetically most favourable transformation into PDL’s.

SR was used to investigate the structure of the amorphous near-surface layer giving evidences of the surface oxide growth upon annealing and of the presence of the As segregated layer below the oxide. The results from the SR have been compared with the corresponding MEIS and SIMS results showing a good agreement.

7. Study of {113}-defects during isothermal annealing

7.1 Motivation and sample preparation

In the previous chapters, it has been shown that GI-DXS is most suited to study EOR defects. So far, this technique has been successfully applied to investigate dislocation loops and "magic clusters" [1.77, 1.78, 6.2], while the characterisation of {113}-defects (113's) is still pending in the literature. To achieve this aim, pioneering experiments on the beamline ID01 have been performed during the last year. The atomistic simulation of the DXS signal from 113's published in [1.62], and summarised in Sec. 2.1.3, was the starting point for such experiments. In this chapter, the first systematic application of the GI-DXS method to study 133's in ion-implanted Si is reported. We studied the temporal evolution of 113's in Ge pre-amorphised Si samples during isothermal annealing at 800°C.

The samples were provided by Mattson Thermal Products, Dornstadt (D), in the frame of a collaboration with the FRENDTECH consortium[a]. Originally, this sample set was prepared to study the stability of the chemical and electrical profile of boron dopant atoms during post-annealing steps of the Si wafers processing. The results from this investigation have been published in Ref. [7.1].

For the experiment, (001) Si wafers were cleaned from the native oxide by a 30 s wet-chemical etching in HF (49%): H_2O (1:40) solution. Later, they were preamorphised by a Ge implant at 30 keV to a dose $1x10^{15}$ cm^{-2}. As a consequence of the PAI treatment, an amorphous layer with a thickness of ~50 nm was created [7.1]. The dopant implantation was performed to a dose of $1x10^{15}$ cm^{-2} with B ions at 0.5 keV on a Varian VIISta-80 ULE high-current implanter. However, this second implantation is not relevant in this study, because it does not affect the evolution of the Ge-induced EOR damage. A pre-annealing treatment was performed in order to achieve full SPER at 650 °C for 10s in a 100 ppm partial pressure of O_2 in N_2. This was followed by soak annealing at 800 °C for a time variable from 10 to 900 s, performed in a Mattson RTP system. This annealing temperature was chosen, because boron dopant deactivation was observed in the range between 750 and 850°C, due to the interaction of the dopant atoms with the evolving EOR defect population [7.1]. A total of 7 samples was studied that will be addressed hereafter as 10S, 30S and so on, as indicated in Table 7.1.

[a] FRENDTECH (Front-End Models for Silicon Future Technology) is a project centred on the modelling of physical properties in Si-based devices. FRENDTECH was financed by the European community as IST project 2000-30129.

Table 7.1: Samples characterised using GI-DXS. A PAI treatment was performed with Ge ions at 30 keV to a dose of $1x10^{15}$ cm^{-2} followed by a B ions implantation to a dose of $1x10^{15}$ cm^{-2} at 0.5 keV. The samples were annealed using the conditions reported in the Table. RTA means Rapid Thermal Annealing.

Sample	Annealing conditions
10S	RTA 800°C, 10s
30S	RTA 800°C, 30s
60S	RTA 800°C, 60s
120S	RTA 800°C, 120s
300S	RTA 800°C, 300s
600S	RTA 800°C, 600s
900S	RTA 800°C, 900s

The GI-DXS measurements were carried out with a 8.2 keV x-ray beam at $\alpha_i = 1.32\alpha_c$ ($\Lambda \approx 400$ nm), in order to reach the EOR damage region. The intensity from a non-implanted Si wafer (not belonging to the same lot as the examined implanted Si) was measured and used as a reference for evaluating the background scattering. This is justified for angles of incidence α_i bigger than the critical angle α_c.

7.2 Measurements close to (1.3, 1.3, 0) position in reciprocal space

As explained in Sec. 2.1.3, the 113-induced DXS intensity shows a unique feature that enables to undoubtedly identify these defects: a DXS signal arises close to the position *h*, *k*, *l* = (1.3, 1.3, 0) in reciprocal space. No other defect type gives rise to a DXS intensity signal in this position far from any Bragg peak. Therefore, the measurement close to (1.3, 1.3, 0) is particularly sensitive to 113's.

As shown in Fig. 2.9, the DXS distribution in the q_r-q_z enables the determination of the main type of 113's present in the sample. The reciprocal space maps of the q_r-q_z and q_a-q_z planes are shown in Fig. 7.1 for sample 30S. The existence of a defect-induced DXS intensity in this region is the direct evidence of the presence of 113's in the sample. A single broad intensity stripe oriented in the [001] direction and centred at $h = k = 1.25$ is found, for the radial scan.

The calculated GI-DXS pattern in q_r direction for {1Hex}ZD (i.e. zig-zag) defects in Si is plotted in Fig. 7.2. Following the comparison between the calculation and the experiment, the orientation of the measured intensity streak along [001] and the position of the maximum intensity at $h = k = 1.25$ are both strong indications that most of the 113's in the sample are of {1Hex}ZD type. The 113's contained in the sample present a size distribution that smears out the DXS signal of the satellites peaks. For this reason, only the central and most intense stripe

of the scattering pattern is detected in the experiment. Similar scattering pattern in the q_r-q_z and q_a-q_z planes is observed for the whole sample series, where only the stripe width changes.

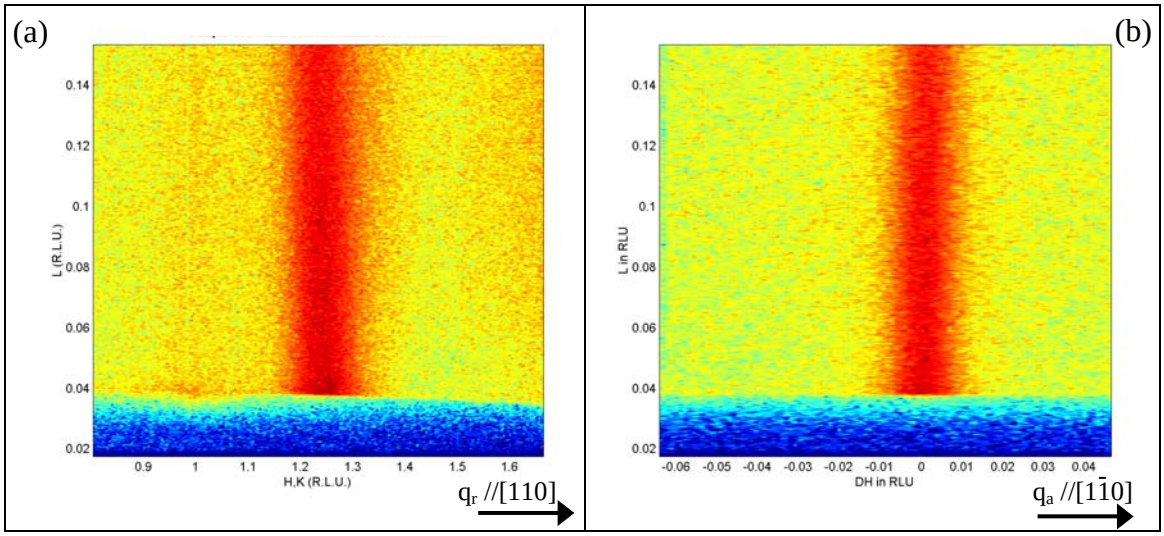

Figure 7.1: Sample 30S. (a) Reciprocal space map of diffuse scattering in the q_r-q_z plane close to (1.3, 1.3, 0) position in reciprocal space. (b) Reciprocal space map of diffuse scattering in the q_a-q_z plane. The centre of the transversal scan is located at $h = k = 1.25$.

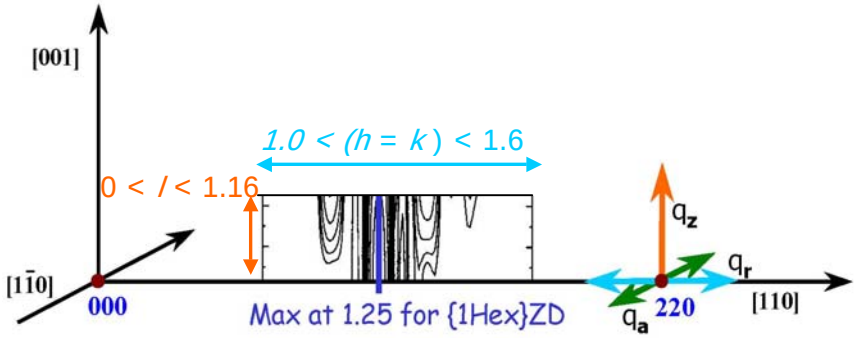

Figure 7.2: Calculation of the diffuse scattering from {1Hex}ZD defects in measured range of the q_r- q_z. The position of the 220 surface Bragg reflection and the orientation of the q_r, q_a and q_z directions are shown as reference. Adapted from Ref. [1.62].

The predominant type of defect is identified in the {1Hex}ZD. Therefore, its width can be determined from a scan in q_r //[110] direction through the (1.25, 1.25, 0) position, while its length is obtained from a q_a scan in $[1\bar{1}0]$, centred at the same position in reciprocal space.

For this purpose, Fig. 7.3 illustrates the defect-induced DXS measured for the whole sample series in radial, part (a), and angular, part (b), directions close to the (1.25, 1.25, 0) position. The maximum of the q_z-integrated intensity is increasing up to 120 s and reduces again for longer annealing times. The same qualitative behaviour is observed for both the radial and the angular scans.

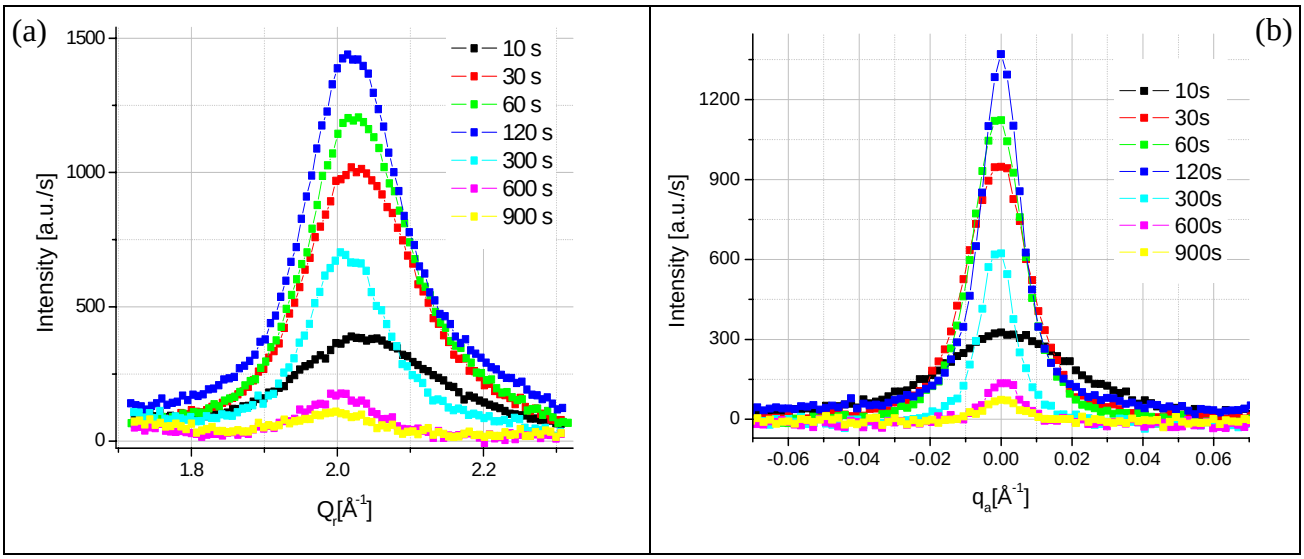

Figure 7.3: (a) Defect-induced diffuse scattering from the radial (a) and angular (b) measurements close to (1.25, 1.25, 0) position for the whole sample series.

The recorded intensity distribution can be fitted with a Lorentzian curve, from which quantitative information on the defect properties is obtained. As an example, Fig. 7.4 shows the Lorentzian fit to the radial and the angular scans performed on the sample annealed for 60s.

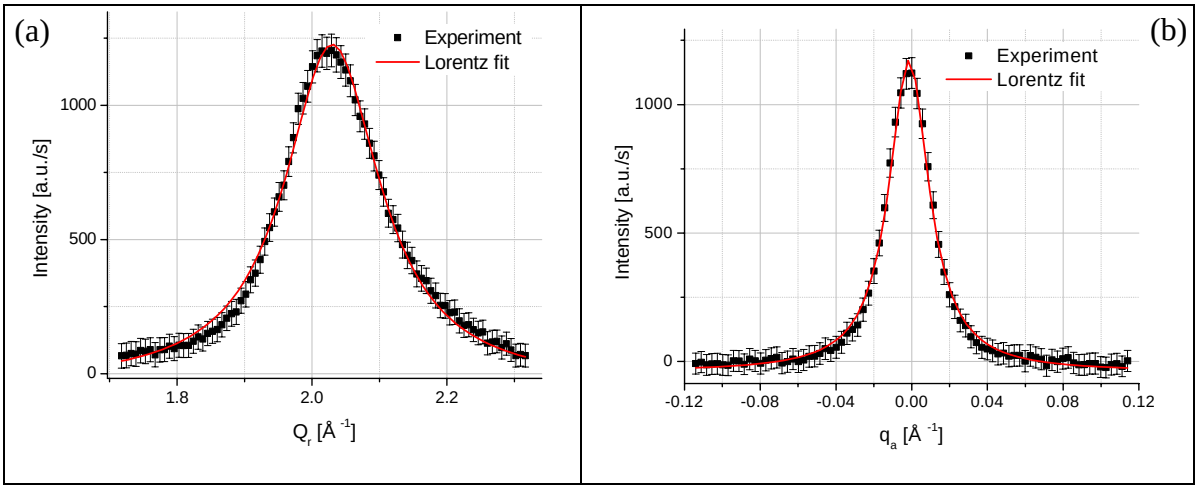

Figure 7.4: Data and fit for sample 60S. (a) Defect-induced diffuse scattering from the radial (a) and angular (b) measurements close to (1.25, 1.25, 0) position.

Using the equation $d = 2\pi/\Delta q_{r,a}$, which relates the halfwidth, $\Delta q_{r,a}$, in reciprocal space to the size in real space, the mean width of the 113's is derived from the Lorentz FWHM in the radial direction and the mean length from the FWHM in the angular direction [1.62]. The evolution of the 113's size with the annealing time is reported in Fig. 7.5: the mean width in part (a) and the mean length in part (b). The width of the 113's evolves from (28 ± 5) Å, after

10 s of annealing, up to (64 ± 10) Å after 900 s, following a √t growth law (i.e. diffusion limited process [6.3]).

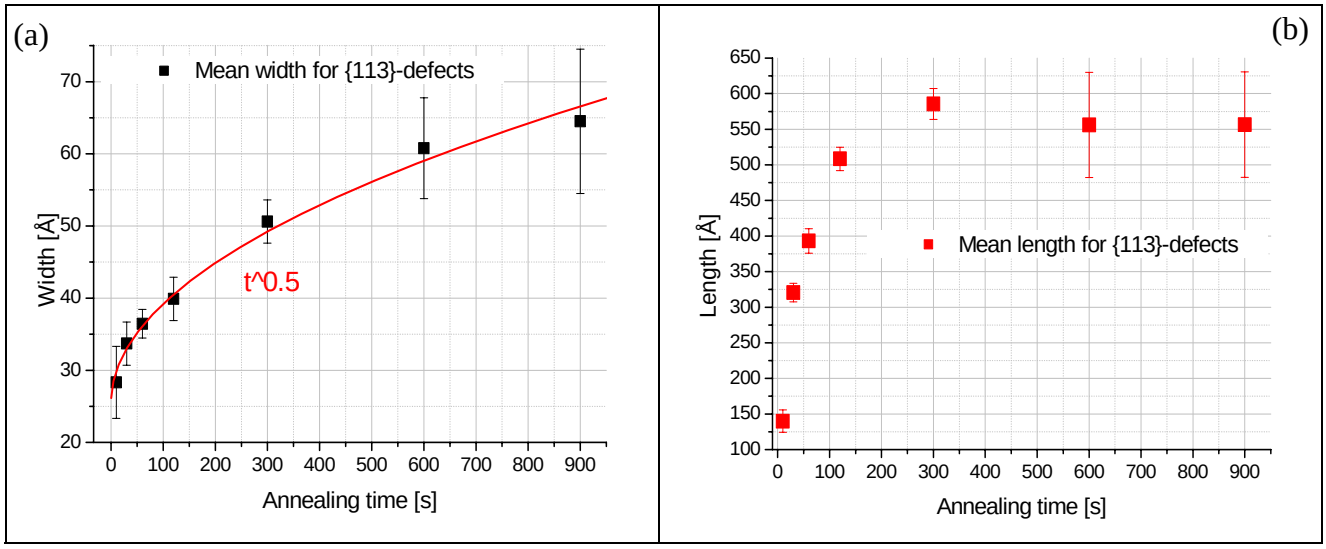

Figure 7.5: (a) Mean width of the 113's as a function of the annealing time. (b) Mean length of the 113's as a function of the annealing time

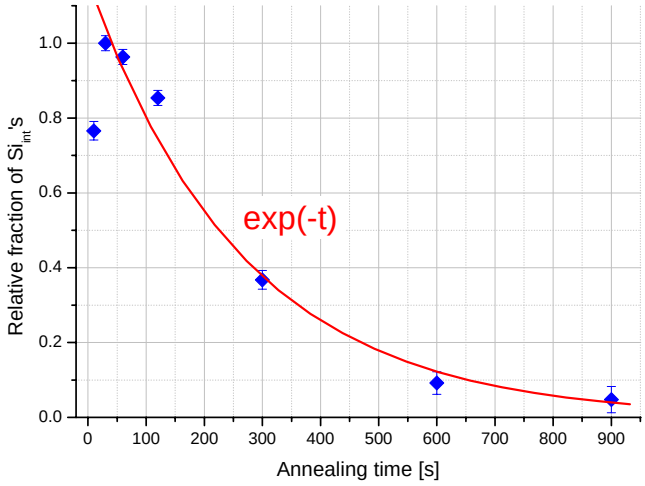

Figure 7.6: Relative fraction of Si interstitials bound to 113's as a function of the annealing time *t* normalized to 1 at 30 s. An exponential decay as a function of *t* is observed for *t* > 30 s as shown by the fit, red curve.

The length varies from (140 ± 15) Å to (585 ± 20) Å at 300 s of annealing. After 300 s the defect length of (556 ± 70) Å remains constant within the error bars. The GI-DXS results confirm that the 113's growth rate is higher for the length direction than for the width, which explains the typical rod shape of this type of defects. The area below the 113-induced intensity hump is proportional to the number of SiI's belonging to the defects. The results obtained from the variation of the hump area (here the area under the Lorentzian fit to the curve is used) in angular direction are reported in Fig. 7.6 as a function of the annealing time

t. The number of bonded Si atoms increases up to 30 s of annealing and decreases exponentially for longer annealing times. The relative fraction of bonded atoms has been normalised to unity for sample 30S, which does not imply that all of the excess SiI's present in the EOR damage region are bonded into 113's. On the normalised scale, we observe that a fraction of ≈ 0.77 of excess Si is bonded after 10s of annealing. After 900 s of annealing only a fraction of ≈ 0.05 Si is still aggregated into large 113's.

7.3 Measurements close to the 220 surface Bragg reflection

In addition to the scattering close to the (1.3, 1.3, 0) position, 113-induced DXS is expected close to the 220 Bragg reflection (Sec. 2.1.3). In particular, the linear form of 113, the IRD defect, gives rise to an intensity streak along the <113> directions, as shown in Fig. 2.8(a).

The defect-induce DXS map of the q_r-q_z plane close to the 220 Bragg reflection is shown in Fig. 7.7, for sample 30S. Its main feature is the presence of a weak intensity streak along the [113] direction, as indicated by a red line on the graph.

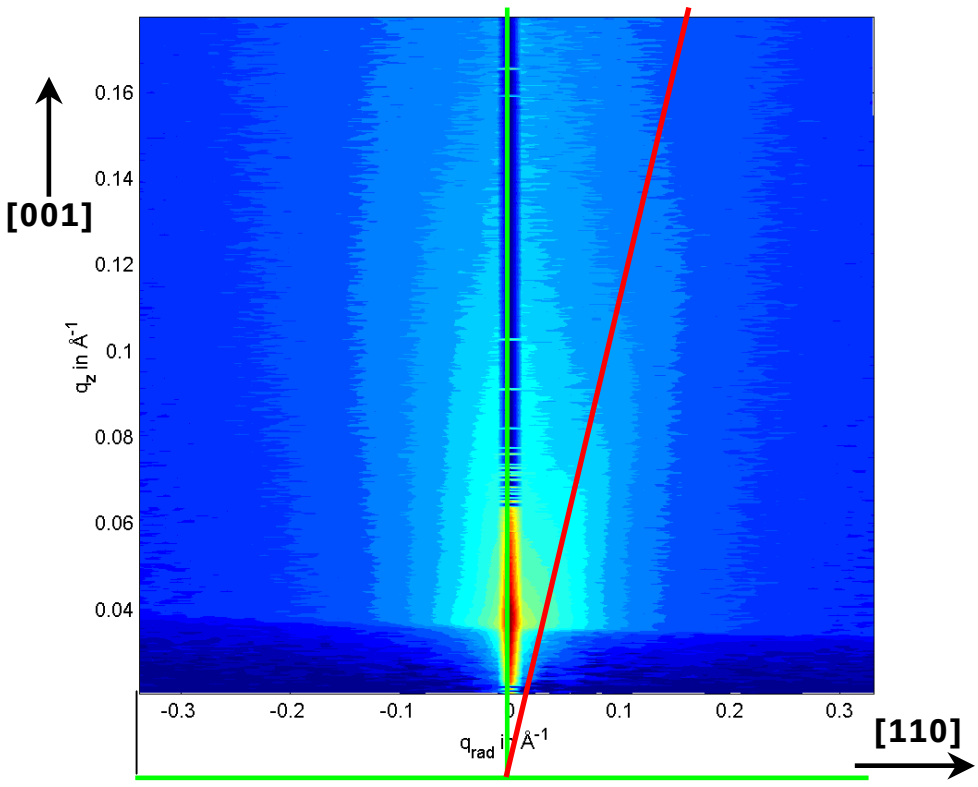

Figure 7.7: Reciprocal space map of DXS from sample 30S in the q_r-q_z plane close to 220. The red line indicates the presence of an intensity streak along the [113] direction.

Figure 7.8 shows the reciprocal space maps in the q_r-q_z plane recorded at the 220 Bragg peak for some of the measured samples. Sample 10S shows some asymmetry in the DXS distribution along q_r from defects that expand the lattice, like interstitial-type defects. The presence of the [113] intensity streak arising from IRD's is observed for 30S (Fig. 7.7) and 60S, as indicated by a red line. For sample 120S a weak intensity streak in the [111] direction indicates the formation of FDL's (yellow line). Starting from 300 s, the streaked DXS intensity becomes too weak for being detected with the integration time used in the mapping experiment.

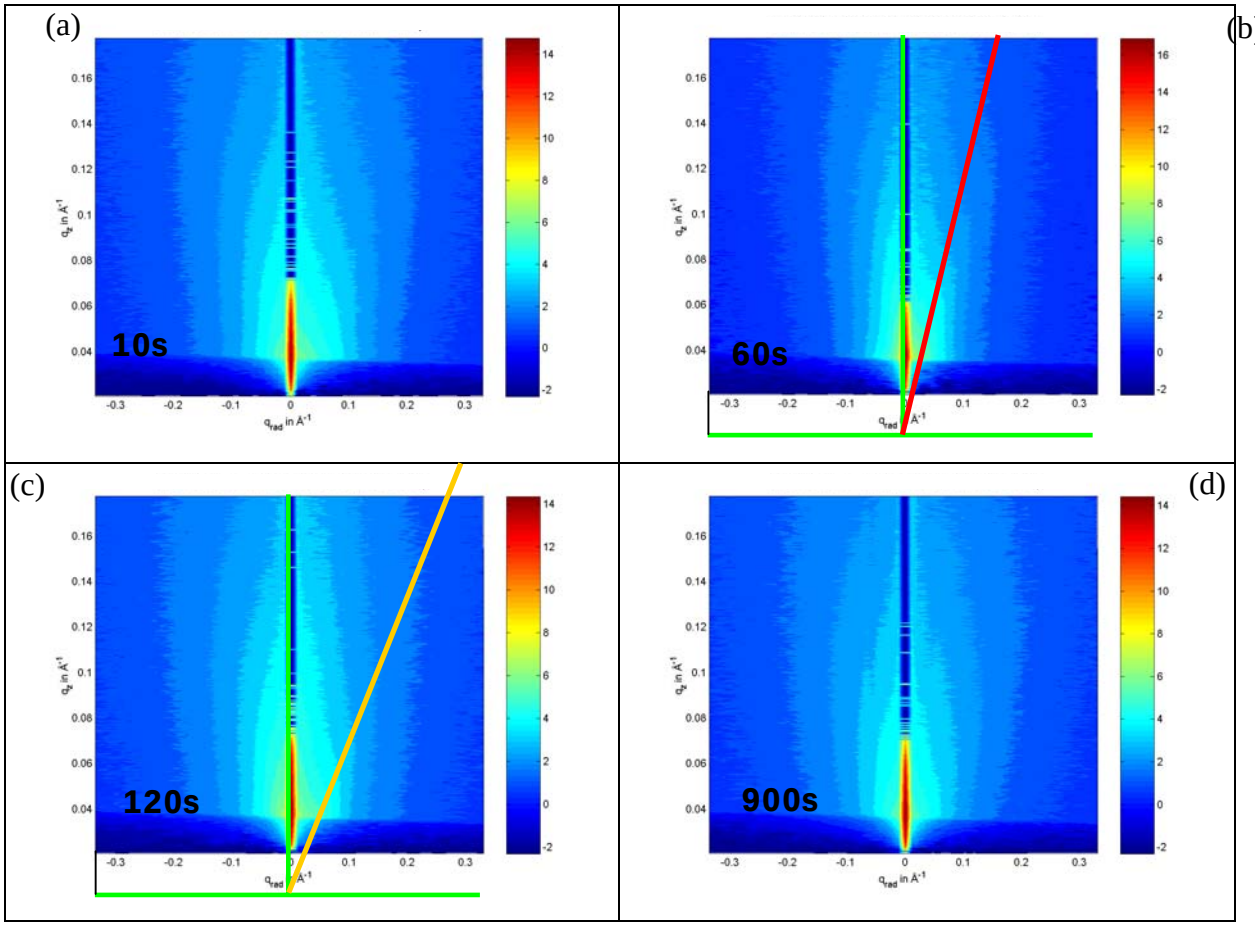

Figure 7.9: Reciprocal space maps of diffuse scattering in the q_r-q_z plane close to the 220 Bragg peak for the sample series annealed at 800°C for the time indicated. The streaks in [111] -yellow- and [113] -red- are plotted on the figure when present.

In order to retrieve a more quantitative information concerning the EOR defects in the samples, q_z-resolved DXS measurements were recorded with a longer integration time at a fixed q_r = 0.145 Å^{-1}. Figure 7.9 illustrates the distribution of the DXS along q_z for the whole sample series. The acquisition performed on a non-implanted sample is shown for comparison and represents the TDS contribution to the total DXS intensity. It has to be emphasised that, close to the Bragg peak, the DXS contributions arising form the long-range displacement

fields of all the defect types present in the sample superimpose. A HDS component from point-like defects, like ”magic” clusters may be present together with streaked-intensity from extended defects, like 113’s and FDL’s.

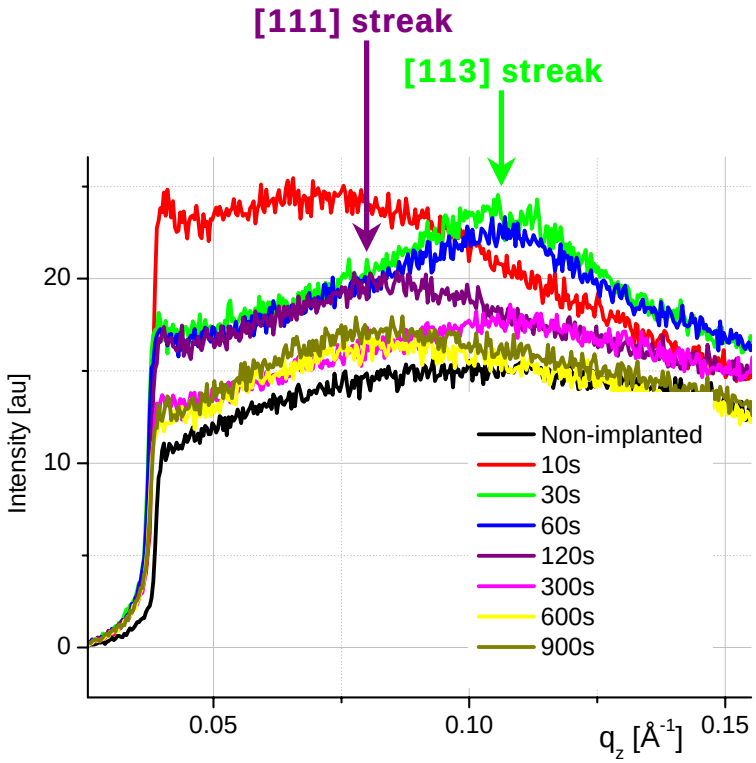

Figure 7.9: DXS distribution along q_z at q_r = 0.145 Å^{-1}, close to 220 Bragg reflection. The intensity from the non-implanted Si is also shown for comparison.

Two arrows on the graph indicate the expected q_z position for the [113] and for the [111] DXS intensity streaks. The intensity hump present in sample 10S at about $q_z \sim 0.07$ Å^{-1} is related to the intensity tail of the DXS enhanced by the maximum of the transmission function located at $q_{z,critical} \approx 0.04$ Å^{-1}. It is attributed to the DXS from residual point defects, like “magic clusters”, still coexisting with 113’s. For longer annealing time, the HDS contribution reduces. Sample 30S and 60S show intensity humps at the [113] streak position, while, for 120S, the hump has shifted to the [111] streak position. Sample 300S shows a diffuse scattering distribution with higher intensity for $q_z > 0.1$Å^{-1}, which is assigned to residual scattering the [113] streak position. Sample 600S and 900S shows weak residual DXS mainly located at the [111] streak position. The overall DXS intensity is progressively diminishing with the annealing time indicating that the total number of SiI’s in the EOR defects area is reducing. Experimental evidence of IRD-113’s presence is clearly attested for samples 30S and 60S. In sample 120S, the main signal arises from FDL’s. For longer annealing time, the characteristic DXS features for FDL’s and IRD 113’s decrease in intensity

and only few residual defects are found for 300S, 600S and 900S. The SiI's supersaturation diminishes upon annealing, because the reduction of the DXS from point and IRD-113's is not compensated by the formation of FDL-induced DXS streaks with high integrated-area, as shown, e.g., for the PAI spike sample (Fig. 5.6 (c)). The evolution of the defect population follows a non-conservative Ostwald ripening mechanism, due to the partial migration of the excess SiI's towards the surface, as confirmed by Ref. [7.1].

The combination of the results from the measurements close to the (1.25, 1.25, 0) position and the ones close to the 220 Bragg reflection attests the simultaneous presence of zigzag {1Hex}ZD and linear IRD defects. This is expected, based on the similar formation energies for the two defects types [1.58]. However, the lack of experimental evidence proving the presence of IRD defects, in the data acquired close to the (1.25, 1.25, 0) position, and of {1Hex}ZD's, in the 220 measurements, needs to be explained. According to [1.62], for {1Hex}ZD 113's and IRD 113's, the intensity distributions in the q_r-q_z plane close to 220 are topologically similar to the region close to (1.25, 1.25, 0). Therefore, for the reciprocal space region close to the 220, the {1Hex}ZD-induced DXS is characterised by a streak in the [001] direction of width ~ 0.1 $Å^{-1}$ and centred on the Bragg peak. Such DXS streak superimposes to the HDS from small point defects and to the crystal truncation rod, thus impeding its clear identification. In addition, the signature of {1Hex}ZD presence cannot be observed at q_r = 0.145 $Å^{-1}$ position, because the q_r value is bigger than the width of the [001] oriented streak. This explains the reason why {1Hex}ZD defects are not detected in the measurements close to the 220 Bragg peak.

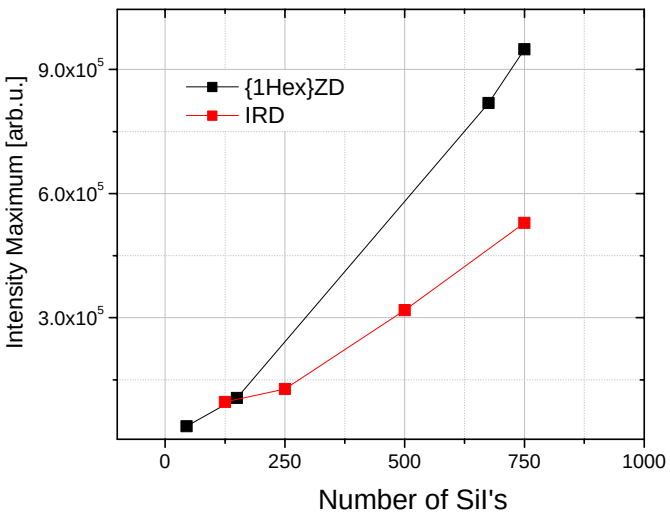

Figure 7.10: Maximum of the calculated DXS intensity in the radial direction close to (1.25, 1.25, 0) position in reciprocal space as a function of the number of SiI's bounded to the {113}-defects for IRD and {1Hex}ZD [7.2].

Following Ref. [1.62], also close to (1.25, 1.25, 0) position, the DXS intensity from both {113}-defect species should be observed. Figure 7.10 shows the results from the atomistic calculations performed for 113's of various sizes for both {1Hex}ZD (black symbols) and IRD (red symbols) defects [7.2]. The maximum of the scattered intensity along the radial direction, in the region close to (1.25, 1.25, 0), is plotted as a function of the number n of SiI's bounded to the defect. The latter was calculated assuming a density of SiI's $\rho = 5$ nm^{-2} for both linear and zig-zag defects [1.47]. Except for very small defects ($n < 150$), the DXS intensity increases linearly for both types of {113}-defects with the {1Hex}ZD-induced DXS higher by a factor 2 respect to the IRD-induced DXS. The maximum defect size for the calculations is limited to 100 x 150 $Å^2$. The {1Hex}ZD defects detected in this sample series are larger than 150 SiI's, thus the DXS they induce has twice the strength of signal from some IRD defects of the same size. As no DXS intensity from IRD defects has been detected close to (1.25, 1.25, 0) position, it is confirmed that more than 50% of the 113's in this sample series are of type {1Hex}ZD. The scattering from IRD defects is too weak to be detected in this reciprocal space region. Close to the 220 surface Bragg reflection, the IRD structure factor must be stronger, thus enabling the IRD-induced DXS detection.

By combining the results obtained from all the measurements performed, a comprehensive understanding of the structural evolution of the EOR defects during annealing is derived in the frame of the "excess interstitial" model (Sec. 1.2.4). After 10 s at 800 °C, we observe the presence of "magic clusters" in co-existence with 113's of type {1Hex}ZD. After 30 s, the small clusters are no longer detected from DXS at the 220 and, simultaneously, the maximum intensity for 113's is observed close to (1.25, 1.25, 0) position, with the maximum number of SiI's bound to 113's. For annealing times longer than 30s, the migration of SiI's towards the surface is evident by a steady reduction of the number of SiI's bonded into 113's (i.e. integrated area in Fig. 7.6) that is not compensated by an increasing FDL-induced signal at the 220. Beyond 120 s, the formation of FDL's is attested from the appearance of a [111]-oriented diffuse streak at the 220. Simultaneously the growth rate of 113's in length reduces, due to the activation of a competing FDL's nucleation. At this stage, two alternative sinks are available for the SiI's that "evaporate" from the 113's: the migration to the surface and their aggregation to form FDL's. For annealing times longer than 120 s, we observe the progressive annealing of the SiI's supersaturation at the surface.

These results are in agreement with the experiment on Si implantation in Si reported in Ref. [7.3], where the evolution of 113's located close to the surface was investigated by TEM. In this reference, the exponential decay of the number of SiI's bonded into 113's is found

starting from the very beginning of the annealing (5 s at 800 °C). In our work, such exponential decay is found only starting from 30 s at 800 °C, probably due to the different initial condition after the implantation process.

7.4 Conclusions

In this chapter, {113}-defects in the EOR damage region have been investigated using the GI-DXS technique. Experimental evidence of the presence of 113's was found from the DXS intensity arising close to (1.25, 1.25, 0) and their evolution in size with the annealing time has been determined. In particular, clear evidence was found and quantified that 113's grow in length and in width, the latter of which cannot be measured by TEM. The presence of a mixed population of both IRD's and {1Hex}ZD's was observed by combining the information from the measurements close to (1.25, 1.25, 0) position and close to the 220 Bragg peak. The relative percentage of IRD and {1Hex}ZD cannot be determined exactly, nevertheless, following the results obtained for DXS close to (1.25, 1.25, 0) position, {1Hex}ZD is the predominant type (> 50%).

8. General conclusions and outlook

In the present work, the development and application of a combination of x-ray scattering methods has been presented, which enable the characterisation of the structural properties of silicon after ultra-low energy ion implantation and annealing.

SR and conventional XRD have been used to investigate the layered structure of the samples. The profiles of the electronic density, obtained by fitting the SR curves, provided information on the amorphous sub-surface layers. In particular, the formation of a sub-nm-thick layer composed of segregated As beneath the SiO_2 surface-layer was found. The crystalline layered structure was studied by XRD to investigate the SPER of the As-induced amorphisation of Si, confirming that the high concentration of As dopant atoms induces a decrease of the SPER rate.

Grazing-incidence diffuse x-ray scattering (GI-DXS) is the main technique applied, because of its unique sensitivity to the defect structure in thin crystalline layers. GI-DXS proved to be ideally suited for the investigation of the end-of-range (EOR) defects, which play an important role in the diffusion of the implanted dopant atoms. GI-DXS was already applied before to study point defects and dislocation loops [1.77, 1.78]. In the frame of this PhD thesis, this capability has been extended to ultra-thin sub-surface layers and to the detection of {113}-defects. The experimental evidence of the growth in width of these rod-shape defects is an important result that will be exploited for the modelling of the evolution of EOR damage upon annealing. In addition, the transformation of small ”magic clusters” into FDL’s following conservative Ostwald ripening has been investigated, showing that GI-DXS enables the simultaneous observation of both the reduction of the ”magic clusters” and the growth of the FDL’s. In conclusion, GI-DXS is sensitive, in particular, to all types of defects based on silicon interstitials present in the EOR region, from small “magic clusters” to extended defects, such as {113}-defects and faulted dislocation loops.

The current industrial process (by AMD) for the fabrication of n-type drain extension channel junctions (DECJ) uses pre-amorphisation and spike annealing processing. The corresponding “PAI Spike” sample was investigated in detail. It was shown that the influence of the EOR defects on the ultra-shallow junction (USJ) structure can be excluded, if the location of this defect band is deep enough (~ 100 nm). In the USJ region (depth < 30 nm), nearly no residual defects were observed, confirming the high crystalline quality of the solid phase epitaxial regrowth. The main defect present in this region is the electrically active substitutional As. Its presence induces a hydrostatic contraction of the Si lattice by affecting

the electronic band structure, but no deviations from the average contracted lattice. As a result, substitutional As does not give rise to DXS intensity. In As-implanted Si, the average contraction of the lattice parameter is observed only in the SPER direction, because the lateral lattice parameter of the implanted layer is pseudomorphically strained.

In the present work, emphasis has been put on the comparison of our results with the ones from other techniques for structural characterisation. To this end, the collaboration among the IMPULSE project partners has been of fundamental importance to access the data from MEIS, SIMS and TEM techniques measured on the very same samples. In the detailed sample-by-sample comparison excellent agreement has been found and/or the combined x-ray scattering methods have given complementary structural information. In this respect, the sensitivity of GI-DXS to the EOR defects, whose detection is not possible by MEIS or by SIMS, is of crucial importance. The EOR defects can be characterised only by TEM and compared to the GI-DXS results. The advantages of GI-DXS are that it is a non-destructive technique, no sample preparation is needed, the statistical accuracy of the information is very high and small point defects can be detected, which cannot be seen by TEM. The main drawback of GI-DXS is the lack of the quantification for the absolute defect concentration.

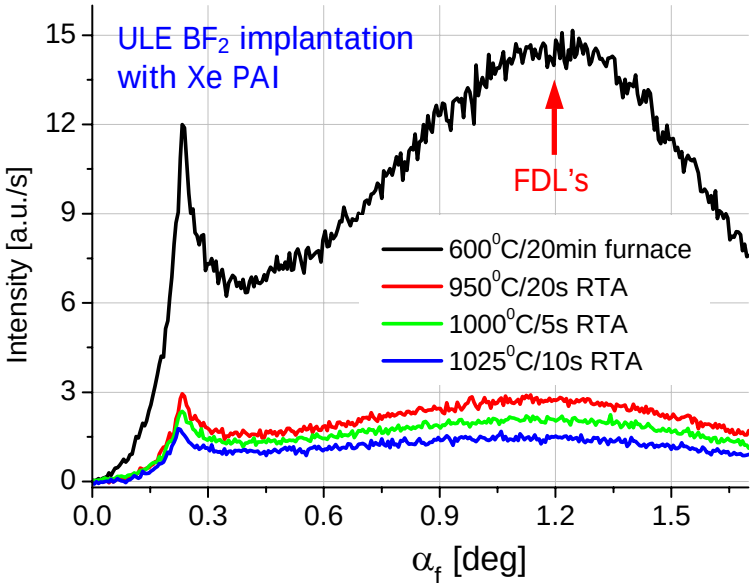

Figure 8.1: Diffuse x-ray scattering intensity distribution along q_z measured at 8 keV, $\alpha_i = 0.68\alpha_c$, $q_r = 0.14$ Å^{-1} for BF_2 implantation at 3keV; dose 7x10^{14} cm^{-2} with Xe PAI at 40 keV; dose 1x10^{14} cm^{-2}.

The advancement achieved with this PhD work has contributed to develop an experimental method that can now be applied to investigate other kinds of ion-implantation processes. In particular, the characterisation of boron and boron fluoride ultra-low-energy implants for the manufacturing of p-type DECJ is a promising field. Some preliminary GI-

DXS measurements have been already performed on ID01, such as the q_z-resolved DXS measurements at $\alpha_i = 0.68\alpha_c$ and $q_r = 0.14$ Å^{-1} shown in Fig. 8.1. A DXS hump centred at $\alpha_f \sim 1.2$ deg is present for all the samples, whose intensity reduces for higher thermal budgets. It is ascribed to the presence of FDL's in SPER region of the BF_2 implanted samples. The concentration of FDL's decreases upon annealing. MEIS and SIMS measurements have shown that, at the same depth, an accumulation of Xe and F atoms is observed [4.3], which is most likely related to the presence of FDL's. This type of defects has never been observed for PAI arsenic-implanted Si samples in the USJ region.

For EOR defects in ion-implanted Si, the formation of di-interstitials followed by the aggregation of "magic clusters" has been derived from the study of dopant diffusion by SIMS and from theoretical calculations. GI-DXS could be exploited to provide direct evidences of the Si self-interstitials clustering during the initial phase of the annealing.

Such a study could also be done *in-situ* to follow the defects evolution upon annealing during the "lifetime" of the Si interstitial in supersaturation from point to extended defects. Simultaneously, the role of the surface as a sink for the excess Si interstitials could be investigated as a function of the parameters of the implantation and annealing process.

Ion implantation at high doses amorphises the Si substrate. For the structural characterisation of these as-implanted systems, x-rays can be used to study the degree of amorphisation by measuring the amorphous structure factor of these ultra-thin layers using the grazing-incidence scattering geometry. The level of local ordering in the amorphised layer could be responsible for the variation of the SPER rate after ion implantation.

In order to improve our knowledge on the complex stoichiometry of native and thermally grown silicon oxides, SR measurements could be applied to study the mechanism of the oxide growth and structure in presence and on top of a segregated layer of dopant atoms.

All these x-ray scattering methods could be performed exploiting the changes of the atomic form factor close to absorption edges, if enhanced chemical sensitivity would be needed.

In conclusion, in the present work the capabilities of the combined x-ray scattering methods have been demonstrated and ideas for new challenging applications of this experimental tool are already available.

Bibliography:

1.1 P. S. Peercy, Nature, **406**, 1023 (2000).
1.2 L. Shon-Roy, *Advanced Semiconductor Fabrication Handbook*, (Integrated Circuit Corporation, Scottsdale, Arizona, 1998).
1.3 T. Feudel, M. Horstmann, D. Greenlaw, *Advanced annealing for μP Technologies*, oral presentation at IMPULSE project meeting, 11th October 2004, Dresden, DE.
1.4 Material Research Society Bulletin, Vol.25, Num. 6, *Defects and Diffusion in Silicon Technology* edited by T.E. Haynes, (Material Research Society, Pittsburg, 2000).
1.5 http://public.itrs.net.
1.6 T. Feudel, M. Horstmann, M. Gerhardt, M. Herden, L. Herrmann, D. Gehre, C. Krueger, D. Greenlaw, M. Raab, Mater. Sci. Semicond. Proces., **7**, 369 (2004).
1.7 P. A. Packan, Material Research Society Bulletin, **25**, 18 (2000).
1.8 T. Feudel, *Prototype Device Characterisation*, internal IMPULSE project report.
1.9 R. S. Ohl, Bell Syst. Tech. J., **31**, 104 (1952).
1.10 E. Chason, S. T. Picraux, J. M. Poate, J. O. Borland, M. I. Current, T. Diaz de la Rubia, D. J. Eaglesham, O. W. Holland, M. E. Law, C. W. Magee, J. W. Mayer, J. Melngailis, A. F. Tasch, J. Appl. Phys., **81**, 10 (1997).
1.11 J. F. Ziegler, SRIM-Stopping and Range of Ions in Matter-, (Pergamon Press, New York, 1985).
1.12 http://www.srim.org
1.13 P. Pichler, *Solid-Phase Epitaxial Regrowth*, unpublished.
1.14 B. L. Crowder, J. Electrochem. Soc., **117**, 671 (1970).
1.15 R. S. Nelson, D. J. Mazey, *A study of irradiation damage produced during ion bombardment in silicon* in International conference on application of ion beams to semiconductor technology, edited by P. Glotin, (Ed. OPHRYS, Grenoble, 1967), p. 337.
1.16 H. Muller, W. K. Chu, J. W. Maier, T. W. Sigmon, T. R. Cass, Appl. Phys. Lett., **26**, 292 (1975).
1.17 L. Csepregi, J. M. Mayer, T. W. Sigmon, Phys. Lett. A, **54**, 157 (1975).
1.18 G. L. Olson, *Kinetics and mechanisms of solid phase epitaxy and competitive processes in silicon* in Mater. Res. Soc. Symp. Prot. Vol.35 in Energy Beam- Solid Interactions and Transient Thermal Processing, edited by D. K. Bieglsen, G. A. Rozgonyi, C. V. Shank, 25 (1985).
1.19 J. S. Williams, R.G. Elliman, Appl. Phys. Lett., **37**, 829 (1980).
1.20 J. S. Williams, R.G. Elliman Nucl. Instr. Meth., **182-183**, 389 (1981).
1.21 J. S. Williams, R.G. Elliman, Appl. Phys. Lett., **40**, 266 (1982).
1.22 G. L. Olson, J. A. Roth, Mater. Sci. Rep.,**3**, 1 (1988).
1.23 C. Carter, W. Maszara, D.K. Sadana, G.A. Rozgonyi, J. Liu, J. Wortman, Appl. Phys. Lett., **44**, 459 (1984).
1.24 T. Sands, J. Washburn, R. Gonsky, W. Maszara, D. K. Sadana, G. A. Rozgonyi, Appl. Phys. Lett., **45**, 982 (1984).
1.25 B. L. Crowder, J. Electrochem. Soc., **118**, 943 (1971).
1.26 H. Nishi, T. Sakurai, T. Furuya, J. Electrochem. Soc., **125**, 461 (1978).
1.27 H. Bracht, Material Research Society Bulletin, **25**, 22 (2000).
1.28 H. Bracht, E.E. Haller, R. Clark-Phelps, Phys. Rev. Lett., **81**, 393 (1988).
1.29 S. R. Aid, T. Sakaguchi, K. Toyonaga, Y. Nakabayashi, S. Matumoto, M. Sakuraba, Y. Shimamune, Y. Hashiba, J. Murota, K. Wada, T. Abe, Mater. Sci. Eng. B, **114-115**, 330 (2004).
1.30 P.M. Fahey, P.B. Griffin, J. D. Plummer, Rev. Mod. Phys., **61**, 289 (1989).
1.31 P.M. Fahey, S.S. Iyer, G. J. Scilla, Appl. Phys. Lett., **54**, 843 (1989).
1.32 S. M. Hu, Mater. Sci. Eng. R**, 13**, 105 (1994).
1.33 A. E. Michel, W. Rausch, P. A. Ronaheim, R. H. Kastl, Appl. Phys. Lett, **50**,416 (1987).
1.34 P.A. Stock, H.J. Gossman, D. J. Ealesham D.C. Jacobson, C. S. Rafferty, H. S. Luftman, T.E. Haynes, J. Appl. Phys. **81**,1 (1997).
1.35 D. J. Eaglesham, P.A. Stoclk, H. J. Gossmann, J. M. Poate, Appl. Phys. Lett., **65**, 2305 (1994).
1.36 C. Bonafos, M. Omri, B. de Maudit, G. Ben Assayag, A. Claverie, D. Alquier, A. Martinez, D. Mathiot, J. Appl. Phys., **82**, 2855(1997).
1.37 E. Lampin, F. Cristiano, Y. Lamrani, A. Claverie, B. Colombeau, N. E. B. Cowern, J. Appl. Phys. **94**, 7520 (2003).
1.38 K. Suzuki, FUJITSU Sci. Tech. J., **39**, 138 (2003).
1.39 G. Mannino, V. Privitera, S. Solmi, N. E. B. Cowern, Nucl. Instr. Meth. Phys. Res. B,**186**, 246 (2002).
1.40 L. Shao, J. Liu, Q. Y. Chen, W. Chu, Mater. Res. and Eng. R, **42**, 65 (2003).
1.41 R. Pinacho, M. Jaraiz, P. Castrillo, J. E. Rubio, I. Martin-Bragado, J. Barbolla, Mater. Sci. Eng. B, **114-115**, 153 (2004).

1.42 S. Uppal, J. M. Bonar, J. Zhang, A. F. W. Willoughby, Mater. Sci. Eng. B, **114-115**, 349 (2004).
1.43 L. Pelaz, G. H. Gilmer, H. J. Gossman, C. S. Rafferty, Appl. Phys. Lett., **74**, 3657 (1999).
1.44 W. Windl, X. Y. Liu, M. P.. Masquelier, Phys. Stat. Sol. B, **226**, 37 (2001).
1.45 B. J. Pawlak, R. Surdeanu, B. Colomeau, A. J. Smith, N. E. B. Cowern, R. Linsay, W. Vandervorst, O. Richard, F. Cristiano, Appl. Phys. Lett., **84**, 2055 (2004).
1.46 E. Lampin, V. Senez, A. Claverie, J. Appl. Phys., **85**, 8137 (1999).
1.47 A. Claverie, B. Colombeau, B. De Maudit, C. Bonafos, X. Hebras, G. Ben Assayag, F. Cristiano, Appl. Phys. A, **75**, 1025 (2003).
1.48 L. Laânab, C. Bergaud, M.M. Faye, J. Fauré. A. Martinez, A. Claverie, Mater. Res. Soc. Symp. Prot., **249**, 381 (1993).
1.49 A. Claverie, C. Bonafos, D. Alquier, A. Martinez, Sol. State Phys. V, **47-48**, 195 (1996).
1.50 M. D. Giles, J. Electrochem. Soc., **138**, 1160(1991).
1.51 J. W. Corbett, J. P. Karins, T. Y. Tan, Nucl. Instr. Meth. Phys. Res. B, **182-183**, 457 (1981).
1.52 N. E. B. Cowern, G. Mannino, P.A. Stolk, F. Roozeboom, H. G. A. Huizing, J. G. M. van Berkum, F. Cristiano, A. Claverie, M. Jaraíz, Phys. Rev. Lett., **82**, 4460 (1999).
1.53 F. Cristiano, A. Claverie, oral presentation at the 1st FRENDTECH workshop, 11th February 2003, Erlagen, DE.
1.54 C. A. Ferreira Lima, A. Howie, Phil. Mag. A, **36**, 1057 (1976).
1.55 I. G. Salisbury, M. H. Loretto, Phil. Mag. A, **39**, 317 (1979).
1.56 D. J. Eaglesham, P.A. Stoclk, J. Y. Cheng, H. J. Gossmann, T. E. Haynes, J. M. Poate, Prot. Microsc. Semicond. Mater. Conf. (Oxford, 20-23 March 1995), edited by A.G. Cullis, A. E. Stanton-Bevan (Institut of Physics, Bristol, 1995), p. 451.
1.57 S. Takeda, Prot. Microsc. Semicond. Mater. Conf. (Oxford, 7-10 April 1997), edited by A.G. Cullis, A. E. Stanton-Bevan (Institut of Physics, Bristol, 1997), p. 25.
1.58 A. Parisini, A. Bourret, Phil. Mag. A, **67**, 605 (1993).
1.59 A. Parisini, A. Bourret, *Société française de microscopie électronique- Société belge de microscopie électronique, colloque Franco-belge, Résume des communications, Villeneuve d'Ascq (Lille)* edited by (SFHE, Paris, 1988), p. 19a.
1.60 S. Takeda, Jpn. J. Appl. Phys., **30**, L639 (1991).
1.61 A. Bourret, *Microscopy of Semiconducting Materials, Institute of Physics Conference Series*, edited by (Institute of Physics, Bristol, 1987), p. 39.
1.62 K. Nordlund, J. Appl. Phys., **91**, 2978 (2002).
1.63 V. C. Venezia, R. Kalyanaraman, H. J. L. Gossmann, C. S. Rafferty, P. Werner, Appl. Phys. Lett., **79**, 1429 (2001).
1.64 C. J. Oritz, F. Cristiano, B, Colombeau, A. Claverie, N. E. B. Cowern, Mater. Sci. Eng. B, **114-115**, 184 (2004).
1.65 B. de Maudit, L. Laânab, C. Bergaud, M. M. Faye, J. Fauré, A. Martinez, A. Claverie, Nucl. Instr. Meth. Phys. Res. B, **84**, 190 (1994).
1.66 M. Stzucki, "Diplom" thesis, University of Munich, DE, January 2001.
1.67 F. Cristiano, J. Grisolia, B. Colombeau, M. Omri, B. de Maudit, A. Claverie, L. F. Giles, N. E. B. Cowern, J. Appl. Phys., **87**, 8420 (2000).
1.68 B. Colombeau, F. Cristiano, A. Altibelli, C. Bonafos, G. Ben Assayag, A. Claverie, Appl. Phys. Lett., **78**, 940 (2001).
1.69 N. E. B. Cowern, D. Alquier, M. Omri, A. Claverie, A. Nejim, Nucl. Instr. Meth. Phys. Res. B, **148**, 257 (1999).
1.70 A. Claverie, B. Colombeau, G. Ben Assayag, C. Bonafos, F. Cristiano, M. Omri, B. de Maudit, Mater. Sci. Semicond. Proces., **3**, 269 (2000).
1.71 R. G. Wilson, F. A. Stevie, C. W. Magee, *Secondary Ion Mass Spectrometry*, (John Wiley Ldt., New York, 1989).
1.72 K. Wittmaack, Appl. Surf. Sci. **203-204,** 20 (2003).
1.73 W. Vandervorst, T. Janssens, B. Brijs, T. Conard, C. Huyghebaerta, J. Frühauf, A. Bergmaier, G. Dollinger, T. Buyuklimanli, J.A. VandenBerg, K. Kimura, Appl. Surf. Sci. **231-232,** 618 (2004).
1.74 P.A.W. van der Heide, M.S. Lim, S.S. Perry, J. Bennett, Nucl. Instr. Meth. Phys. Res. B, **201**, 413 (2003).
1.75 R. M. Tromp, *Medium Energy Ion Scattering* in: *Practical Surface Analysis Vol.2-Ion and Neutral Spectroscopy*- edited by D. Briggs, P. Seah (John Wiley Ldt., New York, 1992).
1.76 J. A. Van den Berg, D. G. Armour, S. Zhang, S, Whelan, H. Ohno, T. S. Wang, A. G. Cullis, E. H. J. Collart, R. D. Goldberg, P. Bailey, T. C. Q. Noakes, J. Vac. Sci. Technol. B, **20**, 974 (2002).
1.77 U. Beck, T. H. Metzger, J. Peisl, J.R. Patel, Appl. Phys. Lett., **76**, 2698 (2000).
1.78 M. Sztucki, T.H. Metzger, I. Kegel, A. Tilke, J. L. Rouvière, D. Lübbert, J. Arthur, J. Patel, J. Appl. Phys., **92**, 3694 (2002).
2.1 K. Huang, Proc. R. Soc. London, Ser. A, **190**, 102 (1947).

2.2 M. A. Krivoglaz, *Diffraction of x-rays and neutrons from Non-Ideal Crystals*, (Springer, Berlin, 1996).
2.3 P. Ehrhart, W. Shilling, Phys. Rev. B, **8**, 2604 (1973).
2.4 P. Ehrhart, J. Nucl. Mater., **69&70**, 200 (1978).
2.5 P. H. Dederichs, J. Phys. F, **3**, 471 (1973).
2.6 P. Ehrhart, J. Nucl. Mater., **216**, 170 (1994).
2.7 B. E. Warren, *X-ray diffraction*, (Dover Publ., New York, 1990).
2.8 J. Als-Nielsen, D. McMorrow, *Elements of X-Ray Physics*, (J. Winley & Sons, Inc., New York, 2001).
2.9 U. Pietsch, V. Holý, T. Baumbach, *High-Resolution X-ray Scattering from Thin Films and Lateral Nanostructures*, (Spinger, Berlin, 2004).
2.10 J. Peisel, *Lattice Distortion, Elastic Interaction, and Phase Transitions of Hydrogen in Metals*, in Festkörperprobleme (Advances in Solid State Physics) edited by P. Gosse, (Vieweg, Braunschweig, 1984), Vol. 24, p.45
2.11 B. C. Larson, W. Schmatz, Phys. Stat. Sol. B., **99**, 267 (1980).
2.12 K. Nordlund, P. Partyka, R. S. Averback, I. K. Robinson, P. Ehrhart, J. Appl. Phys., **88**, 2278 (2000).
2.13 K. Nordlund, U. Beck, T. H. Metzger, J. R. Patel, Appl. Phys. Lett, **76**, 846 (2000).
2.14 P. Ehrhart, T. Trinkaus, B. C. Larson, Phys. Rev. B, **25**, 834 (1982).
2.15 H. Dosch, *Critical Phenomena at Surfaces and Interfaces: Evanescent X-Ray and Neutron Scattering*, (Springer, Berlin, 1992).
2.16 M. Tolan, *X-Ray Scattering from Soft-Matter and Thin Films-Materials Science and Basic Research-*, (Spinger, Berlin, 1999).
2.17 G. H. Vineyard, Phys. Rev. B, **26**, 4146 (1982).
2.18 S. K. Sinha, E. B. Sirota, S. Garoff, H. B. Stanley, Phys. Rev. B, **38**, 2297 (1988).
2.19 U. Pietsch, Curr. Sci., **78**, 1484 (2000).
2.20 I. K. Robinson, D. J. Tweet, Rep. Prog. Phys., **55**, 599 (1992).
2.21 C. Lamberti, Surf. Sci. Rep., **53**, 1 (2004).
2.22 D. Luebbert, J. Arthur, M. Sztucki, T. H. Metzger, P. B. Griffin, J. Patel, Appl. Phys. Lett., **81**, 3167, (2002).
2.23 M. Sztucki, T.H. Metzger, S. Milita, F. Berberich, N. Schell, J. L. Rouvière, J. Patel, Nucl. Instr. Meth. Phys. Res. B, **200**, 52 (2003).
2.24 Y. Takamura, A. F. Marshall, A. Mehta, J. Arthur, P.B. Griffin, J. Plummer, J. Patel, J. Appl. Phys., **95**, 3968 (2004).
2.25 R. I. Barabash, M. A. Krivoglaz, Sov. Phys. Solid State, **29**, 1768 (1987).
3.1 http://www.esrf.fr
3.2 D. Raoux, *Introduction to synchrotron radiation and to the physics of storage rings* in Neutron and synchrotron radiation for condensed matter studies –theory, instruments and methods-, Vol.1 (Springer, Berlin, 1993).
3.3 http://www.esrf.fr/exp_facilities/ID1/user_guide
3.4 M. J. Capitan, D. Thiaudiere, L. Goirand, R. Taffut, S. Lequien, Phys. B, **283**, 256 (2000).
3.5 M. Servidori, F. Cembali, S. Milita, Characterisation of lattice defects in ion-implanted Si in the book *X-ray and Neutron dynamical diffraction: Theory and Application*, A. Autiers, S. Lagomarsino, B.K. Tanner and R. Colella Editors, (Plenum Press, New York, 1996).
3.6 S. Milita, M. Servidori, J. Appl. Phys., **79**, 8278 (1996).
3.7 L. G. Parrat, Phys. Rev., **95**, 359 (1954).
3.8 B. L. Henke, E. M. Gullikson, J. C. Davis, Atomic Data and Nuclear Data Tables Vol. 54, No. 2, (1993); ftp://xray.uu.se/pub/henke
4.1 G. S. Cargill, J. Angilello, K. L. Kavanagh, Phys. Rev. Lett. **61**, 1748 (1988).
4.2 A. Parisini, A. Bourret, A. Armigliato, M. Servidori, S. Solmi, R. Fabbri, J. R. Rignard, J. L. Allain, J. Appl. Phys., **67**, 2320 (1990).
4.3 M. Werner, PhD thesis, University of Salford, Salford, UK, 2005 to be discussed.
5.1 http://sergey.gmca.aps.anl.gov
5.2 Y. Lamrani, F. Cristiano, B. Colombeau, E. Scheid, P. Calvo, H. Schäfer, A. Claverie, Nucl. Instr. Meth. Phys. Res. B, **216**, 281 (2004).
5.3 M. Werner, J. A. van den Berg, D. G. Armour, W. Vandervorst, E. H. J. Collart, R. D. Goldberg, P. Bailey, T. C. Q. Noakes., Nucl. Instr. Meth. Phys. Res. B, **216,** 67 (2004).
5.4 J.A. van den Berg, D. G. Armour, M. Werner, S. Whelan, W. Vandervorst, T. Clarysse, E. H. J. Collart, R. D. Goldberg, P Bailey, T. C. Q. Noakes. Proc Int Conf. on Ion Implantation Technology (ITT 2002), (Sept 2002), IEEE Operations Center, Piscataway, NJ 08855-1331. p. 597 (2003).
5.5 A H Al-Bayati, K Ormannn- Rossiter, J A van den Berg and D G Armour, Surface Sci, **241,** 91 (1991).
5.6 J. Dabrowski, H.-J. Mussig, V. Zavodinsky, R. Baierle and, M. J. Caldas, Phys. Rev. B, **65**, 245305 (2002)
5.7 L. Ottaviano, PhD thesis, University of Catania, Catania, I, 2005 to be discussed.

6.1 G. K. Vemulapalli, *Chimica Fisica*, (EdiSES, Napoli, 1995).
6.2 L. Capello, T. H. Metzger, Mat. Sci. Eng. B, **114-115**, 77 (2004).
6.3 C. Bonafos, D. Mathiot, A. Claverie, J. Appl. Phys., **83**, 3008 (1998).
6.4 D. Giubertoni, M. Bersani, IMPULSE project internal report, 09/2004.
7.1 W. Lerch, S. Paul, J. Niess, F. Cristiano, Y. Lamrani, P. Calvo, N. Cherkashin, D. F. Downey, E.A. Arevalo, Electrochem. Soc. Proc., **2004-01**, 90 (2004).
7.2 K. Nordlund, private communication.
7.3 P. Calvo, A. Claverie, N. Cherkashin, B. Colombeau, Y. Lamrani, B. de Maudit, F. Cristiano, Nucl. Instr. Meth. Phys. Res. B, **216,** 173 (2004).
A.1 www.imm.cnr.it/imm/progetti/projects/impulse/impulse_home.html

Appendix: The IMPULSE project

The work reported in this PhD thesis has been performed within the European project ion-IMPlantation at Ultra-Low energy for future SEmiconductor devices (acronym IMPULSE; IST-2001-32061). The European Union partly financed my PhD grant jointly with the ESRF. This Appendix contains a brief summary of the activities of the IMPULSE project to appreciate the role of my work in the frame of this research consortium.

A.1 Aims of the European project IMPULSE

The IMPULSE project lasted three years starting from November 2001 and was financed within the European call for projects FP5. This project dealt with one of the major issues of concern for the semiconductor industry, namely the realisation of USJ's by means of ultra-low energy ion-implantation and rapid thermal annealing. The main general objectives of the research activity will be briefly summarised.

The first goal concerned the development of a comprehensive view of the atomic transport and electrical activation behaviour of dopants implanted in Si in the ultra-low energy regime. This task was based on the comparison of the dopant profiles obtained by SIMS and spreading resistance profiling (SRP). SIMS provided the chemical profile of the dopant atoms, whereas SPR measured the electrical profile of the activated dopant atoms.

The second aim was the achievement of the complete characterization of the damage induced by implants of arsenic and boron fluoride at energies in the range from 1 to 3 keV, for as-implanted samples and after annealing. The implanted-Si structural characterization has been performed based on the analysis and modelling of the results from MEIS and x-ray scattering methods. TEM imaging was also used.

The final goal of the IMPULSE project was the fabrication of a device with ultra-shallow junctions of high electrical performances, which implemented the knowledge acquired within the project consortium.

A.2 The project partners and their tasks

Five research centres and one industrial partner shared the IMPULSE tasks. The activity was organised on the base of a Gannt chart established in the beginning of the project and

shown in Fig. A.1. The project activities were divided in work packages (WP's) and tasks (T's), following the rules of the European Community.

Under the coordination of M. Servidori from the IMM-CRN Institute of Bologna, who was in charge of WP1 -project management-, the work was organised in the way described hereafter. The industrial partner, AMD Company from Dresden (D), took care of work packages WP2 and WP4. WP2 consisted of the implantation, i.e. the identification of the industrial needs and the preparation of the samples using industrial equipment and processing technology. In WP4, the results from the characterisation of the samples, which was performed within the consortium, were implemented in the industrial products.

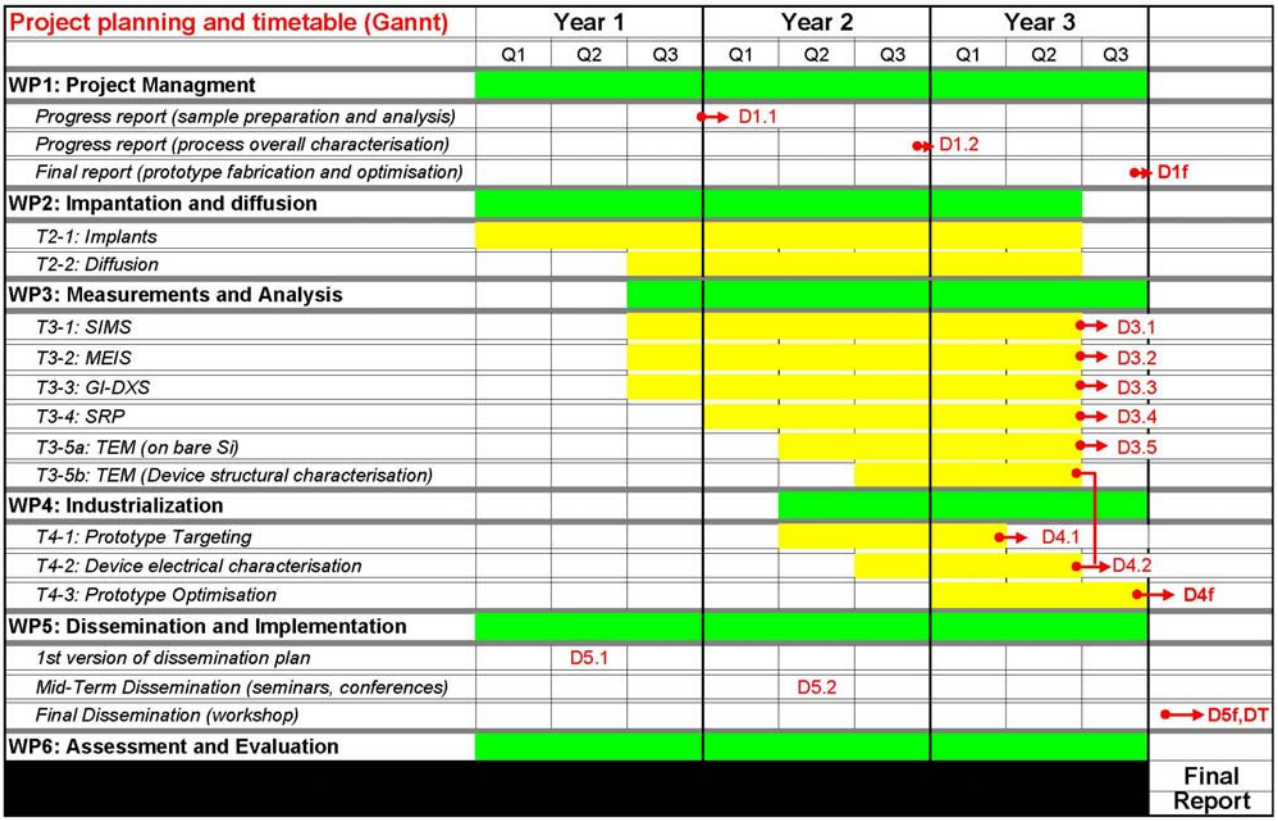

Figure A.1: Gannt chart for the organisation of the activities within the IMPULSE project. Figure taken from [A.1].

The main WP was WP3, where all of the measurements and analysis were included. The SIMS analysis were performed by ITC-Irst from Trento (I). The responsible for this task (T), called T3-1, was M. Bersani. The MEIS measurements (i.e. T3-2) were carried out by the group from the University of Salford, Salford (UK), headed by J. van den Berg. The SPR and TEM analysis were performed by the IMM-CNR partner from Catania (I). Finally, T3-3 was about the characterisation of ion implanted Si using x-ray scattering methods. This task was

accomplished by the ESRF group and a part of the results from the analysis has been reported in this thesis. T. H. Metzger, scientist in charge of the ID01 beamline, was the project responsible for the ESRF partner.

The European Community believes that the dissemination of the scientific knowledge gained within a research project (WP5) is of central interest. To this aim, during the IMPULSE, the consortium organised two workshops. This first one was scheduled in the frame of the European Material Research Society Conference -Strasbourg (F), 24th-28th May 2004- and it was called “Material science issues in advanced CMOS source-drain engineering”. The second was an independent workshop named “Recent advances in ultra-shallow junctions”, held in Trento (I), on the 24th -25th November 2004. All the IMPULSE project partners contributed to the realisation of the workshops.

Moreover, yearly written reports (indicated as $Dn_1.n_2$ in the Gannt Chart, Fig. A.1) were due to the referees from the European Community and several meetings of the members of the consortium were organised every six months at least, in order to enhance the exchange of the information among the IMPULSE partners.

The present PhD thesis was partly financed in the frame of the IMPULSE project.

Etude par des méthodes de diffusion de rayons X des propriétés structurales du silicium après implantation ionique.

L'implantation ionique à très basse énergie (< 5keV) dans le silicium est utilisée pour la production de transistors CMOS. Les défauts présents dans le Si après implantation et recuit jouent un rôle crucial pour les performances du dispositif et, de ce fait, leur caractérisation structurale est fondamentale. Dans ce travail, je vais montrer que la combinaison de différentes techniques de diffusion de rayons X est une méthode puissante et non destructive pour réaliser ce but. La diffraction de rayons X révèle la distribution en profondeur de la contrainte dans le cristal de Si et la réflectivité spéculaire le profil de la densité électronique. La diffusion diffuse à incidence rasante (GI-DXS) permet de distinguer les défauts ponctuels des défauts étendus avec une résolution en profondeur. En raison du faible signal des défauts, l'utilisation du rayonnement synchrotron est nécessaire. GI-DXS est particulièrement adaptée à la caractérisation des défauts de fin de parcours.

Mots clés: implantation ionique, défauts, diffusion diffuse de rayons X, diffusion de rayons X à incidence rasante, rayonnement synchrotron

……...

Structural investigation of silicon after ion-implantation using combined x-ray scattering methods.

Ultra-low energy (< 5keV) ion implantation in silicon is used industrially in manufacturing complementary metal-oxide semiconductor devices. The unavoidable defects present in Si after ion implantation and annealing play a crucial role for the device performance. Therefore, the structural characterisation of such defects is of great relevance. In this work, it will be shown that the combination of different x-ray scattering methods represents an ideal non-destructive tool to achieve this task. X-ray diffraction reveals the depth distribution of the lattice strain and specular reflectivity provides the electron density profile. Grazing incidence diffuse x-ray scattering (GI-DXS) is sensitive to point and extended defects, with depth resolution. The low intensity of the diffuse signal arising from such defects requires the high brilliance of synchrotron radiation. GI-DXS is especially well suited to investigate the "end-of-range" defects.

Key words: ion implantation, defects, diffuse x-ray scattering, grazing incidence x-ray scattering, synchrotron radiation

……...

Discipline: Physique des matériaux

……...

Laboratoires de rattachement: Laboratoire LPMCN, Université Lyon I - Claude Bernard, 43, Bd du 11 Novembre 1918 ; F-69622 Villeurbanne Cedex, France; Department of Inorganic, Physical and Materials Chemistry, Universitá degli Studi di Torino, Via P. Giuria n° 7; I-10125 Torino, Italy